Additive Manufacturing of Architected Structures for Healthcare Applications

by

Elham Davoodi

A thesis
presented to the University of Waterloo
in fulfillment of the
thesis requirement for the degree of
Doctor of Philosophy
in
Mechanical and Mechatronics Engineering

Waterloo, Ontario, Canada, 2021

Examining Committee Membership

The following served on the Examining Committee for this thesis. The decision of the Examining Committee is by majority vote.

External Examiner: Prof. Daniel Therriault
Dept. of Mechanical Engineering
Polytechnique Montreal

Supervisor: Prof. Ehsan Toyserkani
Dept. of Mechanical and Mechatronics Engineering
University of Waterloo

Internal Member: Assoc. Prof. Armaghan Salehian
Dept. of Mechanical and Mechatronics Engineering
University of Waterloo

Internal Member: Assoc. Prof. Hyock Ju Kwon
Dept. of Mechanical and Mechatronics Engineering
University of Waterloo

Internal-External Member: Prof. Boxin Zhao
Dept. of Chemical Engineering
University of Waterloo

Author's Declaration

This thesis consists of material all of which I authored or co-authored: See Statement of Contributions included in the thesis. This is a true copy of the thesis, including any required final revisions, as accepted by my examiners.

I understand that my thesis may be made electronically available to the public.

Statement of Contributions

I would like to acknowledge my co-authors who contributed to the research described in the current thesis:

Prof. Ehsan Toyserkani: Supervising the research, providing ideas for the research, reviewing and editing the papers, and providing the lab facilities.

Prof. Ali Khademhosseini: Guiding the research work, valuable discussions, reviewing and editing the papers, and providing the lab facilities.

Prof. Paul. S. Weiss: Valuable discussions, reviewing and editing the papers.

Prof. Jun Chen: Valuable discussions, reviewing and editing the paper presented in chapter 5.

Prof. Abbas S. Milani: Providing lab facilities, reviewing and editing the papers presented in chapter 5 and 7.

Prof. Mina Hoorfar: Reviewing and editing the papers presented in chapter 5 and 7.

Prof. Homeyra Pourmohammadalia: Reviewing and editing the paper presented in chapter 6.

Prof. Hamid Jahed: Providing lab facilities, reviewing and editing the paper presented in chapter 7.

Dr. Javad Kadkhodapour: Providing lab facilities, reviewing and editing the paper presented in chapter 7.

Dr. Amir Sheikhi: Reviewing the paper presented in chapter 5.

Dr. Samad Ahadian: Reviewing and editing the paper presented in chapter 6.

Dr. Haniyeh Fayazfar: Measuring the size of the 3D printed samples using the confocal laser-optical profilometer and helping with human motion detection experiments for chapter 3.

Dr. Farzad Liravi: Helping with 3D printing of the samples for chapter 3.

Dr. Elahe Jabari: Valuable discussions for the research presented in chapter 3.

Hossein Montazerian: Valuable discussions, helping with biocompatibility studies, helping with material development, reviewing papers.

Reza Esmaeilizadeh: Helping with mechanical and permeability tests presented in chapter 7.

Dr. Reihaneh Haghniaz: The degradation test and SEM images presented in chapter 5 and 6.

Armin Rashidi: Obtaining the profile of the samples in chapter 5.

Masoud Zhianmanesh: Simulations provided in chapter 6.

Ali Ch. Darabi: Simulations provided in chapter 7.

Abstract

This dissertation focuses on the development of architected structures via direct additive manufacturing (AM) and novel template-assisted techniques for sensing and tissue engineering applications. Although AM technologies have eased the fabrication of architected structures, limitations arise while printing high-flex 3D complex shapes. To date, no feasible fabrication method has been introduced for high-flex electronics with architected complex geometries in a three-dimensional system. In the current thesis, employing a high-speed material jetting system for direct 3D printing of high-viscose silicone-based inks with carbon fiber additives is introduced. The 3D printed sandwich-like sensors with a silicone-carbon fiber layer (as the sensitive counterpart) and two silicone layers (as the protective and packaging layers) showed enhanced durability for biomonitoring applications. The carbon fiber content was optimized and set to 30 wt.% for printability, UV curability, and electrical conductivity so that high piezoresistive sensitivity (gauge factor in order of ∼400) was obtained.

However, due to the limitations of direct 3D printing, a novel template-assisted fabrication process is introduced for the development of elastomeric structures with complex-shape designs. The silicone prepolymer was engineered with additives allowing on-demand structural shrinkage upon solvent treatment, and consequently, fabrication of micrometer-size features was feasible. This enabled 3D printing at a larger scale compatible with extrusion 3D printer resolution followed by isotropic shrinkage. This procedure led to a volumetric shrinkage of up to ~70% in a highly controllable manner. In this way, pore sizes in the order of 500–600 μm were obtained.

The proposed low-cost fabrication method not only enabled the high-resolution fabrication of complex-shaped elastomeric structures but was adopted and modified for the fabrication of 3D flexible electronics. In this dissertation, a fabrication scheme based on accessible methods is introduced to surface-dope porous silicone sensors with graphene. The sensors are internally shaped using fused deposition modeling (FDM) 3D printed sacrificial molds. The presented procedure exhibited a stable coating on the porous silicone samples with long term electrical resistance

durability over ∼12 months period and high resistance against harsh conditions (exposure to organic solvents). Besides, the sensors retained conductivity upon severe compressive deformations (over 75% compressive strain) with high strain-recoverability and behaved robustly in response to cyclic deformations (over 400 cycles), temperature, and humidity. The sensors exhibited a gauge factor as high as 10 within the compressive strain range of 2−10% and showed strong capability in sensing movements as rigorous as walking and running to the small deformations resulted by human pulse.

This dissertation also introduces a robust and scalable approach for forming 3D multilayered complexly architected perfusable networks within highly cellularized hydrogel constructs. Perfusable interconnected networks could assist in sustaining thick cellularized tissue constructs through uniform perfusion of body fluids. The hydrogel constructs were patterned through two-step sacrificial molding. The cell-laden hydrogel scaffolds showed high cell viability of over 90% and robust mechanical behavior.

Besides, conflicting design criteria in tissue engineering scaffolds necessitate investigating the structure-properties of the tissue engineering scaffolds and implants. This research shows that defining high local macroporosity at the implant/tissue interface improves the biological response. Gradually decreasing macroporosity from the surface to the center of the porous constructs provides mechanical strength. Furthermore, mechanical studies on the unit cell topology effects suggest that the bending dominated architectures can provide significantly enhanced strength and deformability, compared to stretching-dominated architectures in the case of complex loading scenarios.

Acknowledgments

I would like to express my deepest gratitude and appreciation to my supervisor, Prof. Ehsan Toyserkani for giving me the opportunity to elevate my knowledge and skills under his mentorship. This research would not be possible without his continuous support, guidance, and encouragement.

I truly acknowledge Prof. Ali Khademhosseini and Prof. Paul S. Weiss from UCLA for their guidance and continuous support throughout this research.

I also acknowledge my committee members, Prof. Daniel Therriault, Prof. Armaghan Salehian, Prof. Hyock Ju Kwon, and Prof. Boxin Zhao, for taking the time to review my thesis and for their valuable and constructive insights.

I sincerely thank Prof. Mina Hoorfar from UBC and Prof. Jun Chen from UCLA for their valuable scientific insights and support.

I would like to express special thanks to my colleagues at Multi-Scale Additive Manufacturing laboratory at University of Waterloo for their friendship, assistance, and scientific discussions. This research would not be possible without Dr. Elahe Jabari, Dr. Farzad Liravi, Dr. Haniyeh Fayazfar, and Reza Esmaeilizadeh.

I sincerely acknowledge Jerry Ratthapakdee, Karl Rautenberg, Grace Kurosad, Henry Ma, and Francis Dibia for all their help and advice.

I would like to thank technical staff at University of Waterloo, Mark Griffett and Richard Barber, for assisting me to perform part of my experiments in their labs.

I sincerely thank my colleagues at California NanoSystems Institute and Terasaki Institute for Biomedical Innovation for all their help and support during this research.

The most heartfelt appreciation goes to my mom, Shahla, and my dad, Abbas for continuous encouragement to follow my dreams. None of this would be possible without their kind support. Special thanks to my dear brother, Amir, who helped me to find my passion in engineering.

Finally, I should thank my best friend and colleague, my caring and supportive husband, Hossein for all his help and encouragement. This research would not be possible without our valuable scientific discussions.

To my family

Table of Contents

List of Figures

List of Tables

List of Abbreviations

2D	Two-dimensional
3D	Three-dimensional
AM	Additive Manufacturing
FDM	Fused Deposition Modeling
SLA	Stereolithography
MJ	Material Jetting
DOD	Drop-on-Demand
MCF	Milled Carbon Fiber
SR	Silicone Rubber
S-MCF/SR	Sandwiched Milled Carbon Fiber/Silicone Rubber
ST	Silicone Thinner
UV	Ultraviolet
RTV	Room Temperature Vulcanizing
STL	Standard Tessellation Language
CAD	Computer-Aided Design
DC	Direct Current
SEM	Scanning Electron Microscopy
CT	Computed Tomography
CyT	Cycle Time
OT	Open Time
CT	Closed Time
FCT	Fully Closed Time
PDMS	Polydimethylsiloxane
ABS	Acrylonitrile butadiene styrene
PVA	PolyVinyl Alcohol

PLA	Polylactic acid
SO	Silicone Oil
TPMS	Triply Periodic Minimal Surface
GelMA	Gelatin Methacryloyl
DMEM	Dulbecco's Modified Eagle's Medium
VC	Vinylcaprolactam
TEA	Triethanolamine
CVD	Chemical Vapor Deposition
GnP	Graphene Nanoplatelets
DLS	Dynamic light scattering
EDTA	Ethylenediaminetetraacetic Acid
DPBS	Dulbecco's Phosphate-Buffered Saline
FBS	Fetal Bovine Serum
IPA	Isopropyl Alcohol
SDG	Surface Deposited Graphene
SEG	Surface Embedded Graphene
FE	Finite Element
CAE	Computer-Aided Engineering
TGA	Thermogravimetric Analysis
HSP	Hansen Solubility Parameter
FEA	Finite Element Analysis
SLS	Selective Laser Sintering
DCM	Dichloromethane
TEMED	Tetramethylethylenediamine
APS	Ammonium Persulfate
ANOVA	Analysis of Variances

RD	Relative Density
SLM	Selective Laser Melting
LPBF	Laser Powder Bed Fusion
MA	Methacrylic Anhydride
RVE	Representative volume element

Chapter 1. Introduction

1.1. Motivations

One of the milestones in electronics engineering was the advent of the printed circuit board by an Austrian scientist, Paul Eisler, in 1936 [1]. However, the rigidity of conventional electronics restricts their use for high-flex applications. The development of additive manufacturing (AM) technologies has raised the standards of fabricating stretchable electronics in terms of resolution, complexity, reproducibility, feasibility, and sometimes the total cost or fabrication time, etc. [2-4]. Several AM techniques have been employed for stretchable electronics in the literature, such as extrusion-based printing [5], ink-jet printing [6, 7], aerosol-jet printing [8], screen printing [9], etc. Most of the AM technologies developed for stretchable electronics are either time-consuming like extrusion-based techniques, or wasteful and difficult to control like ink-jet printing. Although AM technologies offer many advantages over conventional methods, there are still many shortcomings, especially in stretchable electronics in architected three-dimensional (3D) shapes. 3D printing of elastomeric electronics is accompanied by limitations in terms of resolutions, scalability, conductivity, and geometry restrictions. AM limitations not only have restricted fabricating architected flexible electronics, but soft tissue engineering scaffolds with complex designs are also challenging to develop using the current 3D printing systems.

Architected elastomeric implants and scaffolds are emerging as potential replacements of flexible tissues, cosmetic and biomedical device implants due to their bioinert and flexible characteristics. The state-of-the-art direct-write silicone 3D printers, however, cannot easily 3D print structures with sub-millimeter dimensions because of the high viscosity and long curing times of their prepolymers. Though there have been some attempts to use template-assisted methods for fabricating elastomeric structures, the low feature size resolution is still an ongoing challenge that has been left unsolved. The low feature resolution and difficulty in forming over-hanging features are the common limitations in the 3D printing of soft materials, including elastomers and hydrogels.

Tissue engineering scaffolds architected with interconnected porosities enable a continuous flow of medium for improved cell viability. Hence, perfusable interconnected pathways are essential for forming 3D engineered hydrogel-based structures highly populated with large-scale cells to mimic natural tissues. To date, direct bioprinting methods have been confined to thin tissues populated with cell densities less than the human physiologic environment. Yet, the lack of a cost-efficient feasible approach for forming complexly architected networks remains a major constraint for the fabrication of thick, highly cellularized tissues.

Besides the fabrication strategies, investigating the design criteria in the architected porous structures is a key point in defining the functionality of the scaffolds. Unlike the structures designed for sensing applications, the design criteria in the tissue engineering scaffolds would not limit to the mechanical properties and deformation mechanisms, but also fluid permeability is of great importance. Conflicting design criteria have limited the development of fully functional porous implants and tissue engineering scaffolds; increasing macroporosity improves body fluid permeability at the expense of compromising mechanical stability. There is still a lack of proper design criteria for architected scaffolds and implants that satisfy all the requirements for improved functionality.

1.2. Objectives

The objective of this thesis is “direct and template-assisted additive manufacturing of architected structures for healthcare applications”. To this end, the following objectives were set for this work:

- Direct 3D printing of silicone inks mixed with carbon-based additives to develop architected flexible wearable biomonitoring devices.
- Developing a novel sacrificial 3D printing technique for shrinkable 3D architected silicone-based structures with enhanced resolution through shrinking and investigating the effect of various triply periodic minimal surface (TPMS) designs on the physical properties.
- Adoption and modification of the developed template-based approach for fabrication of robust silicone-based sensors surface-doped with graphene for wearable biomonitoring.

- Adoption and modification of the template-assisted method for developing architected 3D cellularized tissue engineering scaffolds with macro-channels for enhanced cell viability.
- Investigating the design criteria for architected implants for enhanced mechanical properties and biopermeability.

1.3. Outline

The current thesis includes eight chapters among which 5 research projects are presented (see Figure 1.1). Chapter 1 introduces the current challenges in the field, describes the motivations and objectives of this research, and outlines the structure of the thesis. The current approaches for resolving the aforementioned challenges and a general background of the field are reviewed in Chapter 2. A detailed review of the field related to the projects is discussed at the beginning of each chapter. Chapter 3 proposes material jetting for direct 3D printing of flexible carbon fiber-silicone sensors architected with a sandwich-like design for enhanced durability and flexibility. However, due to the limitations in flexibility of the fabricated sensors arose from mixing elastomer with conductive particles, which diminishes the mechanical properties, template-assisted techniques were focused in the next chapters. Localizing the conductive network on the surface of the sensors can help in maintaining flexibility. Besides, having a porous 3D structural design can enhance the surface area for doping with conductive materials and improve electrical properties as well as flexibility and compressibility of the sensors. Furthermore, TPMS is chosen for the porosity design within the structures which is investigated in detail in the following chapters. Hence, Chapter 4 is focused on introducing a novel sacrificial 3D printing method for fabricating flexible porous 3D silicone-based structures. Furthermore, the structures can be shrunk to the desired size for enhanced feature resolution. These structures enable fabricating flexible sensors by introducing conductivity on the surface that is discussed in the next chapter. Chapter 5 adopts and modifies the proposed method for the development of ultra-robust architected porous silicone sensors surface-doped with graphene nanopowder for biomonitoring applications. Then, the TPMS porosity design along with the template-assisted techniques developed in the previous chapters were modified and combined to address one of the most important limitations of bioprinting which is fabricating 3D thick tissue with interconnected vascularization. Chapter 6 proposes a template-assisted fabrication technique for the development of 3D hydrogel-based tissue engineering scaffolds architected with perfusable interconnected macro-channels. After investigating the hydrogel-based materials in this chapter and noticing their importance for providing a safe microenvironment for cells, the cell-laden hydrogels were incorporated within bone tissue engineering scaffolds. Besides, the TPMS design was further investigated for these types of implants. Hence, Chapter 7 discusses the design criteria for macroporous implants infilled with cell-laden hydrogels for enhanced mechanical properties and biopermeability. Chapter 8 outlines the conclusions and potential approaches for future studies. Chapters 3 to 7 are adopted from the author's published papers or the manuscripts submitted for publication (see Figure 1.1):

Chapter 3:

- Davoodi, E., Fayazfar, H., Liravi, F., Jabari, E., & Toyserkani, E. (2020). Drop-on-demand high-speed 3D printing of flexible milled carbon fiber/silicone composite sensors for wearable biomonitoring devices. Additive Manufacturing, 32, 101016. [10]

Chapter 4:

- Davoodi, E., Montazerian, H., Khademhosseini, A., & Toyserkani, E. (2020). Sacrificial 3D printing of shrinkable silicone elastomers for enhanced feature resolution in flexible tissue scaffolds. Acta Biomaterialia, 117, 261-272. [11]

Chapter 5:

- Davoodi, E., Montazerian, H., Haghniaz, R., Rashidi, A., Ahadian, S., Sheikhi, A., ... & Toyserkani, E. (2020). 3D-Printed ultra-robust surface-doped porous silicone sensors for wearable biomonitoring. ACS nano, 14(2), 1520-1532. [12]

Chapter 6:

- Davoodi, E.[#], Montazerian, H.[#], Zhianmanesh, M., Haghniaz, R., Ahadian, S., Pourmohammadali, H., Weiss, P., Toyserkani, E., Khademhosseini, A. Cost-Efficient

Template-Assisted Fabrication of three-dimensional tissues with Perfusable Engineered Macro-design (Submitting soon)

Chapter 7:

- Davoodi. E.[#], Montazerian, H.[#], Esmaeilizadeh, R., Darabi, A. C., Rashidi, A., Kadkhodapour, J., Jahed, H., Hoorfar, M., Milani, A. S., Weiss, P. S., Khademhosseini, A., Toyserkani, E. Additively Manufactured Gradient Porous Ti-6Al-4V Hip Replacement Implants Embedded with Cell-Laden Gelatin Methacryloyl Hydrogels (Under revision in ACS Applied Materials & Interfaces)

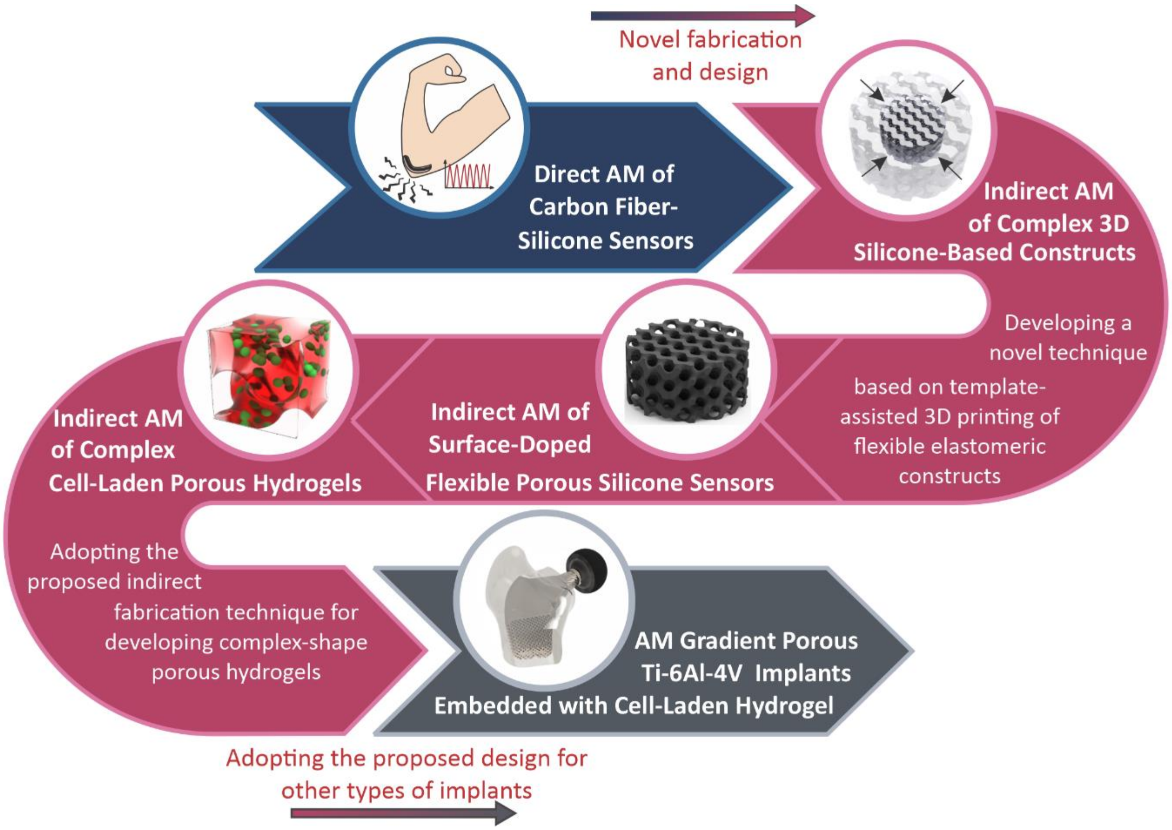

Figure 1.1. Graphical view of the thesis outline

Chapter 2. Literature Review

In this chapter an overall overview of the state-of-the-art research is described while the detailed review of the literature is presented at the beginning of each chapter.

Conventional methods of manufacturing 3D structures0 including molding techniques have some drawbacks making them unfavorable for many applications resulting in a surge of interest directed toward additive manufacturing technologies. Conventional molding techniques are time-consuming; besides more waste is left and much more effort is needed. Over the last decade, AM technologies have been widely employed for 3D printing of conductors to be used in electronic devices. Additive manufacturing techniques make the creation of architected components with complex shapes out of various materials possible, which is not practical with conventional manufacturing methods [13]. Additive manufacturing of 2D and 3D conductive patterns has been feasible by fused deposition modeling (FDM) [14, 15], stereolithography [16], Ink-jet printing [17, 18], aerosol jetting [19, 20], and so on. However, there are still some limitations in employing additive manufacturing techniques depending on the application and the applied technology, including high cost, product size limitations, material limitations, imperfections, mass production, etc. [21-23] Although AM techniques have opened the doors to silicone printing for fabricating 3D flexible conductors; however, there are still some limitations such as complex shapes printing, the product size, and resolution, and so on. Printing complex 3D shapes of silicone rubber composites reinforced with conductive additives in high resolution and large scales are not still feasible using AM techniques. However, AM technologies can incorporate conventional fabrication methods, here called indirect AM techniques, to produce the molds required for casting silicone rubber composites.

Most of the sensors constructed through conventional or additive manufacturing techniques are 2D structures so far. In a study by Amjadi et al. [24], a stretchable sandwich structure strain sensor was developed through the embedment of silver nanowires network in between PDMS layers. Cochrane et al. [25] used a conventional melt-mixing process and solvent technique to build 2D sensors out of carbon black and thermoplastic elastomer composites to sense the deformation of textiles in their movement. Boland et al. [26] developed a stretchable sensor through the infusion of graphene flakes into an elastic band to be used for human motion detection as well as pulse and breath monitoring. Swelling of the rubber band in toluene and diffusion of graphene from graphene dispersion into the rubber resulted in infiltration of graphene in the elastic band and making it conductive. Larimi et al. [27] also fabricated a stretchable conductive pad by soaking the porous adhesive pad in acetone and then transferring it to a dispersion of graphene flakes resulting in the infusion of graphene in its pores. A stretchable PDMS substrate with conductive patterns was produced by Liu et al. [28] through a simple two-step technique. First, the conductive ink composed of multiwall carbon nanotube (MWCNT) and polydimethylsiloxane (PDMS) was spin-coated on a surface and then transferred to another substrate by a microcontact mold. Afterward, PDMS was poured and cured on top of that and finally peeled off. The conductive patterns were embedded in the PDMS substrate. Guo et al. [29] developed carbon nanotube meshes capable of tension and compression sensing. The proposed strain sensor was capable of detecting walking and running motions.

Multiple printing techniques are engaged in flexible electronics manufacturing among them ink-jet printing is one of the most promising methods for 2D structures. Le et al. [30] employed an environmentally friendly water-based graphene ink for ink-jet printing of conductive components on top of a flexible substrate to be used as a gas sensor. Torrisi et al. [31] fabricated flexible thin-film transistors through the ink-jet printing of a graphene-based ink. Fused deposition modeling of multi-materials is also another AM method for printing the conductive filler and polymer matrix simultaneously. In a study by Christ et al. [32], a highly stretchable multidirectional piezoresistive strain sensor was developed by a multi-material printing technique. FDM was utilized to print conductive patterns of MWCNT embedded in an isolative matrix.

Three-dimensional strain sensors are mostly graphene foams fabricated through conventional methods such as self-assembly, chemical vapor deposition (CVD) growth on a template, template-based dip coating, etc. Huang et al. [33] developed a conductive graphene foam by a chemical vapor deposition method, in which a carbothermic reduction of porous silica resulted in graphene growth. After etching the silica network away, elastic porous graphene foam was attained. Samad et al. [34] developed a novel fabrication method for graphene foams with pressure sensing applications. They established a two-step process: first, the biodegradable polyurethane (PU) was dip-coated in graphene oxide (GO), then heated in nitrogen atmosphere through which PU was decomposed and GO was reduced to graphene foam. Li et al. [35] fabricated a graphene/ carbon nanotube foam with application in pressure sensing and adsorbent, through a conventional self-assembly technique. In this method, graphene and carbon nanotube were dispersed in a specific solution thereupon GO sheets self-assembled and a conductive hybrid foam of graphene and CNT formed.

Most of the conductive porous structures proposed in literature consist of internal pores that are random in shape, size, and distribution. Sha el al. [36] employed a laser additive 3D printing method through which after the deposition of every single layer of Ni and sucrose, it was sintered by a laser resulting in graphene growth. After forming the graphene foam, Ni was etched away. Lattice network of bulk graphene aerogels has been recently 3D printed as flexible conductive structures. Zhu et al, [37] developed a graphene oxide ink for printing graphene aerogel lattices. Sayyar et al. [38] fabricated a lattice-shaped conductive biocompatible scaffold through extruding UV-curable graphene/poly (trimethylene carbonate) (PTMC) composite. In another study by Duan et al. [39], an extrusion-based printed polymer lattice was used as a template to be filled with polydimethylsiloxane (PDMS). After etching the polymer template, a dispersion of CNT and GO was introduced to the porous PDMS structure. Then, GO was reduced later and formed a conductive porous stretchable electrode. Albeit there have been some efforts on developing graphene-based flexible electronics, there are still some challenges left unsolved. Introducing designed internal pores to the flexible 3D structures can give better control over mechanical and electrical properties by manipulating the pores in terms of shape and size. Moreover, the short term durability of the sensors due to graphene flake off is an important issue that needs to be addressed [40].

Apart from the limitations of direct 3D printing of architected flexible electronics discussed above, soft tissue engineering scaffolds are also challenging to fabricate by the current 3D printing methods. Interconnected pathways in 3D bioartificial organs are essential to retaining cell activities in thick functional 3D tissues with a high cell population. Three-dimensional bioprinting methods have been widely explored in the biofabrication of functionally patterned tissues; however, these methods are costly, confined to thin tissue layers due to poor control of low-viscosity bioinks, and limited in cell density.

Recently, a growing body of literature has emerged around constructing 3D vascularized tissues that try to mimic the native vascularization system. For example, Norotte *et al*. used micropipettes of 300 and 500 µm diameter to produce smooth muscle cells (SMCs) and fibroblasts containing pellets for extrusion bioprinting of spheroids and cylinders that were used to construct tubular structures in a layer-by-layer fashion [41]. In another study, hollow fibers were produced and then embedded in multilayer hydrogel to form perfusable constructs, where a pressure-assisted co-axial fabrication system was used [42]. In this study, the authors developed cartilage progenitor cell-laden alginate microfluidic channels. Constructs having perfusable alginate hollow fibers embedded in alginate gel were developed by Zhang *et al.* using a co-axial pressure-assisted robotic system (wall thickness of 200 µm) [43].

The ability to construct vascular channels on a large scale mimicking the native vasculatures is critical and important for the clinical application of any engineered tissue. To address the survival and proliferation of larger tissues, Lee *et al*. reported a capillary network and connecting to vascular tissues that can contribute to tissue viability and growth [44]. The microvascular network was formed by EC and fibroblast embedded in fibrin gel between two larger vessels with a size of 0.5-1 mm. In a study by Gao *et al*., hollow filaments of calcium alginate loaded with fibroblasts were 3D printed layer-by-layer using a co-axial nozzle [45]. The hollow microchannels within the construct improved oxygen and nutrient supply to cells residing in the construct, and thus cell viability was improved. In this study, cell viability was 67 ± 4% after 7 days when utilizing the 3D alginate scaffolds with hollow fibers, which is higher than that observed using solid fibers (50 ± 1.6%) after 7 days.

Apart from direct 3D bioprinting of vascularized tissues, template-assisted approaches have also been developed mostly using the advantage of 3D printing for fabricating the sacrificial templates/channels. Most of the current template-assisted approaches are based on direct 3D printing of soft sacrificial gels such as gelatin [46, 47], alginate [48, 49], Pluronic [50-54], etc., which still suffer from the aforementioned limitations. The limitations of the current template-assisted techniques are discussed in chapter 6 in detail. Hence, the lack of robust and scalable approaches for forming 3D multilayered complexly architected perfusable networks within highly cellularized tissue constructs has remained a major constraint.

Chapter 3. Drop-on-Demand High-Speed 3D Printing of Flexible Milled Carbon Fiber/Silicone Composite Sensors for Wearable Biomonitoring Devices

3.1. Introduction

Since the advent of 3D printing technology, complex-shape and customized wearable piezoresistive sensors have facilitated the digital transformation for personalized therapeutics in the health sector. Conductive polymeric composites have paved the way for the development of stretchable and flexible sensors that can be integrated with self-powered platforms, thereby allow real-time monitoring of biosignals. In addition, they offer unique properties such as tunable piezoresistivity and stretchability along with low cost [55, 56], and ease of manufacturing [57]. Thanks to the abovementioned features, conductive polymeric composites have been used in a wide range of applications including tissue engineering [58-60], health monitoring devices [61, 62], soft robotics [63], sensors [64-68], energy harvesters [69], supercapacitors [70, 71], and electronic devices.

Conductive polymeric composite sensors are basically prepared by integrating a conductive micro- or nano-scale filler within a flexible polymer matrix. Among the well-known carbon-based conductive fillers, graphite [72, 73], graphene [31, 74], carbon black [75, 76], carbon nanotubes [77, 78], and carbon fibers [79-81] have received enormous attention due to their high specific conductivity. Despite the extensive progress made so far, there still exist many obstacles in producing robust flexible and sensitive sensors through 3D printing. For instance, depending on the material selection, a high amount of conductive additives needs to be dispersed in the polymer matrix. Although an increase in the conductive filler concentration enhances electrical conductivity, it decays the flexibility, stretchability, and sensitivity [82]. Carbon fibers have led to lower percolation thresholds [82] (compared to other fillers, such as graphite [83]) due to the high aspect ratio of the fibers. In a study by Ram et al. [84], it was confirmed that the percolation threshold of carbon fiber/polymer composites decreases with increasing the aspect ratio of fibers at the constant filler loading for the composite structures prepared by a casting method. Yang et al.

[85] acknowledged the high flexibility and piezoresistive sensitivity of carbon fiber/silicone rubber sensors developed by a melt-mixing method.

Conventional methods, such as those based on melt-mixing (followed by casting) are normally low cost in general, however, they exhibit inconsistencies over the small-scale features, thus unable to address the requirements for personalized medicines. 3D printing, known as AM for industrial applications, offers flexibility in design and material selection, which allows developing engineered conductive features and thereby tuning the electromechanical properties. 3D printing processes have been adapted to the materials of interest for flexible electronic applications. Ink jetting [17, 18] and aerosol jetting [19, 20, 86] were employed for printing 2D conductive patterns with low-viscosity inks. For instance, Le et al. [87] employed a water-based graphene ink for inkjet printing of conductive patterns on the flexible substrates. On the other hand, the limitation of FDM [14, 15] and Stereolithography (SLA) [16] to the particular material types (i.e. thermoplastics and resins) hinders practical translations of these techniques for flexible electronics applications. The aforementioned techniques, therefore, may not be suitable for high-viscosity thermoset polymers, such as flexible silicone rubber. Although extrusion-based 3D printing techniques have been implemented for processing high-viscosity conductive inks; however, low printing speed and poor resolution hinder their industrial applications for serial production [88]. In a study by Huang et al. [89], an extrusion-based 3D printing technique was employed for 3D printing of conductive 3D structures of carbon fiber/silicone rubber composites at the nozzle speed of 50 $mm.s^{-1}$. Moreover, Jakus et al. [90] developed a 3D printable graphene ink for extrusion-based 3D printing of conductive scaffolds as a wearable sensor and implantable biocompatible electronics. To the best knowledge of the authors, there is no report of the use of a high-speed technique for 3D printing of conductive high-viscosity inks (such as those based on silicone rubber) to establish a stand-alone 3D flexible components that satisfy both flexibility and conductivity.

The new generation of material jetting (MJ) systems with piezoelectric-pneumatic printhead have enabled high-speed 3D printing of high-viscosity inks [91]. Therefore, in this study, a drop-on-demand material jetting (DODMJ) system was utilized for high-speed 3D printing of high-viscosity milled carbon fiber/silicone rubber (MCF/SR) ink. The ink was cured layer-by-layer to obtain the final conductive MCF/SR composite structures wherein the flexibility of the sensor is maintained by using the lowest possible MCF content. To this, the 3D printing process was optimized in terms of MCF content to attain the printability, curability and the electrical properties. Subsequently, the MCF/SR sensors were sandwiched between SR layers (S-MCF/SR) to protect the sensing layer and enhance the overall stretchability. Additionally, the electromechanical response of sensors to bending, stretching and cyclic loads were examined at different strain amplitudes. Finally, the potential application of S-MCF/SR sensors for wearable devices and human bodily motion monitoring was addressed.

3.2. Materials and Methods

3.2.1. Materials

The pitch-based milled carbon fibers (MCF) with 10 µm diameter and the average length of 250 µm were purchased from Nippon Graphite Fiber Corp., CA, USA. The pitch-based MCF with 13.8 µm diameter and the average length of 800 µm was supplied by Asbury Graphite Mills Inc., NJ, USA. A one-part high- viscosity (40,000-50,000 mPa.s at 10 s^{-1}) dual UV/moisture curable silicone rubber (RTV 800-400), (SR), was supplied by Novagard Solutions, OH, USA. Silicone thinner (ST) was provided by Smooth-On Inc., Canada, and all organic solvents were purchased from Sigma-Aldrich Corp., USA. The carbon fiber tow consisted of 3k pitch-based carbon fibers with 13µm diameter was supplied Asbury Graphite Mills Inc., USA.

3.2.2. MCF/SR ink preparation

To prepare the conductive ink for the MJ process, the MCF was blended with SR at different weight ratios. In order to decrease the viscosity to an appropriate range for the MJ process, ST was also added where needed (see section 3.2).

3.2.3. Material jetting of MCF/SR composites

In this study, an in-house DODMJ system was used to perform the 3D printing process (Figure 3.1(a)). The MJ system uses a printing strategy different from that of extrusion-based systems wherein a continuous stream of ink is printed layer-by-layer. The MJ process is based on a high-speed deposition of the ink droplets. The system consists of three piezoelectric-pneumatic MJ printheads (Pico Pµlse, Nordson EFD, RI, USA) that enable 3D printing at higher speeds compared to the conventional extrusion-based systems. MJ printheads eject droplets of high viscous ink with controlled volume at high frequencies. DODMJ system works at high speeds (~100 mm/s), which is about 5 times faster than material extrusion and about 20 times faster than conventional material jetting systems [91]. Upon applying a voltage, the piezoelectric actuator is triggered and pushes the rod tappet towards the outlet, leading the ink droplets to quickly eject at high frequency. When the voltage drops at each ejection cycle, the rod tappet is pulled back and the compressed air pushes the ink towards the orifice. The above steps are repeated during the MJ process at a high speed. Apart from the fast material deposition, a lower UV curing time can be spent as the high SR viscosity maintains the material structural stability during the printing even if SR is not cured and thereby UV curing can be irradiated after every few layers. For pure SR, UV curing after every 3 layers suffice to print multilayer structures whereas for MCF/SR at high MCF concentration, every single layer should be exposed to UV light due to the limited penetration of UV light within the ink due to the MCF content. The MJ printhead, ink barrel and the air connections, as well as the cross-section view of the MJ printhead, are represented in Figure 3.1(c). The details of the MJ system along with the fundamentals of droplet formation are completely described in the authors' previous papers [91-93].

The steps followed for 3D printing the flexible sensors are represented in Figure 3.1. To begin the MJ printing process, the barrel was filled with MCF/SR ink and the printing parameters were set. For developing the S-MCF/SR sensors, a second printhead was employed for printing the SR layers using a pure SR base polymer. The printing parameters for MCF/SR and S-MCF/SR composites are introduced in Table 3.1. The composites are then printed layer-by-layer based on a CAD model prepared by SolidWorks software (SolidWorks Corp, Concord, USA). Then the STL files were imported to the Sli3er software to define the printing pathways and generate the G-codes of the toolpath. The images of the printed MCF/SR and S-MCF/SR sensors are illustrated in

Figure 3.1(d). The layer thickness for both SR and MCF/SR layers was set to 0.2 mm in the design. After printing 2 layers of MCF/SR ink, the carbon fiber tow electrodes were placed on the cured layers at two ends with a distance of 19.5 mm. Then the printing process was continued for the rest of the layers (5 layers in total). In the S-MCF/SR sensors, the conductive layers (MCF/SR) were sandwiched between the two layers of SR both sides, resulting in 9 layers in total. The final dimensions of the S-MCF/SR sensor were 35 mm×16 mm×1.8 mm and the dimensions of the MCF/SR (sensing layer in the center) were 35 mm×8 mm×1 mm.

Table 3.1. MJ parameters for the MCF/SR and S-MCF/SR sensors

Parameter	Description	Value (for MCF/SR layers)	Value (for SR layers)
Diameter of Nozzle Orifice (μm)	-	150	150
Printhead Velocity (mm/s)	-	100	100
Temperature (ºC)	The printhead temperature	100	100
Air Pressure (kPa)	The back-pressure applied to the piston inside printing barrel	500	500
Stroke (%)	Stroke=(Opening voltage)/ (Closing voltage)	90	75
Pulse Time (ms)	The time during which the orifice is fully or partially open	3.83	1.40
Cycle Time (ms)	Total time of an opening and closing cycle	4	4
Closing Voltage (V)	The voltage applied for closing the orifice	100	120
Orifice Open Time (ms)	Time taken for the orifice to transfer from fully close to fully open	0.15	0.15
Orifice Close Time (ms)	Time taken for the orifice to transfer from fully open to fully closed	0.15	0.15

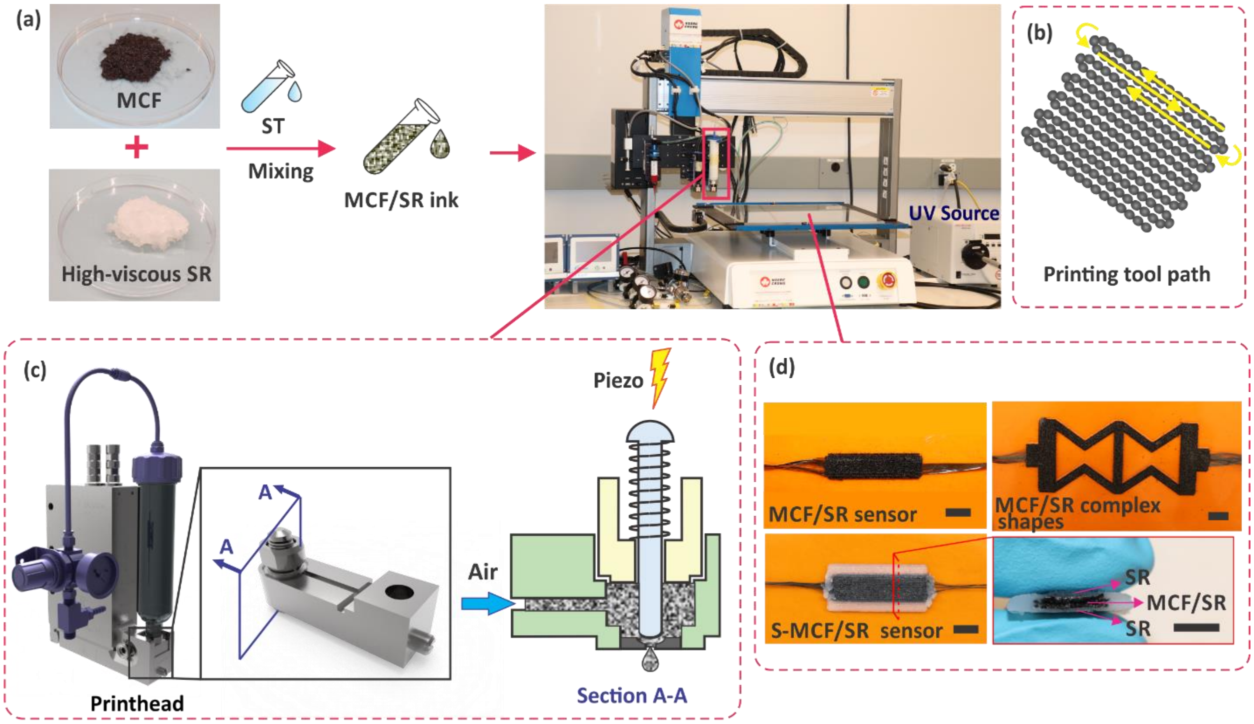

Figure 3.1. (a) The fabrication process of MCF/SR composites. (b) printing tool path (c) The piezoelectric-pneumatic MJ printhead enables DOD jetting the droplets of high viscous ink. The cross-section view of the printhead is represented. (d) The optical images of the printed MCF/SR and S-MCF/SR sensors. Scale bars: 7mm.

3.2.4. Electromechanical testing and Characterizations

The resistance changes of the samples were measured by a 2110 5.5 Keithley digital multimeter (Tektronix, Inc., USA) using a two-probe configuration. The four-point probe can be used for higher precision in reading; however, the two-point probe was precise enough for this study, easier to use, and available in the lab. The measurements were conducted by connecting the electrodes of the multimeter to the carbon fiber tows embedded at two ends of the composites. A DC voltage of 1 V was applied, and the real-time current was recorded to obtain the electrical resistance of the sensors. The resistance changes of the MCF/SR composites due to the bending deformations at various bending angles were addressed. The bending angles were obtained from optical images processed by ImageJ software. For better control over the bending angle, the MCF/SR composites were printed on a thin Kapton substrate and the carbon fiber tows were fixed to the Kapton substrate using copper tape. The electrodes of the multimeter were connected to the copper tape and the resistance was measured at various bending angles. In addition, to evaluate the mechanical performance of the S-MCF/SR composites, a universal test system (MTS Criterion 43, USA) was utilized. The MTS fixtures were insulated to avoid electrical leakage through the universal test system. The sensors were mounted and fixed in the test fixtures. The crosshead displacements of 10 mm/min and 2 mm/min were set for the cyclic and full load tests, respectively. The resistance change of the sensors was evaluated over 30 cycles at 2%, 5%, and 10% strain amplitudes. Full tensile load testing was also conducted to characterize failure mechanisms. After obtaining the force and displacement, the stress (σ) and strain (ε) values were derived through $\sigma=F/A$ and $\varepsilon=\Delta l/l_0$, where F, A, Δl, and l_0 represent load, area, crosshead displacement, and initial distance of electrodes, respectively. The stress is the applied force divided by the initial cross-sectional area, and strain is defined as the crosshead displacement divided by the initial distance of the electrodes.

3.2.5. Structural Characterizations

To characterize the microstructure, a 10 nm layer of gold was sputtered on the samples and scanning electron microscopy (SEM) images at 3 kV were taken by 1550 FESEM, Zeiss, Oberkochen, Germany. The 3D profile of the printed lines was obtained using the confocal laser-optical profilometer (VK-X250, Keyence, Japan). The internal features of the samples were explored by the nano-computed tomography (NanoCT) scanner (Xradia 520 Versa, Zeiss, Germany) at the voltage of 80 kV (7 W) with the voxel size of 8 µm.

3.3. Results and discussion

3.3.1. Length distribution of carbon fibers

The MCF length distribution was obtained by optical microscopy images of the dry MCF (Figure 3.2(a)) and MCF/SR composite ink after the extrusion (Figure 3.2(b)) and jetting (Figure 3.2(c, d)) process. To this, the ink ejected from the nozzle was uniformly spread on a glass slide in a single layer. The length of ~370 fibers was measured for each sample (before mixing with the polymer, after extrusion, and after jetting) and the length distribution histograms were then obtained (see Figure 3.2(f-h)). It was observed that the mean length of the fibers decreased by 16% and 42% after mixing with the polymer followed by extrusion and jetting, respectively (Figure 3.3).

The breakage of fibers in both samples can occur both during the printing and the MCF mixing process with SR. The reduced fiber size after the MJ process can also be attributed to rod tappet's impact crushing the fibers during the 3D printing. This is exacerbated by the small nozzle diameter (150 µm) relative to the MCF length (~250 µm). The fibers pointed by red arrows are crushed due to the transverse force applied through the tappet during the jetting process [94] (Figure 3.2 (d, e)).

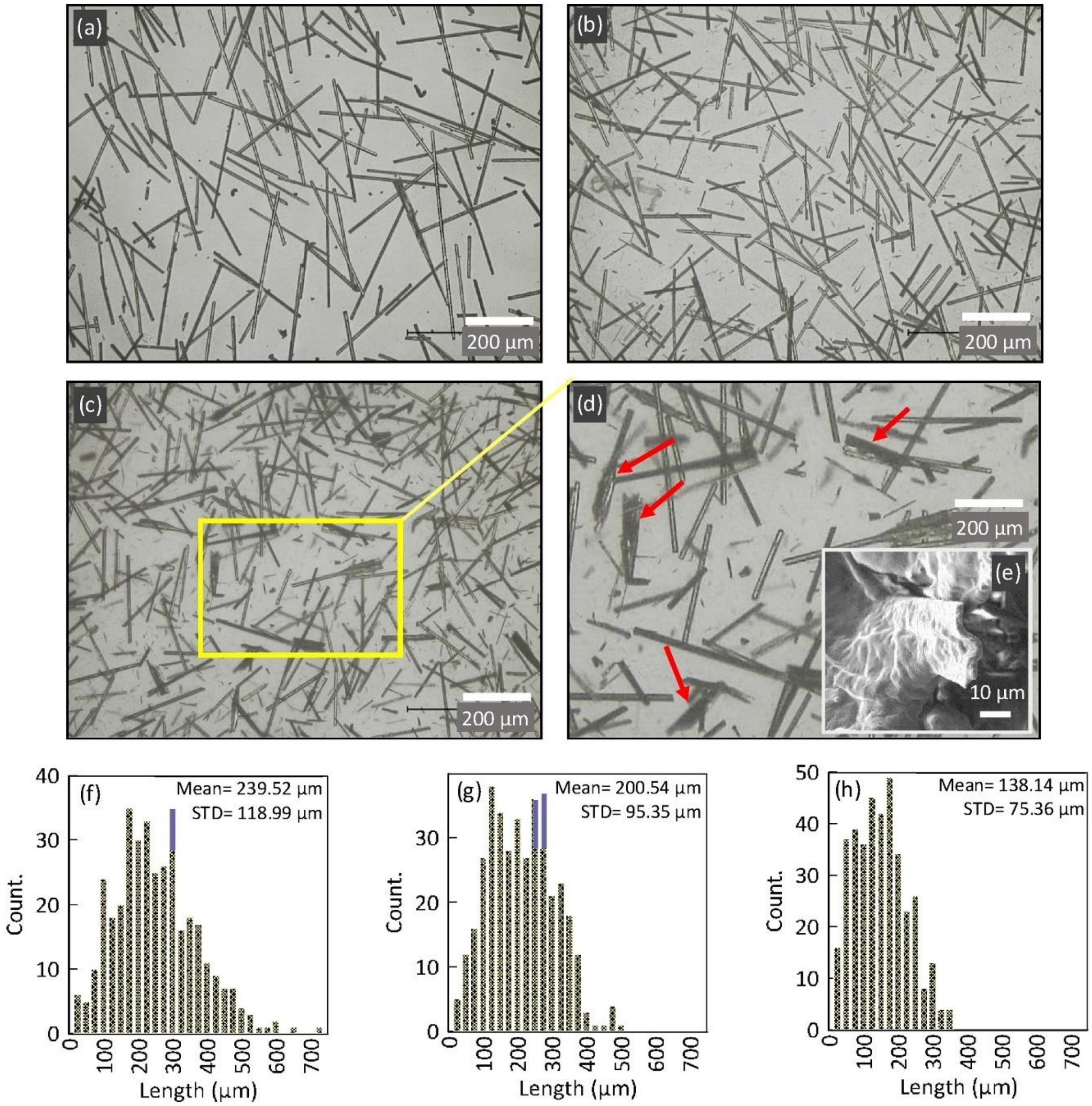

Figure 3.2. Optical microscopy images: (a) dry MCF before mixing with SR and printing. MCF/SR composite inks (b) after extrusion, and (c, d) after jetting (red arrows show the crushed fibers). (e) The SEM image of a crushed fiber after jetting. Length and distribution of MCF: (f) before mixing with SR and printing, (g) after preparing MCF/SR and extrusion, (h) after preparing MCF/SR and jetting.

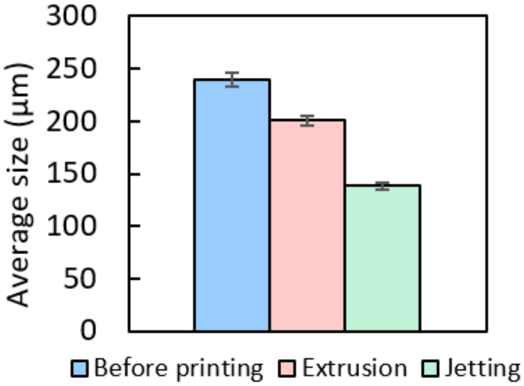

Figure 3.3. The comparison of the average length of MCF before mixing with SR and printing, after preparing MCF/SR and extrusion, and after preparing MCF/SR and jetting.

3.3.2. Ink deposition, curing, and conductivity of MCF/SR composites

Employing long fibers is likely to result in nozzle clogging issues, while it favors attaining lower percolation threshold [82, 95]. In addition, the nozzle orifices that are very large in diameter will reduce the printing resolution. Our preliminary studies demonstrated that MCF size of ~250 µm, offers better printability when using the nozzle orifice with the diameter of 150 µm whereas MCF with the average length of ~800 µm showed clogging issues. As the MCF contents in the MCF/SR ink increases, the viscosity is augmented accordingly, thereby the printing process becomes challenging.

The ink deposition ability of the printer was crucially affected by the ink viscosity. In order to explore the printability of MCF/SR using the MJ system, the MCF/SR composite inks containing various MCF weight-based contents were prepared and their deposition ability via the MJ system was examined. The results depicted in Figure 3.4(a) shows that the MCF/SR inks with the MCF content of up to 30 wt. % were printable. Upon further addition of MCF, the printing was failed due to too high viscosity. Therefore, the MCF/SR could not flow in the nozzle pathways even after applying the pressurized air (Figure 3.4(d)). In this case, the airflow was unable to push the ink forward. In order to widen the range for possible ink deposition, silicone thinner (ST) was added to the inks to lower the viscosity. It was found that adding 2 wt. % ST to the ink, improved the ink deposition ability to ~39% MCF content. Furthermore, the addition of ST to the ink (5 wt. % ST) promotes the ink deposition ability at the maximum MCF contents (i.e., ~43%) (Figure 3.4(b)). However, when the MCF content was increased to larger than 43%, the ink was not printable even with the ST at the concentration of up to 10 wt.%. Given the printability limit window, the ST was jetted while the fibers clogged the nozzle (Figure 3.4(e)). In MJ of MCF/SR/ST inks, not only the viscosity but also the SR content is important. Hence, the printability is limited to the inks with MCF content of up to 43 wt. %.

Another major challenge associated with the MJ process of MCF/SR inks is the UV curability. Adding a high amount of MCF to SR makes the UV-curing process problematic since the MCFs incorporated into the SR matrix prevent the UV light absorption by the polymer thus forming a 3D network elastomer within the structure. Hence, it is critical to discover the highest amount of MCF that allows proper crosslinking. For this purpose, the MCF/SR inks with different ratio of MCF to SR were prepared and the curability of the printed single layer of the composite (10×10 mm) was studied. The blue/white background color in Figure 3.4(a) gives a rough overview of the curability range of the MCF/SR composites under various MCF:SR weight ratios. It was visually observed that by adding up to 33 wt. % MCF, the crosslinking was feasible (dark blue). It is also worth noting that adding low amounts of ST had no remarkable effect on UV-induced crosslinking. In the range of 33 wt. % to 41 wt. %, the integrity of the structures relatively increased upon exposing to UV light that suggests the partial crosslinking. The full crosslinking was not achieved in the light blue gradient region shown in Figure 3.4(a). The white region in Figure 3.4(a) exhibits that the domain where crosslinking did not occur for MCF more than 41 wt. %. This behavior was observed to be dominant on the developed ink regardless of increasing the amount of ST.

To study the percolation threshold of the MCF/SR composites, the electrical resistance of MCF/SR inks with various contents of MCF was measured (Figure 3.4(c)). Increasing the MCF content results in decreasing electrical resistance. No measurable conductive pathway was formed when the MCF content was decreased to less than 17 wt. %. The electrical resistance decreased by 3 and 5 orders of magnitude by increasing the MCF content from 17% to 30% and 50%, respectively. From the above results, it is concluded that a range of ~20-30% MCF can be used for efficient material-jetting of the MCF/SR composite ink for wearable conductive sensors fabrication as it can be deposited properly through the printhead, followed by curing upon exposure to UV while electrical conductivity is retained. In the present study, 30% of MCF content was chosen for the rest of the characterizations. It is worth noting that by increasing the number of conductive layers (MCF/SR) from 3 to 5, the resistance decreases by 3 times (final electrical resistance ranging from 2.5 to 4 kΩ) (Figure 3.5).

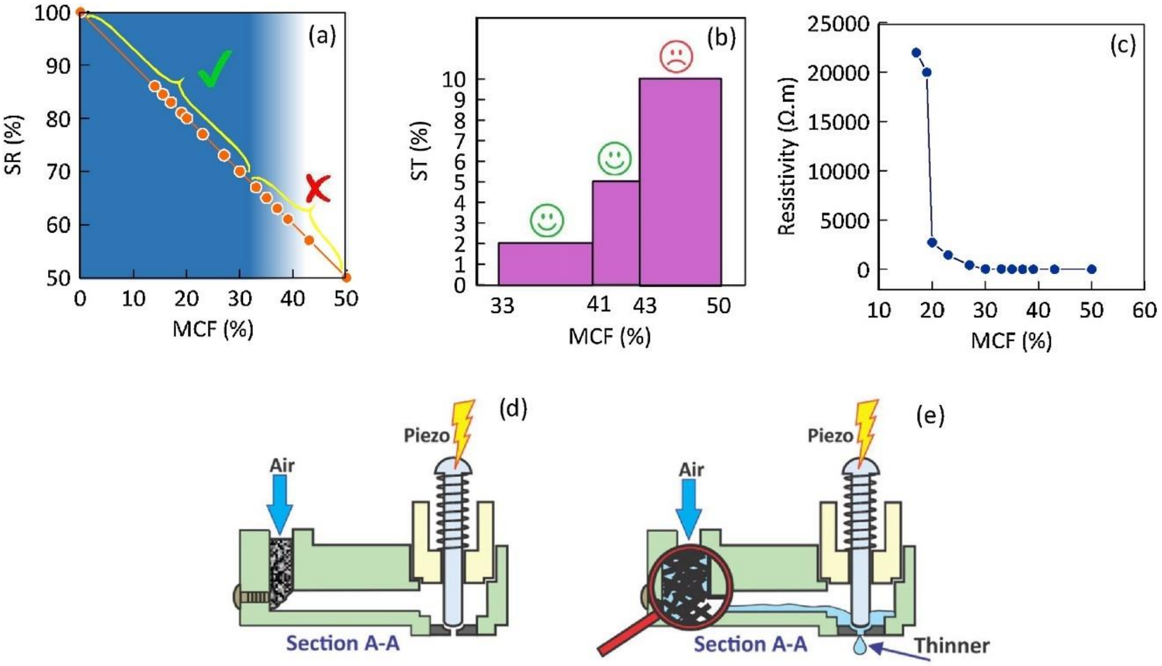

Figure 3.4. (a) The ink deposition ability ranges for MCF/SR with various weight fractions of MCF and SR contents (without using ST). The background blue/white color gives a rough overview on the curability of the MCF/SR composites with various weight fractions of MCF from 0 to 50% by visual observations (Fully cured (dark blue):~0-33%, partially cured (light blue): ~33-41%, and not cured (white): ~41-50%). (b) The effects of adding ST on ink deposition ability of MCF/SR/ST inks. (c) Variation of the resistivity with the weight fraction of MCF. (d) The mechanism of limited ink deposition ability due to the high viscosity of the ink and (e) representation of MCF clogging in the printhead pathways that led the ST to leach out when printing with no MCF and SR deposition at high MCF contents.

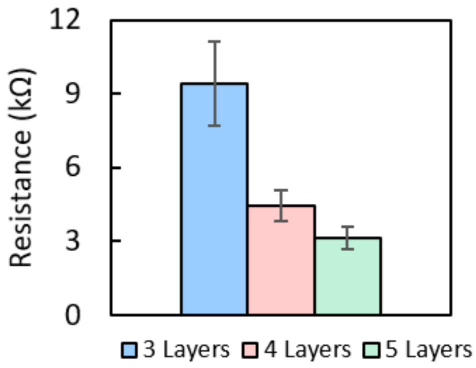

Figure 3.5. The obtained resistance versus the number of printed MCF/SR layers.

3.3.3. Statistical analysis

The preliminary observations showed that choosing proper printing parameters is essential to avoid undesired printing qualities. This is particularly important for highly viscous inks. Hence, it is crucial to investigate the influence of the printing parameters on the printability of the high-viscous MCF/SR composite ink. To this end, the conductive ink with the lowest possible viscosity (MCF content of 17 wt. %) and the printable ink with the maximum MCF content without applying ST (MCF content of 30 wt. %) were chosen for the statistical analysis.

Through the analysis of variance (ANOVA), the factors (printing parameters) that secure the proper jetting of the high-viscous composite ink as well as the amount of jetted material when applying those parameters were identified. For this study, the single line features were printed and analyzed. The significant factors were studied through a resolution VI fractional factorial design with 3 repeats and 6 center points (totally 102 runs). The high and low levels, as well as the center points of the factors, are summarized in Table 3.2. Minitab 18 (Minitab Inc., PA, USA) was employed for the statistical analysis. To this end, single lines with the length of 3 cm were printed and their 3D profile was obtained using the confocal laser-optical profilometer. To minimize the error, a 1.5 cm section at the center of the lines was chosen and its volume was obtained by the profilometer. The obtained response (volume) for different levels of factors are represented in Table A.1.

Table 3.2. The MJ factors and their levels studied for printing the line features

Experimental factors	Levels		
	Low (-1)	Center (0)	High (+1)
MCF (wt. %)	17	23.5	30
Voltage (V)	100	110	120
Cycle Time (CyT)	2	3	4
Open Time (OT)	0.150	0.175	0.200
Close Time (CT)	0.150	0.175	0.200
Fully Closed Time (FCT)	0.020	0.570	1.120

The results of ANOVA with a 95% confidence level suggests that only three factors including MCF concentration, Fully Closed Time (FCT), and Cycle Time (CyT)×FCT have a statistically significant effect on the sample volume (Table A.2). Due to the hierarchy, CyT is also considered as a significant factor. The plots of marginal means illustrate the effect of each parameter on the volume readouts (Figure 3.6(a-g)). The lowest level of FCT and MCF% yields the thickest line with the volume of 3.551 mm^3. While the highest level of FCT and MCF% yields the thinnest line with the volume of 0.153 mm^3. The rest of the interaction plots of marginal means are represented in Figure A.1. Pareto chart of standardized effects also corroborate the findings (Figure A.2). Additionally, the normal plot of the standardized effects is represented (Figure 3.6(h)). The further the points from the reference line, the lower P-value and the more significance of the factor. The positive or negative effect of the factor on the response can be identified by the position of the obtained point for each factor regarding the reference line. The points in the right-hand side have a positive effect, while the points in the left-hand side have a negative effect on the response. Additionally, independence, as well as the normal distribution of residuals, are validated through the residual plots. These plots also confirm that the residuals have constant variance (Figure A.3). The ANOVA results after removing the insignificant factors proved the significance of the remained factors (P-values less than 0.05) and the reliability of the model (Table A.3). The results show the insignificance of the curvature for the proposed model, confirming no need for any subsequent analysis. The following regression model (Eq. (3.1)) relates the significant factors to the response:

$$\begin{aligned}\text{Volume} \;=\;& 4849805465 - 93730735\,(\text{MCF\%}) - 414152416\,(\text{CyT}) \\ & - 2020448287\,(\text{FCT}) + 488165231\,(\text{CyT}\times\text{FCT})\end{aligned} \tag{3.1}$$

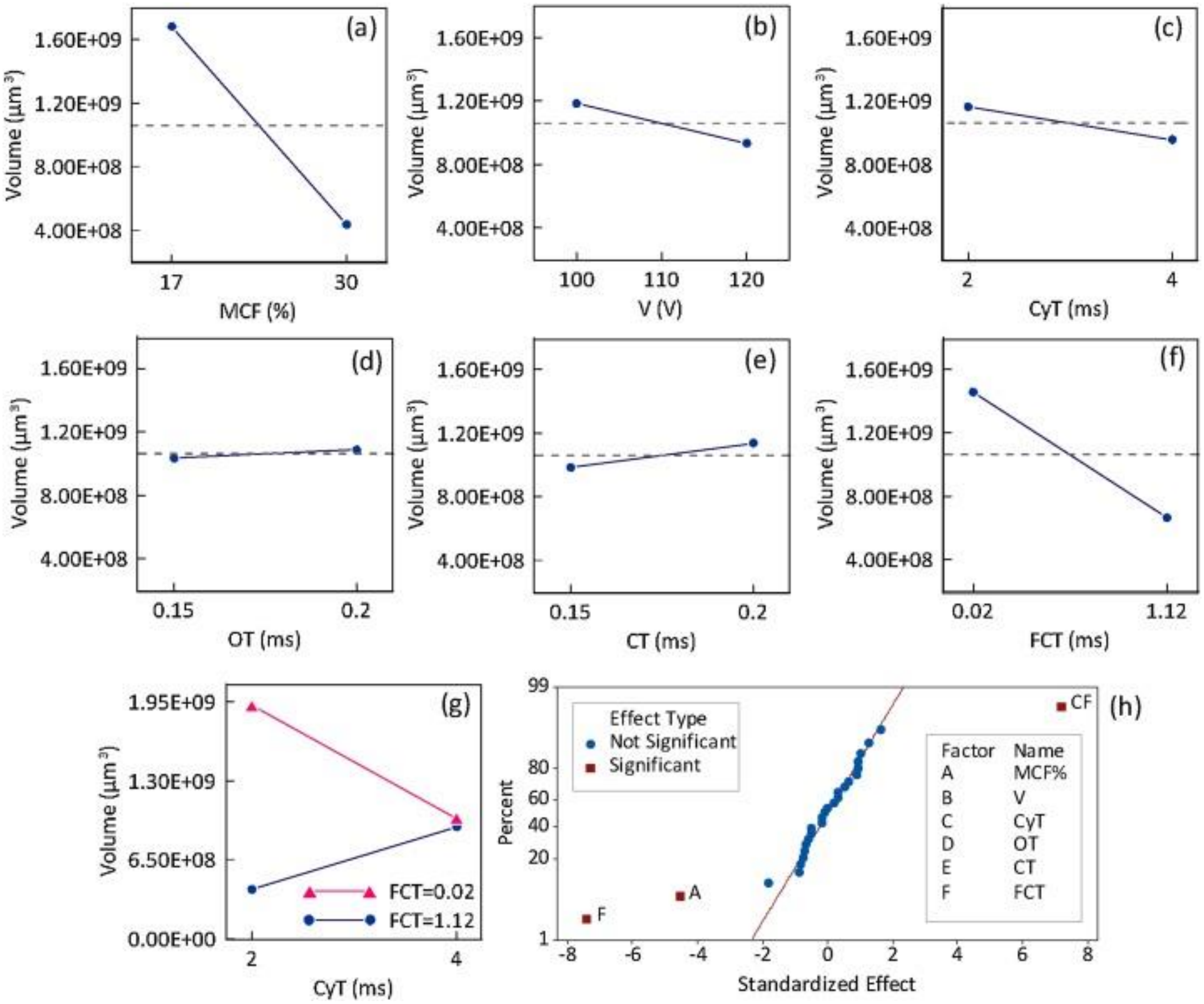

Figure 3.6. (a-f) The plots of marginal means showing the effect of main MJ factors on the volume of the line features. (g) The plot of marginal means representing the effect of FCT and CyT interaction on the volume. This was known as the only significant interaction. (h) Normal plot of the standardized effects in which MCF%, FCT, and the interaction of FCT and CyT are found as the most significant factors on volume.

3.3.4. Structural characterization

The microscale features of MCF/SR sensors are presented in Figure 3.7(a-d). The fibers were well incorporated into the silicone matrix as shown in Figure 3.7(a). The conductive network inside the MCF/SR composite is formed due to the fiber-fiber contacts highlighted by yellow circles in Figure 3.7(b). Unlike the extrusion-based printing process in which the fibers are aligned with the printing direction [96], the fibers show relatively random directions in the 3D structure printed by MJ system. This can be attributed to the force applied to the fibers when small droplets (each containing a few fibers) hit the substrate at high frequencies; while in the extrusion process the fibers retain their orientation even after exiting the nozzle when the fibers are guided through a continues flow of ink (i.e. extruded filament) during deposition on substrate. In MJ system, although the fibers may align due to the shear force in the nozzle, the hitting force may misalign some fibers during deposition of droplets. This favors conductivity due to introducing a uniform 3D conductive network along with the sensor that is independent of the printing direction as illustrated in Figure 3.7(c). Figure Figure 3.7(d) shows the cross-section of a 5-stacked-layer MCF/SR. The internal features of a 3D cubic structure (10mm×7mm×1.5mm) composed of 5 layers of MCF/SR composite were evaluated through the NanoCT analysis at 8 μm voxel size resolution (Figure 3.7(e-g)). The analysis of micropores using a MATLAB code resulted in an overall 11.58% internal porosity in the printed structure.

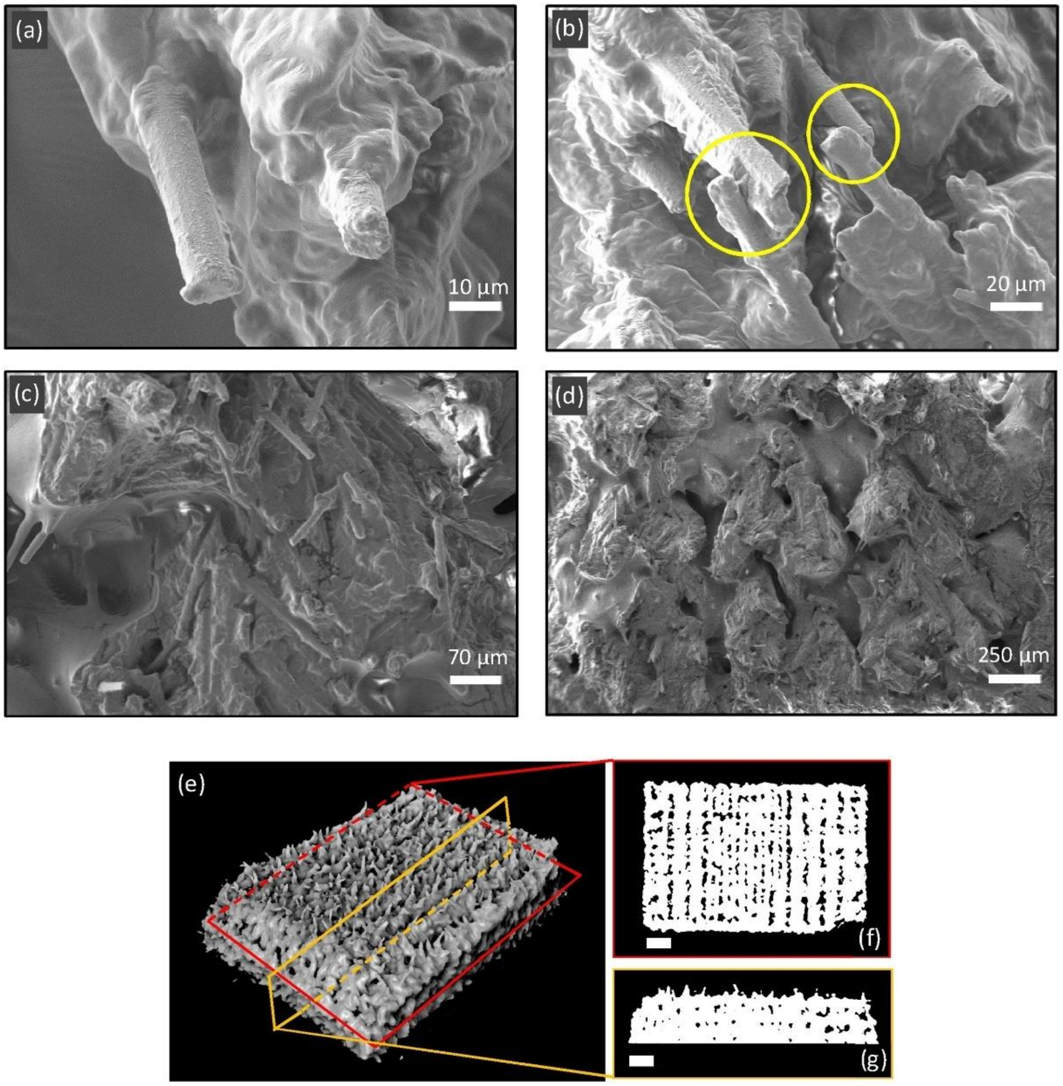

Figure 3.7. (a-d) SEM images of MCF/SR cubic structures: (a, b) carbon fibers are well integrated into the silicone matrix where the fiber to fiber contacts establish conductive pathways. (c) Cross-section view shows the carbon fibers are relatively aligned in various directions. (d) The layers of the printed structure are well integrated and formed continuous conductive pathways. (e-g) NanoCT results at 8µm voxel size: (f) top view cross-section, and (g) front view cross-section represents relatively low internal porosity of the MCF/SR composite structures. Scale bars: 1mm.

3.3.5. Piezoresistive sensing

3.3.5.1. MCF/SR sensors

The fabricated sensor's response was evaluated in terms of their resistance change under mechanical loads. To evaluate the sensitivity of the MCF/SR sensors to the bending deformations, the resistance change under eight different bending angles was measured (Figure 3.8). The resistance increased by about 9 times while changing the bending angle from 0° to 89°. This can be attributed to the disruption in the conductive network resulting in a continuous increase in resistance upon enlarging the bending angle.

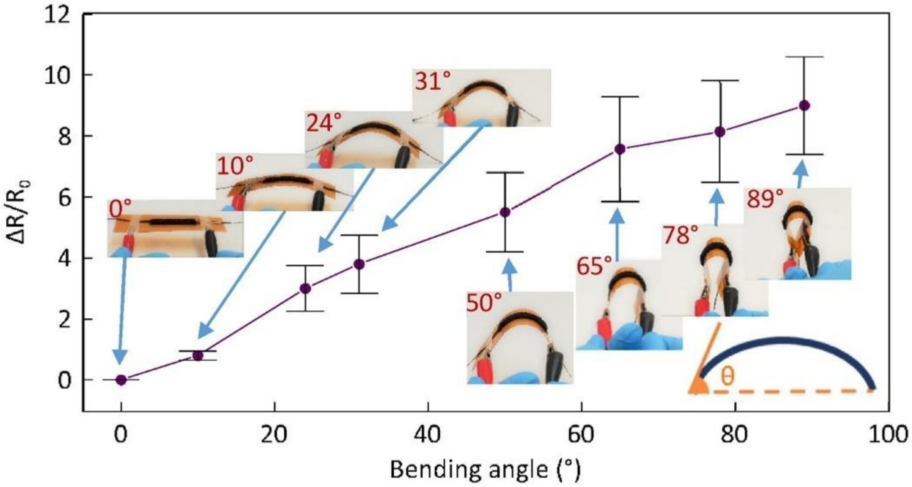

Figure 3.8. Resistance change in MCF/SR sensors with 30 wt.% MCF content upon applying bending deformations with various bending angles

3.3.5.2. S-MCF/SR sensors

To evaluate the cyclic piezoresistive performance of S-MCF/SR sensors, the variation of resistance under cyclic tensile strain was monitored. The results were obtained for three different strain levels including 2%, 5%, and 10% depicted in Figure 3.9(a-c). A relative resistance change of ~40 was observed when the strain amplitude of 10% was applied. Comparing the results of Figure 3.8 with Figure 3.9(c), one can note that the magnitude of the resistance change seems to be significantly smaller. This is basically attributed to the development of compressive regime along with the tensile region when the sensors undergo bending. In essence, the resistance in bending mode of deformation is a result of synergistic contribution of compression and tensile loads within the samples. The resistance changes occur due to the reconfiguration of the conductive network. In fact, an increase in resistance corresponds to the disconnection of the fibers and disruption of the conductive network. However, in some cases, piezoresistivity shifts from positive to negative piezoresistivity could be observed which is mainly assigned to the more complex deformation mechanisms occurring while applying mechanical loads. For example, as stated in the literature for the case of chopped carbon fiber and Polydimethylsiloxane (PDMS) [82], such piezoresistivity transitions can be explained by the Poisson's effect as well as the viscoelastic/time-dependent behavior of the polymeric matrix. Moreover, it is suggested that the fibers may permanently deform upon the first loading cycle leading to a repetitive piezoresistivity transition over the subsequent loading cycles. This is basically assigned to the poor interface adhesion between silicone and MCF which implies the MCF may not fully recover back to its original shape upon applying the first loading (according to Ref. [82]). In essence, when the fibers are stretched, the SR slides on the MCF (in case of those fibers oriented align the loading direction). Upon removing the tensile deformation, the interfacial friction may lead the fibers to buckle and loosen the channels containing MCFs. Now, applying the second cycle of tensile deformation leads the fibers to straighten up to some point which may decrease the resistance (negative piezoresistivity) after which further tensile load results in the normal network disruption (positive piezoresistivity).

The variations of resistance and tensile stress in S-MCF/SR sensors under continuous tensile strain are represented in Figure 3.9(d). The stress-strain curve is in line with the viscoelastic materials in the literature [97, 98]. Elastic modulus, yield strength, and the rupture strain were measured to be 224±21 kPa, 302±18 kPa, and 1.5±0.3, respectively. It is worth noting that SR layers in S-MCF/SR sensors could protect the sensing layer (MCF/SR) against harsh conditions (deformations, humidity, etc.) and increased the overall stretchability of the sensors. While in MCF/SR sensors, fiber additives lowered flexibility that diminish the performance of the sensor in severe stretching deformations. The 3D printed S-MCF/SR sensors showed higher sensitivity (GF up to ~400) as well as stretchability (~150%) compared to the conventional sensors fabricated by mixing conductive nanoparticles with a polymer followed by casting. As an example, the sensors showed ~8 times greater sensitivity (at 5% strain amplitudes) and ~3 times higher rupture strain (due to presence of protective SR layers) compared to sensors fabricated by casting chopped carbon fiber/polydimethylsiloxane composite blends [82]. Comparing the S-MCF/SR sensor with conventional multi-wall carbon nanotubes/PDMS showed about 4 and 20 times higher sensitivity in the 2% and 10% strains, respectively [99]. Moreover, In the range of studied tensile strains (2%, 5%, and 10%), the proposed sensors showed gauge factors comparable to the sensors fabricated by patterning conductive carbon black/PDMS on PDMS substrate by transfer printing method [100].

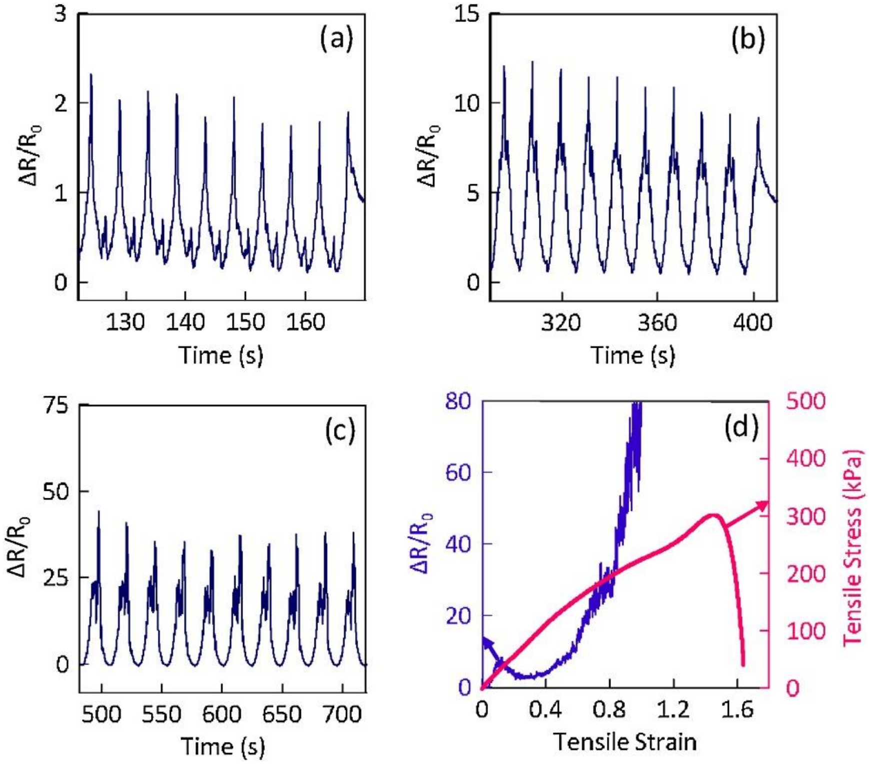

Figure 3.9. Electromechanical characterization of the S-MCF/SR sensors for 30 wt. % MCF contents. Resistance change under cyclic tension for the sensors at (a) 2%, (b) 5%, and (c) 10% strain amplitude over cycles of 20-30. (d) Variations of resistance and tensile stress upon applying tensile strain.

3.3.6. Applications of S-MCF/SR sensors for human motion detection

To examine the practical applications of the S-MCF/SR sensors as wearable devices for health monitoring, a real-time resistance measurement under dynamic deformations was conducted. To this end, the S-MCF/SR sensors were integrated on the human finger and cyclic bending of the finger was performed. The resistance increased by ~8 times upon bending and a reversible performance was observed after moving back to the rest position. Figure 3.10(a) shows the piezoresistive response of the sensor for 22 cycles of bending. The resistance change in the sensor integrated with the human arm for over 17 bending cycles is represented in Figure 3.10(b). The resistance increased by ~6 times upon bending the arm. These results show the reversible performance of the S-MCF/SR sensors is suitable for human motion detection and healthcare applications.

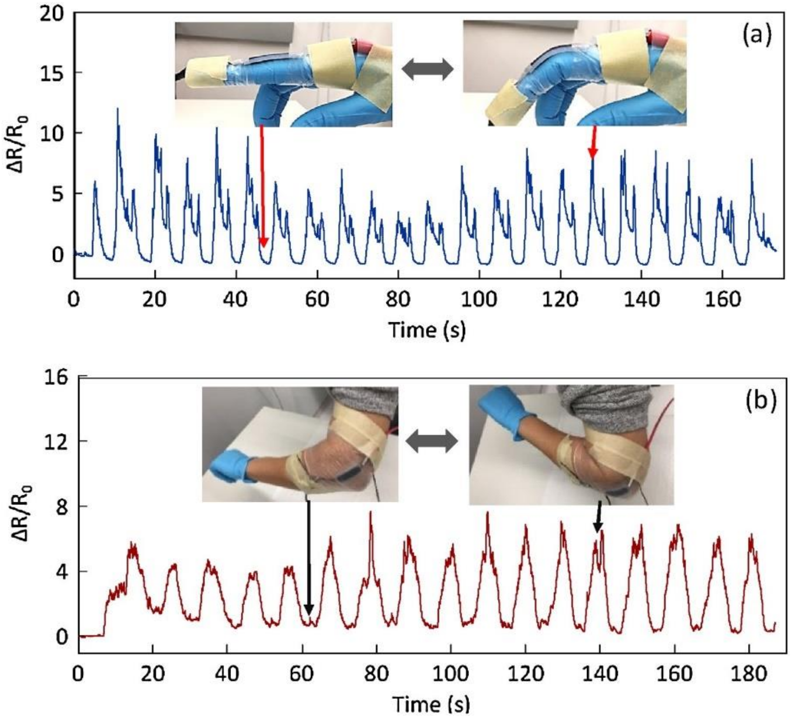

Figure 3.10. Application of the S-MCF/SR sensors (30 wt. % MCF contents) for human health monitoring. Monitoring the bending motions at the (a) index finger, and (b) elbow joint.

3.4. Conclusions

Drop-on-demand material jetting (DODMJ) enables high-speed 3D printing of flexible sensors that can be integrated with the textiles for the purpose of human body motion and vital sign detections. In this study, the electrical properties and curability of silicone rubber (SR) after introducing various contents of milled carbon fibers (MCF) were investigated. The MCF concentration range, at which the MCF/SR composite ink can be printed, was found to be within ~20-30% in order to retain both conductivity and printability (i.e., ink deposition and curing). Moreover, the piezoresistive performance of the MCF/SR sensors under bending deformation up to 89° was characterized where the resistance was increased by 9 times. Sandwiching the MCF/SR composites with protective SR layers (S-MCF/SR) resulted in a better durability in severe deformations (specifically for stretching applications), which was not feasible by the MCF/SR stand-alone composites. The piezoresistive response of S-MCF/SR sensors under cyclic stretching with various levels of strain amplitude was characterized showing a relative resistance change up to ~40, where strain amplitude of 10% was applied and the deformation mechanisms were discussed. The proposed sensors show favorable flexibility with elastic modulus, yields strength and the rupture strain of 224±21 kPa, 302±18 kPa, and 1.5±0.3, respectively. Finally, the application of the S-MCF/SR sensors for detecting the human motions was addressed and the bending motion of index finger and arm was detected as showcases. DODMJ of the S-MCF/SR composites would facilitate the high-speed development of customized wearable sensors.

Chapter 4. Sacrificial 3D Printing of Shrinkable Silicone Elastomers for Enhanced Feature Resolution in Flexible Tissue Scaffolds

4.1. Introduction

Silicone-based elastomers have been attractive candidates for the fabrication of tissue engineering scaffolds, implants (stents, catheters, prostheses, etc.) [101-105], biomedical devices for drug delivery [106-108], microfluidics [108-110], and wearable electronics applications [10, 111-114]. The broad range of silicone in medical applications is mainly due to its flexibility, bioinert character, nontoxicity, thermal and chemical stability [115, 116]. The mechanical properties of the silicone-based elastomers can be further tuned by manipulating the curing agent, curing condition, and thinning reagents to adapt the mechanical properties for the desired application [117].

The promising characteristics and opportunities offered by silicone elastomers have persuaded research towards the ways to integrate silicone-based inks with AM systems, known as 3D printing. This can open new avenues for the development of next-generation customized biomedical devices and implants. For this purpose, several 3D printing techniques have been used including material extrusion [118-120], material jetting [91, 121], freeform reversible embedding [122], and vat photopolymerization [123, 124]. However, the current 3D printing methods are associated with several limitations. Firstly, the viscous nature of the silicone prepolymer makes the silicone-based inks difficult to control during the 3D printing process. Hence, it would be difficult to maintain structural integrity particularly when it comes to hanging geometries with a negative slope which is highly common in porous scaffolds [125, 126]. Besides, the 3D printing resolution in those methods is rather limited, preventing the construction of delicate features and small-scale pore sizes (as required for optimal cell ingrowth in porous scaffolds) [127]. On the other hand, nozzle clogging as a result of curing the base polymer in the printhead can present an issue [91, 128],[129]. Finally, due to the long curing times of the medical-grade silicone elastomers, their 3D printing process is often limited to low resolutions. Recently, new methods have been introduced to 3D print support-free thermoset silicone elastomers; however, the limited printing resolution (~0.4-0.5 mm) and printable angle threshold (~35° from vertical direction) for overhanging features, have restricted 3D printing of complex structures [130].

The above-mentioned obstacles have hindered the potential applications of 3D printed silicone-based elastomers. Therefore, many attempts have been made to circumvent those challenges. For instance, in order to better control the structural integrity, polydimethylsiloxane (PDMS) was 3D printed in a hydrophilic support bath [122]. In combination with more robust 3D printing methods, several fabrication methods were developed to build 3D microfluidic channels by removal of a 3D printed sacrificial template from a cured silicone elastomer. The carbohydrate-based structures were 3D printed as water-soluble templates; however, the need for a modified 3D printer as well as the difficulties associated with handling the carbohydrate ink, confine their applications [126]. Besides, the acrylonitrile butadiene styrene (ABS) molds were printed *via* the low-cost and well-accessible FDM 3D printers that could be later removed in an acetone solution [131]. This process was also demonstrated using the water-soluble polyvinyl alcohol (PVA) templates [132, 133]. A similar approach was employed for the fabrication of PDMS porous scaffolds with the aid of 3D printed polylactic acid (PLA) that was removed in dichloromethane after curing the PDMS [39, 134]. Although FDM systems are well-established and capable of printing complex features (without the need for a support structure in many situations), they have limited resolution (~0.2-0.4 mm) [135]. However, higher resolutions are favored for medical applications. For instance, tissue engineering scaffolds with pore sizes in the range of ~300-500 µm are shown to be favorable for cell growth, proliferation, and diffusion [127, 136]. Hence, there is a need for a low-cost, robust, and high-resolution 3D printing technology for complex-shaped silicone-based elastomeric scaffolds with high specific surface area and fine topological features.

Stimuli-responsive elastomers wherein the structure dimensions change with an external trigger have recently received attention for the development of shape-shifting structures [137]. This concept has shown the possibility of inducing structural shrinkage upon treatment with organic solvents [138-142]. In the present research, we adopt our previously developed indirect 3D printing technique [12] to fabricate silicone elastomers (*i.e.*, silicone rubber (SR) and PDMS scaffolds) architected with sub-millimeter interconnected pores. The developed structures had high resolution within the context of the extrusion-based techniques and could be used for silicone-based materials. To do so, the low-cost FDM technology is used where the complex-shaped pore architectures based on triply periodic minimal surfaces (TPMS) are initially fabricated at a larger scale (where it is compatible with the resolution of the FDM 3D printer). Subsequently, the elastomeric scaffolds are shrunk down *via* a solvent treatment process. For this purpose, we introduce thinners to the silicone-based prepolymers acting as a shrinking agent (*i.e.*, silicone thinner (ST) to SR and silicone oil (SO) to PDMS) that is later extracted by dissolving in an organic solvent. We further assess the process in the context of the mechanical properties of the 3D printed constructs. Finally, we evaluate the cell compatibility of 3D printed scaffolds infilled with a cell-laden gelatin methacryloyl (GelMA) hydrogel.

4.2. Materials and Methods

4.2.1. Materials

Mold Max-10T silicone rubber (SR) and silicone thinner (ST) were provided by Smooth-On Inc., Canada. Polydimethylsiloxane (PDMS) or Sylgard 184 Silicone Elastomer was purchased from Electron Microscopy Sciences Inc., USA. The ABS filament was purchased from Stratasys, Minnesota, USA. Silicone oil (SO) and all organic solvents were provided by Sigma-Aldrich Corp., USA.

4.2.2. TPMS architected design

The sacrificial cellular molds were designed based on TPMS topologies. Each specific TPMS topology was mathematically defined based on the explicit Eq. (4.1) [143]:

$$\varphi(\mathrm{r}) = \sum_{l=1}^{L} \sum_{m=1}^{M} \mu_{lm} \cos\left(2\pi\kappa_l(P_m^T . r\right) = C \tag{4.1}$$

Where μ_{lm} represents the periodic moment, κ_l is the scale parameter, $P_m = [a_m, b_m, c_m]^T$ is the basis vector in the 3D-Space R^3, and $r = [x, y, z]^T$ is the location vector. The left-hand and right-hand sides of the equation determine pore shape and relative density of the design, respectively.

The geometries studied in the current study are defined by the following equations:

P-surface: $\varphi_P(\mathrm{r}) = \cos x + \cos y + \cos z = C,$ **(4.2)**

D-surface: $\varphi_D(\mathrm{r}) = \cos x \cos y \cos z - \sin x \sin y \sin z = C,$ **(4.3)**

G-surface: $\varphi_G(\mathrm{r}) = \sin x \cos y + \sin z \cos x + \sin y \cos z = C.$ **(4.4)**

Constant C values can be manipulated to attain various relative densities of the TPMS geometry. C values corresponding to the constant uniform relative densities (i.e. 0.30, 0.42, 0.58, and 0.70 in this study) were embedded into the above equations. The relative density was denoted as the volume of the solid phase to the total volume of the scaffolds. For the radially gradient molds, C was determined by $C = AR + B$ (R is the local radius). A and B were constants defined specifically for every pore shape to yield 0.25 volume fraction at R=0 (scaffold center) and 0.75 volume fraction at R=r (scaffold periphery). Hence, the density was defined to change linearly in the radial direction. In this way, the molds with gradient relative density (*i.e.*, 0.25 in center and 0.75 in the periphery) were designed. The STL models for the elastomeric samples were generated based on the domains that satisfy $\varphi < C$ that corresponds to the volume surrounded by TPMS [144]. However, to design the sacrificial ABS molds, the negative phase (i.e., $\varphi > C$) was chosen. A MATLAB code was employed to generate white (for $\varphi < C$) and black (for $\varphi > C$) cross-sectional images of each model which from there we generated the STL CAD models. The bulk molds were cylindrical with the diameter and height of 20 mm and 10 mm, respectively, consisted of 6×6×3 cubic unit cells (the unit cell was set to 3.33 mm×3.33 mm× 3.33 mm unless otherwise noted). A cup with the height of 30 mm embraced the porous molds as the reservoir to facilitate casting the silicone mixture.

4.2.3. 3D printing of TPMS-based ABS molds

The printing parameters and tool paths were designated to the generated STL models using a GrabCAD (GrabCAD Inc., Massachusetts, USA) software. Then the G-code was imported to an F370 3D printer (Stratasys, Minnesota, USA) for layer-by-layer 3D printing of the plastic molds through the FDM process. ABS filament was utilized for fabricating the mold with a layer height of 125 μm. The nozzle temperature and chamber temperature were set at 255°C and 80°C, respectively. No support material was used. In this study, ABS molds architected with P-, D-, G-surface topologies at the uniform relative densities of 0.30, 0.42, 0.58, 0.70, and gradient relative density (0.25 in periphery and 0.75 in the center) were 3D printed.

4.2.4. Fabrication process of elastomeric constructs

We evaluated the capability of two different sets of silicone prepolymer/thinner for integration with our indirect 3D printing platform. These material systems involve SR/ST and PDMS/SO. After 3D printing of the sacrificial ABS mold, for the SR/ST, the SR base prepolymer was blended with its curing agent at 10:1 ratio and then ST as the thinner was added at the desired concentration (in the range between 0 wt.% and 50 wt.%). Then the mixture was poured into the ABS mold, degassed under vacuum for 20 min to remove bubbles and ease the liquid mixture casting under gravity and left to cure overnight. The structure composing a sacrificial mold filled with cured silicone composition was immersed in acetone (stirring at ~500 rpm) for 12 h to wash away the ABS plastic and final porous scaffold of silicone rubber and silicone thinner (SR/ST) was left behind. The SR/ST scaffold was then immersed/treated in 30 ml of a treating solvent for 7 days to shrink.

For the PDMS/SO, PDMS base prepolymer was blended with its curing agent at 10:1 ratio, and afterward, the desired ratio of SO (0 wt.% to 70 wt.%) was added to the mixture. The rest of the fabrication process for the PDMS/SO scaffold was the same as SR/ST scaffold. All the porous TPMS scaffolds were fabricated using 50 wt.% thinner and treated in acetone as the treating solvent, if otherwise is not noted. Adding ST to SR and SO to PDMS lowered the viscosity and eased the polymer mixture infilling into the mold. The ABS molds were free of defects so that no polymer leakage was observed.

4.2.5. Characterization of shrinking behavior

For evaluating the effect of fabrication and material parameters on the shrinking characteristic of SR/ST and PDMS/SO samples, bulk SR/ST, and PDMS/SO structures (with the cylindrical shape) were prepared. To prepare the samples, hollow ABS molds with the diameter, height, and thickness of 10 mm, 10 mm, and 1 mm, respectively, were 3D printed by the FDM process. Then, SR and ST mixture was cast into hollow cylindrical molds and left at room temperature to cure overnight. PDMS/SO structures were fabricated following the same process. The cylindrical samples were used to assess the shrinking behavior of SR/ST and PDMS/SO systems (independent from the structure design) in response to various solvent treatment conditions (i.e. treating solvent type) and the concentration of thinner added to SR and PDMS during the fabrication process. To study the effect of thinner concentration on the shrinking characteristics of SR/ST and PDMS/SO structures, acetone was chosen as the treating solvent for all samples. Similarly, to evaluate the effect of treating solvent type on shrinking behavior, the concentration of thinner was fixed to 50 wt.% for all samples. The volumetric shrinkage and weight loss were measured by weighing over time. Before each measurement, the samples were dried on a hotplate at 100°C for 30 mins. After ~750 h the samples were removed from the solvents and the final dimensions and weight were measured. The measurements were performed for 4 replicated of the samples.

4.2.6. Structural and physical characterizations

To study the microfeatures on the scaffold surfaces, the scanning electron microscopy (SEM) images were captured. First, a thin layer of gold (10 nm) was sputtered on the surface of the samples, then images at 20kV were obtained using 1550 FESEM, Zeiss, Oberkochen, Germany. The internal features and the overall shape of the TPMS samples were assessed by an X-ray computing tomography (CT) scanner (Xradia 520 Versa, Zeiss, Germany) at a voltage of 40 kV. The scanning resolution (voxel size) was 20 µm and 14.5 µm for the TPMS samples containing 10 wt.% and 50 wt.% of ST, respectively.

4.2.7. Mechanical characterizations

We assessed the mechanical properties of the cylindrical and TPMS samples under monotonic compressive loading using a universal test system (MTS Criterion 43, USA) equipped with a 30 kN load cell. The samples were held by the compression grips and the monotonic full compressive load tests at crosshead displacement up to 85% strain with a displacement rate of 2 mm/min were conducted. The force and displacement obtained by the compression tests were used to calculate stress and strain. To measure the mechanical properties in porous materials, the dimensions of the entire scaffold including the pores are involved in the calculation of the stress-strain data according to the literature [145]. Therefore, the mechanical properties not only represent the material behavior but also, they are a function of pore shape and porosity. Hence, the stress was calculated by $\sigma = F/A$, where F and A are force and the nominal contact area of the scaffolds including pores, respectively. The strain was defined by $\varepsilon = \Delta l/l0$, where Δl and l0 represent crosshead displacement and initial distance of the compression platens, respectively. The elastic modulus was calculated by the slope of fit to stress-strain data in the strain range of 5 to 15%. For all the mechanical tests, the R2 < 0.93 ensured the linearity of the elastic region. Within this chapter and the following chapters related to the TPMS structures, elastic modulus, stress, and strain represent effective stiffness, effective stress, and effective strain in the porous structures, respectively.

4.2.8. Biocompatibility evaluation

NIH/3T3 mouse fibroblasts were cultured in 175 cm^2 flasks at a CO_2 concentration of 5%, the temperature of 37 °C, and relative humidity of ~95% in an incubator (Thermo Forma, Thermo Fisher Scientific, MA, USA). The cells were supplied with 25 ml of Dulbecco's Modified Eagle Medium (DMEM) including 1% streptomycin and penicillin and 10% fetal bovine serum. The media culture was refreshed regularly (~ twice a week) and cell confluency was examined daily. When cell confluency reached 80-90%, the cells were detached using trypsin for 5 min (in the incubator) and fresh media was added. The cells were counted using a hemocytometer (Thermo Fisher Scientific, USA).

4.2.8.1. Live/Dead assay test

For 3D cell culture experiments, the scaffolds were filled with cell-encapsulated GelMA. GelMA was synthesized according to a previously published protocol [146, 147]. The SR/ST and PDMS/SO TPMS scaffolds with G-surface topology at φ=0.30 were sterilized in ethanol for 30 min and left in the hood overnight to dry. Then, the oxygen plasma treatment was performed on the scaffolds to enhance the hydrophilicity and assure full infilling of the samples' pores with cell-encapsulated GelMA. To prepare cell-encapsulated GelMA, at first, trypsin was used to detach the cells from the flask, and fresh media was added. Then, the media mixed with cells was centrifuged (at 1000 rpm for 5 min). The supernatant media was then aspirated, and the cell pellet was mixed with a 10% GelMA solution (at the cell density of 10^7 cells/ml). The GelMA solution contained: 6.92×10^{-3} wt.% of Eosin Y as a photoinitiator, 1 wt.% of N-vinylcaprolactam (VC) as a co-monomer and 1.33 wt.% of Triethanolamine (TEA) as a co-initiator (all prepared in DMEM). The pH of the GelMA solution was regulated to pH~7. The cell-encapsulated GelMA solution was cast within SR/ST and PDMS/SO scaffolds and cured by exposure to visible light (with the wavelength of 450–550 nm and intensity of ~100 mW/cm2) for 7 min to crosslink the GelMA solution. Then, the cell-encapsulated GelMA/scaffolds were cut for the biocompatibility experiments. A bulk cell-laden GelMA sample (with a thickness of ~1 mm) was also prepared as a control. A live/dead assay (Biotium, Fremont, CA, USA) was performed to examine the viability of the cells encapsulated in GelMA (both bulk GelMA and GelMA infilled into porous scaffolds) at days 1, 3, and 5. To prepare the live/dead staining solution, 3 μL of calcein acetoxymethyl (to stain live cells) and 12 μL of ethidium homodimer-1 (to stain dead cells) were mixed with 6 mL of Dulbecco's phosphate-buffered saline (DPBS). The samples were first washed with DPBS a couple of times. Then, 2 ml of staining solution was added to each sample and placed in the incubator for 30 min. Afterward, the staining solution was removed, and the samples were rinsed with DPBS. Finally, the cells were imaged with a fluorescent microscope (Axio Observer 5, Zeiss, Germany) where the excitation/emission wavelengths were ~528/617 nm and ~494/515 nm for ethidium homodimer-1 and calcein, respectively. The final green color imaged the live and red color indicated dead cells. Cell viability of each sample was defined as the ratio of live cells to the total number of cells (live and dead) and obtained by ImageJ software (version 1.52e, National Institute of Health, USA).

4.2.8.2. PrestoBlue cell viability assay

To measure the metabolic activity of the cells, 3D scaffolds filled with cell-encapsulated GelMA were prepared following the same method explained in section 4.8.1. The metabolic activity of 3T3 cells was examined on days 1, 3, and 5 utilizing PrestoBlueTM assay. 2 mL of

PrestoBlue (10% v/v in complete media) was added to each sample and the samples were incubated for ~2.5 h. Then, 100 µL of the PrestoBlue sample was transferred to a 96 well plate. Using a microplate reader (BioTek UV/vis Synergy 2, VT, USA), the absorbance values were obtained at 530 nm.

4.2.9. Statistical analysis

One-way analysis of variance (ANOVA) was used for analyzing the reported data and P values less than 0.05 were considered significant. Error bars represented the standard error of mean among at least three replicates.

4.3. Results and discussion

4.3.1. Fabrication process

Figure 1 illustrates a schematic of the developed fabrication process, which combines a template-based 3D printing with a post-curing on-demand shrinkage process. We demonstrate the fabrication of the porous constructs designed based on complex shapes such as that of TPMS structures. TPMS geometries are defined based on the implicit equations representing smooth and curvy spatial shells that divide the 3D space into two co-continuous phases. Cubic unit cells of the TPMS geometries are periodically repeated throughout the 3D structure of the scaffolds. A library of the pore shapes and porosity values of the TPMS-based scaffolds designed in this study is presented in Figure 4.1. P-surface consists of the tubular horizontal and vertical linkages meeting at the cubically pattered joints. D-surface and G-surface are other examples of TPMS geometries where tilted elements connect an oriented set of cellular patterns to form an interconnected construct. Porosity was maintained constant throughout the scaffold in the uniform structures while for the radially gradient porosity scaffolds, the porosity was set to 0.25 at the center and linearly varied to 0.75 at the periphery of the scaffold.

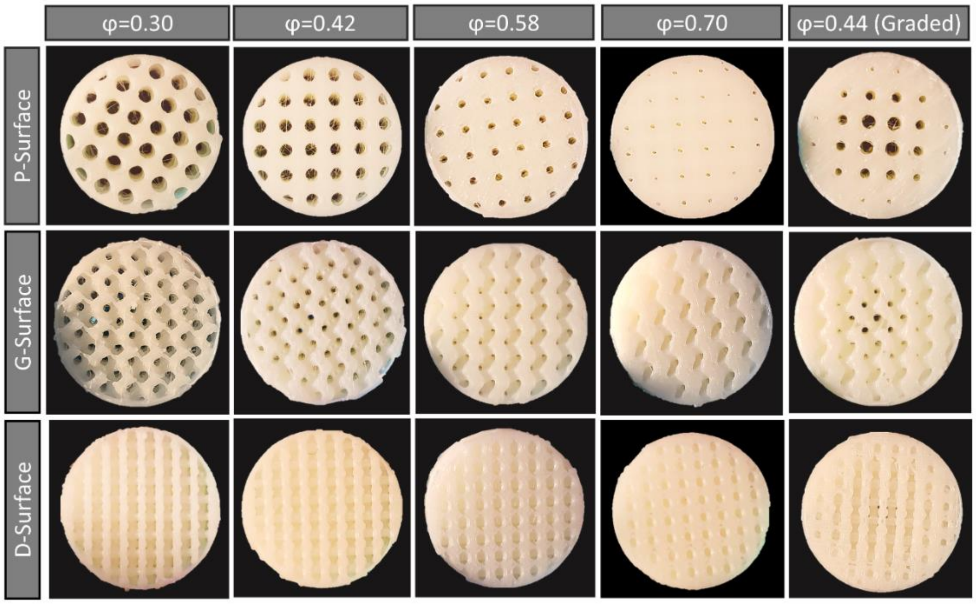

Figure 4.1. Optical images of ABS molds designed with P-, D-, and G-surfaces at various uniform porosity values of φ=0.30, 0.42, 0.58, and 0.70 and gradient relative density φ=0.75-0.25 (varying from center to periphery with average relative density of φ=0.44).

Sacrificial porous ABS molds, representing the negative image of the desired elastomeric structures, were first 3D printed using the FDM technology (Figure 4.1, Figure 4.2(a)I, Figure 4.2(b)I). The porous ABS molds were then filled with mixtures of silicone-based prepolymer with a thinner playing role as a shrinking agent (Figure 4.2(a)II, Figure 4.2(b)II). For this purpose, two combinations of silicone rubber/silicone thinner (SR/ST) and polydimethylsiloxane/silicone oil (PDMS/ST) were studied separately. The interconnected continuous porous phase in ABS mold created with the aid of TPMS designs enabled the full infusion of the SR/ST prepolymer into the molds. After the curing process, the ABS plastic was removed by dissolution in acetone (Figure 4.2(a)III, IV, Figure 4.2(b)III, IV). The porous scaffolds were then further acetone treated for a longer period (~7 days) to obtain the maximum shrinkage (Figure 4.2(a)V, Figure 4.2(b)V). No wrinkles was observed on the surface after the shrinking step. Although fabricating a single sample takes about one week but high throughput fabrication is possible by creating hundreds/thousands of samples at the same time. The proposed method offers a low-cost fabrication scheme that uses accessible tools and materials when it has the potential for serial production. For this purpose, all samples can be immersed in a bath of acetone to reduce solvent waste material. Besides, acetone can be recycled and separated from plastic through some methods such as fractional distillation due to its low boiling point (~56°C). This template-assisted method outperforms that of direct-write 3D printing methods developed earlier for silicone-based materials in terms of resolution and the ability to form complex ordered porous elastomeric scaffolds.

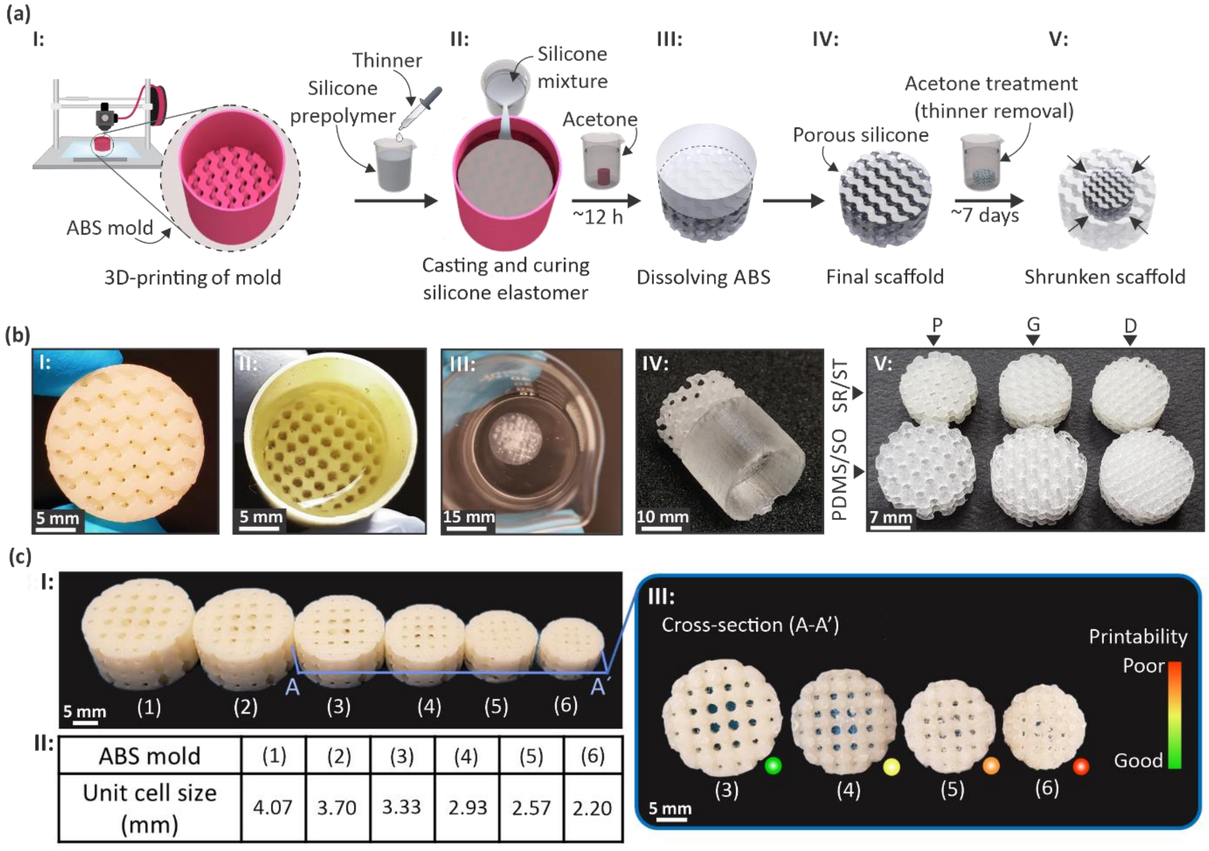

Figure 4.2. The fabrication process development for manufacturing high-resolution porous silicone-based elastomeric scaffolds. (a) Step-by-step schematic illustration of the fabrication procedure. I: the porous ABS molds are FDM 3D printed in which II: the silicone prepolymer mixed with a shrinking agent (a thinner) is cast and cured. III: After the elastomer is fully cured overnight, the sacrificial molds are dissolved in acetone. IV, V: the porous elastomeric scaffolds are further treated in acetone for an extra ~7 days until full shrinking was attained. (b) The optical images of I: ABS sacrificial mold, II: ABS mold infilled with the silicone prepolymer mixture, III: the dissolution of ABS mold in acetone, IV: porous PDMS attached to bulk PDMS, and V: final porous silicone rubber (SR)/silicone thinner (ST) and polydimethylsiloxane (PDMS)/silicone oil (SO) scaffolds designed with P-, D-, and G-surface topologies at φ=0.42. (c) I, II: The printability of the ABS molds designed with gradient relative density (φ=0.75-0.25) with various unit cell sizes as shown in III.

4.3.2. Unit cell size effect on printing fidelity

FDM is a versatile, well-established, and low-cost technique for 3D printing of complex shapes from thermoplastics such as ABS and PLA. This technique is capable of supportless fabrication of submilimeter overhanging features. However, the coarse resolution and limited minimum printable feature size compared to the more advanced technologies prevent successful 3D printing at scales below a certain limit. To minimize the final scaffold pore size and also maximize the specific surface area, we examined the printing fidelity of the ABS molds to identify the smallest unit cell size where all the molds can be 3D printed with no visible defects. The ABS molds designed with P-surface topology with a gradient radial relative density distribution from 0.75 at the periphery to 0.25 at the scaffold center (average relative density of 0.44) with various unit cell sizes of 2.20, 2.57, 2.93, 3.33, 3.70, and 4.07 mm (see Figure 4.2(c)I, II) were fabricated and their cross-section were inspected for any defects as shown in Figure 4.2(c)III. It was observed that some of the small struts in the center and pores in the periphery were failed in the molds with the unit cell sizes of 2.20 and 2.57 mm (Figure 4.2(c)III). We found minor defects in the samples with the unit cell size of 2.93 mm. The samples with the unit cell sizes of equal or greater than 3.33 mm were successfully 3D printed with no visible failure. Thus, the unit cell size of 3.33 mm was chosen for the design of the ABS molds. The same unit cell size was used to confirm the successful fabrication of the D-surface and G-surface topologies, and thereby this unit cell size was used for the rest of characterizations.

After casting the SR/ST or PDMS/SO mixtures and dissolving the molds, all elastomeric scaffolds were fully formed. This also confirmed that the unit cell size was large enough to assure the mixtures fully diffuse through the pores and fill the molds. Hence, SR/ST and PDMS/SO scaffolds designed with P-, D-, and G-surface topologies (see Figure 4.2(b)V) at uniform relative densities of 0.30, 0.42, 0.58, and 0.70, as well as the gradient relative density (0.25 in periphery and 0.75 in the center) were successfully fabricated, except P-surface at $\varphi=0.30$ that failed during the acetone treatment process. The failure happened because of the small thickness of vertical struts in P-surface topology after shrinking (see Figure 4.3).

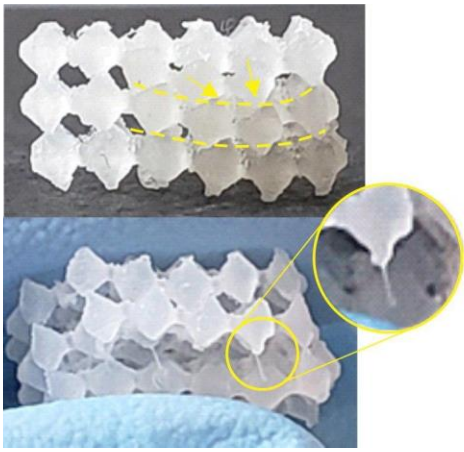

Figure 4.3. Failure of the P-surface model at φ=0.30 during the acetone treatment process, due to the weak connections in the model topology.

4.3.3. Shrinking behavior of silicone elastomers

4.3.3.1. Effect of thinner concentration

The SR/ST and PDMS/SO cylindrical constructs shrank in acetone over 1 month. Both SR/ST and PDMS/SO samples lost weight at higher rates at the beginning and afterward at lower rates until they reached a plateau following ~7 days of the solvent treatment process (Figure 4.4(a, b)). As the concentration of the thinner in the samples increased to 50 and 70 wt.% for ST/SR and SO/PDMS, respectively, a higher weight loss (at each time point) was observed (see Figure 4.4(a, b)). Adding more thinner to the silicone prepolymer resulted in failure in crosslinking. At the maximum thinner contents for SR and PDMS based elastomers, the highest steady weight loss values of ~63.7%, and 62.5% were observed, respectively.

The samples with larger thinner contents possessed a lower concentration of crosslinking agent due to the dilution of silicone base prepolymer with thinner. This results in a lower crosslinking density as a further increase in the thinner concentration was found to hinder the elastomer crosslinking [148, 149]. The observed shrinking behavior of silicone/thinner compositions is basically explained by the extraction of thinner from the loosely crosslinked 3D silicone network. This process is further facilitated by the swelling behavior of silicone-based elastomers in acetone (PDMS can swell in acetone solution by ~30%) [150], allowing short chains of thinner components to easily leach out from the 3D polymer network. In addition, we noted that the observed final weight loss levels overtake the concentration of the silicone thinner. This suggests that the acetone treatment process not only involves the extraction of thinner, but also the unreacted silicone chains could potentially leach out from the swollen polymer network in the solution. This also explains the observed weight loss for the silicone elastomers in the absence of silicone thinners (0 wt.%). Although this value for PDMS/SO was negligible, SR/ST displayed ~30.6% weight loss. This observation can imply the larger amount of silicone chains left unreacted and thereby lower crosslinking density in the SR/ST compared to PDMS/SO silicone elastomers.

The volumetric shrinkage results were also in line with the weight loss measurements (see Figure 4.4(c)). The volume measurements after shrinkage represent a maximum reduction of ~63.6% and ~68.7% in the bulk material volume for PDMS/SO and SR/TR, respectively. A linear trend was observed for the volumetric shrinkage with the concentration of thinner. The fact that these figures are in the same order as the results of weight loss suggests a homogeneous and uniform shrinkage over the entire structure. Similarly, the SR/TR samples with no thinner additives exhibited volumetric shrinkage levels of ~35.2%, whereas this was negligible for the PDMS/SO samples (~4.2%).

4.3.3.2. Effect of solvent type

The impact of the treating solvent on the final shrinkage behavior of bulk silicone-based elastomers is studied in this section. The shrinkage results of SR/ST and PDMS/SO samples (prepared with the same thinner concentration of 50 wt.%) in different organic solvents (*i.e.*, acetone, isopropanol, ethanol, and dichloroethane) are represented in Figure 4.4(d-f). The SR/ST samples treated in acetone and isopropanol showed the greatest weight loss and volumetric shrinkage. This is attributed to the synergistic role of silicone-based extracts' solubility as well as the swelling behavior of silicone elastomers in those solvents. The lowest weight loss and volumetric shrinkage were observed in the samples soaked in ethanol (Figure 4.4(d, f)). The samples immersed in water showed negligible shrinkage, which can be attributed to the hydrophobic nature of silicone extracts. Similarly, treating the PDMS/SO samples in isopropanol and acetone resulted in the highest while immersing in ethanol led to the lowest weight loss and volumetric shrinkage (Figure 4.4(e, f)). Due to the high shrinking of SR/ST and PDMS/SO samples in acetone and efficient solubility of ABS, we selected acetone for the fabrication of porous samples. Acetone is also preferred over the aggressive solvents such as dichloromethane due to its lower toxicity.

4.3.3.3. Shrinkage of microporous TPMS

In this section, we implement the fabrication parameters associated with high shrinkage in the silicone-based elastomers to examine the shrinking behavior of the porous constructs. To assess the effect of relative density and pore-shape on shrinking behavior of SR/ST and PDMS/SO scaffolds, the porous scaffolds architected with P-, D-, and G-surface topologies at uniform relative densities of 0.30, 0.42, 0.58, and 0.70, as well as the gradient relative density (0.25 in periphery and 0.75 in the center) were fabricated. Then, the scaffolds were treated in acetone for ~7 days. All the scaffolds contained 50 wt.% thinner. As shown by the results of Figure 4.4(g), the effect of relative density and pore shape on volumetric shrinkage of SR/ST and PDMS/SO scaffolds did not seem to play a critical role in the shrinkage amount, whereas the material system effect was found to be more effective as also highlighted in the shrinkage results of Figure 4.4(a-c). In the case of SR/ST TPMS scaffolds, the volumetric shrinkage was in the range of 66.5±0.5% to 71.0±0.4% for various relative densities and pore shapes. PDMS/SO TPMS scaffolds exhibited less volumetric shrinkage in the range of ~44.8±1.6% to 50.1±1.2%. The shrinkage levels for the porous structures were in the order of that of bulk solid samples (Figure 4.4(c)). Both SR/ST and PDMS/SO scaffolds showed homogenous shrinkage without any evidence of structural distortion. The overall change in diameter and height of SR/ST and PDMS/SO scaffolds compared to the ABS mold is presented in Figure 4.4(h) for better visualization. The scaffold diameter for SR/ST and PDMS/SO was reduced by 21% and 34%, respectively (approximately similar changes were observed for the scaffold height suggesting isotropic shrinkage).

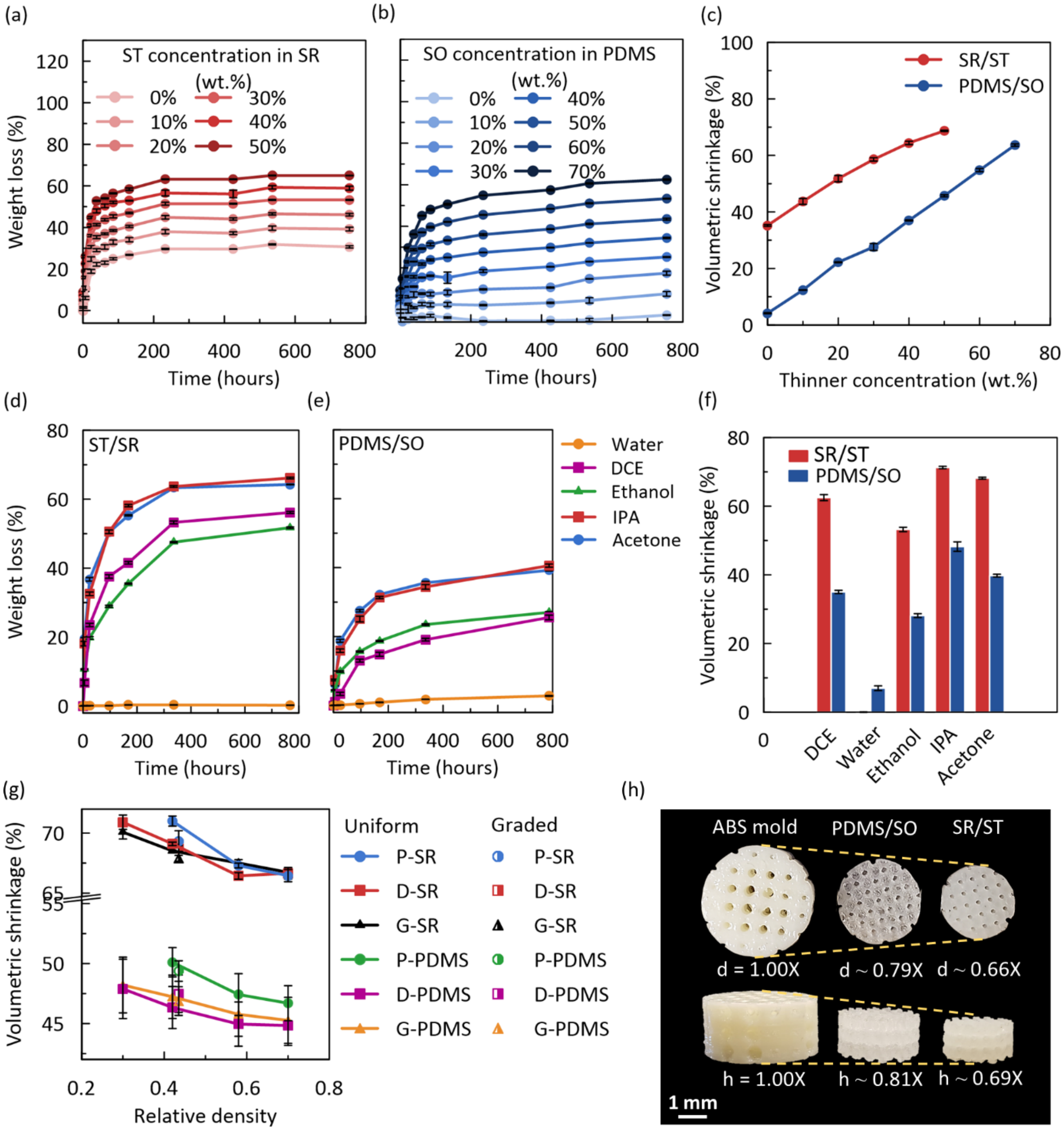

Figure 4.4. Shrinking characterization of elastomeric constructs. (a, b) Weight loss of SR/ST and PDMS/SO cylindrical constructs overtime for the samples treated in acetone, as a function of thinner concentration (i.e., silicone thinner (ST) and silicone oil (SO)) content. (c) Volumetric shrinkage of SR/ST and PDMS/SO constructs, after ~ 1 month acetone treatment, as a function of thinner content. (d, e) Weight loss of SR/ST and PDMS/SO cylindrical constructs, respectively. The samples contained 50 wt.% thinner before the treatment in various solvents. (f) Volumetric shrinkage of SR/ST and PDMS/SO constructs after ~754 h immersion in various solvents. (g) Volumetric shrinkage of SR/ST and PDMS/SO scaffolds, designed with TPMS topologies (i.e., P-, D-, and G-surface) at various relative densities, after 7 days of acetone treatment (silicone-based prepolymers contained 50 wt.% thinner). (h) Optical images of the SR/ST, and PDMS/SO scaffolds (designed with P-surface topology at φ=0.58 and treated in acetone for 7 days) comparing the dimensional changes (d is diameter and his height) of the scaffolds.

4.3.4. Structural and surface topology characterization

Microscale features of the ABS molds, SR/ST, and PDMS/SO structures are presented in the SEM images in Figure 4.5(a-d). The stair-like surface features on the ABS mold surface (white arrow in Figure 4.5(a) and Figure 4.6(a)) are formed due to the layer-by-layer 3D printing of the ABS filament in the FDM process. The mold surface roughness and the height of the stairs (the printed layer thickness) is in the order of nozzle diameter. The shell-like molds were totally sealed to prevent any polymer leakage during and after casting. During the casting process, SR/ST and PDMS/SO mixtures could flow into the interconnected pores/channels to fully fill the molds and there was no evidence of considerable defects (e.g., trapped bubbles) within SR/ST or PDMS/SO. Figure 4.5(b) and Figure 4.6(b) show the SR/ST scaffold designed with D-surface at $\varphi=0.42$. Figure 4.5(c, d) and Figure 4.6(c, d) demonstrate the PDMS/SO scaffolds architected with G-surface and D-surface at $\varphi=0.75$-0.25, respectively. The pore size at $\varphi=0.75$ and $\varphi=0.25$ were measured ~410 μm and ~720 μm, respectively. Moreover, no ABS residue was observed on the surface of the elastomeric scaffolds confirming the full dissolution of the sacrificial mold.

The X-ray images of SR/ST scaffolds designed with P-surface geometry at $\varphi=0.42$ containing 10 wt.% (cross-section in yellow) and 50 wt.% (cross-section in blue) ST, along with the distribution of isolated micropores in the solid phase were represented in Figure 4.5(e-g). According to the CT imaging data, the total volumetric shrinkage for SR/ST scaffolds with 10 wt.% ST was measured to be ~40.5% while for the scaffolds with 50 wt.% ST the shrinkage raised to ~69.4%. The 3D imaging (Figure 4.5(g)) was indicative of micro-scale voids and isolated pores inside the silicone elastomer which is assigned to the trapped air during the casting process. The micropores were smaller than 6×106 μm^3 and total volume of those micropores in SR/ST scaffolds was found to be fairly insignificant (total volume of 3.1×107 and 6.1×107 μm^3 for the samples with 10 wt.% and 50 wt.% ST, respectively) compared to the total volume of the solid model (representing ~0.004-0.015 v/v% of the solid volume as shown in Table 4.1). The X-ray imaging results presented in Table 4.1 confirm the fabricated structures match the original CAD models in terms of the relative density (deviations within ~5%) for the SR/ST models. The volumetric deviations of the solid phase in the X-ray images from the CAD models were found to be in the order of the shrinkage results presented in Figure 4.4(c, g).

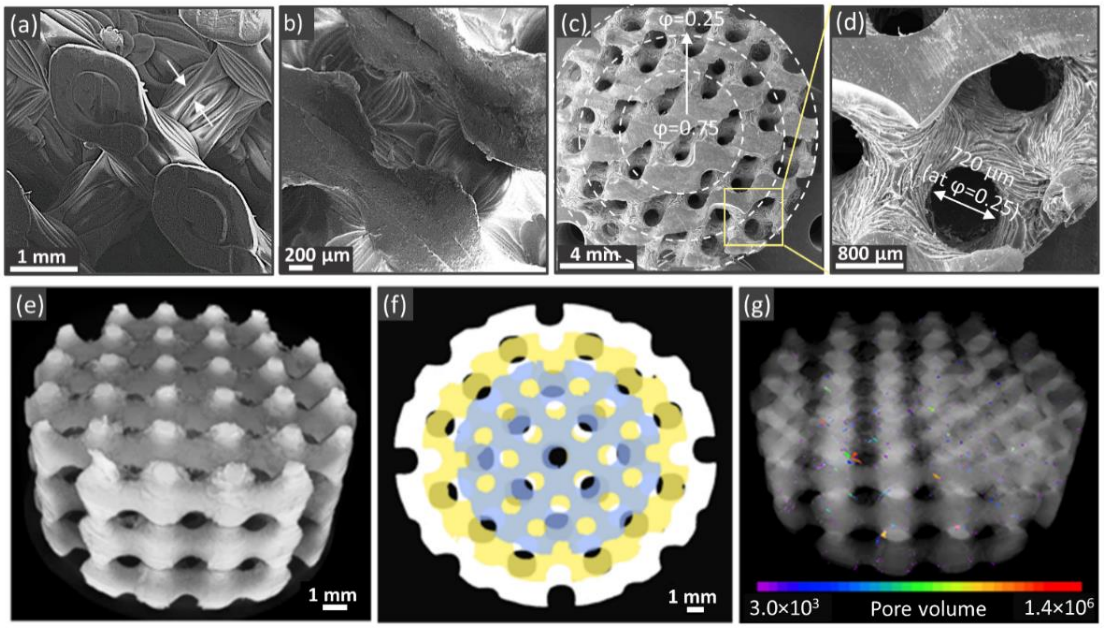

Figure 4.5. SEM and 3D X-ray images showing the surface and internal features of the mold and scaffolds after shrinkage. (a) SEM image of ABS mold designed with D-surface geometry at φ=0.30, (b) SR/ST scaffold designed with D-surface geometry at φ=0.42, and (c, d) graded PDMS/SO scaffold architected with G-surface geometry at φ=0.75-0.25 (e) 3D X-ray image of SR/ST scaffold designed with P-surface geometry at φ=0.42. (f) cross-sectional images of ABS mold (white), SR/ST scaffold with 10 wt.% ST (yellow), and SR/ST scaffold with 50 wt.% ST (blue) designed with P-surface at φ=0.42. (g) Distribution of internal voids and micropores in the SR/ST scaffold due to the trapped air when casting SR/ST mixture in ABS mold.

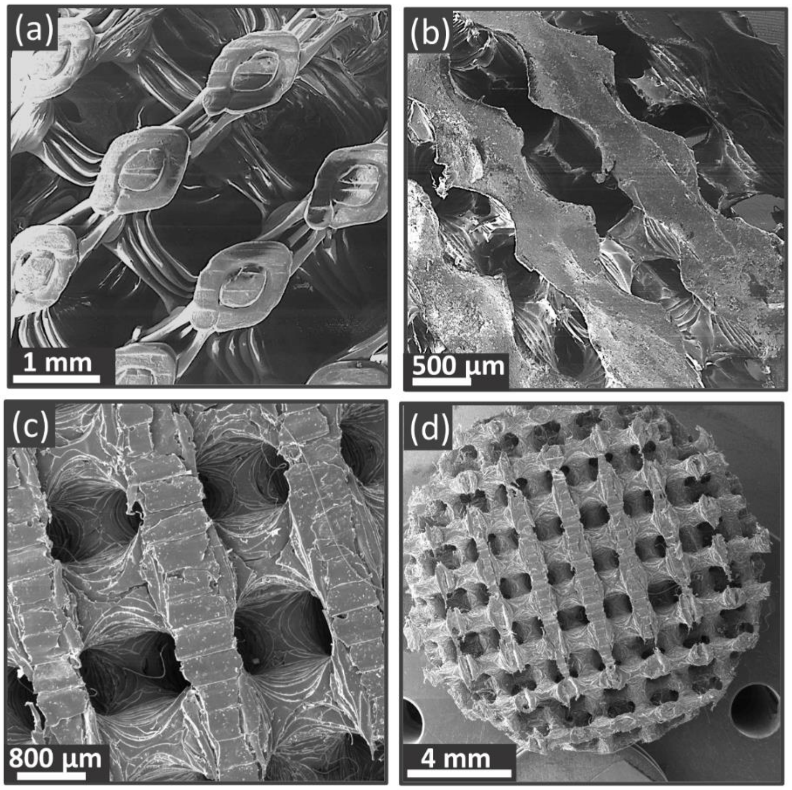

Figure 4.6. SEM images of (a) ABS mold (D-surface, φ=0.30), as well as (b) SR/ST (D-surface, φ=0.42), (c) PDMS/SO (D-surface, φ=0.42), and (d) PDMS/SO (D-surface, φ=0.75-0.25) scaffolds after shrinkage.

Table 4.1. The comparison between the CAD models and X-ray imaging of the fabricated models in terms of relative density (φ) and volume of the fabricated SR/ST scaffolds with 10 wt.% and 50 wt.% ST after shrinkage (the samples designed with P-surface topology at φ=0.42).

Thinner concentration	Relative density (φ)			Volume (mm^3) of solid phase			Relative volume of micro-porosity %
	CAD	X-ray	Deviation %	CAD	X-ray	Deviation (Volumetric shrinkage %)	
10 wt.%	0.42	0.43	2.38%	1319.47	784.82	40.52%	0.004%
50 wt.%	0.42	0.44	4.76%	1319.47	403.25	69.44%	0.015%

4.3.5.Compressive mechanical properties

4.3.5.1. Compression response of the bulk silicone-based elastomers before/after shrinkage

In this section, the effect of thinner concentration on the mechanical compressive properties of the bulk material (cylindrical silicone-based constructs) before and after acetone treatment is studied. For this purpose, the cylindrical SR/ST and PDMS/SO constructs composed of various thinner contents (from 0 wt.% to 50 wt.% ST for SR and from 0 wt.% to 70 wt.% SO for PDMS) were prepared and subjected to compressive monotonic loading up to 85% strain. The compressive stress-strain curves for the SR/ST and PDMS/SO samples are demonstrated in Figure 4.7(a, b) and Figure 4.7(c, d), respectively. In general, the stress-strain curves showed an identical trend to that of flexible elastomers; they started with a linear region followed by a continuous strain hardening at high strains due to the barrelling-induced increase in cross-sectional area as well as compaction of the chain entanglements with compression. The results of mechanical properties, i.e. the elastic modulus and deformation energy are represented in Figure 4.7(e, f), respectively. As it can be seen in Figure 4.7(e), before the samples were subjected to any solvent treatment process, the elastic modulus was reduced by 87.7% and 93.9% as a result of adding thinner content at the maximum concentrations for the SR/ST and PDMS/SO material compositions, respectively. The reduction in stiffness with the addition of thinner additives is explained by the lower crosslinking density because of the dilution of silicone prepolymer with the thinner. In essence, the thinner molecules remain within the elastomer network without participating in the crosslinking reaction. This means that those molecules do not participate in load-bearing and can easily comply with the chain movements.

After treating the samples with acetone, the elastic modulus of the samples significantly increased commensurate with the thinner content (*e.g.,* up to 750% and 169% for the SR/ST and PDMS/SO material systems at their highest thinner content). A larger increase in stiffness for the SR/ST compared to PDMS/SO is in line with the greater volumetric shrinkage of SR/ST observed in the results of Figure 4.4(c). In fact, extraction of the thinner from the crosslinked network leads the compaction of polymer chains thereby larger crosslinking density that eventually increases the overall stiffness of the construct. Even the constructs with no thinner additives were characterized with significant stiffening post solvent treatment (250% for SR and 60% for PDMS) probably due to the removal of unreacted silicone chains as explained in section 2.3.1. The changes of mechanical properties in the neat silicone-based elastomers were in accordance to the results of Figure 4.4(c) since the SR was characterized with a significantly larger shrinking behavior. This may suggest that the larger amount of prepolymer in PDMS contributes in crosslinking as opposed to SR. Besides, the SR/ST structures showed lower loading energies compared to PDMS/SO structures either before or after acetone treatment (Figure 4.7(f)) which can be indicative of lower crosslinking density/reaction, further confirming the above justification on the observed stiffness changes.

Aside from the elastic properties, flexibility and strain reversibility of the SR/ST bulk structures were diminished with acetone treatment, whereas acetone treatment had a lower influence on the strain recovery behavior of PDMS/SO. In case of PDMS elastomers, our experiments demonstrated a brittle permanent failure and crack propagation under excessive compression for the neat PDMS samples whereas addition of over 10 wt.% SO to the PDMS prevented the crack growth and led the structure to maintain its structural shape after unloading (following a loading up to 85% compressive strain). Similarly, for the acetone treated PDMS, the addition of over 30 wt.% SO was associated with full strain recovery in response to the excessive compressive deformations (~85% strain).

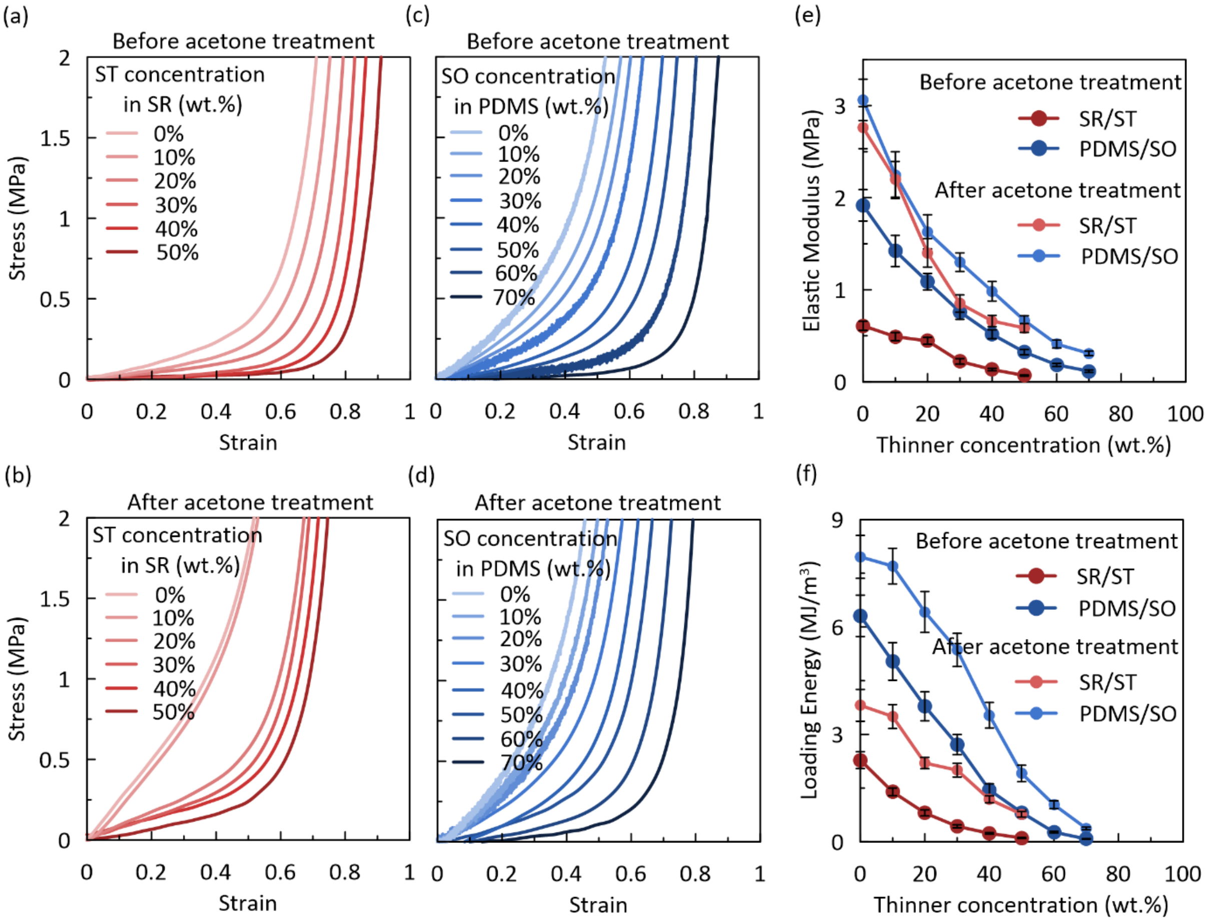

Figure 4.7. The effects of material composition and solvent triggered shrinkage on the mechanical properties of bulk silicone elastomers under monotonic compressive loading. Compressive stress-strain curves of SR/ST samples (a) before and (b) after acetone treatment and PDMS/SO (c) before and (d) after acetone treatment at different thinner concentrations. The effects of acetone treatment and thinner concentration on the (e) elastic modulus and (f) absorbed energy during the compressive loading.

4.3.5.2. Compressive behavior of TPMS scaffolds

Here, we evaluate the effects of pore design on the mechanical characteristics of porous scaffolds based on SR/ST and PDMS/SO prepolymers containing 50 wt.% ST and 50 wt.% SO, respectively, subjected to a ~7 days period of acetone treatment for full shrinkage. To this aim, the scaffolds architected with P-, D-, and G-surface topologies at uniform relative densities of 0.30, 0.42, 0.58, and 0.70, as well as the gradient relative density (0.25 in periphery and 0.75 in the center) were fabricated and tested as represented in Figure 4.8(a-f). The compressive stress-strain curves showed a similar trend to that of flexible porous materials and polymeric foams.[12]

Initially, the stress varied linearly with compression. Then, as the scaffold underwent densification, a remarkable increase in stress at higher strains was observed (Figure 4.8(a-f)).

The deformation mechanism of the scaffolds mainly depends on the unit cell shape and relative density. The scaffolds architected with P-surface topology undergo axial compression or buckling in the linkages along the loading direction (Figure 4.8(g)I). This deformation mechanism is recognized as stretching dominated behavior. Unlike the P-surface topology that is formed of struts oriented in the loading direction, the D- and G-surface topologies mainly comprise 45° inclined linkages. Hence, the linkages in the scaffolds designed with D- and G-surface topologies develop shear stress induced by bending deformation (Figure 4.8(g)II and Figure 4.8(h)). This deformation mechanism is recognized as bending dominated deformation. The augmented flexibility (lower elastic modulus) observed in D-surface scaffolds compared to the P-surface based structures, can be explained by the bending dominated deformation in the former versus the stretching dominated deformation in the latter one. We further observed that unlike the acetone treated SR/ST bulk cylindrical structures that showed irreversible deformation under sever compressive loading (see section 3.5.1), the porous scaffolds were much more flexible and reversible after applying 85% strain (Figure 4.8(h)).

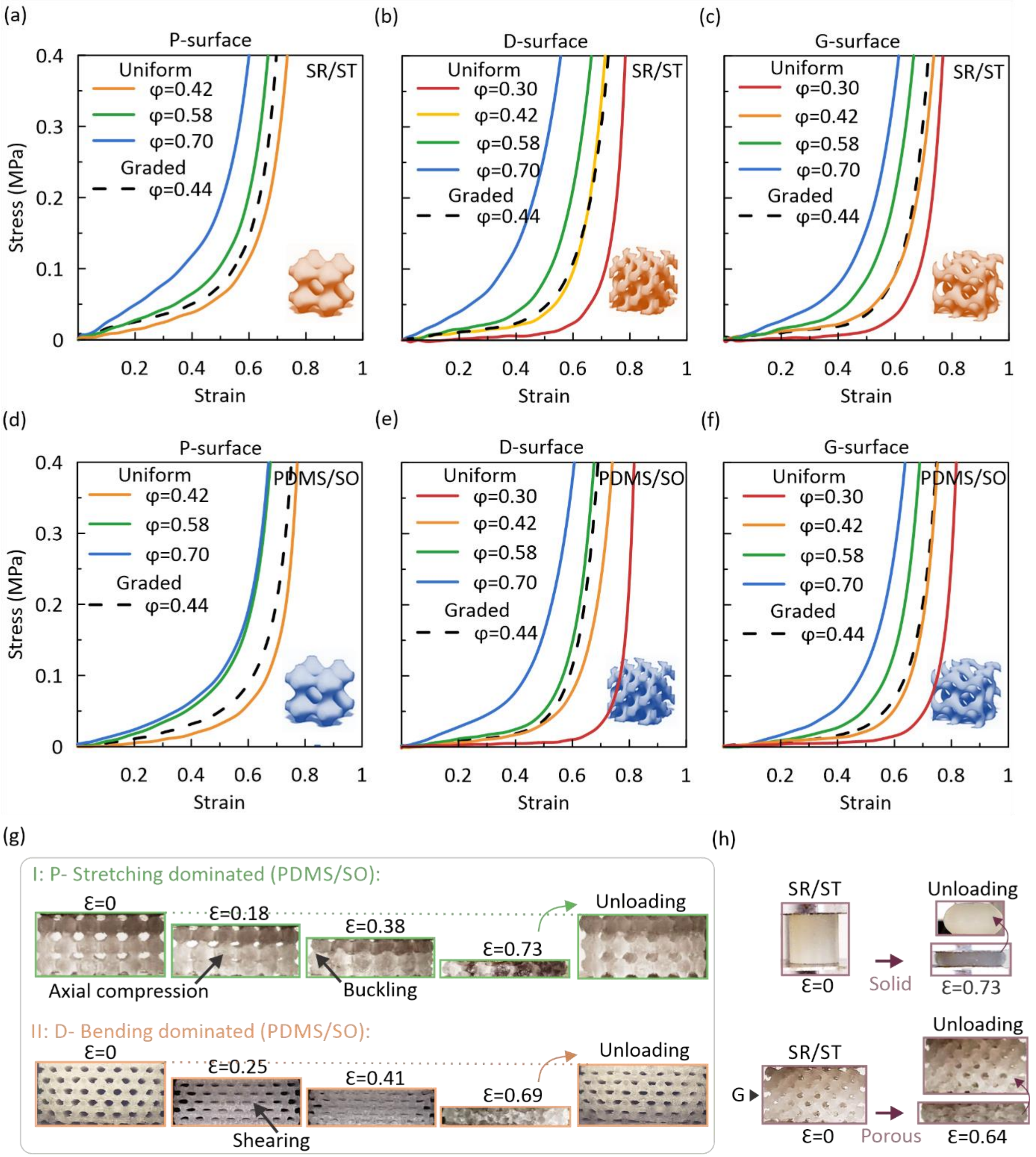

Figure 4.8. Stress-strain curves and deformation mechanisms of the elastomeric scaffolds under monotonic compressive loading. Compressive stress-strain curves of SR/ST designed with (a) P-surface, (b) D-surface, and (c) G-surface, as well as PDMS/SO scaffolds designed with (d) P-surface, (e) D-surface, and (f) G-surface geometries at different relative density values and porosity distribution patterns. (g) Mechanical deformation under compressive loading and the failure mechanism of scaffolds; classified as I: stretching dominated (i.e. P-surface at φ=0.42), and II: bending dominated (i.e. D-surface at φ=0.42) depending on the topology design. (h) Comparison of strain reversibility between porous SR/ST (designed by G-surface at φ=0.42) and solid SR/ST (both were treated in acetone and contained 50 wt.%ST) following deformations of up to 85% compressive strain.

The elastic modulus, loading energy, and densification strain of the scaffolds can be tuned by manipulating the unit cell shape, relative density, and the silicone material composition. The mechanical properties for SR/ST and PDMS/SO are shown in Figure 4.9(a-c) and Figure 4.9(d-f), respectively. An elastic modulus in the range of 13.60 kPa to 292.35 kPa for SR/ST and 16.50 kPa to 167.78 kPa for PDMS/SO scaffolds were obtained (Figure 4.9(a, d)) that is in the range of most soft tissues and organs such as cartilage.[141, 142, 151] In terms of densification strains, changing the relative density from 0.30 to 0.70 accelerated the onset of densification for SR/ST and PDMS/SO scaffolds by ~9.8% and ~12.5%, respectively (Figure 4.9(c, f)). The gradient scaffolds showed the mechanical properties close to the expected properties of the uniform scaffolds with their average relative density (i.e., ~0.44%).

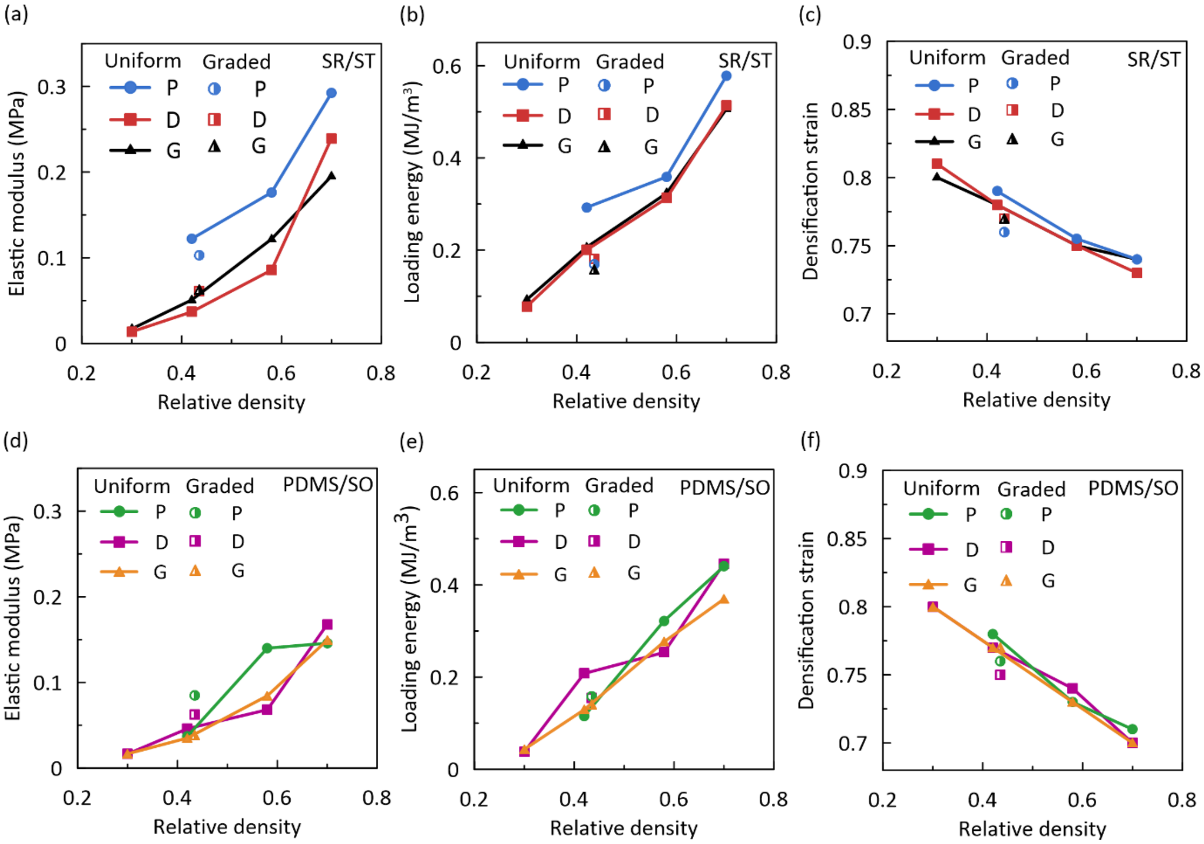

Figure 4.9. Mechanical properties of the SR/ST and PDMS/SO scaffolds (containing 50% thinner) under monotonic compressive loading. The relationship between (a) Elastic modulus, (b) loading energy, (c) densification strain, and relative density for SR/ST scaffolds. (d) Elastic modulus, (e) loading energy, and (f) densification strain changes with relative density for the PDMS/SO scaffolds.

4.3.6. Evaluation of Biocompatibility

To evaluate the potential of the fabricated scaffolds for use as implantable tissue replacements, we incorporated the scaffolds with a cell-laden hydrogel based on GelMA, which is known as a highly biocompatible and biodegradable extracellular matrix mimicking characteristics. We further studied the biocompatibility of the cell-incorporated silicone/GelMA constructs. The SR/ST and PDMS/SO scaffolds (designed with G-surface and fabricated with 50 wt.% thinner concentration) were chosen for the study of cell viability and metabolic activity within 5 days of culture. As shown in Figure 4.10(a), the 3T3 fibroblast cells remained alive (green) in all samples (i.e., SR/ST and PDMS/SO scaffolds filled with cell-encapsulated GelMA as well as control bulk GelMA) after 5 days of encapsulation. The results from live/dead assay confirmed cell viability of over 90% at day 1 for both SR/ST and PDMS/SO scaffolds (Figure 4.10(b)). The high cell viability of ~85% was maintained after 5 days for all samples which were in the range of the control bulk GelMA. This confirmed the biocompatibility of the scaffolds and potential suitability for use as tissue implants. Besides, cell metabolic activity was assessed by a PrestoBlue assay through measuring the absorbance at days 1, 3, and 5 after encapsulation. Figure 4.10(c) shows the metabolic activity of the cells in the GelMA-infilled SR/ST and PDMS/SO scaffolds were in the range of the control bulk GelMA. High biocompatibility corroborated the potential application of the proposed scaffolds in tissue engineering and confirmed the implemented fabrication process leads to a final biocompatible construct.

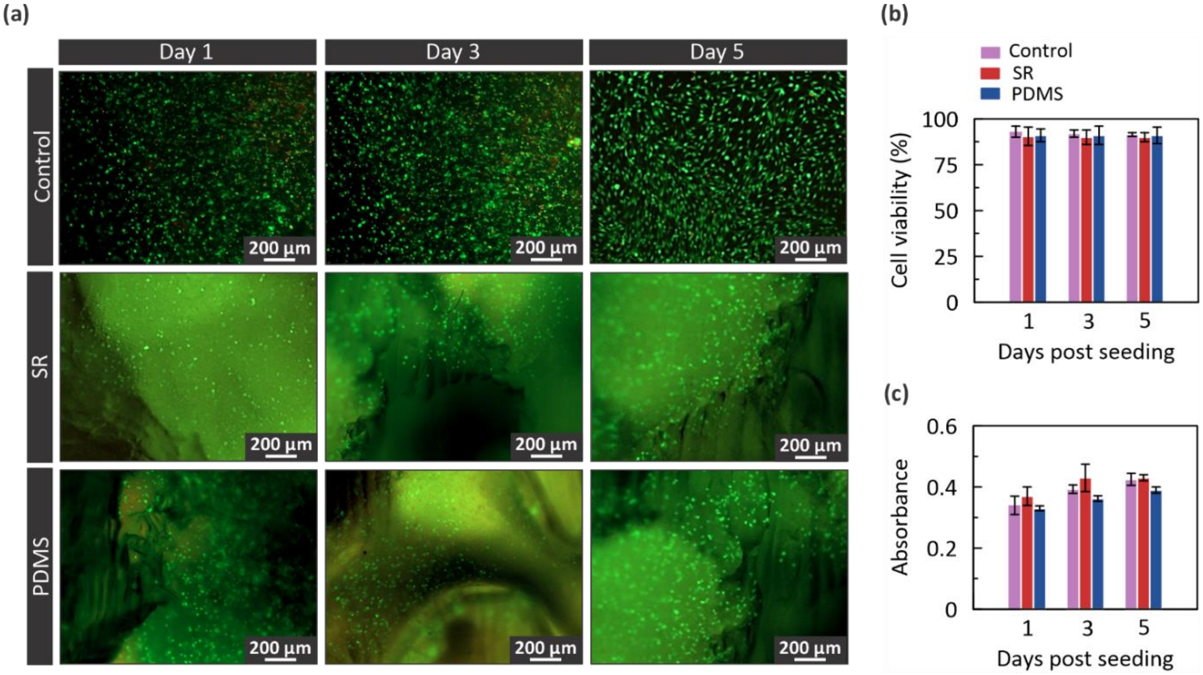

Figure 4.10. *In vitro* biocompatibility analysis of elastomeric scaffolds. (a) Live/dead cell staining of 3T3 fibroblasts encapsulated in control bulk GelMA hydrogel and GelMA infilled into SR/ST and PDMS/SO scaffolds designed with G-surface at φ=0.30. The fluorescent microscope images of cells after 1,3, and 5 days from encapsulation. Green color shows live cells and red color indicates dead cells (b) Cell viability and (c) metabolic activity of fibroblasts on days 1, 3, and 5.

4.4. Conclusions

The current study introduced a low-cost shrink-induced fabrication technique for developing higher resolution customized silicone-based scaffolds architected with micrometer-sized interconnected tortuous channels. The elastomeric scaffolds were shaped with the aid of sacrificial templates that were fabricated by FDM 3D printers at a printable size scale. The silicone-based elastomeric scaffolds could be shrunk down following an acetone treatment procedure in a controllable manner. The sacrificial molds with a unit cell size of 3.3 mm guaranteed the defect-free manufacturing of various geometries designed by TPMS geometries at a wide range of relative densities. The fabricated scaffolds posed post-shrinkage pore sizes in the range of ~500 µm. The shrinking behavior of the elastomer was found to be well tunable with the concentration of thinner, treating solvent type, treatment time, as well as the silicone/thinner material system. Thinners not only enabled on-demand shrinkage of the silicone-based elastomeric constructs, but they also contributed to the strain recovery characteristics under extreme compressive deformations. Despite the PDMS/SO system showed lower volumetric shrinkage limit (i.e., ~50%) compared to SR/ST elastomer system (i.e., ~70%), the PDMS/SO surpassed SR/ST in terms of strain recoverability. The strain recovery was found to be even more prominent, when the constructs were fabricated with porous micro-architecture (as per the strain reversibility in response to up to ~85% compressive strains). For the porous scaffolds, the deformation mechanism (bending versus stretching dominated) and from there, the mechanical properties could be well-tuned by the relative density and unit cell shape. Due to the high biocompatibility and desirable mechanical properties as well as the tunable design of microchannels, the elastomeric scaffolds fabricated with the proposed template-based fabrication method, outrank similar counterparts manufactured by direct 3D printing techniques and can pave new avenues toward advanced biomedical wearable devices/sensors and implants.

Chapter 5. 3D-Printed Ultra-Robust Surface-Doped Porous Silicone Sensors for Wearable Biomonitoring

5.1. Introduction

Three-dimensional porous graphene nanocomposites have provided new opportunities for development of multi-physical sensors with tunable and high specificity response [152-156]. Flexible porous polymer/carbon nanocomposites hold promise to become an important material in wearable electronics [157-162] as stretchable motion sensors [163, 164], temperature sensors [165], and humidity sensors [166-170], supercapacitors [171-174], and vapor/gas detectors [175, 176] due to their superior piezoresistive properties. Thanks to the advent of 3D printing techniques, these properties can be engineered through the pore architecture for optimized signal sensitivity, high flexibility, pore interconnectivity, and mechanical durability.

Multiple examples have addressed the use of direct ink-based 3D printing techniques to construct conductive porous structures out of nanocomposite inks [177-182]. However, a non-trivial drawback associated with direct printing of porous sensors is the significant decay of mechanical flexibility when additives such as carbon nanoparticles are blended with the base polymer ink. In particular, for the material compositions with high percolation thresholds (greater than 10 wt.%) [183, 184], the inherent polymer flexibility is entirely deteriorated. Adding any additives itself is a serious obstacle for the curing process [120]. Hence, a substantial attention is paid to the alternative ways such as coating based methods [185-187] to attain conductivity in nanocomposite materials.

The main approaches undertaken for coating flexible substrates with carbon nanomaterials involves physical infusion [188], chemical vapor deposition [189, 190], and dip coating [191, 192]. Dip coating process has been favorable since the scalability of fabrication process. Moreover, due to the electrostatic interactions between the nanoparticles and polymers, the dip coating process offers a high rate of nanoparticle uptake at each coating cycle. However, this process is not without its drawbacks. Dip coated sensors are susceptible to degradation of electrical properties due to the lack of a strong bond between the nanoparticles and the underlying substrate. This leads to limited shelf life and sensing performance decay, particularly in harsh environments (e.g., mechanical loads or solvent treatment). Therefore, further attempts should be made to improve integration of the nanoparticles with the underlying flexible substrates during the coating process.

Additive manufacturing of the flexible substrates out of silicone elastomers has been demonstrated for complex-shaped structures and features [193]; however, when it comes to tortious porous structures with fine features, it may be challenging, if not impossible, to maintain structural integrity and printing fidelity throughout the 3D printing process. Despite the high flexibility of silicone rubber, the viscous nature of silicone base polymer makes it difficult to print due to the poor mechanical integrity of printed layers (particularly in case of support-free hanging features) [91, 93] which limits the number of layers that can be printed [122]. Nozzle clogging is also a hindering factor as the prepolymer may partially cure into the nozzle while being extruded [123]. Template-assisted fabrication of porous graphene has been introduced as a potential solution to fabricate self-standing porous conductive nanocomposites [194-199]. However, the current methods primarily emphasize on the sacrificial structures based on the porous metallic foams. This process lacks controllability on the architecture of conductive sheets, needs more costly coating methods such as CVD, and typically requires aggressive solvents for removing the sacrificial mold layer [200-206].

Here we aim to fabricate durable and flexible 3D porous sensors for wearable devices. High specific surface area in 3D porous materials enables coating more amounts of conductive materials on the surface and improves electrical properties. We introduce a sacrificial template-assisted 3D printing method based on accessible and inexpensive 3D printing techniques (*i.e.* FDM) for fabrication of shape-customized, flexible, and strain-reversible porous sensors with interconnected pores. Triply periodic minimal surfaces [156] are used to topologically engineer the piezoresistive performance of the sensors. In this process, a highly durable and continuous coating of graphene nanoplatelets (GnP) throughout the surface of porous silicone rubber (SR) is obtained by surface-doping GnP within a thin layer of SR. The sensors are assessed in terms of temperature, humidity, and strain sensitivity in the context of incorporation of the (GnP) on the porous SR surface. Then, the long-term durability (over 12 months), resistance to harsh environments (e.g., solvents), as well as sensor robustness under cyclic mechanical loads (400 cycles) are evaluated. Finally, we demonstrate the biocompatibility of the sensors and their potential application in wearable sensor devices for monitoring human movements and vital signs.

5.2. Materials and Methods

5.2.1. Materials

Graphene nanoplatelets (AO-3) with 12 nm average flake thickness (30-50 monolayers) and 4500 nm (1500-10000 nm) average particle lateral size was supplied by Graphene Supermarket, USA. The particle size distribution was analyzed separately using DLS analysis (Figure 5.1). Mold Max-10T silicone rubber and silicone thinner were provided by Smooth-On Inc., Canada. The organic solvents were supplied by Sigma-Aldrich Corp., USA. The ABS filament was provided by Stratasys, Minnesota, USA. Mouse embryo fibroblast cells (NIH/3T3) were procured from the American Type Culture Collection (ATCC, VA, USA). All the cell culture media and supplements including DMEM with glucose concentration (4.5 g/L), 0.25% trypsin-0.02% ethylenediaminetetraacetic acid (EDTA) 1X, sterile Dulbecco's phosphate-buffered saline (DPBS, 1X), and heat-inactivated fetal bovine serum (FBS), streptomycin (10,000 µg/ml)/penicillin (10,000 U/ml) solution were bought from Gibco (NY, USA). PrestoBlueTM cell viability reagent and LIVE/DEADTM viability/cytotoxicity kits were purchased from Invitrogen (OR, USA). Cell culture flasks (75 cm^2) were provided from Corning (NY, USA). Polystyrene 12-well and 96-well tissue culture-treated plates were obtained from Falcon (NC, USA).

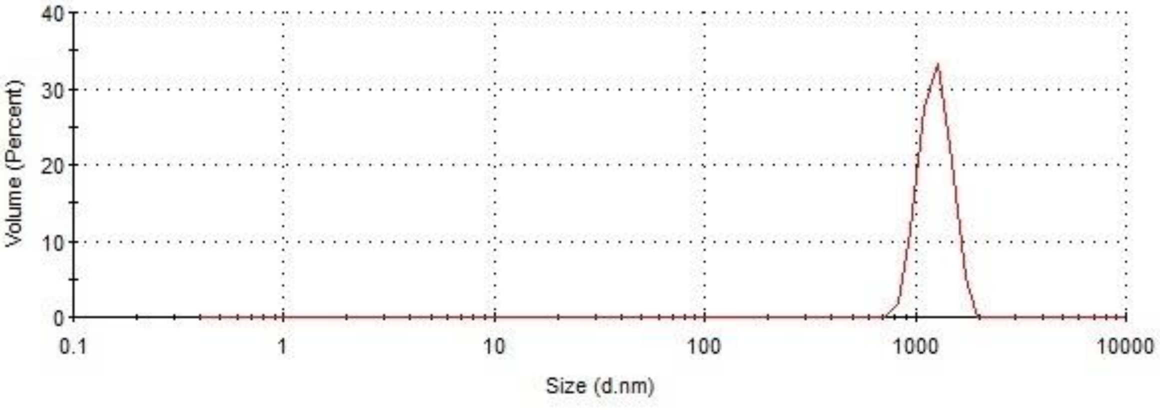

Figure 5.1. The size distribution of GnPs measured by Dynamic Light Scattering (DLS). Polydispersity (PDI) = 0.612.

5.2.2. Design/3D printing of Sacrificial Molds

The porous SR sensors were designed with the TPMS architecture. TPMS geometries are mathematically defined based on the following general equation (Eq. (5.1)):

$$\Gamma(\mathbf{r}) = \sum_{l=1}^{L}\sum_{m=1}^{M} \mu_{lm} \cos\left(2\pi\kappa_l(\mathbf{P}_m^T.\mathbf{r})\right) = C \tag{5.1}$$

where $\mathbf{P}_m = [a_m, b_m, c_m]^T$ represents a basis vector in the 3D-Space E^3; κ_l is the scale parameter; μ_{lm} represents the periodic moment; and $\mathbf{r} = [x, y, z]^T$ shows the location vector. In this equation, the constant value C corresponds to the overall porosity. The left-hand side of the equation defines the pore shape. In the present paper, the equations associated with the P-surface and D-surface (i.e., $\Gamma_P(\mathbf{r}) = \cos x + \cos y + \cos z = C$ and $\Gamma_D(\mathbf{r}) = \cos x \cos y \cos z - \sin x \sin y \sin z = C$, respectively) were considered with different C values corresponding to the relative densities of 30, 42, 58, 70% (as specified in Table 5.1). To define the 3D SR solid model, the space domain $\varphi < C$ was considered; this refers to the inward volume trapped by the continuous TPMS sheets.

For generating the STL files, a MATLAB code was used to produce black and white cross-sectional images of the TPMS models based on their defining equations. To print the sacrificial molds, the negative image of the porous SR sensors ($\varphi < C$) were defined as a solid model for the purpose of 3D printing. The original CAD models consist of cylindrical porous geometries with a height of 10 mm and diameter of 20 mm where 6×6×3 unit cells were repeated along with the global coordinates (corresponding to a 3.33 mm cubic unit cell size). The STL files were then imported to the GrabCAD (GrabCAD Inc., Massachusetts, USA) software to define the printing parameters and generate the tool path G-codes. In order to facilitate the sacrificial mold removal, the geometries were printed with zero infill (resulting in hollow molds). The generated G-code was subsequently imported to an FDM F370 3D printer (Stratasys, Minnesota, USA) and the printing process was performed with a 100-µm layer thickness using an ABS filament at 310 ˚C nozzle temperature and 80 ˚C bed temperature. Also, no support material was needed to form the final geometries.

5.2.3. Sensor Fabrication Process

After the printing process, two methods were followed to incorporate the GnPs onto the porous SR surface:

(i) for the SDG sensors, the SR-base polymer was mixed with the curing agent with a weight ratio of 10:1, and then silicone thinner was added to the mixture with a weight ratio of 10:90 to reduce the viscosity and ease base polymer infiltration into the ABS molds. The molds were degassed under vacuum in a desiccator for approximately 30 min to extract the bubbles, and then the SR was cured overnight at the room temperature. Subsequently, the mold/SR samples were immersed into a 40 ml acetone solution for approximately 5 h while stirred at ~500 rpm. The solution was refreshed every ~1 h during the ABS removal process. This made the ABS mold to completely dissolve, leaving behind the porous SR attached to a solid silicone bulk which was later cut. The obtained porous SR samples were dip coated (in a multistep process) in a 30-ml graphene/Isopropyl alcohol (IPA) solution (1 wt.%) following dehydration (by exposing the sample to a heat gun for 1 min at each dipping cycle). This was done to accelerate dehydration to avoid the downward flow of the graphene solution (due to gravity) and non-homogeneity in the coating. The dip coating process continued for 20 times. Finally, copper tape electrodes were attached to both ends of the sensors by applying silver paste on the top and bottom surfaces of the sensor.

(ii) for the SEG sensors, the obtained ABS molds were dip coated similar to the process explained above for the SDG sensors. Then, the SR was poured into the mold, degassed in a desiccator for 30 min and curing process was completed at the room temperature overnight. Subsequently, the ABS mold was washed off, the solid bulk was cut from the porous region, and copper tape electrodes were attached (see the details in the SDG sensors above).

5.2.4. Electrical Conductivity Measurement

The resistance of the sensors was measured over time using a 2110 5.5 Keithley digital multimeter (Tektronix, Inc., USA) by a two-probe configuration. A DC voltage of 1 V was applied, and the real-time current was measured to obtain the electrical resistance of the sensors. The electrical conductivity calculated by $\sigma = L/AR$ for the porous samples with height L and cross-section of A. R is the ohmic electrical resistance measured by the multimeter.

5.2.5. Surface Characterization

To characterize the microstructural features of the surface, scanning electron microscopy (SEM) images were taken using a 1550 FESEM, Zeiss, Oberkochen, Germany instrument. A 10-nm layer of gold was sputtered before taking the images and the images were taken at 4 kV accelerating voltage. The internal features of the sensors were evaluated using nanocomputed tomography scanner (Xradia 520 Versa, Zeiss, Germany) with the voltage of 40kV at 20μm voxel size. The surface energy was measured by the water contact angle. To this, an optical photo of the droplet formed by a 10 μl DI water sample was taken by a digital microscope (AM7915MZT, Dino-Lite, Taiwan).

5.2.6.Mechanical Compression Test and Piezoresistivity Characterization

Mechanical performance of the sensors was evaluated by a universal test system (MTS Criterion 43, USA). The samples were placed between the compression grips so that the gap between the sample and the grips vanished. The quasi-static compression tests were conducted at a cross-head displacement rate of 2 mm/min while the electrical resistance was monitored over time and the force values was recorded. This rate was changed to 60 mm/min in the cyclic loading tests. The sensor sensitive towards mechanical deformations was characterized by the gauge factor ($GF =$

$d(\frac{\Delta R}{R_0})/\varepsilon$), where GF represents the gage factor, $\frac{\Delta R}{R_0}$ is the relative resistance change, and ε represents the applied strain.

5.2.7. Finite Element Simulation

Finite element (FE) simulations were conducted by an Abaqus explicit solver. The FE models were created by voxel meshes generated based on the cross-sectional images of the models. A MATLAB code was used to prepare the CAE models of the porous structures according to the images. The mesh size was chosen based on a mesh convergence study presented in our previous study [143]. For each model, the mesh size was tuned so that the final number of meshes exceed ~2500 voxels per unit cell to limit the divergence within the range of 5%. An elastoplastic constitutive material model was defined with an elastic modulus of 137 kPa and Poisson's ratio of 0.3 based on the standard tensile test performed on the SR material. a Displacement corresponding to the experimental compressive test was defined as the boundary conditions and the resulted computational stress-strain curves were reported.

5.2.8. Thermogravimetric analysis (TGA)

TGA tests were performed on the flat sheet samples. A 3 mm diameter sample was punched from a ~1 mm thick coated SR sheet. The samples were placed in an alumina holder in a Pyris Diamond TG/DTA instrument (PerkinEimer instruments, USA). Heating was performed from the room temperature (25˚C) to 800 ˚C at a rate of 15 ˚C/min in argon atmosphere; the mass loss as a function of temperature was recorded.

5.2.9. Dynamic light scattering (DLS) measurements

To characterize the GnP size and polydispersity, a DLS experiment was performed using a Malvern Instruments, UK, Series 4700 device. A pre-cleaned cuvette was filled with 1 ml of ~0.01 wt.% GnP solution in IPA with 1.3776 refractive index and 1.96 cp viscosity at the room temperature. Then, DLS measurements were conducted after equilibrium was reached.

5.2.10. Temperature and Humidity Test

Sensitivity of the sensors towards environmental factors i.e. temperature and humidity was evaluated by a Thermotron Environmental Chamber (SM-4-8200 Venturedyne Ltd.). Temperature and humidity profile were defined manually in a cyclic manner, and the tests were conducted while the electrical resistance recorded with time. Sensitivity to humidity and temperature was defined as the rate of the changes in relative resistance versus humidity and temperature data points, respectively.

5.2.11. PrestoBlue^{TM} Cell Viability Assay Test

NIH/3T3 mouse fibroblast cells were cultured in 75 cm^2 tissue culture flasks supplied with a 10 ml DMEM containing 1% streptomycin and penicillin, and 10% FBS solution. The cells were placed in a 37 ˚C standard incubator (Thermo Forma, Thermo Fisher Scientific, MA, USA) under a relative humidity of ~ 95% and CO2 concentration of 5%. Culture medium was exchanged twice a week and the cells density was monitored daily until confluence. At the confluency of ~ 90%, the cells were detached using trypsin-EDTA, centrifuged (Thermo Fisher Scientific, USA) at 1200 rpm for 3 min, resuspended in fresh complete media and counted with a hemocytometer (Thermo Fisher Scientific, USA).

For two-dimensional (2D) culture experiments, the fibroblast cells at the density of 1×10^5 cells per well were cultured in 12-well plate and cultured in 2 ml of complete DMEM for 24 h until > 80% confluency. The synthesized SDG and SEG sheets were cut using a biopsy punch (5 mm in diameter), sterilized under UV and placed at the corner of each well after adding the fresh culture medium. Metabolic activity of the cells was then measured on days 1, 3 and 7 using PrestoBlueTM assay following the manufacturer’s protocol. The medium was removed from the wells and 1 ml of PrestoBlue reagent (10% v/v in complete medium) was replaced. After ~ 1.5 h incubation, 100 µl of the sample was taken from each well. Then the samples were transferred to a 96-well plate in which the the fluorescence intensity. The intensity was measured at excitation/emission wavelengths of 530/590 nm, using a microplate reader (BioTek UV/vis Synergy 2, VT, USA). The measured fluorescence intensity was subtracted from the background signal of the PrestoBlue-containing cell-free media and reported as an arbitrary unit (a.u.). After the measurement, the PrestoBlue reagent was removed from the wells and replaced by fresh culture medium.

5.2.12. Live/Dead Assay Test

A live/dead fluorescence assay was performed to determine the cell viability in the well-plate. Briefly, the cells were incubated for ~10 min with 1 ml of the live/dead staining solution. The solution was prepared by adding 20 µl ethidium homodimer-1 and 5 µl of calcein in DPBS (10 ml). The staining solution was aspirated, the cells were washed with DPBS and imaged using fluorescent microscope (Axio Observer 5, Zeiss, Germany) at excitation/emission wavelengths of 528/617 nm for ethidium homodimer-1 and ~ 494/515 nm for calcein. The cell viability was quantified using ImageJ software (Version 1.52e, National Institute of Health, USA) by normalizing live cells count with the total cells.

5.3. Results and Discussion

5.3.1. Fabrication Process

Figure 5.2(a, b) schematically illustrates the two different coating procedures undertaken for fabricating the shape customized flexible porous sensors. In the first type of sensors (i.e. surface deposited graphene (SDG) coating (Figure 5.2(a)), graphene is dip coated on the interconnected surface of the porous SR (Figure 5.2 (a)IV) through the electrostatic interactions with the underlying polymer. In the second fabrication procedure (*i.e.*, surface embedded graphene (SEG) coating (Figure 5.2(b)), the porous SRs are continuously doped with a thin layer of GnP on surface so that GnP well integrated within the SR polymer.

In order to shape SR in the desired pore designs, negative hollow templates were fabricated using FDM from ABS (see Figure 5.2(a)I and Figure 5.2(c)). The hollow shaped molds enabled efficient and fast removal of the sacrificial material by simultaneously exposing the entire mold to the solvent. SR was cast into the mold and vacuum infused into the continuous pore phase of the mold (Figure 5.2(a)II and Figure 5.2(d)). After fully curing the SR, ABS mold was washed away by dissolving into acetone, leaving behind the porous SR (Figure 5.2(a)III and Figure 5.2(e)). A multistep dip coating process was performed to form a continuous layer on the top of the porous SR surface in the SDG sensors (Figure 5.2(a)IV). It is worth noting that since the range of pore sizes (above ~0.7 mm) is much larger than the GnP size, the coating was not affected by the pore characteristics.

For the SEG sensors, the fabricated ABS mold was dip-coated with graphene (Figure 5.2(b)II and Figure 5.2(f)); then, the SR was cast and cured similar to the process described above (Figure 5.2(b)III). This process resulted in the GnP coated on the ABS mold to be transferred/adsorbed to the SR surface at the ABS/SR interface during the SR curing process. After the SR was completely cured, the ABS mold was dissolved into acetone, led to the final porous sensor with a concentrated graphene layer on the surface (see Figure 5.2(b)IV and Figure 5.2(g)) embedded within the SR surface. In fact, the GnPs is bound on the surface by integrating them with SR on surface.

The proposed method offers a low-cost fabrication process for fabricating porous sensors coated with GnP. In this method, well-established, accessible, high-resolution, and inexpensive FDM 3D printer is used while direct 3D printing of the SR requires complex printing platforms and lowers the printing resolution [122]. As opposed to the stochastic foams [206], this approach enables producing 3D shape customized sensors with organized and controllable internal structure.

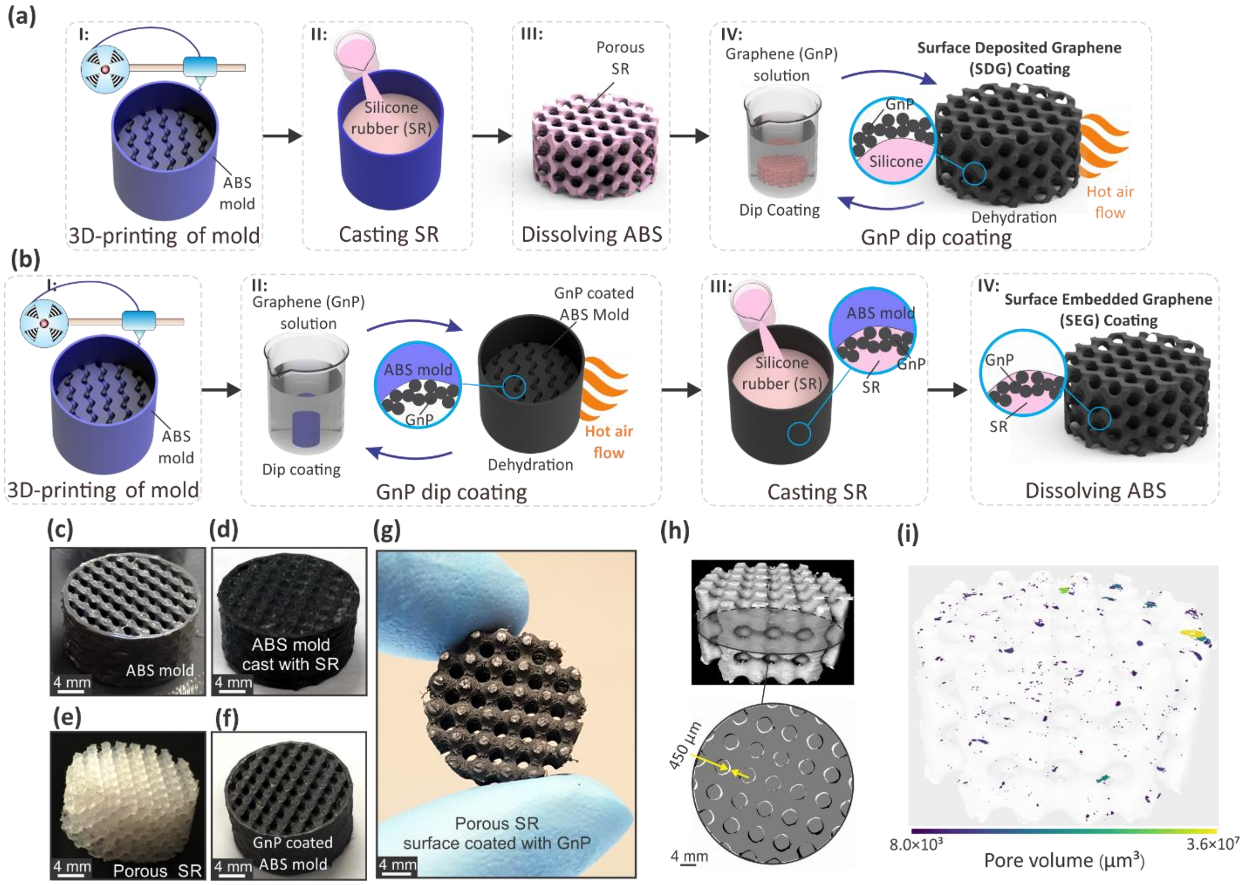

Figure 5.2. Schematic representation of the fabrication processes for (a) SDG sensors and (b) SEG sensors. In SDG sensors, FDM printed ABS molds cast with SR prepolymer. Porous SR substrate is obtained by dissolving ABS in acetone and a layer of graphene is deposited on the SR surface by multistep dip coating. SEG sensors are fabricated by graphene coating the ABS mold followed by cast curing SR leading to GnP transfer to the SR surface after dissolving ABS mold. Optical images of (c) ABS porous mold, (d) SR filled ABS mold, (e) porous SR substrate, (f) ABS coated with GnP, and (g) an example GnP-coated porous SR sensor. (h) 3D X-ray images of the fabricated sensors and comparison of the cross-section with the CAD model. Gray color represents the agreement between the printed sensor and CAD model, Black and white colors represent the printing mismatch. (i) Distribution of the micro-pores throughout the sensor due to the trapped air prior to SR curing.

5.3.2. Printing Fidelity

The capability of the presented printing method for fabricating tortious TPMS-based geometries was assessed in terms of printability and matching with the CAD model. The CAD models representing the sensor structures are presented in Figure 5.3. Representation of the CAD models for different pore shapes and porosity values of the porous sensors. The molds CAD models used in 3D printing were the negative image of the above models. Among the different TPMS architectures, the most well-known topologies called P-surface and D-surface were chosen to design the porous sensor models due to their unique deformation mechanisms. This allows distinguishing the sensor signal resulted by stretching (P-surface) versus bending (D-surface) dominated deformation mechanisms. More details on the constitutive equations and modeling procedure associated with these models are given in Methods section. The SDG porous structures with P-surface and D-surface were successfully fabricated at the design volume fractions ranging from 0.3 to 0.7; except the SEG sensors with P-surface architecture that failed at 0.3 volume fraction designs. This failure was caused as the GnP clogged the thin (~0.7 mm) connecting linkages in the ABS mold and did not allow the SR to completely diffuse into the pores.

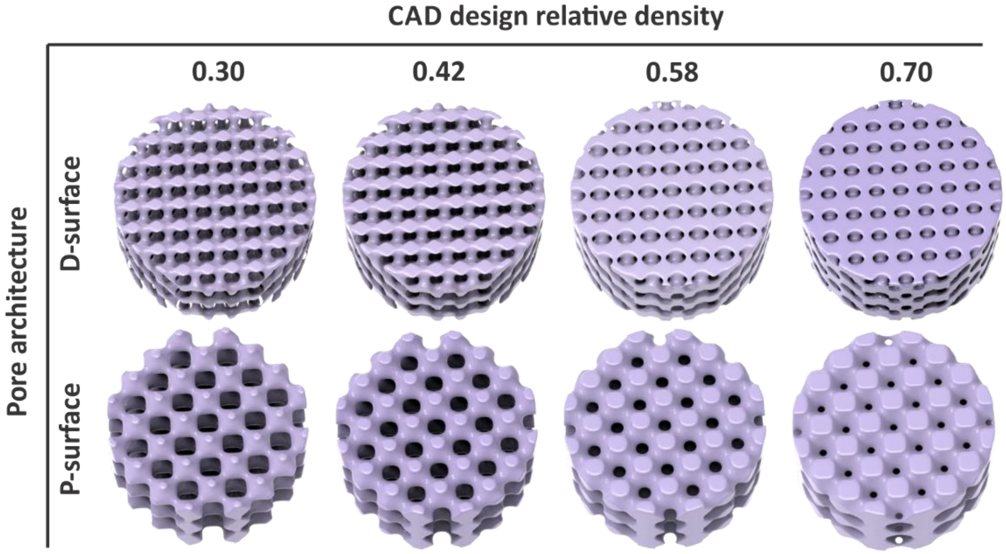

Figure 5.3. Representation of the CAD models for different pore shapes and porosity values of the porous sensors. The molds CAD models used in 3D printing were the negative image of the above models.

The results of Table 5.1 and Figure 5.4 compare experimental porosity values obtained by dry weighing for the fabricated structures with the design CAD porosity values. As seen, the measured porosity matches that of designed CAD model with a relative difference of less than 18%. A ~1-3mm global shrinkage in the diameter was seen, which is related to the thinner leached out during the fabrication process. X-ray images were also taken from the samples with 0.42 design relative density (Figure 5.2(h, i), Figure 5.5(a, b)) confirming a good agreement between the printed part with the CAD model cross section with ~450 µm maximum tolerance. As seen from Table 5.2, the 3D X-ray imaging results confirmed a similar order of errors in terms of both porosity and surface area compared to those obtained by dry weighing (Table 5.1). The higher surface area compared to the CAD design is justified by the stair-like surface inscribed to the SR by the 3D-printed mold (Figure 5.8(a)). It was also seen that micro-pores of smaller than 5×106 μm^3 are present due to the trapped air permeated into the SR polymer prior to curing (Figure 5.2(i) and Figure 5.5(c, d)).

Table 5.1. Comparison of the porosity designed in the CAD model and the experimentally measured porosity by dry weighing for the samples considered in this study as well as the constant C values used for modeling porous geometries with the desired relative density in the global TPMS equations. The sensor sample size was designed to be 20 mm in diameter and 10 mm in height.

Pore Type	C	Design Relative Density	Measured from the fabricated part							
			SDG				SEG			
			Diameter (mm)	Height (mm)	Relative Density	Error %	Diameter (mm)	Height (mm)	Relative Density	Error %
D-surface	-0.340	0.30	16.60	7.80	0.34	15.80%	17.30	8.40	0.35	15.26%
	-0.138	0.42	16.80	8.00	0.49	17.51%	17.30	8.80	0.48	13.01%
	0.135	0.58	17.05	8.40	0.66	13.32%	17.45	8.70	0.69	18.35%
	0.340	0.70	17.05	8.40	0.78	11.64%	17.70	8.70	0.73	4.59%
P-surface	-0.699	0.30	15.90	8.40	0.32	8.16%	N/A	N/A	N/A	N/A
	-0.280	0.42	16.40	8.40	0.43	1.28%	17.00	8.30	0.43	2.71%
	0.280	0.58	16.50	8.50	0.61	5.72%	17.00	8.20	0.60	2.99%
	0.699	0.70	16.30	8.60	0.71	1.54%	17.10	8.30	0.73	4.04%

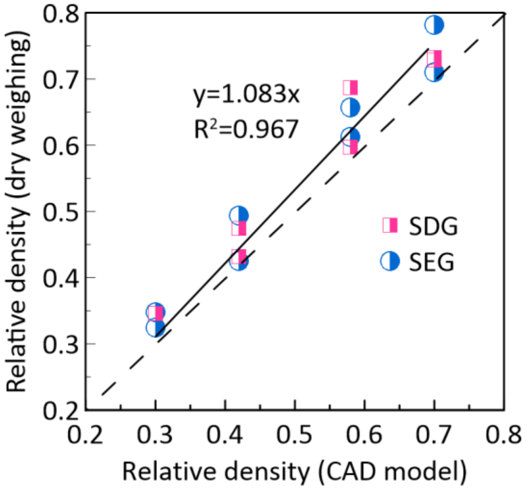

Figure 5.4. Graphical comparison of the relative density values obtained by dry weighing and the CAD design models.

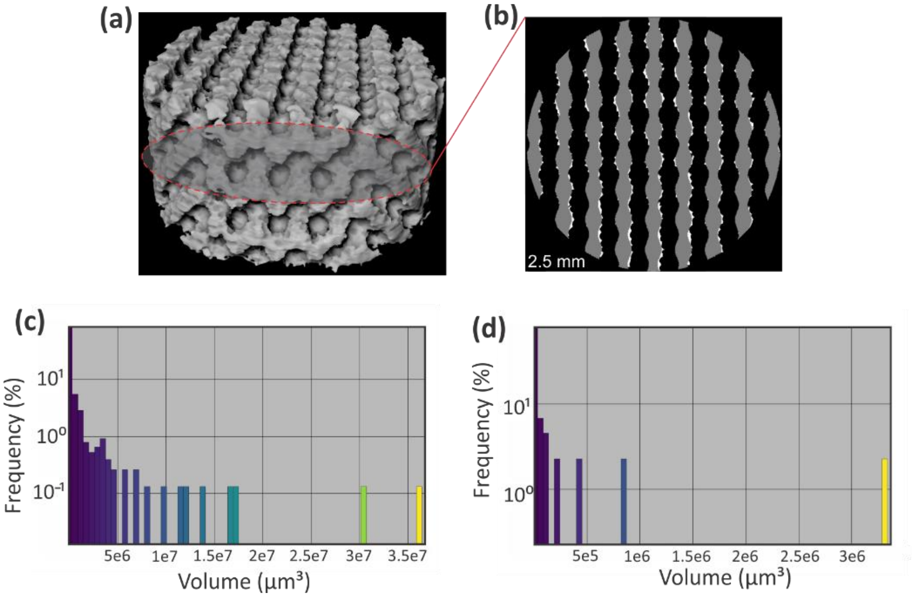

Figure 5.5. (a) 3D X-ray imaging of the structure D-surface at the 0.42 design relative density, and (b) comparison of the cross-sectional image with that of the CAD model. Volume histogram of the micro-pores for (c) P-surface and (d) D-surface models at the 0.42 design relative density.

Table 5.2. Comparison between the printed porous sensors with the CAD model in terms of the relative density and surface area measured by X-ray tomography.

	Relative density			Surface area		
Pore Type	CAD	X-ray	Error %	CAD (mm^2)	X-ray (mm^2)	Error %
P-surface	0.42	0.50	18.83%	3033.0	3594.2	18.50%
D-surface	0.42	0.37	12.91%	4182.0	5279.8	26.25%

5.3.3. Structural Characterization of Sensors

Microscale features of the materials and structures in different stages of the fabrication process are demonstrated in Figure 5.6(a-e). In addition, a schematic illustration of the mold/SR/GnP interface at different stages of the fabrication process is represented in Figure 5.7. The layer-by-layer printing of the ABS molds representing TPMS shells led to a stair-like morphology on the mold surface with a roughness in the order of printing layer thickness (Figure 5.6(a), Figure 5.7(a, b)I). As seen in Figure 5.6(a), the molds were sealed enough to prevent the SR from leaking into the hollow molds, and hence, the mold could keep the SR in the desired shape.

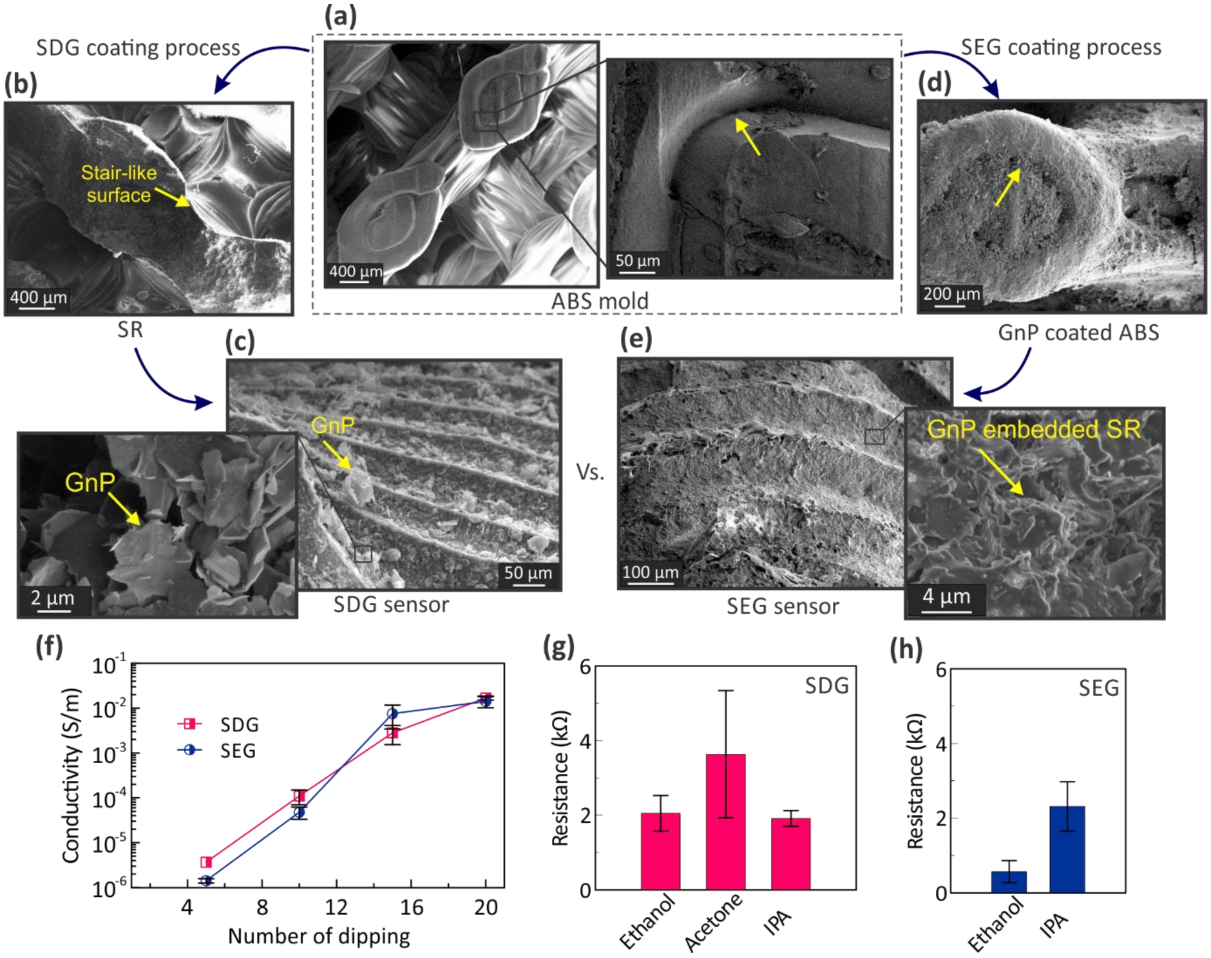

Figure 5.6. Representation of the SEM images of the structures obtained at different stages of the fabrication process. (a) ABS mold (the arrow shows the micro-corners that favor GnP agglomeration), (b) SR surface, (c) GnP deposited on the surface of SR through direct dip coating. (d) GnP coated ABS mold (arrow showing the entrapped GnP into the micro-corners) and (e) structural integration of the GnP into the SR in the surface of the SEG sensors. (f) Variations in sensor conductivity as a function of the number of immersion times during the dip coating process. Electrical resistance after 20th dipping times for the (g) SDG and (h) SEG sensors.

Despite high viscosity of the SR prepolymer, the SR passed through the pores/channels and fully filled the molds in the SDG sensors. Figure 5.6(b) shows the surface features of the porous SR after dissolving the ABS mold. As seen, the features in microscale (e.g., sharp corners and stair-like surface morphology of the ABS molds) were fully transferred to the SR (Figure 5.7(a)III). Upon dipping the porous SR into the GnP solution, progressive agglomeration of GnP particularly at the sharp edges was evident since they could trap the GnP in the solution (Figure 5.6(c), Figure 5.8(b, c), and Figure 5.7(a)IV). This implies that the SR rough surface pattern inscribed by the FDM process would physically favor GnP uptake during the dip coating process. The GnP in the

SDG-based sensors are vulnerable to flake off as no strong physical binding exists between the flakes and no binding agent is added to GnP. Likewise, in the case of the SEG sensors, the GnPs deposited on the ABS mold crevices (Figure 5.6(d), Figure 5.7(b)II) were transferred and thereby embedded into the SR surface as shown in Figure 5.6(e), Figure 5.9, and Figure 5.7(b)III, IV. In essence, a high concentration conductive GnP/SR composite layer wherein the SR keeps the GnPs strongly bound in place, covered the porous SR surface, which induces electrical conductivity while retaining the SR intrinsic flexibility. Based on the coating mechanism explained above, mechanical interlock within the surface grooves as well as electrostatic interactions between the SR and GnP led to the GnP coating (Figure 5.7(c)) while in the SEG sensors, GnPs are physically infused within a thin layer of SR (Figure 5.7(d)).

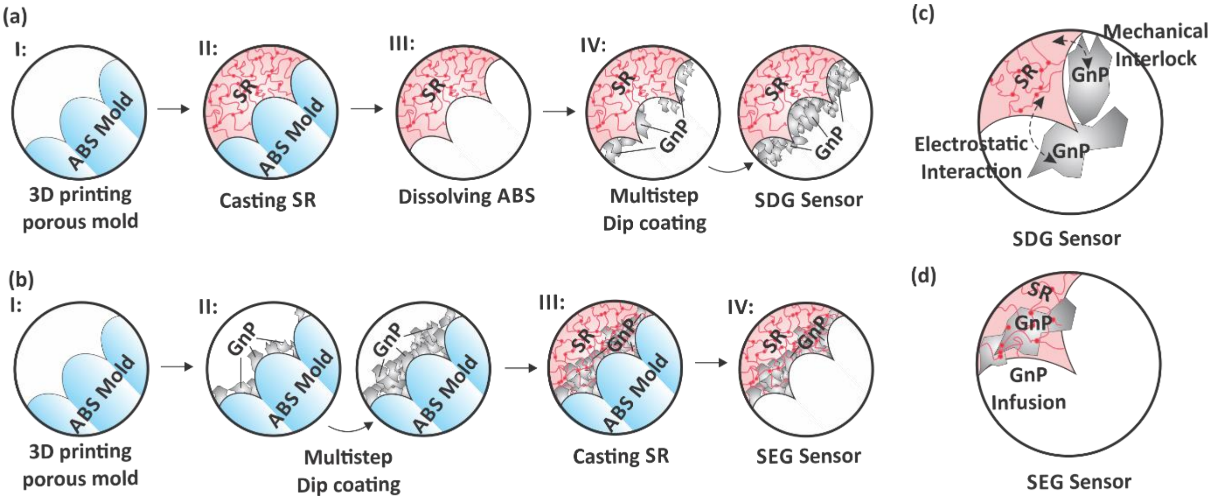

Figure 5.7. Schematic representation of the ABS mold/GnP/SR interface during the stages of fabrication process for (a) SDG and (b) SEG sensor. Mechanisms of GnP attachment to the SR matrix in (c) SDG and (d) SEG sensor fabrication.

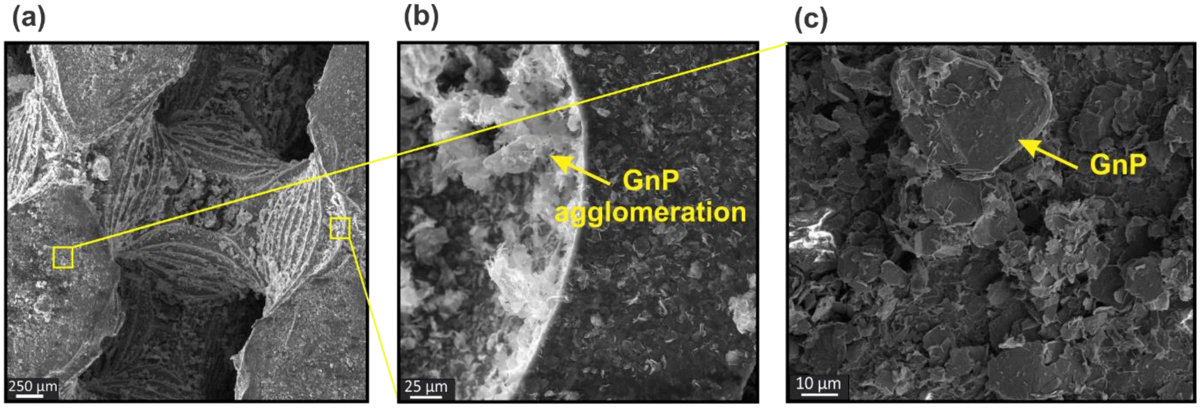

Figure 5.8. **(a-c) SEM images of the surface features of the SDG sensors. The GnPs are deposited on the SR surface due to the electrostatic interaction with the underlying substrate. The lack of a strong bond between the GnP and SR makes GnP vulnerable to flake off. The agglomeration of GnP at the corners of the stair-like surface is evident.**

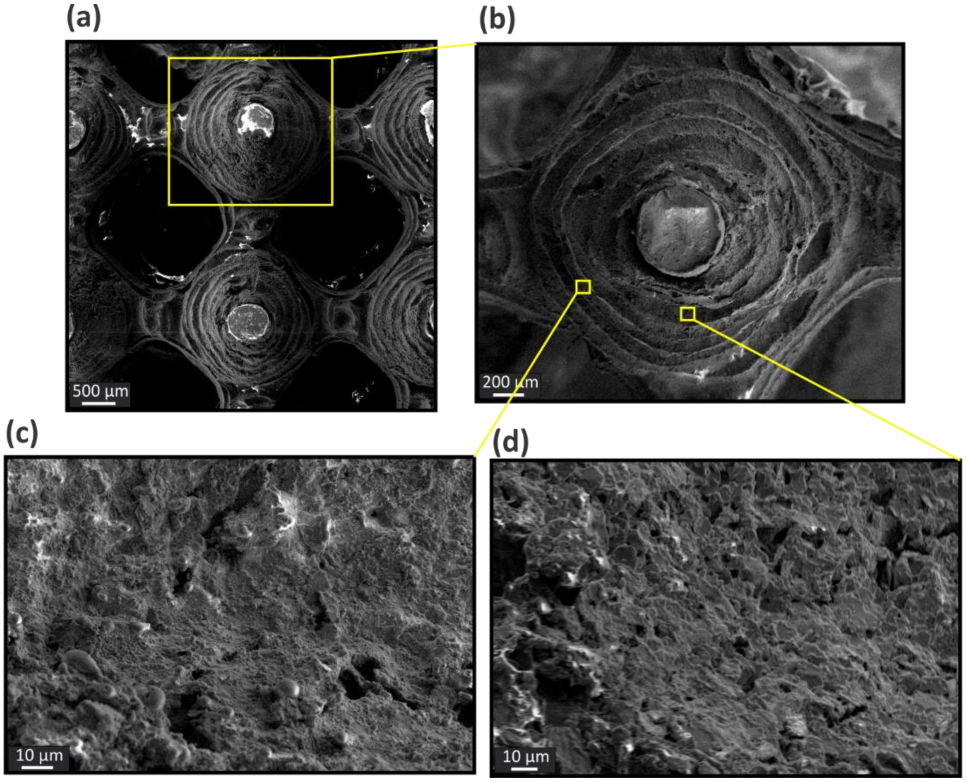

Figure 5.9. **(a-d) SEM images of the SEG sensor surfaces. The GnPs are glued by the SR into the polymer surface and keep them stable in place.**

The depth of GnP infusion in both sensors was evaluated by the SEM imaging, providing the GnP thickness in the cross-sectional images (see Figure 5.10). It is observed that the groove-and-ridge surface patterns on the sensor surface play a key role in the GnP coating mechanism. In microscale, for SDG sensors, a thicker layer of GnP was accumulated inside the SR grooves and thinner GnP was attracted to the ridges (Figure 5.10(a, b)). In the case of SEG sensors however, because the GnPs are originally aggregated at the ABS mold grooves, the GnP accumulation was observed to be more prominent at the SR ridges (Figure 5.10(c, d)). It should be noted that the GnP thickness locally varies at different locations of the sensors depending on the local orientation and curvature. The sensor thickness could reach to ~300 μm at the highest dip coating cycles in both SDG and SEG sensors (see Figure 5.10(a, c) and Figure 5.11). Despite the scattered thickness measurement, an overall thicker GnP layer can be observed for the samples with larger dip coating cycles. For better clarification of the dip coating cycle effect, macroscale coating uniformity on the surface was studied for the flat sheet SR surfaces of ~3 mm thick following the same fabrication scheme as the porous sensors. Microscope images of the sample surfaces for both SDG and SEG fabrication schemes are represented in Figure 5.12. In both sensors, it is confirmed that overall GnP coverage enhances as the number of dip coating cycles increases. The GnP growth with dip coating cycles was found to start with formation of GnP islands (black color) on the surface that meet each other when a global electrical percolation network is formed with more dip coating cycles. The printing patterns are well discernible in GnP coating which is assigned to the groove-and-ridge oriented coating mechanism in the sensors as explained above.

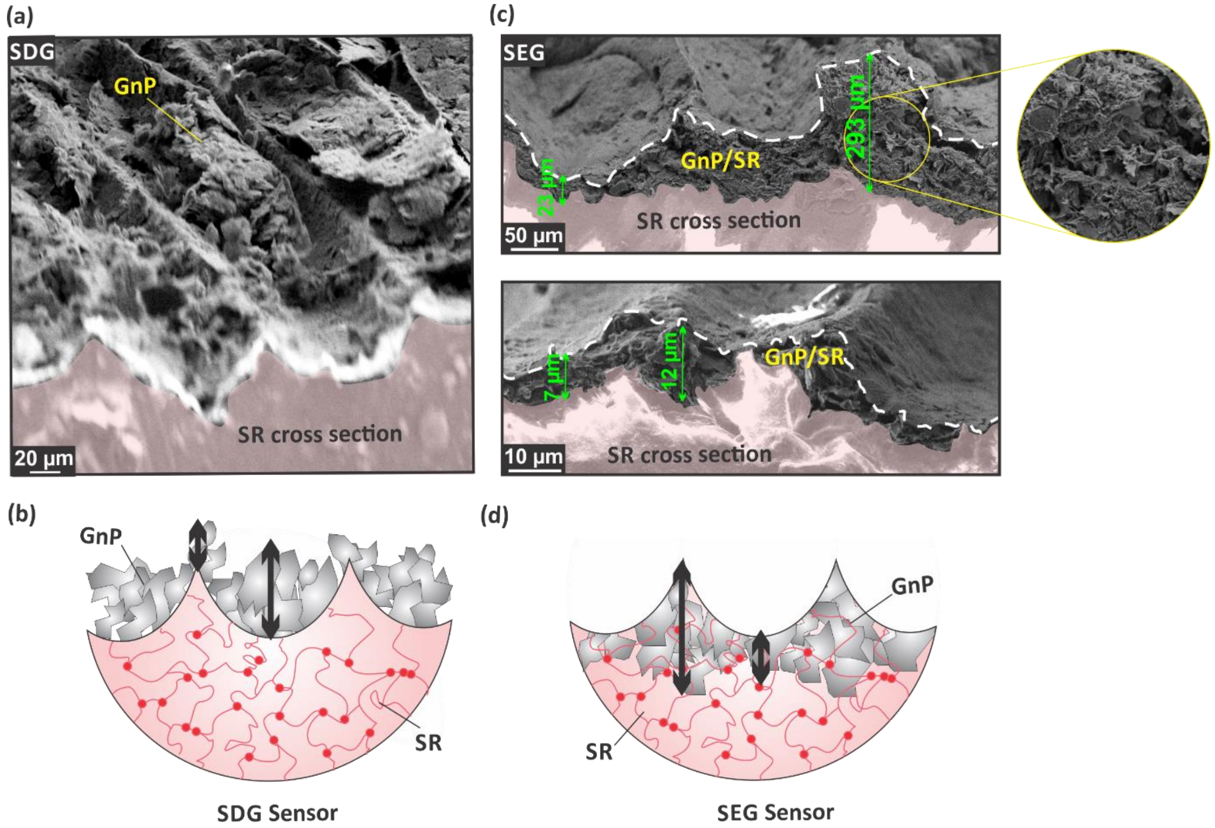

Figure 5.10. Microscale thickness uniformity of the (a, b) SDG and (c, d) SEG sensors dip coated for 20 cycles. In SDG sensors, GnPs are trapped into the grooves leading to a thicker layer of GnP in the grooves and thinner in the ridges. In the case of the SEG sensors, GnPs are mainly trapped inside the ABS mold grooves which correspond to the ridges in the final sensor. Therefore, a thicker layer of GnP has been observed in the ridges and a thinner layer in the grooves.

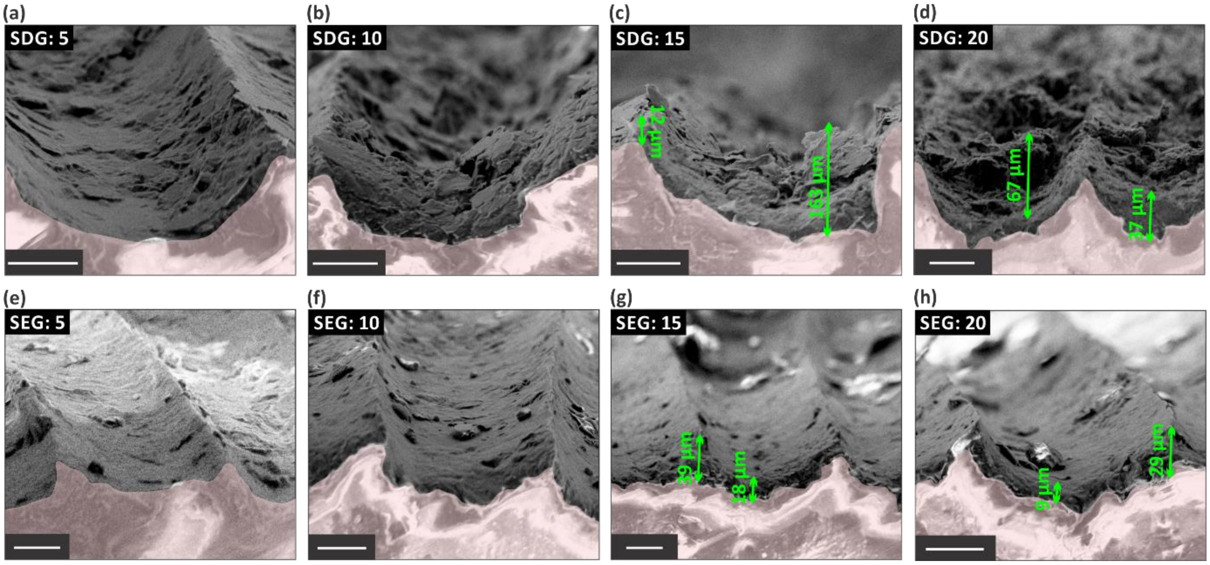

Figure 5.11. Cross-sectional view of the coating for the flat sheet surfaces with SDG coating following (a) 5, (b) 10, (c) 15, and (d) 20 dip coating cycles, and SEG coating following (e) 5, (f) 10, (g) 15, and (h) 20 dip coating cycles. The scale bars are 40 µm.

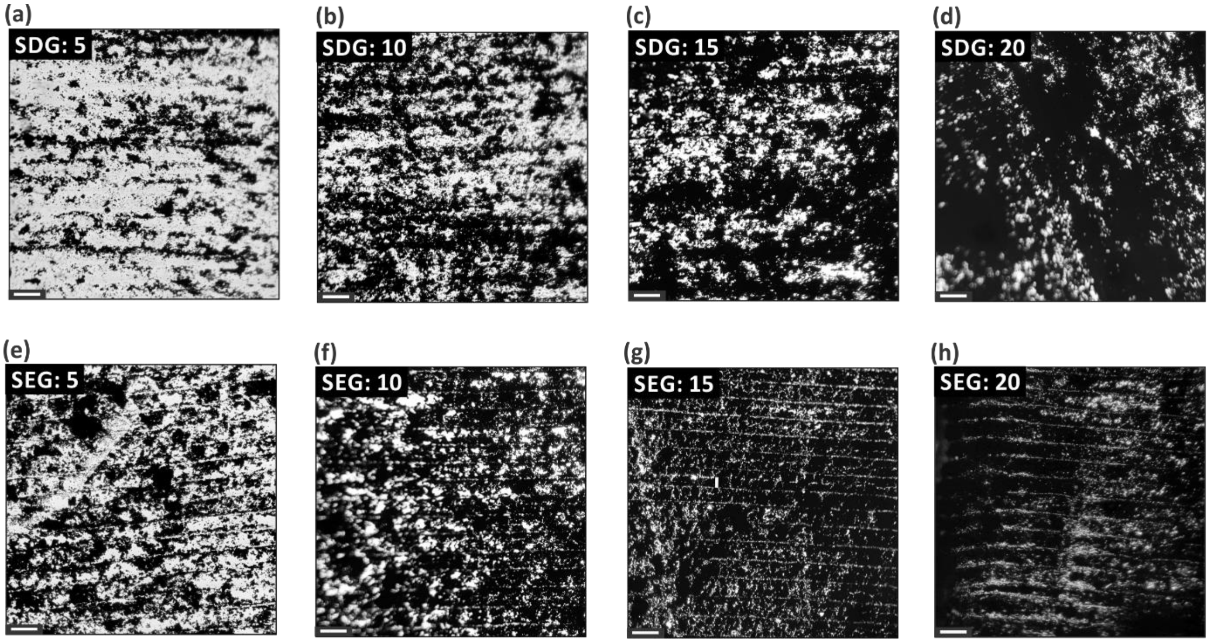

Figure 5.12. GnP coating uniformity on the flat sheets for the SDG sensors following (a) 5, (b) 10, (c) 15, and (d) 20 dip coating cycles, and for the SEG sensors following (e) 5, (f) 10, (g) 15, and (h) 20 dip coating cycles. GnP coating forms GnP islands that develop over the surface with more dip coating cycles in both sensor types. The scale bars are 300 µm.

5.3.4. Electrical Conductivity of Porous Sensors

The effect of dip coating parameters on the electrical conductivity of the porous sensors is addressed in Figure 5.6(f) for the sample with P-surface pore shape at 0.42 design relative density. In terms of the variation in conductivity as a function of the dip coating cycles, statistically, no significant difference was observed between the SDG and SEG porous sensors (1 wt.% GnP/ Isopropyl alcohol (IPA) solution was used for dip coating). In both cases, the exponential percolation model ($\sigma = cP^n$ where σ is conductivity and P represents immersion times) was found to well describe the conductivity behavior with the exponents of n=6.15 and 7.10 for the SDG and SEG sensors, respectively. As a rule of thumb, the resistance dropped below 30 kΩ after ~5-6 dip times; and thereafter, the electrical conductivity increased by 4 orders of magnitude as the dip coating was continued up to 20 immersion times (final electrical resistance ranging from 1.7 to 3.3 kΩ). In addition, no significant changes in electrical resistance were observed between 15 and 20 dip coating cycles for the SEG sensors. This can be assigned to (i) limited infusion of SR into GnP and removal of unstable GnP during the mold dissolution stage, and/or (ii) rearrangement of GnP as a result of the shear forces applied to the GnP when casting SR. This observation is in line with the results presented in Figure 5.11 and Figure 5.12 where GnP uptake seems to be in the same order for the 15 and 20 dip coating cycles in terms of coating thickness and surface coating uniformity. Besides, we noticed slightly darker color of the acetone solution when dissolving the ABS mold due to the detachment of unstable GnPs; on the other hand, we measured lower resistance for the GnP coated mold than the final sensor during the sample fabrication process which can further support the removal of the unstable or unbound GnP from the sensor. Moreover, electrical conductivity values measured for the SDG and SEG sensors were close for a large number of dip coating cycles (20 times). Apart from similar thickness distribution observed in Figure 5.11 for the case of both SDG and SEG sensors, the GnP coating coverage (Figure 5.12) on the flat sheet samples for these two sensors was also in the same range which is in line with the observed similar conductivity values measured at the 20 time dip coating cycle.

Another parameter to control the sensor conductivity is the GnP concentration in the dip coating solution the effect of which is shown in Figure 5.13 on the electrical resistance for the SDG and SEG porous sensors. The figures represent the electrical resistance following 20th dipping times (using IPA to disperse GnP). The results indicate that except for the highest GnP concentration (1 wt.%) where no difference was observed between and SDG and SEG, the SEG sensors showed lower conductivity at the lower GnP concentrations (0.5 and 0.2 wt.%). Therefore, 1 wt.% GnP solution was considered for the fabrication of sensors for all experiments. The results imply that the GnP concentration in the dip coating solution controls the rate of the GnP uptake. The lower conductivity values attained for the SEG sensors (compared to those obtained for SDG) at low GnP concentrations (as well as smaller dip coating cycles but high GnP concentrations) is basically due to disconnection of GnPs as a result of the shear force applied by SR during the casting process; whereas as the number of the coating cycle increases, the amount of GnPs in SEG increases to a point that there is enough GnP to fully cover the SR surface after removing the mold. The conductivity value remains constant at the higher dip coating cycles particularly when a high concentration of the GnP solution (over ~1 wt.%) is used. This is due to the limited GnP uptake capacity in both SDG and SEG sensors. The excess dip coating cycle leads to the detachment of GnPs which are dispersed back to the solution. On the other hand, SR infusion in GnP is limited in SEG, and therefore at 15-20 dip coating cycles, the same order of conductivity was attained.

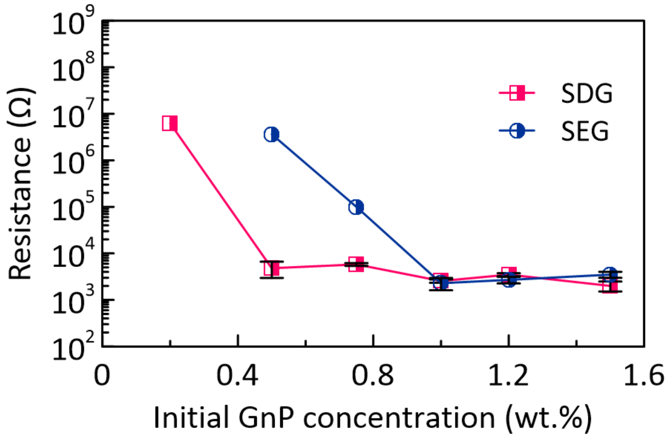

Figure 5.13. Dependence of the resistance to the initial GnP concentration at the 20th dip coating during the dip coating process for both SDG and SEG fabrication processes. SEG sensors do not show electrical conductivity corresponding to the initial GnP concentration of 0.2.

The choice of the GnP dispersing solvent can also affect the eventual resistance of the sensors as represented in Figure 5.6(g, h) (values represent resistance measured after 20th dipping times using 1 wt.% GnP solution). Although in our previous work[207] we found that water (general solvents with high polarity) can result in faster GnP uptake, hydrophobicity of the porous SR and ABS mold hindered penetration of the aqueous GnP solution into the pores. This is supported by the measured contact angle results illustrated in Figure 5.14. In the SDG sensors, acetone led to lower conductivity compared to IPA and ethanol. This can be due to the higher intrinsic desire of GnP to remain in acetone rather than being attracted to the SR.

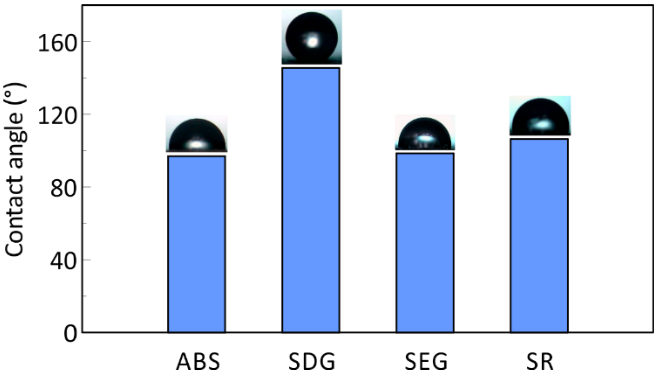

Figure 5.14. Contact angle of the materials and structures used for fabrication of the sensors.

5.3.5. Sensor Durability: Shelf Life and Response to Organic Solvents

Sensor's durability in terms of overtime electrical degradation in long-term, as well as structural deterioration under harsh conditions (e.g., exposure to the organic solvents), are addressed in Figure 5.15. The electrical resistance for the SDG sensors kept in the shelf increased by 5-6 times over the course of 12 months, while the SEG sensors indicated no significant resistance change and thereby retained their conductivity. This may be due to GnP flaking off caused by e.g., electrostatic interactions between the GnP and the container. In contrast, the SEG sensors offered highly stable long-term conductivity as the GnPs were integrated within the SR on surface.

We further examined the structural resistance of the GnP to flaking off by monitoring the conductivity change upon exposure to the liquids and organic solvents (Figure 5.15(b-e)). The sensors were immersed into a liquid in an ultrasonic bath, and the resistance was measured every 30 min in a course of 4 h test (sensors were dried by hot air and cooled down to room temperature each time prior to the next measurement to stabilize). The SDG sensors showed a significant increase (by 4 orders of magnitude) in response to acetone, ethanol, and IPA due to the delamination of GnP from the SR in the solution (Figure 5.15(b)). This trend was more prominent in the case of acetone compared to IPA and ethanol as acetone could better attract GnPs, favoring dispersion rather staying coated on the SR. This is in line with the results shown in Figure 5.6(g) where a poor electrical conductivity obtained following dip coating in acetone solution. In fact, acetone hindered the GnP attraction towards SR, and hence the solvent became darker for acetone compared to IPA/Ethanol (see Figure 5.15(d)). However, the SDG sensor exposure to water led to a slight decrease in resistance since the water molecules are adsorbed onto the graphene on the SR surface and act as electron acceptors [208]. On the other hand, it is energetically more favorable for GnPs to remain on the SR surface than dispersing into water based on the Hansen solubility parameters (HSP). The distance of HSP of GnP to SR is closer than water [209-211] (see Table 5.3). This accounts for the less GnP delamination or dispersion into water (Figure 5.15(d)).

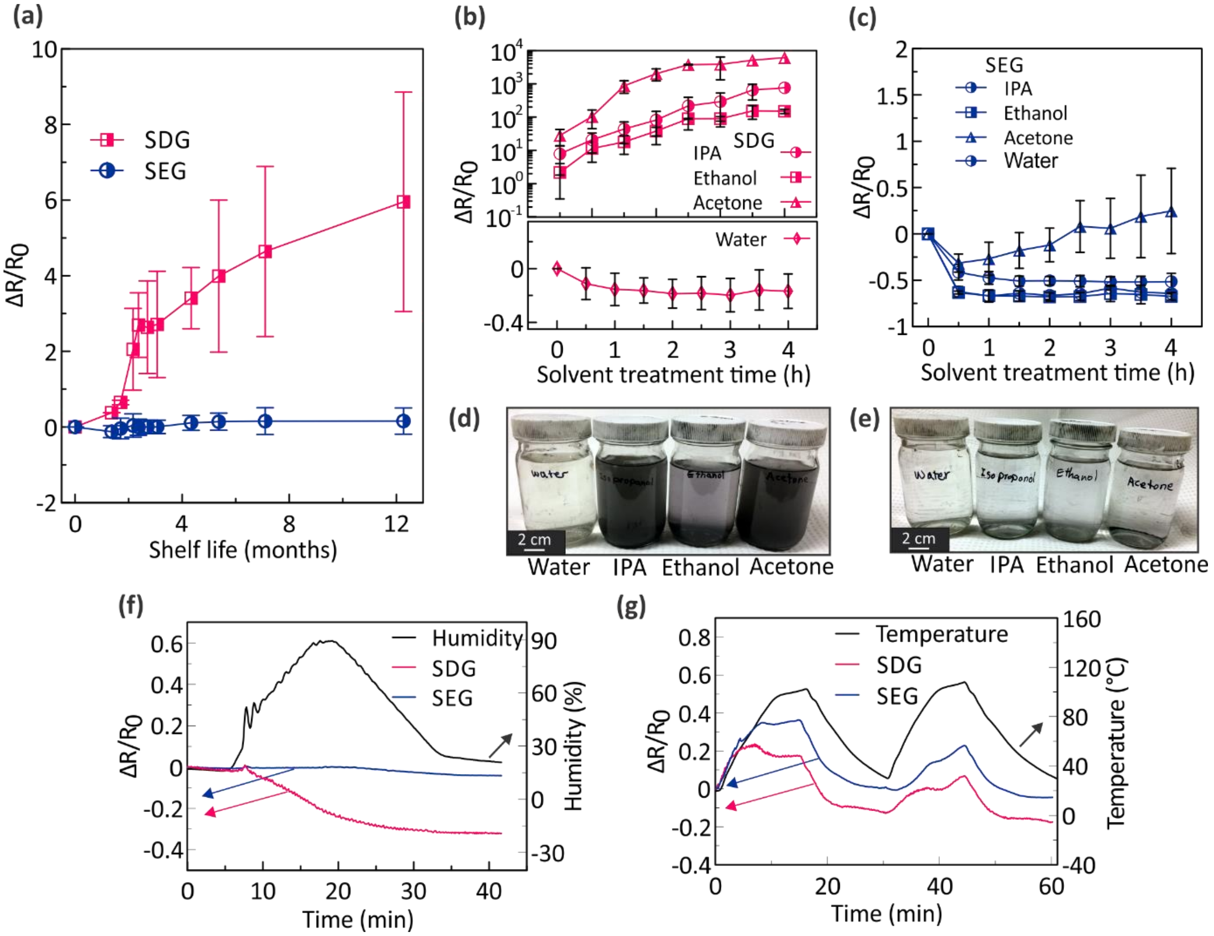

Figure 5.15. Sensitivity and durability of the SDG and SEG sensor upon exposure to harsh conditions and environmental conditions. (a) Long-term monitoring of the resistance variation in the sensors kept on the shelf. SDG sensors lose conductivity spontaneously as the GnP is highly vulnerable to flake off by e.g. the present electrostatic forces, etc. Electrical resistance changes of the (b) SDG and (c) SEG sensors upon exposure to liquids and organic solvents in an ultrasonic bath. Resistance dramatically increased in the SDG sensors exposed to the solvents except for water due to the thermodynamically disfavored dispersion of GnP in water. SEG sensors were highly stable after the first treatment cycle due to the extracted thinner in the first cycle. The resulted solutions containing the (d) SDG and (e) SEG sensors after solvent treatment is in accordance with the resistance changes. The sensitivity of the sensors to (f) humidity and (g) temperature changes. SEG was found to be insensitive to humidity; the same order of sensitivity to temperature resulted in both types of sensors.

Table 5.3. Comparison of the Hansen solubility parameters for SR, GnP, and water. The distance between the solubility parameters ($\Delta = \sqrt{(\delta_{D_1} - \delta_{D_2})^2 + (\delta_{P_1} - \delta_{P_2})^2 + (\delta_{H_1} - \delta_{H_2})^2}$) of GnP and water is larger than GnP and SR implying the tendency of GnP to interact more strongly with SR.

Component	$\delta_D (MPa^{1/2})$	$\delta_P (MPa^{1/2})$	$\delta_H (MPa^{1/2})$	$\Delta_{GnP} (MPa^{1/2})$
Silicone	15.9	0.0	4.1	10.1
GnP	18.0	9.3	7.7	-
Water	15.5	16.0	42.3	35.3

The SEG sensors response to the solvent treatment was different than those observed for the SDG sensors. In case of water, a decreasing trend can be similarly explained by adsorbing electron acceptor water molecules onto the SR surface. For the other solvents (i.e., acetone, ethanol, and IPA), a resistance drop (~30-60%) was observed following the first 30 min of the solvent treatment. This can be assigned to the fact that a global shrinkage is developed over the SR due to the extraction of the silicone thinner (trapped in between the SR crosslink network) and dissolution into the solvent. This was confirmed by the volumetric SR shrinkage characterization presented in the reduction in dimensions after fabrication (Table 5.1) and Figure 5.16, where the SR volume was found to reduce by 38% upon treatment with different solvents. Following the subsequent solvent treatment cycles, the resistance remains almost constant over subsequent ultrasonic treatment cycles for IPA and ethanol. This is due to the already removed thinner from the crosslink network from the previous treatment cycles. Nevertheless, a continuously-increasing trend was observed for acetone. This is similar to the SDG sensor response to acetone compared to the other solvents (however to a much lesser extent for SEG) and can be explained by the partial GnP detachment from the SR surface due to the potential SR swelling and small detachment of GnP.

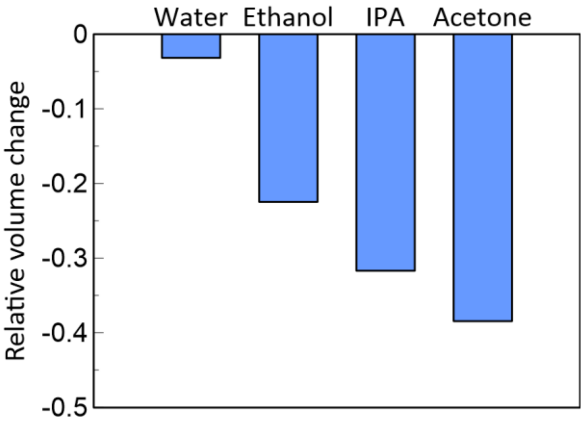

Figure 5.16. Characterization of the volumetric shrinkage of the SR owing to extracting the thinner trapped into the crosslinked network when immersed into the fluids and solvents. The permanent shrinkage values were measured 7 d after treatment with the solvents.

In order to evaluate the GnP delamination effect (after thinner extraction/dissolution) without the impact of the liquid molecules, the resistance change of the dried sensors (after 24 h of the solvent treatment) relative to the resistance following the first solvent treatment process (first 30 min of the ultrasound solvent treatment) was measured and presented in Figure 5.17. In water, the relative resistance changes fall within 10% in both the SDG and SEG sensors as the GnP is energetically reluctant to disperse in water, as opposed to acetone, where in both cases the highest GnP delamination is seen. Overall, the SEG sensors were found to be markedly more durable against the organic solvents/harsh conditions. The sensor's temperature resistance was evaluated by thermogravimetric analysis (TGA) on the flat sheet samples of 3 mm diameter and ~1 mm thickness. The data presented in Figure 5.18 suggests the GnP coating presents no adverse effect on the thermal stability of the sensors; additionally, no significant thermal degradation was observed up to ~300 ˚C for both sensor types.

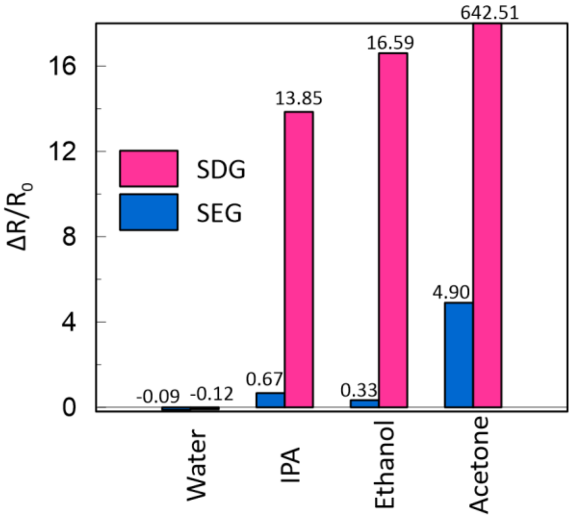

Figure 5.17. Comparing the relative resistance change between the steady-state completing the solvent treatment relative to those obtained after the first cycle of the solvent treatment process. The SEG sensors showed negligible resistance change compared to the SDG sensors suggesting that GnP still remains stable enough on the SR surface under harsh conditions such as exposure to the organic solvents.

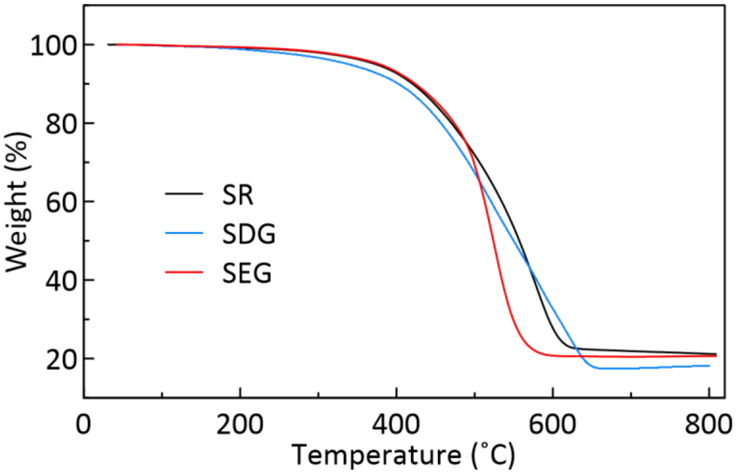

Figure 5.18. **Results of the thermogravimetric analysis (TGA) for the SDG and SEG flat sheet samples following 20 dip coating cycles. The coating seems to have no adverse effect on the thermal stability of the sensor. The samples were stable up to ~300˚C.**

5.3.6. Temperature and Humidity Sensing Performance

Resistance sensitivity of the fabricated sensors versus temperature and humidity is demonstrated in Figure 5.15(f, g). In terms of humidity, resistance was found to decrease with relative humidity due to the GnP exposure to the elevated amount of water vapors (see Figure 5.15(f)). In addition, no resistance recovery was observed upon changing the environmental humidity from 90% back to 20%. This suggests the presence of water vapors despite reducing the chamber relative humidity. Sensitivity to humidity was found to be negligible for the SEG sensors compared to the SDG sensors (by two orders of magnitude, see Table 5.4). The resistance in the SDG sensors, however, irreversibly decreased by ~38% upon elevated humidity (90%). This is originated from the fact that in the SEG sensors, the water molecules cannot pass through the hydrophobic SR surface and thereby the SR hinders H_2O molecules to reach to and engage with the conductive network. Hence, the SEG sensors offer a humidity insensitive sensing performance.

Table 5.4. **Temperature and humidity sensitivity values obtained by the slope of the relative resistance change versus temperature/humidity.**

Sensitivity	SDG	SEG
Temperature (1/°C) (60°C magnitude)	4.49E-03	4.65E-03
Temperature (1/°C)	3.55E-03	2.64E-03

(120°C magnitude)		
Humidity (1/%)	-2.49E-03	-3.86E-05

The porous sensors showed a reversible resistance response to the cyclic temperature changes up to 60 and 120 °C as it is demonstrated in Figure 5.19 and Figure 5.15(g), respectively. The electrical resistance proportionally increased with the temperature ranging from 20-120 °C for both SDG and SEG sensor types with sensitivities ranging from 2.64×10^{-3} to 4.49×10^{-3} /°C (see Table 5.4). The variation in resistance with the temperature basically stems from the reversible thermal expansion of the SR. This results in GnP separation, causing conductive network disruption and, hence lowering conductivity.

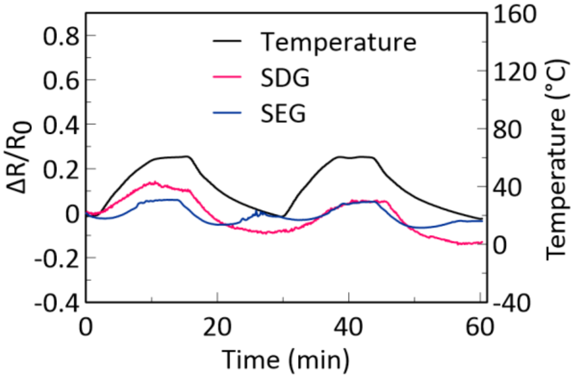

Figure 5.19. Variation in resistance as a function of temperature for temperature cycles varying between 20 to 60 °C for SDG and SEG sensors.

5.3.7. Mechanical Characterization and Compressive Deformation of Porous Sensors

The mechanical characteristics (compressive stress-strain curves) of the fabricated cellular SR with different cell designs properties (i.e., cell shape and porosity) as well as the GnP coating approaches are represented in Figure 5.20(a-d). The stress-strain curves followed the same trend as that of typical porous materials: initially, the deformation continued with low stress (the plateau in Figure 5.20(a)) corresponding to the progressive collapse of the layers. This was then followed by a marked increase with the development of densification at high strains. The densification strain for the cellular SR sensors is presented in Figure 5.20(d). The onset of densification is strongly dependent on the porosity of the structure that varied between 0.32 and 0.62 at the designed volume fractions. The elastic modulus for different cell designs is compared in Figure 5.20(c). The stiffness could be tuned by controlling cell design in the range of 70-660 kPa; this reveals that unlike the conventional GnP mixing methods the proposed fabrication approach does not make a negative impact on the flexibility and shape recoverability of the base SR polymer. Furthermore, the structures fully recovered their original shape after severe mechanical compression strains of up to 0.75 due to the hyperelastic behavior of the SR. In general, the D-surface showed higher flexibility compared to the P-surface due to the deformation mechanism dominated during compression. Deformation in the P-surface based cellular structures (Figure 5.20(b: II)) accompanied by the axial compression (at a high volume fraction) and buckling (at a low volume fraction) of the linkages along the loading direction (which is known as the stretching-dominated deformation). However, for the SR with the D-surface cell architecture (Figure 5.20(b: I)), shear of the internal linkages was evident upon global compression, signifying a bending-dominated deformation mechanism. In fact, the lower stiffness associated with the D-surface ties back to the nature of bending that dominates the deformation mechanism.

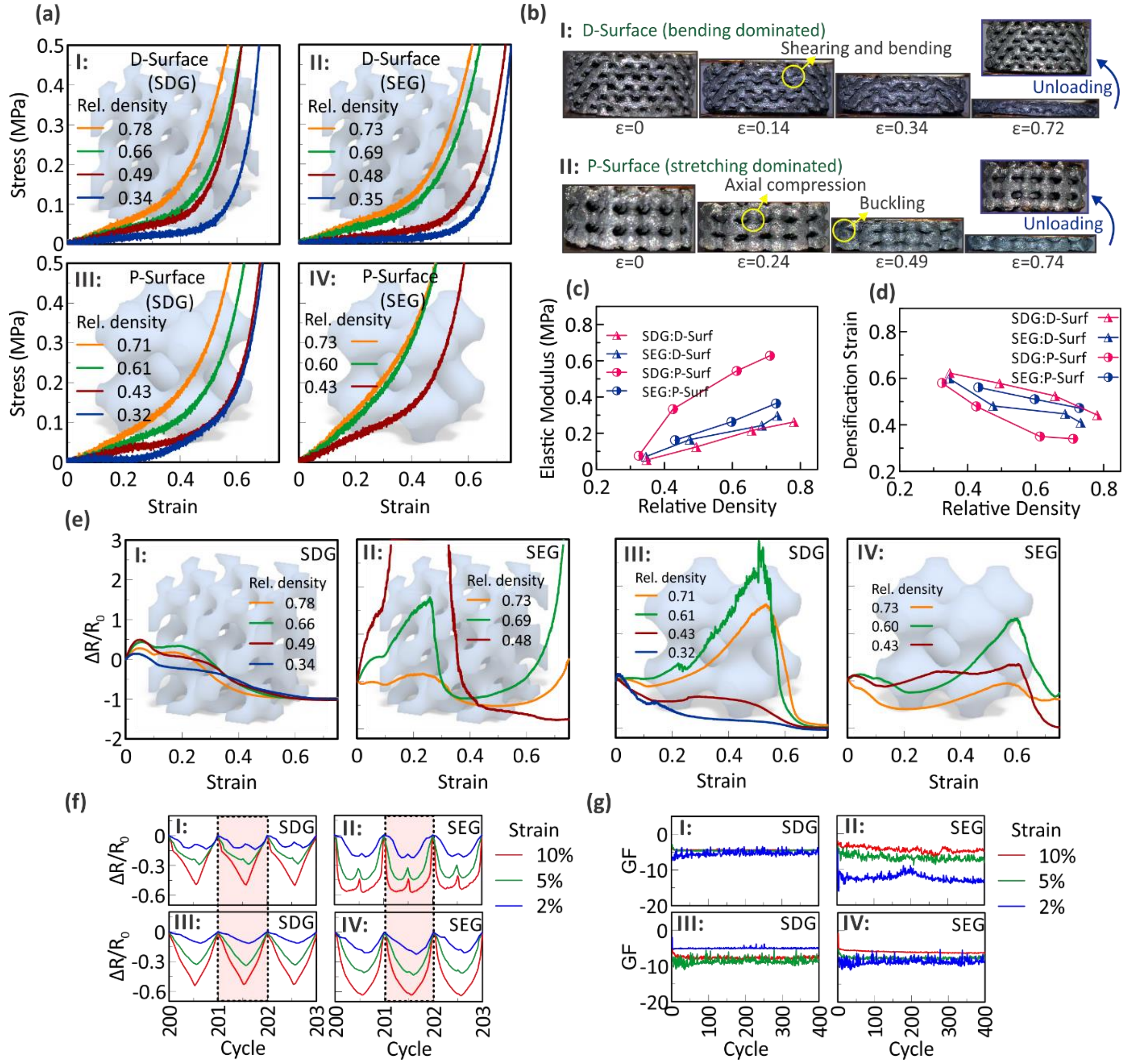

Figure 5.20. Electromechanical characterization of the porous sensors with different pore characteristics and fabrication approaches. (a) Compressive stress-strain curves and (b) the associated deformation mechanism for I: the bending-dominated structure (i.e., D-surface), and II: the stretching-dominated structure (i.e., P-surface). Variations in (c) elastic modulus and (d) densification strain with the dry weight measured relative density. (e) Changes of resistance under static compressive deformation for the sensors with I and II: D-surface, III and IV: P-surface pore types at different relative densities. The piezoresistive responses are found to be identical for each fabrication approach and pore shape due to the identical deformation mechanism in each pore shape. (f) Resistance changes under cyclic loading over cycles of 200-203 for I and II: D-surface, III and IV: P-surface pore types at different strain amplitudes. (g) Stability of piezoresistive behavior over 400 repeated cycles of compressive loads for I and II: D-surface, III and IV: P-surface pore types.

Due to the critical effect of unit cell shape on the deformation mechanism and mechanical properties, FE simulations were performed to evaluate numerical predictability in the mechanical design of the cellular sensors. The results of FE simulation are compared with the experimental compression tests for the sensors at ~30% volume fraction in Figure 5.21. The results suggest a good agreement between the numerical and experimental stress-strain curves. Besides, the deformation mechanism was identical to that observed experimentally in Figure 5.20(b).

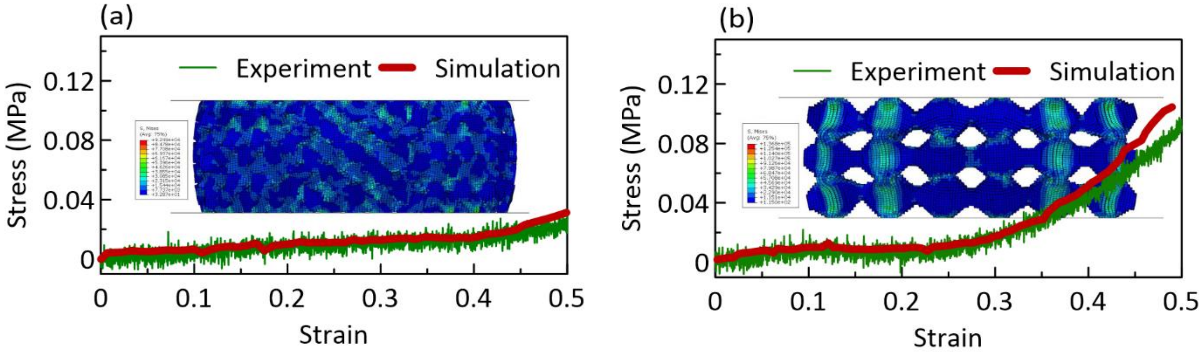

Figure 5.21. The results of Finite Element simulation for the (a) D-surface and (b) P-surface at ~30% volume fraction. The simulation data was in good agreement with the experimental results. The insets represent the Von Mises stress contour associated with the applied compressive deformations.

5.3.8. Piezoresistive Properties: Compressive Strain Sensing Performance

In this section, the resistance response of the sensors to different mechanical loading scenarios (including compression test, cyclic strain, as well as monotonic loading) is examined for the sensors with different internal cell architectures. These results are presented in the following subsections:

5.3.8.1. Piezoresistive response under compressive deformation

The electrical resistance of the SDG and SEG sensors architected with different porosities of the P- and D-surface structures was monitored during the compression test as shown in Figure 5.20(e-g). As seen in Figure 5.20(e), all of the sensors retained conductivity up to 75% strain and remained conductive upon removing the load. The sensors were highly strain reversible as they did not show permanent failures after removing the extreme deformation.

In both SDG and SEG sensors, the overall piezoresistive trends were similar for each cell type. This stems from the fact that the deformation mechanism is the unique function of unit cell architecture. For the sensors with a P-surface geometry (Figure 5.20(e)III, IV), the resistance changes can be explained by two competing effects induced by the deformation mechanism: (i) Poisson's effect, which is more prominent at low porosity values, takes apart the GnPs located on the horizontal linkages and finally leads to an increase in the resistance; and (ii) the stretching-dominated deformation of the P-surface under compression causes the vertical linkages either deform axially (in case of samples with low porosity values) or buckles (for the samples with high porosity values). In the former case, resistance tends to decrease as the GnPs are compacted; however, in the latter case, the bending nature of deformation can cause both possibilities of GnPs to be compacted on and separated from the surface. The heterogeneous distribution of GnP coating may also affect the piezoresistive mechanism. The GnP agglomeration in SEG can locally stiffen the surface and therefore deformation is more localized in the low GnP density areas. The GnP effect on deformability of the SR surface, however, is expected to be less prominent. As the deformation continued, the contribution of the Poisson's effect augmented, and thereby the resistance increased up to the point close to the densification strain. Thereafter, the resistance decreased as the layers collapsed and the contact density between the layers and GnPs increased.

The piezoresistive behavior for the bending-dominated deformation structure (D-surface) was initiated with an increase in the resistance (Figure 5.20(e)I, II). This suggests that GnP network on the surface was disrupted (to some extent) due to the shearing-type deformation induced in the 45° unit cell linkages under global compression. The resistance began to recover at approximately 30% strain (a sharp drop was observed for the case of SEG sensors) as the layers started to collapse on each other, while the Poisson's effect was seen to be less effective probably due to the absence of horizontal linkages.

Although the piezoresistive behavior of the SDG and SEG sensors followed an identical global behavior (corresponding to each pore type), the resistance at high strains reached a minimal plateau for the SDG sensors (resulted by the densification effect), while a sharp increase was observed for the SEG sensors. This can be due to the fact that in response to the Poisson's effect the GnP can slide on each other at the minimal surface-based interface in the SDG sensors; however, in the case of the SEG sensors, a lateral SR expansion constrains the embedded GnPs to detach and thereby disrupt the conductive network.

5.3.8.2. Cyclic piezoresistivity

The cyclic piezoresistive performance of the sensors was assessed for different pore characteristics at different strain amplitudes over 400 compressive loading cycles. Figure 5.20(f) demonstrates the resistance profile over the 200th-203rd cycles for the sensors at the 0.42 design relative density (the results for the samples with other relative densities are represented in Figure 5.22 and Figure 5.23). The cyclic piezoresistivity was studied at strain amplitudes within 10% (this range is applied to the sensor when used in the wearable devices. For both SDG and SEG type sensors under compression, the resistance decreased proportionally to the strain magnitude. However, the degree of piezoresistive linearity was found to be primarily sensitive to the cell shape. The results suggest that the stretching-dominated P-surface offers a more linear and one-to-one piezoresistive response compared to frequent piezoresistive nonlinearity and instantaneous positive-to-negative piezoresistivity transitions seen in the bending-dominated D-surface based sensors.

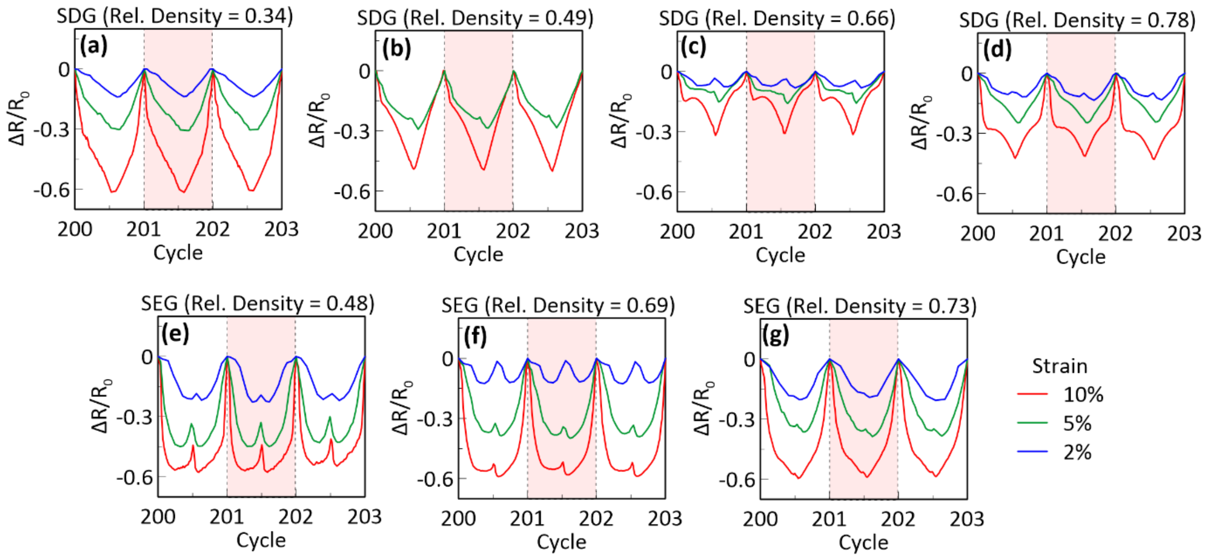

Figure 5.22. Representation of the reversible resistance changes of the sensors at different strains under repeated cyclic loading at cycles of 200-203 for the D-surface pore shape.

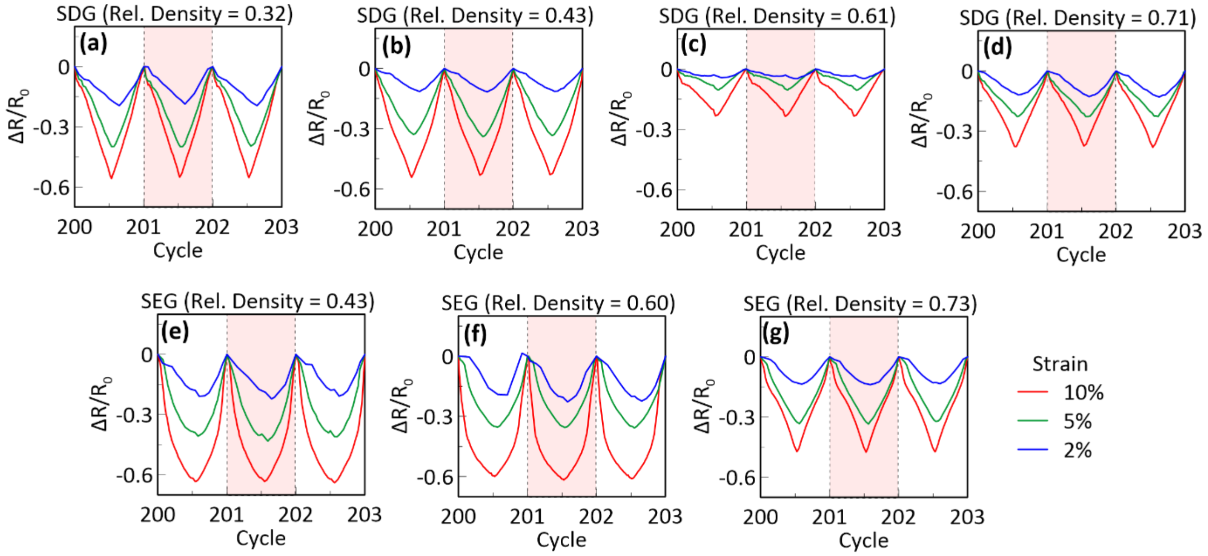

Figure 5.23. Representation of the reversible resistance changes of the sensors at different strains under repeated cyclic loading at cycles of 200-203 for the P-surface pore shape.

In terms of sensitivity, the gauge factor at each loading cycle is represented in Figure 5.20(g) for the sensors with the 0.42 design volume fraction (the results for other sensors are illustrated in Figure 5.24 and Figure 5.25). Overall, the gauge factor was fairly stable over the course of 400 cyclic loading; however, more instability was evident in the case of the D-surface architected SEG sensors (particularly those with a lower density value). The magnitude of the gauge factor was found to vary within the range of 1-10 for both SDG and SEG sensors depending on the relative density and unit cell shape. The results indicate that the sensors with higher porosity possess greater sensitivity regardless of the pore architecture. This can be due to more complex and severe induced deformations and thereby more vulnerability of GnP conductive networks to disruption in the low-density TPMS-based sensors. Based on the above-mentioned results, the proposed fabrication technique allows optimizing the deformation mechanism towards stretching-dominated deformation to attain high signal repeatability, stability, and low hysteresis over repeated cycles.

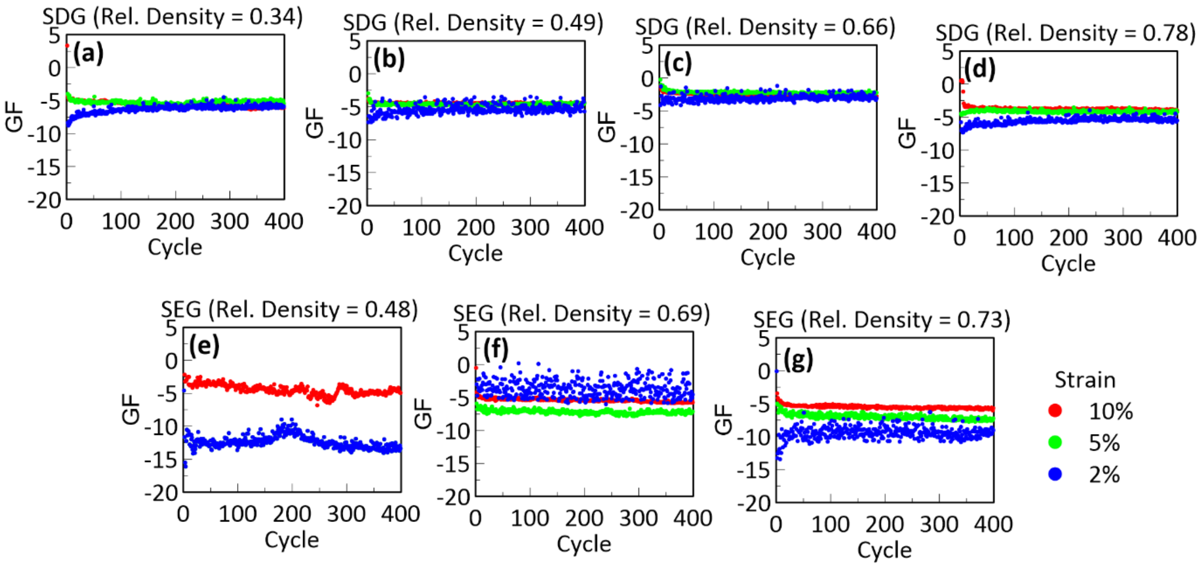

Figure 5.24. Stability of the gauge factor over 400 cycles of compressive loading at different magnitudes for SDG and SEG sensors with D-surface pore shape.

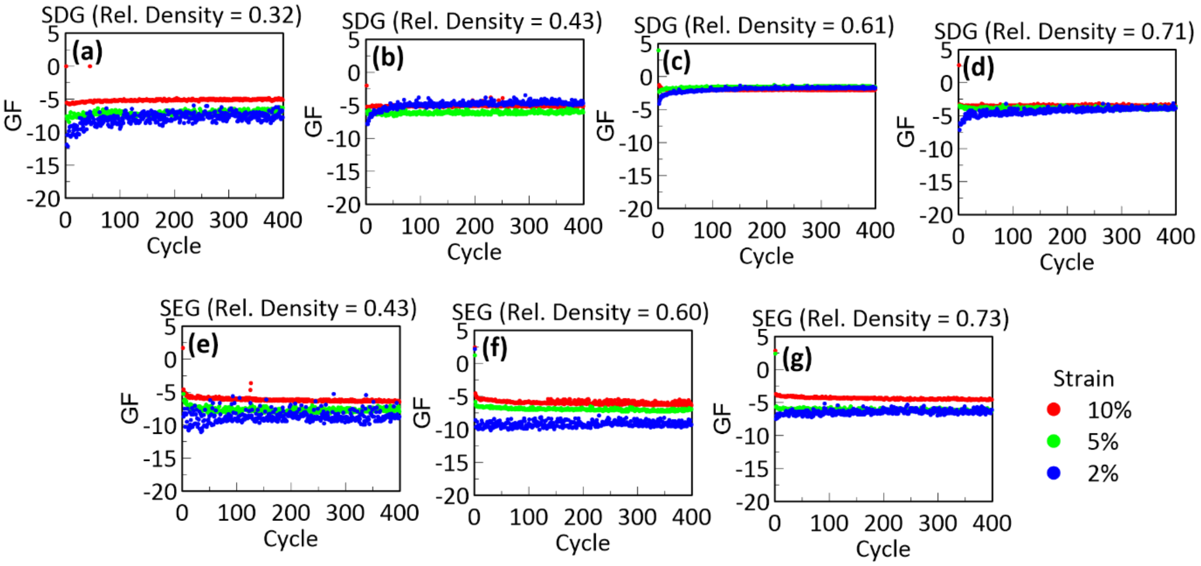

Figure 5.25. Stability of the gauge factor over 400 cycles of compressive loading at different magnitudes for SDG and SEG sensors with the P-surface pore shape.

Sensitivity of the SEG sensors was evaluated under varying loading rates (from 10-60 mm/min) at the constant strain magnitude of 5% (Figure 5.26). The sensor was found to show higher sensitivity towards faster loading rates as the GF increased from 7 to 10.5. This is due to the fact that at the small loading rates the resistance changes were attenuated due to dynamic viscoelastic effects (relaxation) while at large loading rates, the GnP did not have enough time to reorient themselves; hence a sharper and higher magnitude of the resistance change was obtained. Though the sensors showed various GF at different loading rates, but they can still detect the maximum resistance peak and also number of the peaks per time. Hence, they can be utilized for wearable applications to detect heart beats, pulse, and number of muscle contractions. Further research for calibration of the sensors especially for higher frequencies would be conducted in future works.

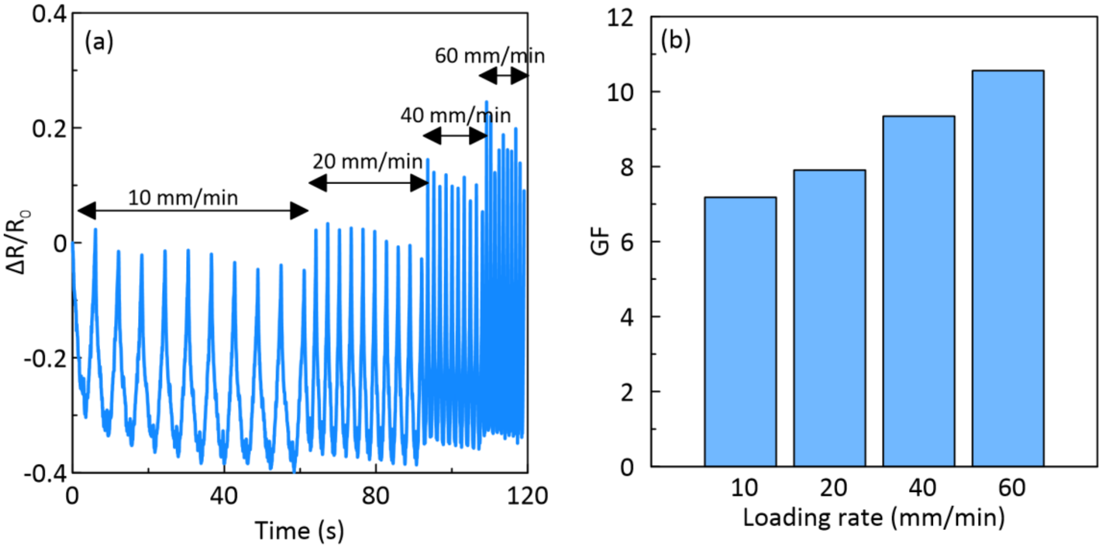

Figure 5.26. Effect of the loading rate on the cyclic piezoresistive behavior of SEG sensors (fabricated following 20 dip coating cycles) subjected to 5% compressive cyclic loading. (a) The relative resistance change versus time at different successive cyclic loading rates, and (b) variations in the average sensitivity as a function of the loading rates.

5.3.8.3. Piezoresistive relaxation under monotonic loads

The electrical relaxation was characterized for the sensors through the monitoring the resistance under a monotonic load (10% compressive strain) for 10 min (see Figure 5.27). The electrical resistance decreased so that after 10 min the relative resistance change reached a more stable range (within -0.14 to -0.4). No significant correlation was observed in terms of the GnP coating method, unit cell architecture as well as density. The time dependent relaxation behavior is defined as Eq. (5.2) [212]:

$$\mathrm{R(t)} = R_0 t^{-n'} \tag{5.2}$$

where n' represents the resistance relaxation rate index of the material which is listed for SEG and SDG sensors with different pore characteristics in Table 5.5. The range obtained for the sensors (2.17-4.49) was in the order reported in previous studies [212]. The time-dependent electrical relaxation behavior originates from the viscoelastic behavior of SR under compression, leading to the augmented probability of GnP connections over the surface. Electrical relaxation is an indication of the solidity of the material (large electrical relaxation is associated with soft materials with lower nanoparticle additives).[213] The range of the relaxation observed here is in the order those reported for piezoresistive sensors with cured PDMS and PU based polymers [212]; in these cases, slightly greater electrical relaxation is assigned to high flexibility of SEG and SDG sensors due to the GnP/additive-free SR core coated with a thin layer of GnP. It is also worth noting that deformation in 3D porous materials is highly complex and impose more sensitivity (and thereby electrical relaxation) due to the high specific surface area of the percolation network. For a similar reason, we did not see any significant changes between the relaxation behavior of the samples with different coating thickness (obtained by different number of dip coating cycles) as shown in Figure 5.28.

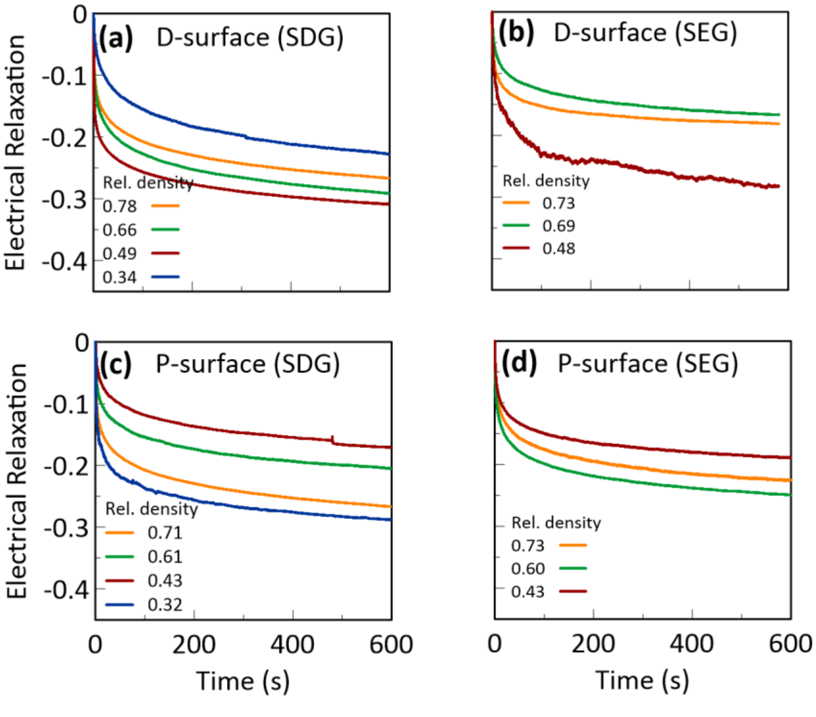

Figure 5.27. The electrical relaxation as the resistance change under monotonic loading of 10% compressive deformation.

Table 5.5. Relaxation rate index ($R(t) = R_0 t^{-n'}$) constants for the sensors with different pore shape and porosity.

Pore shape	Sensor type	Relative Density	n'×100

D-surface	SEG	0.73	2.1764
		0.69	2.5992
		0.48	4.4961
	SDG	0.78	3.9295
		0.66	4.3997
		0.49	3.7837
		0.34	4.3674
P-surface	SEG	0.73	2.6393
		0.6	3.3987
		0.43	3.5498
	SDG	0.71	3.919
		0.61	3.1709
		0.43	2.938
		0.32	3.8073

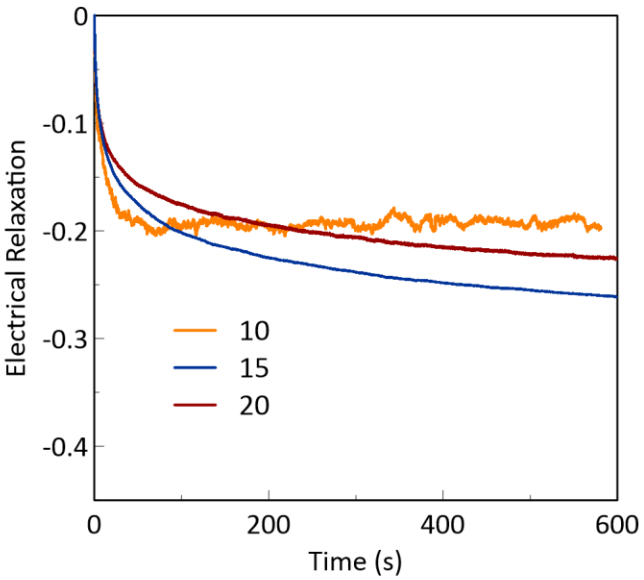

Figure 5.28. Electrical relaxation behavior for the SEG sensors with P-surface (0.42 relative density) for three different dip coating cycles (10, 15, and 20).

5.3.9. Application in Wearable Devices

To address the application of the cellular sensors in monitoring human motions, the SEG sensor was inserted into a shoe pad; the sensor was 2 mm thicker (taller) to allow for transferring the pressure. The resistance change was monitored for walking and running cases; the results for 5 steps were presented in Figure 5.29(a-c). The electrical resistance reversibly changed over the course of motion. The signals can distinguish the pressure applied and the pattern of which can be used for diagnostic purposes, e.g. in sports applications. Moreover, porous sensors were employed to sense heartbeat and pulse. The results of resistance change due to the pulse is represented for a period of 6.2 s involving 7 beats in Figure 5.29(d, e). The measured signals represent a heartbeat rate of 68 bpm which is in normal range for adults under normal circumstances. The signals show that the sensor could successfully capture the human pulse. Each peak involved two extrema which correspond to different levels of pressure in the pulse waveform. The wave patterns resemble slippery pulse type[214] in the waveform which can be used to extract and communicate the pulse information.

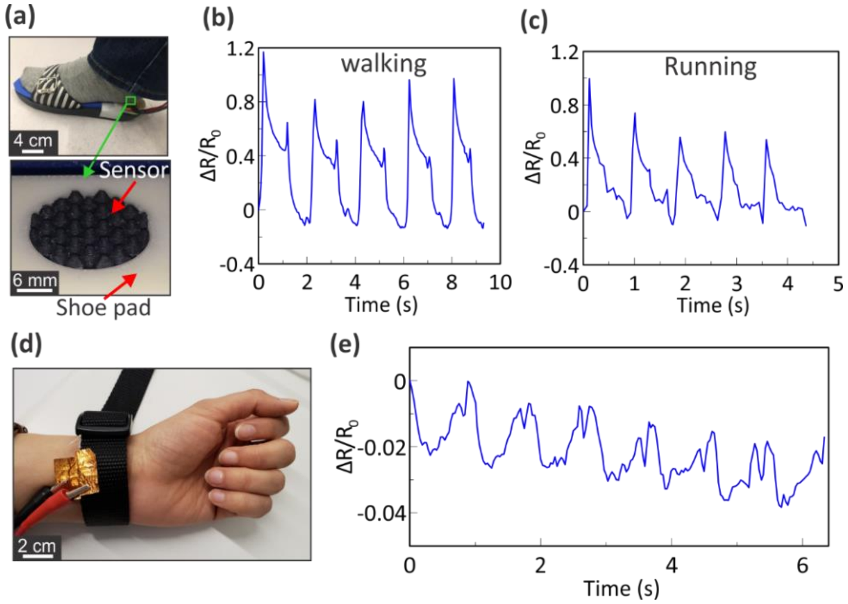

Figure 5.29. Demonstration of the porous sensors as wearable biomedical devices. (a) Integrating the porous sensor into a shoe for body motion monitoring (b) moving speed under walking and (c) running. (d)A photograph showing the porous sensor for wearable biomonitoring (e) continuous human pulse wave measurement.

5.3.10. Evaluation of biocompatibility

According to the proposed application of sensors in wearable devices, the sensors were evaluated in terms of their cytocompatibility in contact with fibroblast cells (Figure 5.30). Herein, we monitored the viability of the cells in contact with both the sensors up to 7 days using live/dead viability assay. As shown in Figure 5.30(a, b), fibroblast cells showed their normal elongated shape in contact with both SDG and SEG sensors. Majority of the cells remained alive (green in color) on day 7 of the culture and only a few dead cells (red spots) were observed in contact with SDG (Figure 5.30(a)). The cell viability estimated by normalizing the number of live cells to the total cell count demonstrated ⩾ 80% viability for both SDG and SEG in days 1 and 3 (Figure 5.30(c)). By maintaining the culture up to 7 days, the cells could adopt the condition and resumed increased viability up to 90% and 100% for SDG and SEG, respectively.

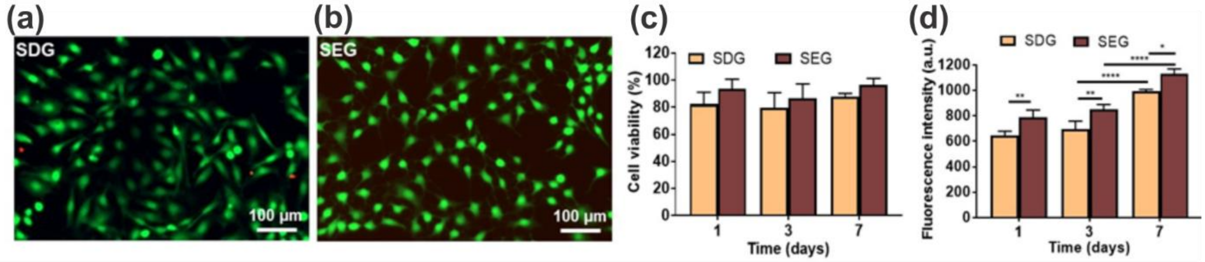

Figure 5.30. Representative fluorescence images (merged images) of a live/dead viability assay of fibroblasts cultured for 7 days in contact with (a) SDG and (b) SEG sensors. (c) Cell viability of fibroblast cells defined as the number of live cells divided by the total cells. (d) Metabolic activity of the cells measured by PrestoBlue assay.

Further, the metabolic activity of the cells was evaluated by PrestoBlue reagent at pre-determined days and compared with day 1. As seen in Figure 5.30(d), the cells in contact with SEG significantly show higher metabolic activity compared to SDG in all the pre-determined days. The total increase in metabolic activity was 1.5-fold for both SDG and SEG in day 7. The observed biocompatibility of the fabricated graphene coated-silicone sensors suggests that they are suitable for wearable applications although, further *in vivo* toxicity studies may give further information on their biosafety.

5.4. Conclusions

In the present paper, an accessible and low-cost fabrication process was introduced to fabricate 3D conductive cellular structures with high flexibility and mechanical recovery for sensing applications. The proposed approaches incorporate safe materials and accessible methods into the process chain. Embedding GnPs within the thin layer of porous SR surface ensures high stability of GnPs against harsh conditions unlike that of direct dip-coated sensors. This is confirmed by the long-term durability over 12 months as well as improved wash durability in the organic solvents. The proposed fabrication scheme also provides a controllable sensing performance due to the superior control over the internal pore architecture.

Ordered and complex 3D conductive structures based on interconnected TPMS were successfully printed. As a result, the piezoresistive characteristics were easily tuned by manipulating the deformation mechanism (either stretching or bending) under the compressive loads. Overall, different structural cell types resulted in gauge factors ranging between 1-10 (low-density samples exhibited the highest sensitivity). The results of FEA also demonstrated that the deformation mechanism and mechanical properties are in agreement with the experimental data which confirms high FE capability as a tool to predict and design such sensors. The piezoresistive signals were stable over repeated mechanical loads with high cyclic repeatability and stability. The sensitivity towards humidity/water vapors was found to be negligible for the SEG sensors as compared to the SDG sensors. The sensors did not result in loss of cell viability, provided mechanical flexibility as well as electrical sensitivity suggesting its utility for wearable devices for monitoring human bodily motions. For the future work, the sensors can be combined with the flexible circuits for the wireless transmission of the signals.

Chapter 6. Template-Enabled Biofabrication of Thick Three-Dimensional Tissues with Patterned Perfusable Macro-Channels

6.1. Introduction

Continuous delivery of oxygen and nutrients and removal of waste products are essential functions for the survival of bulky multi-cellular tissues and promoting the metabolic activities of living organs [215]. Blood vessels, as interconnected pathways, can facilitate such deliveries by the blood circulation in many tissues. Engineering synthetic multi-cellular and functional tissues is not feasible without a comprehensive network of interconnected channel pathways to enable the distribution of metabolites [51, 52, 216]. Tremendous efforts have been made to recapitulate the vasculature networks in native organs; however, state-of-the-art techniques nonetheless fail to fabricate scalable and robust vascularized tissue constructs.

Multiple approaches have been explored to develop 3D complex tissues engineered with incorporated internal pores/channels. Conventional techniques such as gas foaming [217, 218], freeze-drying [219] and particulate leaching [220, 221] have been proved to be less appropriate for biofabrication of functional tissues, due to their limited pore interconnectivity and/or insufficient control on the pore shape. Bioprinting, which is a layer-by-layer assembly of bioinks, has shifted the focus of biofabrication interests within the last few decades. Extrusion-based 3D bioprinting [108, 222-224], material-jetting [10, 225, 226], digital light processing [227, 228], and stereolithography [229, 230] have been widely reported. Extrusion 3D bioprinting is based on deposition of a cell-laden bioink through a nozzle with the aid of a back pressure. Despite many advantages offered by 3D bioprinting techniques, they have been accompanied by drawbacks such as nozzle clogging and low resolution, particularly in the case of extrusion 3D bioprinting methods [231-233]. The low viscosity of most bioinks, which are often difficult to handle, and the demand for layer-by-layer curing impose other challenges such as control over the physical properties of the bioinks and structural integrity of the final 3D bioprinted tissue constructs [234]. In these methods, increasing the cell density beyond a certain limit results in nozzle clogging, and thereby the augmented shear forces transferred to the cells from the bioink flow can cause cell death [235]. Besides, cell sedimentation during the 3D bioprinting process (particularly for the light-based 3D bioprinting techniques) has been a major concern due to the heterogeneous distribution of cells in the final construct [236].

Three-dimensional bio-templating of vasculature patterns has been able to obviate some of the above-mentioned obstacles. In this approach, a sacrificial template is fabricated and embedded into a soft hydrogel platform that is cured later after the casting process. This step is followed by sacrificing the template to reveal the resulting hydrogel with an internal 3D interconnected network of open channels inscribed by the original interconnected templates. The sacrificial templates must be transparent to prevent shadow artifacts that would hinder the curing process for the infilled hydrogel matrices with the crosslinking mechanism activated by ultraviolet (UV) or visible lights [216, 237]. The template removal process should be safe for living cells. Three-dimensionally printed sacrificial templates from a multitude of candidate materials such as gelatin [46, 47], pluronic [50-54], polyvinyl alcohol [238], alginate [48, 49], and carbohydrate mixtures [216, 237, 239] have been demonstrated in the literature, each of which, however, has its own limitations. For instance, carbohydrate-based templates [216] can be fabricated by hot melt extrusion-based 3D printing; however, the 3D printed constructs have been mostly restricted to lattice-shaped networks due to difficulties in controlling the ink physical properties and its deposition in multi-layered constructs. The right viscosity and stability at room temperature was crucial in obtaining structurally self-standing templates for fabrication of glassy carbohydrates [216]. The ink characteristics need to be tuned *via* the ink formulation and/or mixing with other additives such as dextran, sucrose, and glucose, which requires further practice and burdensome optimization processes [216]. For example, a mixture of isomalt powder and cornstarch has been used for fabricating vasculature templates, using a selective laser sintering (SLS) platform. Selective laser sintering may face challenges in the depowdering stage when it comes to bulky constructs with fine porous architectures. The opaque optical properties of the templates can present another obstacle to the later prepolymer photopolymerization to obtain 3D thick constructs. Gelatin, a thermoresponsive (liquid at 37˚C and forms gel at the room temperature) and water-soluble candidate, could be more favorable as sacrificial material in template-based biofabrication, due to its cell friendly nature. However, direct extrusion printing of gelatin could be highly challenging due to its low viscosity and slow physical gelation with temperature, leading to structural self-collapse, especially for printing overhanging features. This matter limits the resolution, complexity, and precision of the final constructs and therefore only works for printing patterned 2D structures [237].

Leveraging our previous experience in developing high-resolution silicone constructs through template-assisted techniques [12], we propose a biocompatible fabrication process for engineering 3D thick cell-laden hydrogel biomaterials with interconnected complex channels enabled by transparent gelatin sacrificial templates. We describe the fabrication of 3D patterned cell-laden GelMA hydrogel scaffolds with high cell viability as a proof of concept. The 3D patterns were robustly inscribed in the gelatin templates by PLA primary templates. The PLA templates were designed based on triply periodic minimal surface (TPMS) architectures (known as P and D structures) and fabricated *via* a low-cost and accessible desktop FDM 3D printing method. FDM offers a higher resolution and precision compared to most extrusion 3D bioprinting techniques. In addition, the fabrication process is highly versatile for 3D bioprinting of low viscous cell-laden prepolymers. Replacing the nozzle injection in conventional 3D bioprinting methods with casting processes facilitates loading larger populations of cells and eliminates shear force-induced cell death. The complex design with tortuous interconnected macropores maximizes the scaffold surface area, enabling effective diffusion of nutrients through the hydrogel matrix for uniform cell proliferation. Robust fabrication of the GelMA constructs facilitates tuning the mechanical and biopermeability properties due to the superior control on the internal pore architecture. The proposed fabrication process is a versatile tool for developing bulky tissues from a multitude of polymer backbones.

6.2. Experimental section

6.2.1. Design of triply periodic minimal surface (TPMS) sacrificial templates

The PLA sacrificial templates were designed based on triply periodic minimal surfaces (TPMS). TPMS topologies are defined by the following general formula (Eq. (6.1)):

$$\varphi(\mathrm{r}) = \sum_{l=1}^{L}\sum_{m=1}^{M} \mu_{lm} \cos\,(2\pi\kappa_l(P_m^T.r) = C \qquad \textbf{(6.1)}$$

where μ_{lm} is the periodic moment, κ_l indicates the scale parameter, and $P_m = [a_m, b_m, c_m]^T$ and $r = [x, y, z]^T$ are the basis vector and the location vector in 3D space, respectively. The topology of the TPMS is governed by the left-hand side of Equation (1) and the RD is defined by C value. $\varphi < C$ represents the domain that is embraced by the TPMS topology and $\varphi > C$ indicates the negative phase. In this study, since two sacrificial templates are used, the final GelMA scaffold would mimic the shape of the initial sacrificial template. Hence, PLA templates were designed by defining $\varphi < C$. The designed models in the present paper involve P and D structures at relative density values of 0.30, 0.42, 0.58, and 0.70. The corresponding offset values and explicit functions defined to obtain the models were explained elsewhere [240]. To produce the STL models for 3D printing, black and white cross-sectional images of each scaffold were generated using a MATLAB code and imported into an image processing software (FIJI) to stitch as an STL file. Then, the cylindrical scaffolds with a unit cell size of 3.33 mm shaped with P-surface and D-surface topologies at uniform relative density values of 0.30, 0.42, 0.58, and 0.70 were generated. A cylindrical shell-like wall (with outer diameter of 23.2 mm, height of 25 mm, and thickness of 0.6 mm) was also added to the STL design to perform as a reservoir to guide liquid gelatin into the PLA templates

6.2.2. Three-dimensional (3D) printing of sacrificial templates

The STL files were then imported to GrabCAD (GrabCAD Inc., Massachusetts, USA) software to define the printing parameters and tool paths. The 3D printing process was performed using a FDM system (LulzBot TAZ, Colorado, USA) for layer by layer 3D printing of the PLA templates (first sacrificial template). The PLA filament was fed into the 3D printer and layer height was set to 0.1 mm. The nozzle and bed temperature were set to 210 °C and 60 °C, respectively. The PLA templates with P- and D-surface topologies at uniform relative density values (including 0.30, 0.42, 0.58, and 0.70) were 3D printed. No extra supporting material was used for 3D printing the PLA templates.

6.2.3. Fabrication process for porous hydrogels

The GelMA hydrogel was used to fabricate the porous hydrogel scaffolds, as a proof of concept. To fabricate the second sacrificial templates, the gelatin from porcine skin was dissolved in deionized water (10%) at 80 °C, and cast into the PLA templates when heating at 80 °C and under vacuum conditions. Then, the PLA/gelatin structures were cooled down to 5 °C to solidify the gelatin phase. Then, the construct was immersed in dichloromethane (DCM) for 12 h (stirring at ~120 rpm) at the room temperature to dissolve the PLA templates. The dichloromethane was refreshed two times during the dissolution process. The samples were then kept in DI water for ~1 day to remove the DCM from gelatin. For the cell-encapsulated samples, the gelatin templates were sterilized under UV for 30 min for cell studies.

GelMA was synthesized based on a published protocol [241]. Then, a 10% GelMA solution, containing $6.92\times10^{-3}\%$ Eosin Y as a visible light photoinitiator, 1.33% of TEA as a co-initiator, and 1% of VC as a co-monomer, was prepared in medium and filtered. To encapsulate cells for cell studies, 3T3 cells were suspended in GelMA solution and infilled within the gelatin templates (at 10 million cell/ml). The cell-encapsulated GelMA was cured by exposing visible light at the wavelength of 450–550 nm and intensity of ~100 mW/cm^2 for ~8 min using a Genzyme FocalSeal LS1000 Xenon Light.

The cell-encapsulated GelMA/gelatin samples were left in a 75 cm^2 cell culture flask containing 10 ml fresh DMEM media and placed on a shaker (at ~110 rpm) in a standard incubator (Thermo Forma, Thermo Fisher Scientific, MA, USA) set at 37°C, 5% CO_2, and relative humidity of 95%, to allow gelatin template to dissolve overnight and make porous cell-encapsulated GelMA scaffolds. For the studies where no cells were involved, the gelatin was removed by soaking and agitating the construct in warm (~60 ˚C) water for ~1 min and the GelMA prepolymer solution was prepared in DI water.

6.2.4. Structural characterization

Scanning electron microscopy (SEM) images were taken to characterize the microscale features on the surface of the scaffolds. First, a thin layer of gold (10 nm) was sputtered on the surface of the samples, then images at 20 kV were obtained using 1550 FESEM, Zeiss, Oberkochen, Germany.

6.2.5. Swelling and degradation

To measure the mass swelling ratio, porous GelMA scaffolds were weighed as fabricated. Then, the samples were incubated in DPBS at a 37 °C incubator. The mass values were recorded at various time points, and the swelling ratios were obtained accordingly.

To assess the degradation behavior of the scaffolds, the samples were washed with DPBS and freeze-dried for 3 days using a benchtop freeze drier (Labconco, MO, US). The initial dry weight was recorded as W_0. Subsequently, the dry samples were placed in a 12-well tissue culture plate and immersed in 4 ml of freshly prepared collagenase (10 µg/ml) followed by incubation at 37 ºC for pre-determined time points. At each time point, samples were removed, thoroughly washed with DPBS, blotted with a Kimwipe, and freeze-dried before measuring their weight (W_d). The percent degradation rate (DR) was calculated using Eq. (6.2):

$$\text{DR}\ (\%) = (W_0 - W_d) \times 100/W_0 \qquad \textbf{(6.2)}$$

The collagenase enzyme was replaced every 2 days to maintain the enzyme activity. All the measurements were repeated for four samples.

6.2.6. Mechanical characterization

To assess the mechanical response of the scaffolds, monotonic and cyclic compressive tests were performed using a universal testing system (Instron 5943, USA) equipped with a 100 N load cell. To prevent sliding the GelMA scaffolds, the grippers were covered with a coarse tissue paper. The monotonic compressive load was performed at crosshead displacement of 90% with a rate of 2 mm/min. The cyclic tests were conducted in an increasing strain amplitude for each cycle (including 5, 10, 15, 20, 30, 40, and 50%) at the rate of 5 mm/min. Hysteresis was defined as $h = \frac{R_{unloading} - R_{loading}}{R_{loading}}$, where R illustrates the area under the stress-strain curves.

6.2.7. Permeability test

A constant head experimental test setup was employed for measuring the water permeability of the scaffolds. Initially, the scaffold was fit in a hole at the bottom of a tank. Then, the tank was filled with water and the height of the water was kept constant while the water was flowing through the scaffold under gravity and there was no water leakage from the scaffold/tank interface. The volume of water passing through the scaffold in 30 s was measured and this experiment was repeated for various fluid levels including 15, 25, 35, and 45 mm for all the scaffolds. The longitudinal permeability of the scaffolds was calculated by Darcy's equation (Eq. (6.3)):

$$k = -\frac{\mu\, \mathrm{q}}{A\, \frac{\Delta p}{l}} \tag{6.3}$$

Where μ is the viscosity of the fluid, q is the fluid flow rate measured for each scaffold, A and l represent the cross-sectional area and length of the scaffold, respectively, and Δp is the hydrostatic pressure ($\Delta p = \rho g h$, where ρ, g, and h indicate fluid density, acceleration of gravity, and height of the fluid, respectively) [105].

6.2.8. Live/dead assay

To evaluate the biocompatibility of the fabrication process and confirm the viability of the cells encapsulated in the GelMA scaffolds, a live/dead assay was conducted. Mouse fibroblast 3T3 cells were cultured in 175 cm^2 cell culture flasks and supplied with 25 ml DMEM mixed with 1% streptomycin-penicillin and 10% FBS. The cells and medium were placed in a standard incubator (Thermo Forma, Thermo Fisher Scientific, MA, USA) set at 37°C, 5% CO_2, and relative humidity of 95%. The cell density was monitored daily under the microscope, and the medium was refreshed every other day. After reaching ~90% confluency, the cells were dissociated from the flask using trypsin-EDTA for 5 min at 37°C, and then neutralized with 10 ml fresh media [242]. The cell/media mixture was centrifuged at 1000 rpm for 5 min. Then, the supernatant was removed, and cells were resuspended in fresh media and counted by a hemocytometer (Thermo Fisher Scientific, USA). For this purpose, the cells were stained with Trypan blue with 1:1 dilution with the cell/media suspension.

To perform 3D cell culture, gelatin templates (designed with P-surface at 0.42 RD) were prepared and sterilized under UV for 30 min. Then, 10% GelMA was mixed with photoinitiator (as described in section 6.2.3) and pH of the solution was adjusted by adding HCl to be fixed at ~7. Then, 3T3 cells were suspended in the GelMA solution with a cell density of 1×10^7cells/ml. The gelatin template was placed in a 12-well plate and 1.25 ml of cell-encapsulated GelMA was cast into the gelatin template and crosslinked. The porous GelMA scaffold was obtained after dissolving the gelatin template in media during the incubation at 37ºC. Bulk solid cell-encapsulated GelMA (thickness of ~1 mm) samples were prepared as a control. A live/dead assay (Biotium, Fremont, CA, USA) was conducted to evaluate the cell viability of the cell-encapsulated scaffolds at days 1, 3, and 5. The live/dead cell staining solution was prepared by mixing two fluorescent probes (3 µl of calcein and 12 µl ethidium homodimer-1) in 6 mL DPBS. After washing the samples in DPBS, they were immersed in the staining solution and incubated for 30 min at 37°C, 5% CO_2, 90% humidity. Then, the staining solution was removed, and samples were washed by DPBS. Eventually, 3T3 cells were imaged using a fluorescence microscope (Axio Observer 5, Zeiss, Germany). The excitation/emission wavelengths were ~528/617 nm for ethidium homodimer-1 and ~494/515 nm for calcein. The green color depicted live and red color represented dead cells. Finally, the cell viability of porous and bulk GelMA samples was defined as the ratio of live cells to the total live and dead cells and calculated using image processing software (FIJI).

6.2.9. Statistical Analysis

The reported quantities represent the mean ± SD of at least three replicates unless otherwise noted. The data were analyzed by one-way analysis of variance (ANOVA) and the comparisons with P values of < 0.05 were considered as statistically significant.

6.3. Results and discussion

6.3.1. Fabrication process of GelMA porous constructs

Template-assisted biofabrication schemes can enable engineering 3D constructs from soft hydrogels that are often challenging to be directly 3D bioprinted. Bio-templating requires sacrificial templates that can be safely washed away and ideally are water-soluble and biocompatible, such as gelatin. Such materials are often difficult to be directly 3D printed into 3D cell-laden hydrogels. The FDM-based extrusion 3D printing techniques are well established and accessible with the lowest cost among other 3D printing techniques. Plastic constructs can be precisely shaped with higher resolution than most extrusion 3D bioprinters. In addition, the bulky 3D tortuous features of porous TPMS architectures can be 3D printed, often with no need of support materials. Therefore, we propose a multi-step fabrication process in which 3D printed PLA constructs serve as the primary sacrificial template (Figure 6.1aI,bI) to develop a secondary gelatin template. Note that we initially considered water-soluble carbohydrate secondary templates such as isomalt. However, molten isomalt (at ~130 ˚C) tends to quickly solidify while casting in the PLA template, hindering full penetration into the pores. Hence, we found it difficult to form carbohydrate templates as higher temperatures could also thermally distort the 3D printed plastic PLA template.

Dissolving FDM 3D printed plastic templates, however, requires harsh solvents that could damage living cells. Hence, the PLA templates were cast with water-soluble gelatin to enable precise fabrication of secondary gelatin templates. Gelatin at higher temperatures (~80 ºC, well below the melting temperature of PLA, *i.e.*, 150-160 ºC) was liquid enough to infuse fully within the channels of the PLA template with the aid of vacuum. Cooling the gelatin infilled PLA template down to 4 ºC led to the *in situ* physical gelation of gelatin. This step was followed by DCM treatment that led to the successful removal of PLA, leaving behind the porous gelatin construct to which the PLA pattern was fully transferred (see Figure 6.1aII,bII,bIII). Note that we initially used ABS and acetone as a primary sacrificial template and the solvent in our gelatin template fabrication system (for dissolving ABS), respectively; however, the gelatin was distorted upon immersion in acetone, whereas no visible shape changes were observed in the case of DCM. In addition, DCM is highly volatile and hardly miscible with water, thereby it could be easily removed from gelatin when immersed in aqueous media (for ~1 day), as illustrated in Figure 6.1aIII,bIII. In essence, a thin film of DCM, which can easily evaporate, was observed on the surface of the water bath after soaking the DCM-treated gelatin template [243]. Part of the DCM, as it replaces with water, sank into the water bath per the higher density of DCM that facilitates its removal from the gelatin template. Visible light crosslinkable cell-laden GelMA prepolymer was pipetted into the gelatin templates followed by a photo-crosslinking process. Due to the hydrophilicity of both GelMA and gelatin, and co-continuous phases of the templates, the gelatin template was fully filled upon casting GelMA prepolymer with no observable evidence of bubble formation (Figure 6.1aIV,bIV). Radiation of visible light resulted in GelMA prepolymer (containing Eosin Y as a photoinitiator, VC as a co-monomer, and TEA as a co-initiator), to change color from red to yellow, which was indicative of crosslinking reaction (Figure 6.1bV). The gelatin template was fully dissolved in the cell-culture media during the incubation at 37 ºC (or in warm water for the cell-free experiments), leaving behind the 3D self-standing porous GelMA construct shaped in accordance with the primary PLA template (see Figure 6.1aV,bVI,c). The use of visible light crosslinking in this approach poses a lower risk of cell damage compared to the UV light initiated polymerization.

The proposed fabrication process enabled the successful transfer of the designed patterns to the cell-laden GelMA hydrogels and allowed multiple layered constructs with complex channel shapes at thickness levels significantly larger than those demonstrated in the literature [244, 245]. The proof-of-concept scaffolds with ~1 cm thickness and ~2 cm diameter with micro-scale pore features corresponded well to the original topology of 3D printed PLA templates. Since the main geometry originates from the FDM 3D printing technology, the pores with fine resolution and high precision compared favorably to what direct extrusion 3D bioprinting technologies could achieve. The presented fabrication process offers flexibility in terms of the encapsulated cell population due to the elimination of nozzle clogging issues and from high cell densities. This method can be easily tuned to form a wide range of cell-encapsulated hydrogels with desirable architectures, based on different biopolymers.

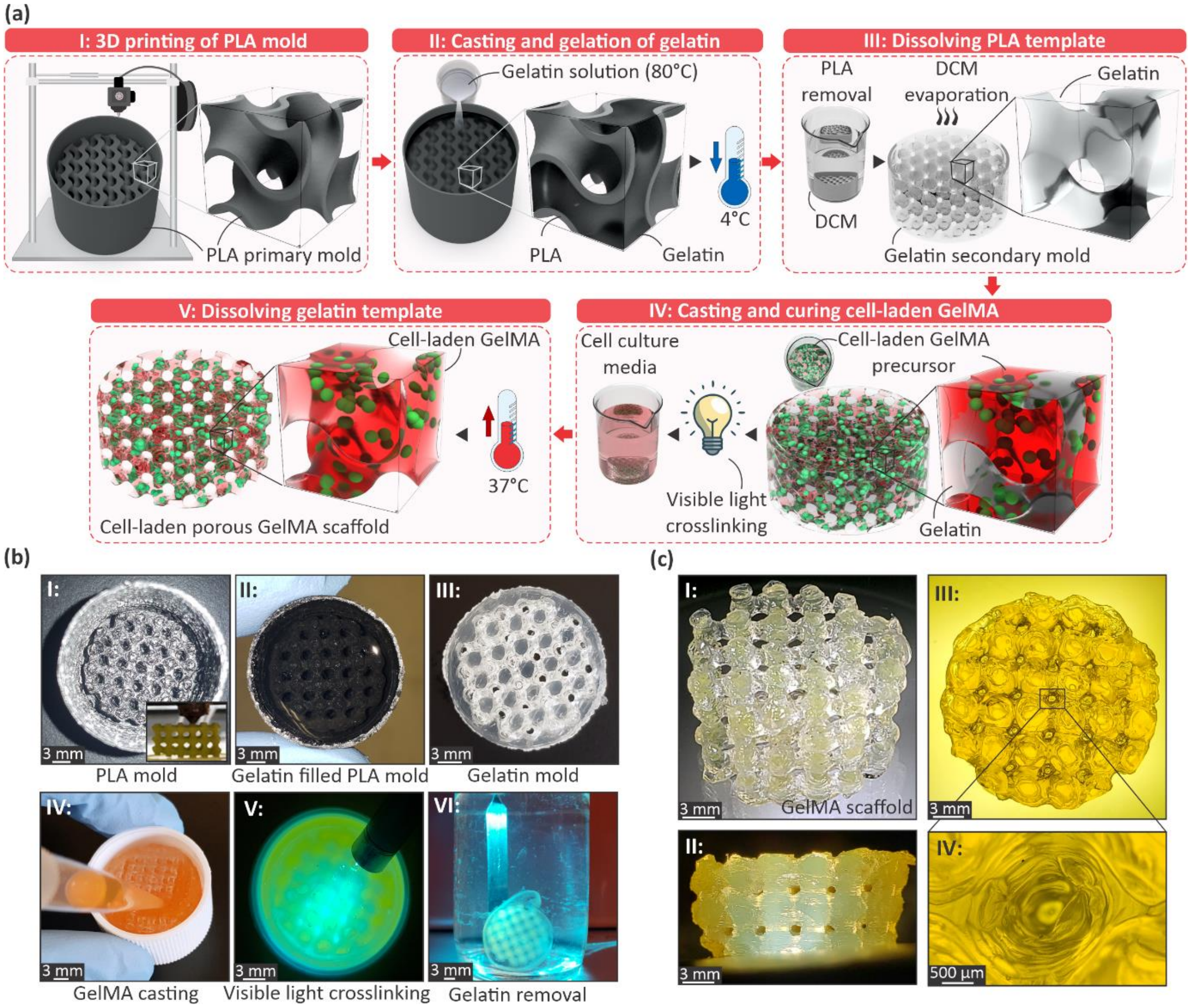

Figure 6.1. The three-dimensional (3D) bio-templating scheme for fabrication of thick 3D structured cell-laden gelatin methacryloyl (GelMA) constructs with patterned tortuous macro-channels. (a) Schematic illustration of the fabrication steps. I: 3D printing of the primary templates using extrusion techniques based on fused deposition modeling (FDM), II: casting gelatin at high temperature (80 ºC) in the polylactic acid (PLA) template followed by physical gelation of gelatin at the low temperature (4 ºC). III: Development of the porous gelatin template by the dissolution of PLA plastic in dichloromethane (DCM), and DCM removal in water for ~1 day. IV: Casting a cell-laden GelMA prepolymer solution *via* a visible light crosslinking procedure. V: removing the gelatin template from a network of photo-crosslinked cell encapsulated GelMA hydrogel at the incubation temperature during the cell culture (37 ºC). (b) Optical images of the samples formed at different fabrication steps. I: 3D printed PLA templates, II: gelatin infilled PLA templates, III: the gelatin secondary template after dissolving PLA template, IV: casting the GelMA solution in gelatin template, V: photo-crosslinking of the GelMA phase using visible light, and VI: gelatin dissolution process. (c) Images from different views of the fabricated GelMA hydrogel constructs. I: Top-side view of hydrogel with the P structure at 0.42 relative density (RD). II, III: Side and top views of the scaffold with 0.70 RD, respectively. IV: Magnified image of the micro-scale pores in the fabricated scaffolds.

6.3.2. Optimization of the fabrication process for printing fidelity

The first stage of the fabrication process, *i.e.*, 3D printing of PLA template, determines the basic topology of the final GelMA constructs. Hence, in our initial attempt, we strived to find the smallest feature sizes where (i) the FDM 3D printer could properly fabricate the samples and (ii) gelatin could fully infill the templates. The most challenging geometry in our experience (*i.e.*, the D pore shape at 0.70 relative density (RD) due to its topological tortuosity and small room for gelatin diffusion) was 3D printed at different unit cell sizes, as represented in Figure 6.3a and inspected for defects. The results showed that at the unit cell sizes above ~3.3 mm, the pores could be successfully formed as in their corresponding CAD models, whereas the scaffolds with smaller unit cell sizes had notable defects, and the pores were not coherently formed. Accordingly, the gelatin negative image of the PLA template was formed with no evident flaws or defects (Figure 6.3b), suggesting complete infusion of the gelatin into the PLA pores. At this scale, the sub-millimeter size features (pore sizes and connections) starting from ~800 µm were measured in both PLA and gelatin constructs. Moreover, the stair-step topology of the PLA surface due to the layer-by-layer 3D printing was clearly transferred onto the gelatin template in micro-scale.

In the next step, the physical properties of the secondary gelatin templates were optimized for providing an efficient function in forming the GelMA constructs (Figure 6.3c-e). Gelatin in the first place was required to be self-standing and firm enough to support the casting material. We examined gelatin contents over the range of 5, 10, 15, and 20% [246] for the fabrication of P structures at 0.42 gelatin RD. Gelatin templates at 5% tended to collapse as they failed to withstand their own weight and thereby could lead the final GelMA scaffold to deviate structurally from their designed models. The swelling behavior of gelatin in water during the DCM removal could be another aspect of topological deviation, as investigated in Figure 6.3c-e. The volumetric swelling ratio decreased from ~37% to ~14% as the gelatin concentration was reduced from 20% to 10% (Figure 6.3d). This difference is because the lower dry gelatin content was less capable of absorbing fluids [247]. Thus, the lowest gelatin concentration of 10% was chosen in our fabrication process as it minimized gelatin swelling while maintaining the required structural integrity. In the context of pore size, the swelling behavior can have a competing effect: water uptake in gelatin templates simultaneously caused an overall expansion, while thickening the internal linkages and connections locally reduced the pore size. Apart from the minimal volumetric swelling, the low gelatin content facilitated gelatin removal from the GelMA network in the later stages of the fabrication process. We investigated the effect of gelatin RD on the volumetric swelling behavior. The results of swelling across different RD values for the P structure suggested an overall increase in gelatin swelling with RD, where the maximum volumetric swelling remained within ~28% at the maximum RD.

Next, we sought to engineer self-standing patterned GelMA hydrogels, yet with minimized prepolymer concentration, in order to provide a more favorable extracellular matrix (ECM) for cell encapsulation and media diffusion. We noted that the initiation mechanism for the polymerization of GelMA played a key role in our fabrication process to successfully form crosslinked GelMA networks in the gelatin templates (Figure 6.3f). For instance, we initially attempted to crosslink a 10% GelMA prepolymer using a 0.5% Irgacure 2959 photoinitiator solution under UV light (25 mW/cm^2) for 2 min, the condition that is known to be safe for the encapsulated cells. However, GelMA failed to fully crosslink as it completely dissociated in warm water during the gelatin removal process (Figure 6.3fI). Therefore, a redox ammonium persulfate (APS)/*N*,*N*,*N*,*N*-tetramethylethylenediamine (TEMED) initiator system, which is widely used for free radical polymerization in hydrogels, was used at different 1:1 compositions to crosslink 10% GelMA prepolymers. A GelMA prepolymer solution containing 0.3% of APS and 0.4% of TEMED was left overnight at room temperature for the crosslinking reaction. The resulting hydrogel had poor mechanical stability, containing partially crosslinked hydrogel clumps (Figure 6.3fII). On the other hand, increasing the APS and TEMED concentrations to 0.5% led to the rapid gelation of GelMA and thereby failed to fill the gelatin templates completely. The observed failures in crosslinking can be explained by either limited penetration length of light or possible initiator dilution driven by the diffusion of small initiator molecules into the gelatin phase. Switching over to the EosinY/VC/TEA visible light-triggered initiation system, however, enabled the successful fabrication of 10% GelMA constructs with the designed internal pore architectures (Figure 6.3fIII). The use of visible light is highly preferred over UV light due to biosafety. Note that lowering the GelMA concentration to 5% failed, as the structure was not strong enough to withstand its own weight and thereby collapsed after the gelatin removal process. Therefore, we selected the 10% GelMA as the lowest concentration for hydrogel formation for the remaining characterizations.

The fabrication process was implemented on a variety of pore shapes (*i.e.*, P and D pore shapes) and RD values (*i.e.*, 0.30, 0.42, 0.58, 0.70) to test the versatility of the proposed process for engineering complex 3D GelMA constructs. The optical microscopic images of the PLA and gelatin templates as well as GelMA scaffolds in various pore shapes and relative densities are presented in Figure 6.2.

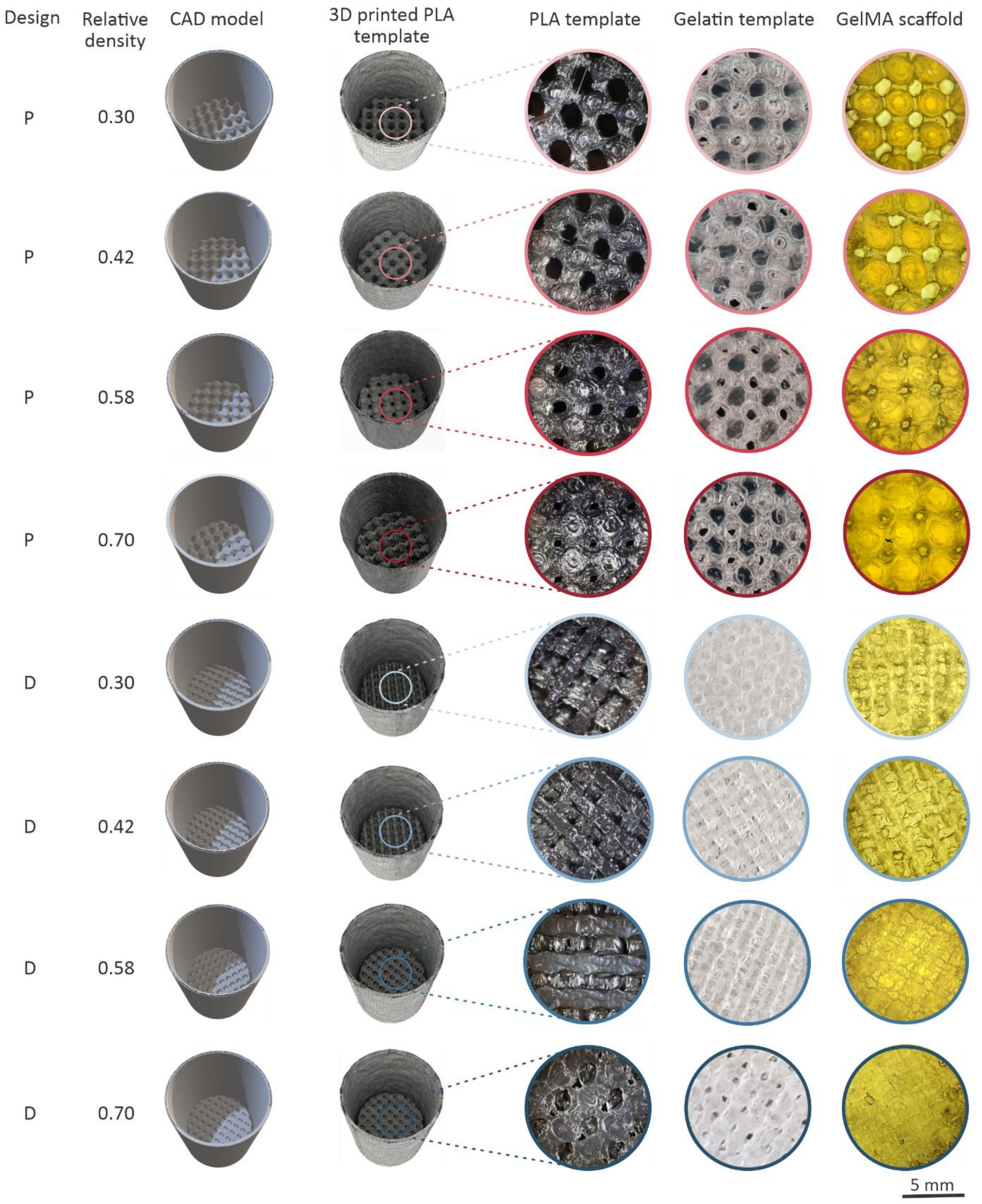

Figure 6.2. Optical microscopy images of poly(lactic acid) (PLA) and gelatin sacrificial templates as well as gelatin methacryloyl (GelMA) scaffolds designed with P and D structures at 0.30, 0.42, 0.58, and 0.70 relative density (RD) values.

The overall RD of the final constructs was obtained by dry weighing and compared with the designed CAD models in Table 6. The results suggest that the RD for the as-fabricated samples deviated within ~17% from the designed CAD model. Figure 6.3g demonstrates the pore size and topology of connections in swollen P structure at different RD values. As can be seen, the pore/channel sizes in the range of ~0.9 mm to ~2.2 mm could be fabricated in a controllable manner. The measured pore sizes were also found to be in agreement with those of CAD models (Table 6). The somewhat smaller measured pore sizes compared to the CAD model are attributed to the competing effects of swelling on gelatin template pore size, as discussed above.

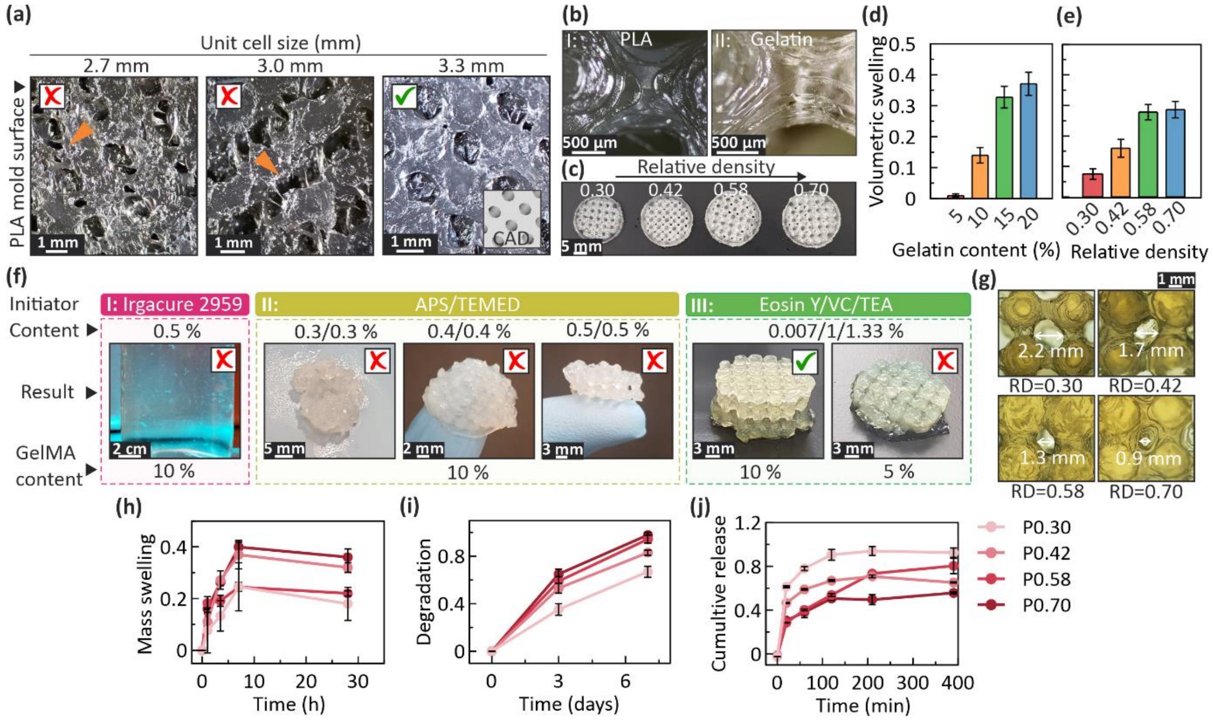

Figure 6.3. Optimization of the fabrication process and physical characteristics of the gelatin methacryloyl (GelMA) scaffold constructs. (a) Printability evaluation of polylactic acid (PLA) at different unit cell size scales of 2.7 mm, 3.0 mm, and 3.3 mm. Arrows show the defects in the 3D printed constructs. Minimum feature sizes were maintained at 3.3 mm unit cell sizes and above. (b) Microscope images of the scaffold structure and surface stain step patterns for I: PLA templates and II: gelatin templates. (c) Optical image of the swelling behavior of gelatin templates at different gelatin relative density (RD) values. Characterization of volumetric swelling of gelatin templates as a function of (d) gelatin concentration and (e) the gelatin scaffold RD. (f) Polymerization behavior of GelMA using different initiator systems I: Irgacure 2959, II: ammonium persulfate (APS)/*N*,*N*,*N*,*N*-tetramethylethylenediamine (TEMED), and III: EosinY/*N*-vinylcaprolactams (VC)/ triethanolamine (TEA) to form crosslinked GelMA structures at 10% GelMA concentration. (g) Microscopic images of the pore topology and size for the GelMA scaffolds with P structure at different RD values. Characterization of (h) mass swelling ratio, (i) degradation, and (j) cumulative release of Rhodamine B overtime from scaffolds with P structure at different RD values.

Table 6. Comparing the fabricated cylindrical scaffolds with the designed CAD models in terms of relative density (RD) and pore size for the samples with P structure.

Sample label	RD			Pore size (mm)		
	CAD	Dry weighing	Deviation (%)	CAD	Imaging	Deviation (%)
P0.30	0.30	0.35	17.36	0.91	0.90	1.11
P0.42	0.42	0.43	4.44	1.43	1.33	7.00
P0.58	0.58	0.53	8.65	1.96	1.71	12.76
P0.70	0.70	0.66	5.21	2.56	2.24	12.50

6.3.3. Swelling, degradation, and drug release responses

The physical properties of the GelMA constructs fabricated with the P structure at different RD values were characterized in terms of their swelling, degradation, and drug release performance in response to exposure to biofluids (see Figure 6.3h-j). The scaffolds had swelling ratios in the range of 24% to 40% for various relative density values (Figure 6.3h). The swelling ratio of the scaffolds was not significantly correlated with the RD. The swelling ratio is mainly governed by the crosslinking density in hydrogels, which ties back to the irradiation as well as photoinitiator/co-monomer concentrations [248]. The enzymatic degradation of the GelMA scaffolds with a 10 µg/ml collagenase solution showed accelerated degradation rates for the samples with larger RD (Figure 6.3i). In addition, porous GelMA constructs were evaluated in terms of their drug release performance. To load drug molecules, the GelMA scaffolds were soaked for 4 h in a 30 mg/L Rhodamine B solution, as a model molecule representative of small-molecule drugs such as those with antimicrobial functions. The release of Rhodamine B was obtained over time for scaffolds with different RD. Overall, the lower the RD, the faster the release kinetics due to the thinner internal features and thereby easier transfusion of the drug molecules.

6.3.4. Quasi-static compressive mechanical behavior

The mechanical properties of the scaffolds were evaluated under monotonic quasi-static compressive deformations. The effect of GelMA concentration on the compressive response of the P scaffolds at 0.42 RD is shown in Figure 6.4a. The compressive stress-strain curves of the GelMA scaffolds were in line with soft porous materials [134]. The stress-strain curves started with a linear region followed by a sharp increase in stress, corresponded to the collapse of the layers and densification while compaction of the polymer chains and failure progressed. Elastic modulus was increased by ~250% as the GelMA concentration raised from 10% to 20% (Figure 6.4b). The systematic failure in scaffolds was originated from the brittle failure of the connections in the internal scaffold structure (Figure 6.4c).

Deformation and failure mechanism of the scaffolds are critical in determining the mechanical behavior of scaffolds. Figure 6.4d illustrates the mechanism of structural instabilities in different pore shapes and RD levels. Deformation and failure in porous biomaterials are often classified with respect to the pore shape as stretching (P structure) and bending (D structure) dominated mechanisms. The compressive deformation of the P structure strongly depended on the scaffold RD. At low RD, *i.e.*, 0.30, axial deformation was transferred to buckling of the vertical connections (Figure 6.4dI), whereas, at 0.70 RD, most elements were subject to axial compression (Figure 6.4dII). For the D structure, compression loads were transferred to shear deformation across the RD values (Figure 6.4dIII). The stress-strain curves for the porous GelMA scaffolds are shown in Figure 6.4e. The linear elastic region continued up to the strains of ~0.4 for most samples before the first failure was observed. The brittle failure of internal linkages corresponded to sharp drops in stress-strain curves. This result is in accord with a layer-by-layer failure mechanism in both P and D surface topologies. As shown in the magnified plot insets in Figure 6.4e, while P structures showed failure at compressive strains below 0.4, D structures showed rather smooth behavior, suggestive of better compressibility of bending-dominated architectures. As shown in Figure 6.4f, the elastic modulus of the scaffolds increased with RD. The elastic modulus was in the range of 2.8 to 12.5 kPa and 1.6 to 6.5 kPa for P and D structures, respectively. The observed range of elastic moduli matches those of soft tissues such as skeletal muscle tissue, smooth muscle tissue, as well as arteries [249]. The larger elastic moduli for P structures can be due to the stretching dominated deformation mechanism. The results of scaling analysis (power fit) to the elastic modulus-relative density data are represented in Table 7. The exponential constants of 1.64 and 1.53 were obtained for P and D structures, respectively, which are comparable to previously reported results [240].

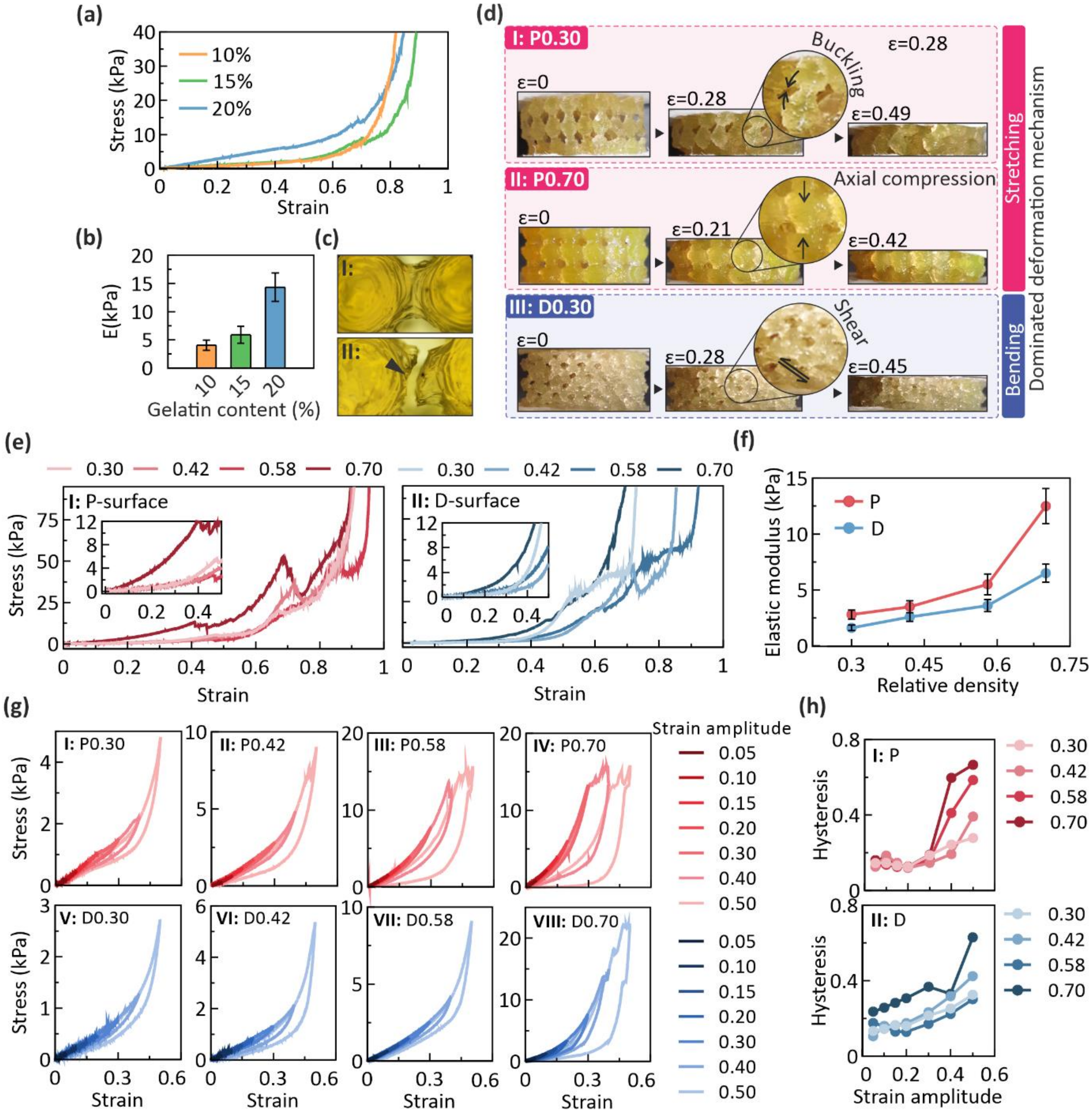

Figure 6.4. Mechanical characterization of porous gelatin methacryloyl (GelMA) constructs. (a) The effect of GelMA concentration on the stress-strain curves for P structure at 0.42 relative density (RD), and (b) variation of compressive elastic modulus with GelMA concentration. (c) Optical images representative of brittle failure of linkages in P structure scaffold under compressive deformation. Representation of the linkage I: before and II: after failure. (d) The deformation mechanisms of GelMA scaffolds for P structure at I: 0.30 and II: 0.70 and III: D structure at 0.30 RD. (e) The stress-strain curves corresponding to the cyclic load for I: P and II: D structures at different RD values, and (f) elastic modulus-RD relationships for P and D structures. (g) The cyclic stress-strain curves with increasing strain amplitude for P structure at I: 0.30, II: 0.42, III: 0.58, IV: 0.70, and D structure at V: 0.30, VI: 0.42, VII: 0.58, and VIII: 0.70 RD values. (h) The results of hysteresis versus the strain amplitude for I: P and II: D structures.

Table 7. The results of mathematical models fit to the experimental elastic modulus (E)- and permeability (K)-relative density (RD) data.

Structure label	$E_n = a\,(RD)^n$			$K_n = ae^{-n(RD)}$		
	a	n	R^2	a	n	R^2
P	17.28	1.64	0.86	4.58E-09	4.99	0.98
D	9.84	1.53	0.95	2.14E-09	3.59	0.93

6.3.5. Cyclic Compression test on GelMA scaffolds

Tissue constructs are often subject to dynamic deformations. Hence, the compressive stress-strain response of the GelMA scaffolds was evaluated under cyclic loads with increasing strain magnitudes from 0.05 to 0.50 (see Figure 6.4g). A wide hysteresis region and stress-strain shift with increasing loading cycles are indicative of plastic and irreversible deformations. As shown in Figure 6.4e, the hysteresis curves indicated reversible deformations with minimal energy loss at the strain amplitudes below their corresponding failure strain. For instance, the evidence of large hysteresis was more prominent in P structures at higher RD values of 0.58 and 0.70 (and D structure at 0.70 RD) as the curves tend to shift with increasing deformation amplitudes beyond its failure point. The hysteresis ratio, as an indicator of permanent deformations and dissipated deformation energy under dynamic loading, was quantified in Figure 6.4h. Hysteresis ratio varied in the same range of ~0.10 to ~0.65 within the applied deformation range for both P and D structures and increased with both strain amplitude and RD. In general, a reversible elastic behavior was maintained in D structures at higher RD than P structures. This result is consistent with postponed failures in quasi-static loading data (Figure 6.4e) for D structures and could be due to the capability of bending-dominated structures in reversible deformation energy absorption. The larger hysteresis cycles in P structures indicated buckling/axial deformation induced permanent failures.

6.3.6. Permeability analysis of hydrogel scaffolds

Permeability measurement is a quantitative approach representing the capability of the scaffolds to transfer nutrients and body fluids. Here, the effect of pore shape and RD on the permeability of the scaffolds was assessed through a constant head permeability test (Figure 6.5a). The fluid flow, measured at various fluid heights (15-45 mm), showed a linear correlation between pressure (P) and flow rate (Q) for all scaffolds, as shown in Figure 6.5b. The higher slope of the P-Q plots observed for the scaffolds with higher relative density signifies the lower fluid permeability based on Darcy’s law [144]. As the fluid height increased, the permeability decreased for the scaffolds with lower relative density values, potentially due to the deviations from the laminar flow and pressure head loss (Figure 6.6). The permeability of the scaffolds was obtained by using a linear fit to the P-Q curve; the calculated permeability values are shown in Figure 6.5c. The permeability of the scaffolds varied inversely with relative density values from 1.34×10^{-10} to 9.18×10^{-10} m^2. The experimental permeability was exponentially correlated to the relative density according to the results of the fit to data presented in Table 7. The fluid flow was computationally analyzed, and corresponding computational permeability values were calculated using computational fluid dynamics (CFD). Figure 6.7a presents the computational permeability data. The larger permeability for the P structure at lower RD values was reflected in the experimental data and can be explained by the predicted fluid flow streamlines. Figure 6.5d illustrates the 3D fluid flow patterns along a linear path at the scaffold inlet for P and D structures (0.42 RD). The full 3D and 2D (top view) demonstration of the fluid flow is shown in Figure 6.8 and Figure 6.9, respectively. The fluid flow for the P structure mostly fell onto a 2D plane and followed more direct pathways compared to the D structure, whereas the flow in D scaffolds followed a swirling path due to the tortuous nature of the unit cell topology in the internal scaffold structure. At high RD values, this trend switched due to the inhomogeneous distribution of channel width in P structure.

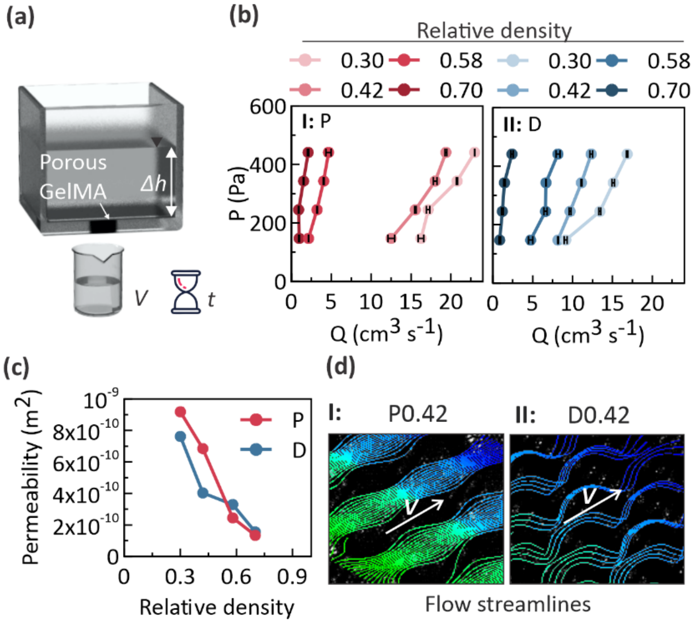

Figure 6.5. Fluid flow permeability of porous gelatin methacryloyl (GelMA) scaffolds. (a) Schematic representation of the constant head permeability test setup. (b) Pressure drop (P) as a function of fluid flow rate (Q) for GelMA scaffolds designed with I: P-surface and II: D-surface topologies. (c) Permeability analysis of GelMA scaffolds as a function of pore shape and relative density (RD). (d) The results of computational flow streamlines obtained from the computational fluid dynamics (CFD) analysis of fluid flow in I: P and II: D structure at 0.42 RD.

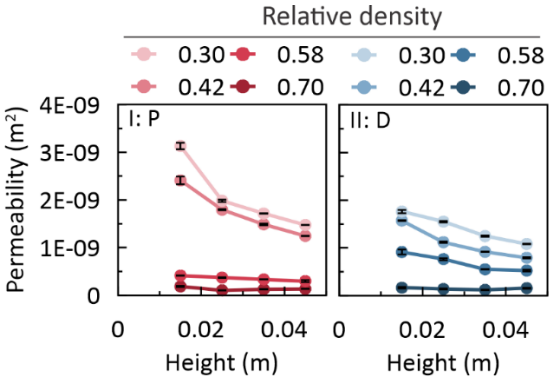

Figure 6.6. The effect of fluid height on the permeability of gelatin methacryloyl (GelMA) scaffolds for I: P and II: D structures at various relative density (RD) values.

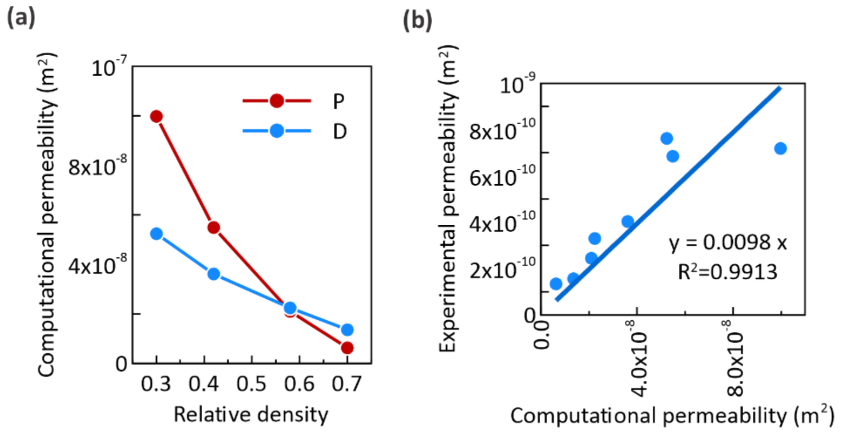

Figure 6.7. (a) The results of computational permeability as a function of relative density (RD) for P and D structures. (b) Experimental versus computational permeability data points showing a linear correlation factor of 0.0098.

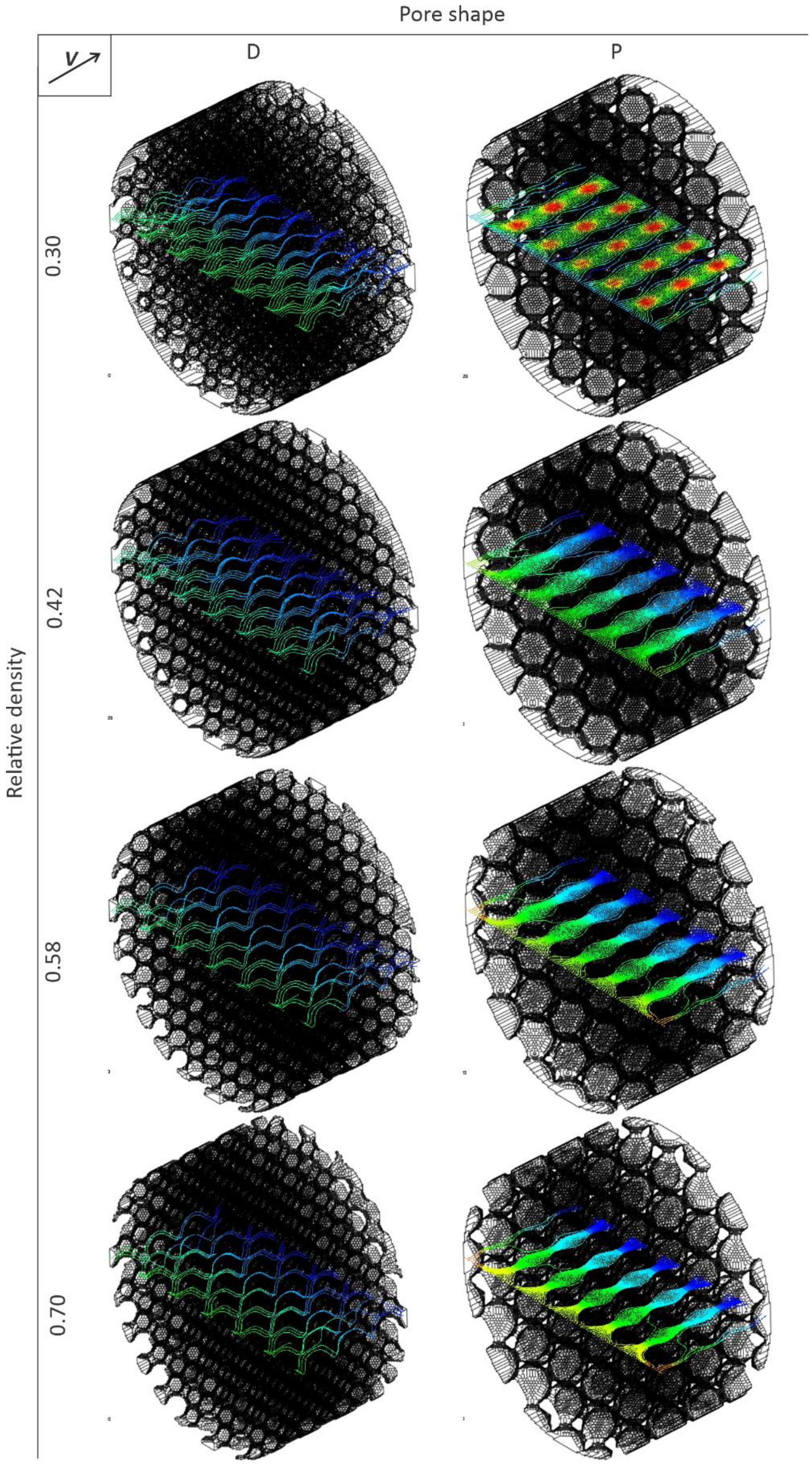

Figure 6.8. Three-dimensional (3D) representation of the fluid flow streamlines obtained by the computational fluid dynamics (CFD) analysis of flow through the scaffold structures.

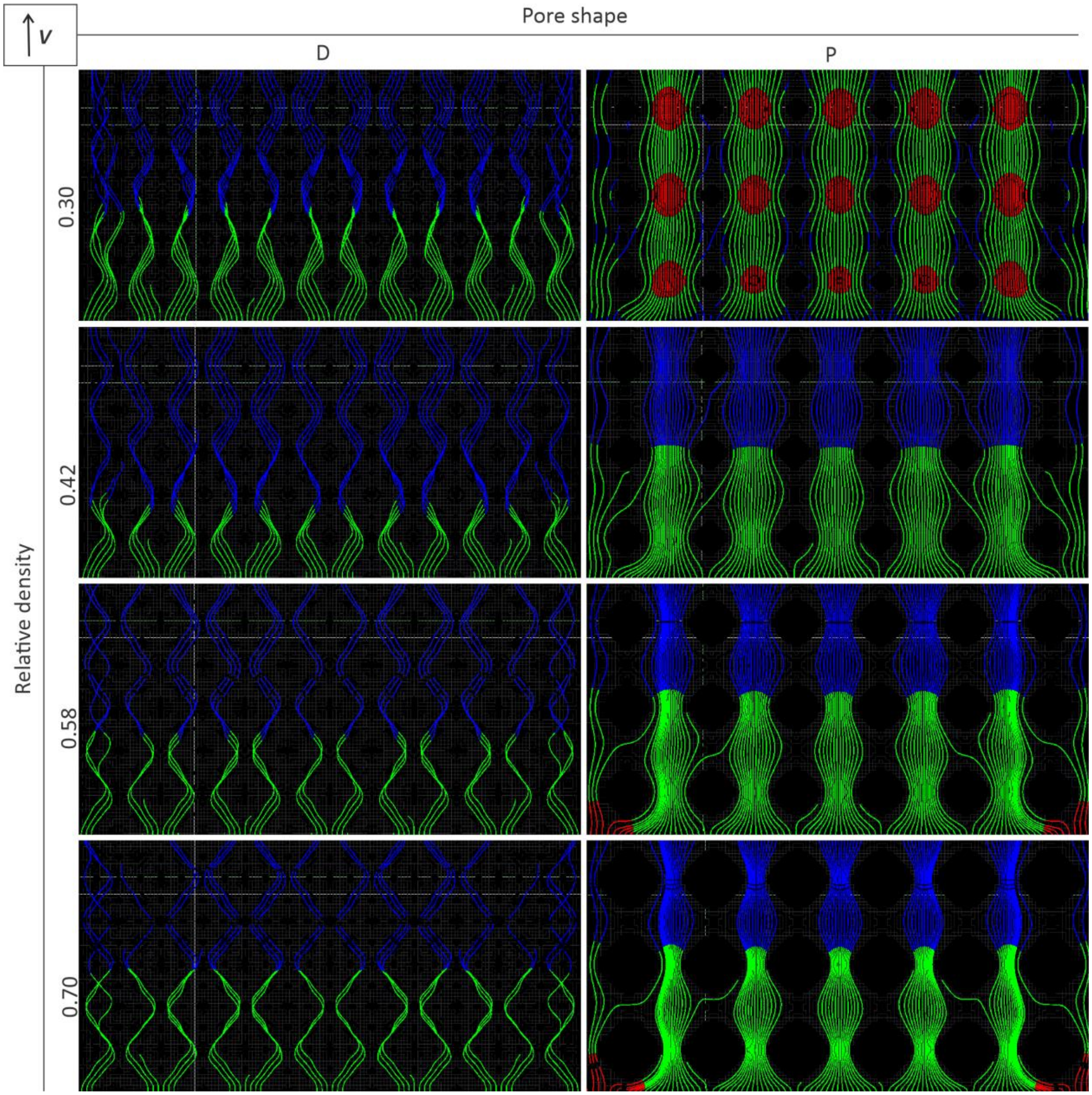

Figure 6.9. Two-dimensional (2D) top view of the fluid flow streamlines obtained by the computational fluid dynamics (CFD) analysis of flow through the scaffold structures.

6.3.7. Biocompatibility

To assess the biosafety of the proposed fabrication process and the GelMA porous constructs for potential use as tissue substitutes, *in vitro* cell compatibility of the cell-laden constructs was evaluated by using a live/dead assay. For this purpose, the cell-encapsulated GelMA scaffolds (P-surface at 0.58 RD) and GelMA sheets as control (~1 mm thickness) were prepared and evaluated in terms of cell viability for a period of 5 days. Representative live/dead fluorescent images of cell-laden scaffolds for days 1, 3, and 5 are presented in Figure 6.10a. For both sheet-like and porous GelMA samples, the 3T3 fibroblast cells (10 million cells/ml) remained alive (shown in green) and only a few dead cells (shown in red) were observed. The live/dead assay confirmed cell viability of over 90% throughout the course of the experiments (Figure 6.10b). This result indicated that the final gelatin templates were free of toxic residues (e.g., DCM) and was consistent with the biocompatibility of the proposed fabrication process. The interconnected macropores formed in the hydrogel matrix enabled continuous perfusion of nutrients and maintaining high cell viability in thick scaffolds (Figure 6.10c). The fluorescent images captured from different sections of the porous GelMA scaffolds confirmed the viability of cells in all regions (Figure 6.11).

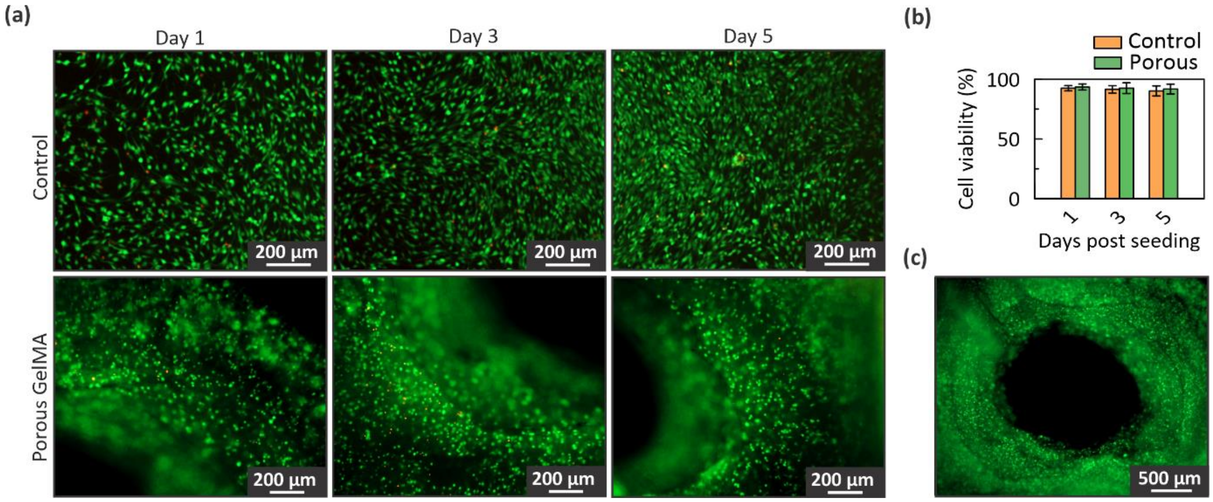

Figure 6.10. ***In vitro*** **live/dead cell biocompatibility analysis of cell-laden porous gelatin methacryloyl (GelMA) scaffold (green: live and red: dead cells). (a) Live/dead fluorescent images of cell-laden control and porous bulk GelMA scaffold. (b) Cell viability of cell-laden control and porous scaffold on days 1, 3, and 5 after encapsulation. (c) The interconnected pores in the GelMA scaffolds maintained high cell viability in thick scaffolds.**

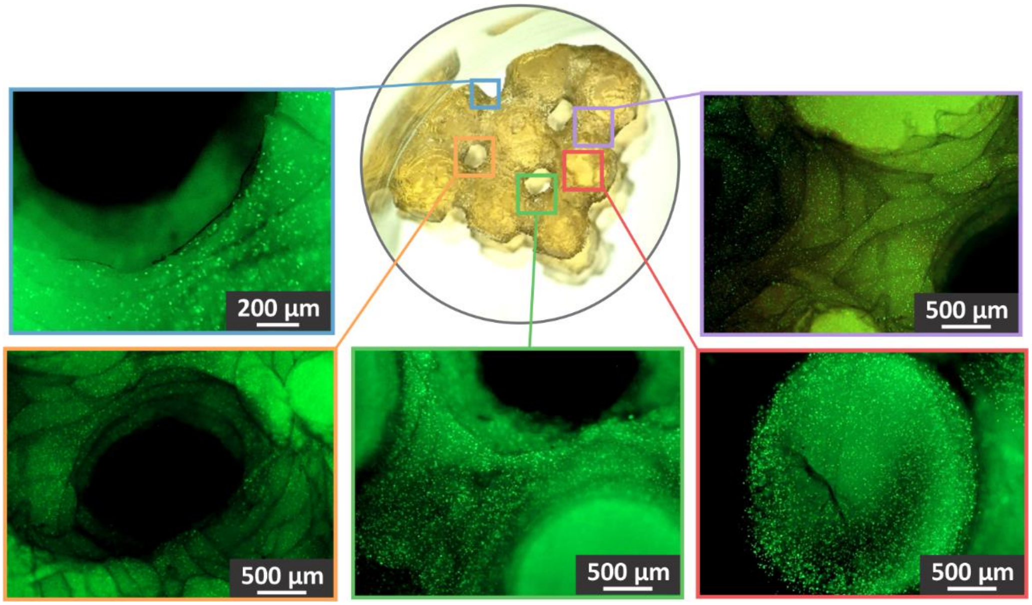

Figure 6.11. Live/dead fluorescent images of gelatin methacryloyl (GelMA) scaffolds showing cell viability at day 5 in various regions of the scaffold.

6.4. Conclusions and Prospects

Direct 3D bioprinting methods have been constrained to thin tissue constructs with simple shape and low cell populations. In the present study, we demonstrate a bio-templating fabrication scheme to enable biofabrication of 3D thick micro-engineered tissue with better versatility to incorporate complex-shaped interconnects inside the construct compared to the direct extrusion bio 3D printing techniques. The proposed fabrication method employed accessible and low-cost materials and 3D printing instruments to provide an easy-to-access tissue fabrication platform. This method can overcome the limitation of precision and resolution in the 3D bioprinted artificial tissues. Using the proposed fabrication technique, highly biocompatible cell-laden GelMA hydrogel scaffolds with tunable designs of perfusable networks and tortuous complex pathways for the desired mechanical and fluid transport properties were successfully fabricated. The cell encapsulated hydrogels showed high cell viabilities (~90%) that corroborated the biocompatibility of the process. The fabrication strategy is designed to be compatible with low viscosity hydrogels that are difficult to 3D-print. The possibility of visible light-activated crosslinking mechanisms provided a safe means of incorporating living cells with large populations inside the scaffold matrix. The hydrogels can be encapsulated with the different types of mammalian cells at physiologic density values mimicking human tissues for long-term sustainability. The facile and cost-efficient nature of the proposed fabrication strategy can provide a transformative platform for a wide range of applications and can be scaled up to form thick tissue constructs.

Chapter 7. Additively Manufactured Gradient Porous Ti-6Al-4V Hip Replacement Implants Embedded with Cell-Laden Gelatin Methacryloyl Hydrogels

7.1. Introduction

Total hip implant replacement is a necessary procedure when severe damage to the hip joint limits a patient’s mobility. Osteoarthritis, rheumatoid arthritis, septic arthritis, bone dysplasia, and hip fracture are the major disorders [250] accounting for most total hip replacement surgeries, and are anticipated to reach to 635,000 procedures per year by 2030 [251]. However, the burden of revision surgery, which is often more costly and complicated [252], is expected to grow to 72,000 procedures per year by 2030 [251]. One major cause of implant failure is poor implant integration with the native bone at the implant interface [253]. Since the advent of additive manufacturing techniques, state-of-the-art hip implants with porous internal design have enabled bone ingrowth as a potential solution to diminish stress-shielding [254] and to achieve strong bone-implant integration [255-257]. Recent studies have indicated the significant impact of the internal unit cell design on the mechanical and biological performance of the porous bone scaffolds [105, 144, 258, 259]. Therefore, unit cell characteristics can be exploited to regulate the host tissue response and mechanical stability of the implant [260-262].

Metal 3D printers have enabled precise shaping of the complex unit cell features in medical-grade titanium (Ti-6Al-4V) hip implants in a highly controllable manner [263, 264]. Selective laser melting (SLM) has become a versatile technique to produce ordered porous constructs for hard tissue engineering applications [265-267]. Conflicting design requirements for the implants, however, leads to a trade-off in porous implant functionalities [240, 268, 269]. In a porous scaffold with a uniform porosity distribution, moving from low porosity to high porosity means larger spaces for cell migration and thereby improved bone ingrowth contingent on having sufficient surface area. However, increasing porosity is associated with decay in mechanical strength [270-272]. Difficulties with the 3D printing procedures at the extremities of porosity are another obstacle

[143]. This complexity entails proper non-uniform distributions of porosity to design the implant locally with the desired functionalities to combine mechanobiological benefits obtained from different unit cell characteristics [273]. Functionally graded designs have been introduced as a solution through different design algorithms [274]. However, the majority of the literature remains focused on porous scaffolds with simple geometries for which their quasi-static compressive behavior is well documented [275-279]. Hip implants undergo rather different loading scenarios during daily activities, often a combination of tensile and compressive regions (due to the off-axis loading configuration) [280],[281]. Besides, the desired functionalities defined thus far mostly emphasize the mechanical aspects and lack sufficient understanding of the biological requirements. Hip implants with combined cellular structures (negative Poisson's ratio, auxetic, with that of conventional positive Poisson's ratio) have been demonstrated in a recent study addressing bone resorption, due to the retraction of the implant from the native bone in the conventional implants [255]. In this approach, the tensile region of the implant was architected with auxetic bio-metamaterials. Therefore, the implant was aimed to expand locally at the regions where it is prone to separation from the native bone due to the deformation induced by the loading on the implant. In this way, the integration with the surrounding bone during daily activities could be improved. This study demonstrated that unit cell shape can be *adjusted* to address the challenges related to bone-implant integration. In terms of unit cell size, the range of 300-500 µm has been reported to be optimal for bone formation [136]. However, 3D printing at this unit cell size scale, particularly for the high porosity values, is challenging as the 3D printed scaffold fails to maintain its structural integrity. Therefore, it is important to identify the minimal unit cell size for different unit cell shapes during the implant design process. Unit cell shape can also alter the deformation mechanism between bending- versus stretching-dominated behaviors, and from there, it also determines damage localization density and failure point [282]. The porosity gradients in hip implants can further enable multifunctionality required from both mechanical and biological aspects, which remains to be explored.

In the present study, we introduce a functionally graded porous Ti6-Al-4V hip implant fabricated by laser powder bed fusion (LPBF), conventionally known as SLM, following a design approach wherein the porosity linearly increases from the center to the surface of the implant (Figure 7.1). In this way, the tissue/implant surface interface is provided with higher porosity associated with enhanced bone ingrowth and aims to improve implant-bone integration. Conversely, the larger relative density deep at the center of the stem axis contributes to the mechanical strength under compressive loads. The implants are compared to those designed with uniform porosity in terms of mechanical properties and fluid permeability. In addition, the LPBF-made implants fidelity is examined to maximize the specific surface area without compromising structural features. Finally, we evaluate the implants in terms of their tissue regenerative capabilities: the implants are incorporated with cell-laden GelMA as a biocompatible and biodegradable matrix to load cells viably into the interconnected pores of the porous structure. The porous structures are then evaluated in terms of their biocompatibility.

7.2. Materials and Methods

7.2.1. Computer-aided design and modeling of porous constructs and implants

Triply periodic minimal surfaces were used to define unit cell shapes in scaffolds and implants. These TPMS geometries can be defined mathematically, explicitly, using Eq. (7.1) as periodic co-continuous 3D shells resulting in two interconnected phases in the design space:

$$\Gamma(\mathbf{r}) = \sum_{l=1}^{L} \sum_{m=1}^{M} \mu_{lm} \cos\left(2\pi\kappa_l (\mathbf{P}_m^T . \mathbf{r})\right) = C \tag{7.1}$$

where $\mathbf{r} = [x, y, z]^T$ is the location vector in 3D space, $\mathbf{P}_m = [a_m, b_m, c_m]^T$ represents the basis vector, κ_l is the scale parameter, and μ_{lm} indicates the periodic moment. The offset value of C is defined as a function of location, which controls porosity over space for designing the scaffolds with graded porosity [12]. The left side of Eq. (7.1) governs the topology of the unit cell shapes. To generate the stereolithography (STL) models for the additive manufacturing process, we followed an image-based approach. The procedure uses a MATLAB routine (available on request) to generate stacked images of the model based on which the STL models were created.

For the porous scaffolds, the stack of binary images representative of TPMS cross-sections were generated via MATLAB routines (available on request) by defining $\Gamma(\mathbf{r}) < 0$ as the solid phase. The cubic scaffolds of 10-mm length were CAD modeled with different unit cell sizes (UC = 1 mm, 2 mm, 3 mm, 4 mm), unit cell shapes (P, G, D), and porosity distributions (Uniform: φ = 0.25, 0.5, 0.75, and gradients: φ_i=0.25, φ_o=0.75), as presented in Table 7.2. The porosity (φ) was defined as the ratio of the volume of the macro-pores to the total volume of the scaffold. Uniform porosity scaffolds were obtained considering constant offset levels. The algorithm for gradient porosity structures used the minimum distance ($D_{\text{boun,min}}$) of each pixel/location with the boundary pixels in the design domain (scaffold/implant cross-section) for each image to determine the offset value. Porosity at the closest locations to the periphery of the construct was fixed to φ_o and changed linearly to φ_i corresponding to the location with the largest minimum distance to the boundary (center of each cross-section) according to Eq. (7.2):

$$\varphi\left(D_{\text{boun,min}}\right) = \frac{\varphi_i - \varphi_o}{\max\left(D_{\text{boun,min}}\right)} D_{\text{boun,min}} + \varphi_o \tag{7.2}$$

Therefore, the offset value C was determined locally according to the porosity calculated using Eq. (7.1).

For the porous implants, the first solid implant models were designed using SolidWorks software (Dassault Systèmes SOLIDWORKS Corp., United States) and exported as STL (Figure 7.2). Using a MATLAB routine (available on request), the solid implant STL model was converted to a binary stack of cross-sectional images ($S_{implant}$). Having the boundary pixels from $S_{implant}$, the images involving the porous regions were incorporated with TPMS-based pore shapes using a Boolean operation. This way, we applied the gradient pattern expressed by the aforementioned equation leading to the final porous implant models ($S_{implant,porous}$). Porous implants were designed with different unit cell shapes (P as stretching dominated and D as bending dominated structure) and porosity distribution (uniform: φ =0.5 and gradient: φ_i=0.25, φ_o=0.75).

7.2.2. Additive manufacturing procedure

The designed STL models were imported to the Renishaw QuantAM software (United States) to set up the printing parameters and laser scanning path. Additive manufacturing was performed using LPBF technology, with Renishaw AM400 equipped with a modulated laser. The printing powder Ti-6Al-4V supplied by Renishaw with 30-µm average size was used to manufacture the implants. The 3D printing was conducted vertically using argon gas as the build process inert gas. The scanning and hatching parameters are given in Table 7.1. The laser spot size was ~70 µm and the build plate temperature was set to 80 ºC. After the printing process finished, the samples were depowdered, and the supports were removed manually.

Table 7.1. Parameters of additive manufacturing.

Printing parameter		Value
Border Parameters	Power (W)	120
	Layer thickness (µm)	30
	Point distance (µm)	45
	Exposure time (µs)	40
	Drill delay time (µs)	10
	Laser scanning speed (mm/s)	900
Core parameters	Power (W)	200
	Layer thickness (µm)	30
	Point distance (µm)	55
	Exposure time (µs)	50
	Drill delay time (µs)	10
	Laser scanning speed (mm/s)	920
Hatching: Borders	Number of borders	2
	Border distance (µm)	100
Hatching: Fill hatch	Hatch offset (µm)	150
	Hatch distance (µm)	100
	Rotation increment angle (˚)	67
	Repetition limit	20
Hatching: Fill hatch pattern	Stripe size (mm)	5

7.2.3. Structural scanning and surface characterization

To evaluate the internal structure and micro-porosity in the manufactured scaffolds, X-ray computed tomography (CT) imaging was performed using a ZEISS Xradia 520 (Versa, Germany) scanner. Image processing and porosity analysis were accomplished using Dragonfly Pro v3.1 (Object Research Systems Inc., Montréal, QC). The scanning was conducted with a voxel size of 20 μm at 10 W and 40 kV. The surfaces of the samples and their fracture surfaces were characterized by scanning electron microscopy (SEM) images taken with a VEGA3, TESCAN (Brno, Czech Republic), instrument. The SEM images were obtained at 20 kV accelerating voltage. The surface roughness (R_a) was defined as the average area per unit length that is off the mean line and measured by profilometry using a three-dimensional laser confocal scanning microscope (LEXT OLS5000, Olympus Corporation, Tokyo, Japan) with a 20× magnification lens. Each scan covered an area of ~260 μm × 260 μm, and to determine the surface values, a Gaussian filter was applied. Surface roughnesses were calculated using dedicated software (Olympus Stream image analysis software, Olympus IMS).

7.2.4. Permeability test

A constant head permeability test setup was used to evaluate the experimental water permeability of the samples. The cubic scaffolds were fixed at the bottom of a water tank (outlet). While the fluid head was kept constant by maintaining the water level, the fluid flow rate under gravity was determined by measuring the volume of the outlet fluid over a course of 30 s. The permeability was calculated using Darcy's equation (Eq. (7.3)):

$$k = -\frac{\mu\,\mathrm{q}}{A\,\frac{\Delta p}{l}} \tag{7.3}$$

where $A = 10\times10\ \mathrm{mm}^2$ represents the scaffold cross-sectional area, $l = 10$ mm is the scaffold height, and $\mu = 1000$ Pa·s defines the viscosity of the working fluid (water), q was substituted with the measured fluid flow rate, and Δp was the hydrostatic pressure due to the level of the water ($h = 50$ mm).

7.2.5. Mechanical compression tests

Quasi-static mechanical compressive tests were performed to determine the mechanical response of the scaffolds and the implants. The scaffolds were compressed via two compressive plates whereas the implants were fixed using a gripper at the bottom gripper that was oriented relative to the implant stem according to the BS ISO 7206-4 standard. The mechanical tests were performed using a universal testing machine (Instron, 8874, USA) equipped with a 25 kN load cell. Compression tests were conducted with a crosshead displacement rate of 0.75 mm/min for both scaffolds and implants. The force and displacement data were registered during compression and used to calculate the stress-strain curves for the cubic scaffolds.

7.2.6. Finite element simulation

The compressive behavior of the implants was simulated and compared with the experimental data. The FE simulations were conducted using Abaqus (Rhode Island, United States) explicit solver. To prepare the FE model, a MATLAB routine (available on request) was developed wherein the stack of images used for CAD modeling were used as inputs to build hexagonal meshes from the material representative voxels in the cross-sectional images. An input file was generated that could be imported in Abaqus for defining model parameters. The models contained between 1,300,000 to 1,500,000 meshes according to a previous mesh convergence study [143]. The bottom base of the implant was fixed, and a rigid plate was defined to simulate the loading in the compression test setup. The constitutive material model for Ti-6Al-4V was taken from our previous work [282]. Further, a damage model was defined based on the Johnson-Cook model where the elements are removed if they exceed the fracture criteria Eq. (7.4):

$$\varepsilon_{failure} = (D_1 + D_2\, exp(D_3\sigma^*)\ \ [1 + D_4 ln\ (\dot{\varepsilon}^*)][1 + D_5 T] \tag{7.4}$$

where D_1, D_2, D_3, D_4, and D_5 represent the material constants. The terms involving D_4 and D_5 were cancelled due to the testing condition (room temperature and similar loading rate). D_1, D_2, *and* D_3 however, which are dependent to the failure strain and stress triaxiality relationships were set to −0.68, 0.73, and -0.25 according to our previous work [282]. σ^* is the stress triaxiality ratio and is defined as $\sigma^* = {}^{\sigma_h}/_{\sigma_q}$ (σ_h: hydrostatic stress and σ_q: equivalent stress).

7.2.7. Live/dead assay

To evaluate biocompatibility and assess the interaction of the implants with cells, a live/dead assay was performed. NIH-3T3 mouse fibroblasts were cultured in 175 cm^2 cell culture flasks while maintaining the cell and medium at 37 °C, 95% relative humidity, and 5% CO_2 in a standard incubator (Thermo Forma, Thermo Fisher Scientific, MA, USA). To prepare the cell culture medium, 10% FBS solution, and 1% penicillin-streptomycin were added to DMEM. The cell density was monitored daily, and the media was exchanged every 2-3 days. Once the cells reached ~90% confluence, the cells were detached from the culture flasks by adding trypsin-EDTA. The removed cells were centrifuged at 1200 rpm for 4 min. Then, supernatant was removed, the cells were resuspended in fresh media and counted using a hemocytometer (Thermo Fisher Scientific, USA).

For the planar static culture experiments, the scaffolds (P0.25-0.75) were first sterilized with an ethanol solution (70 v/v%) for 30 min followed by drying under UV for 1.5 h. Then they were placed in a 24-well plate and submerged in 3 ml cell suspension (1×10^5 cells per well), and the wells were kept in the incubator until they were stained later. For the 3D cell culture, a cell-encapsulated hydrogel was prepared and incorporated into the interconnected macro-pores of the P0.25-0.75 scaffold as follows: GelMA was prepared using a previously described procedure.[146] Briefly, 10 g gelatin was dissolved in 100 ml DPBS, followed by the addition of 8 ml methacrylate anhydride (MA). The reaction was stopped after 3 h and the final solution was lyophilized after 7 days of dialysis. A GelMA solution (10 wt.%) was prepared in cell media supplemented with 0.00692 wt.% Eosin Y as a visible light photoinitiator (excited by visible light at 450–550 nm), 1.33 wt.% TEA as a co-initiator and 1 wt.% VC as co-monomer. Then, the cell-laden hydrogel prepolymer was obtained by suspending the cells in the GelMA solution with a concentration of 1×10^7 cells/ml. One ml cell-laden prepolymer was added to each well in a 24-well plate, and the scaffolds were placed into the wells allowing the prepolymer to fully diffuse through the interconnected macro-pores. The cell-laden GelMA was cured by radiating visible light at an intensity of ~100 mW/cm^2, Genzyme FocalSeal LS1000 Xenon Light (United States). After the hydrogel was cured, the Ti-6AL-4V scaffolds filled with cell-encapsulated GelMA were immersed in fresh media and kept in the incubator for the later live/dead assays.

To test the viability of cells, a 10-ml staining solution of 20 µl ethidium homodimer-1 and 5 µl of calcein in PBS was prepared. The samples were treated with the staining solution at different time points and incubated for 30 min for full infusion into the hydrogel. The solution was then aspirated, and the samples were imaged via a fluorescent microscope (Axio Observer 5, Zeiss, Germany) at excitation/emission wavelengths of ~494/515 nm for calcein and ~528/617 nm for ethidium homodimer-1. The cell viability was calculated using image processing software (FIJI)[283] defined as the ratio of the live cells to the total number of cells.

7.3. Results and Discussion

7.3.1. Porous implant design

The design of unit cell characteristics in porous implants is of utmost importance due to their critical role in biological and mechanical performance. Triply periodic minimal surfaces have received tremendous attention due to their versatility in design, interconnectivity, and smooth curvatures across different porosity levels (φ). Therefore, the hip implant geometries were incorporated with porous architectures with the dimensions represented in Figure 7.2. Distinct unit cell shapes (P, G, D), porosity distribution (uniform, gradient) and levels (uniform: 0.25, 0.50, 0.75, and gradient: 0.25-0.75 linearly varying from the center to the surface) were designed through the computer-aided design (CAD) modeling procedure (see Table 7.2). The local porosity was defined based on the normalized distance of each point with respect to the external boundaries of the geometry at each cross-section of the model.

Table 7.2. Design parameters used for computer-aided design (CAD) modeling of the scaffolds and implants. See Section 4.1 for definitions of the parameters listed here.

Pore shape	$\Gamma(\mathbf{r})$	Porosity distribution	φ_i	$C(\varphi_i)$	φ_o	$C(\varphi_o)$	Sample label
P	$\cos(2\pi x) + \cos(2\pi y) + \cos(2\pi z)$	Uniform	0.25	0.87	0.25	0.87	P0.25
		Uniform	0.5	0.00	0.5	0.00	P0.5
		Uniform	0.75	-0.87	0.75	-0.87	P0.75
		Gradient	0.25	0.87	0.75	-0.87	P0.25-0.75
D		Uniform	0.25	0.43	0.25	0.43	D0.25

	$\cos(2\pi x)\cos(2\pi y)\cos(2\pi z)$ $- \sin(2\pi x)\sin(2\pi y)\sin(2\pi z)$	Uniform	0.5	0.00	0.5	0.00	D0.5
		Uniform	0.75	-0.43	0.75	-0.43	D0.75
		Gradient	0.25	0.43	0.75	-0.43	D0.25-0.75
G	$\sin(2\pi x)\cos(2\pi y)$ $+ \sin(2\pi z)\cos(2\pi x)$ $+ \sin(2\pi y)\cos(2\pi z)$	Uniform	0.25	0.76	0.25	0.76	D0.25
		Uniform	0.5	0.00	0.5	0.00	D0.5
		Uniform	0.75	-0.76	0.75	-0.76	D0.75
		Gradient	0.25	0.76	0.75	-0.76	D0.25-0.75

It is essential to understand the biological and mechanical responses from different unit cell characteristics in the form of design maps that can be used to tune hip implant structures locally. First, the range of porosities for TPMS-based unit cell shape libraries is primarily limited by the loss of interconnectivity and failure of the 3D printing process. At extreme porosity levels, TPMS topologies lose their continuity and turn into multi-phase topologies, limiting their applicable porosity range for interconnected porous scaffolds [143]. In addition, to obtain a high specific surface area favorable for cell differentiation [284],[285], the minimum unit cell size where the 3D printing process can form defect-free unit cell shapes is desired. Hence, here we first focus on uniform porosity scaffolds comprised of patterned representative volume elements (RVE) to determine the printing fidelity, design ranges, and unit cell characteristics with the desired properties. Then, commensurate with those data, we apply functional porosity gradients to the hip implant geometries to evaluate their function *in vitro*. Here, we propose a gradient pattern wherein the porosity at different locations of a cross-section in the implant varies linearly proportional to the distance from the surface of the implant (Figure 7.1(a, b)) which can be fabricated via LPBF process (Figure 7.1(c)). A higher porosity at the region closer to the surface of the implant targets larger permeability and thereby enhanced infusion of cell-laden hydrogels. This arrangement will result in enhanced bone ingrowth (as shown in previously [286],[287]) and hence better implant integration. Lower porosity levels constrained at the deepest central regions of the implant cross-section provide the implant with greater mechanical support.

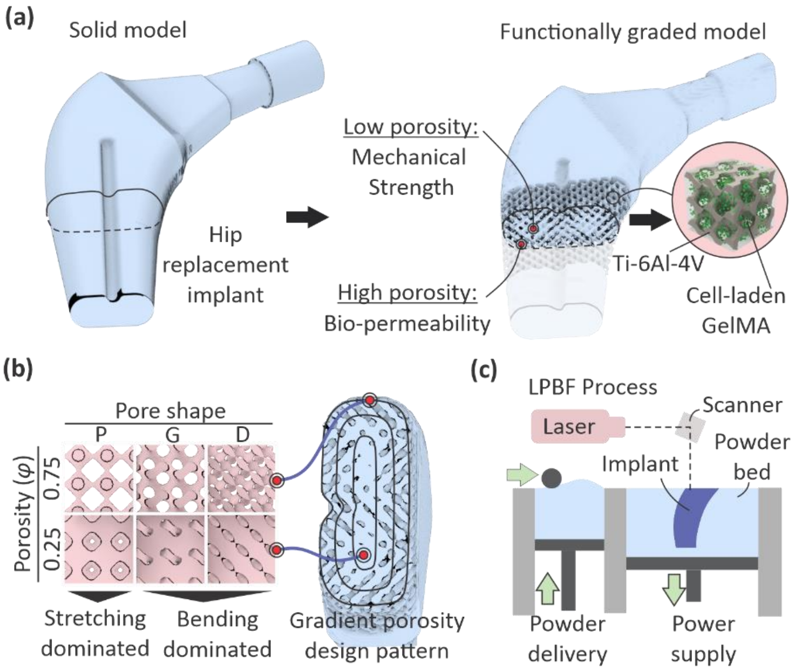

Figure 7.1. Design of multifunctional porous hip implants for additive manufacturing. (a) Schematic illustration of the design approach for gradient porous implants aiming for high mechanical stability and bio-permeability. (b) The library of unit cell shapes (*i.e.*, P, G, and D structures based on triply periodic minimal surfaces (TPMS), topologies) and porosity ranges (*i.e.*, 0.25 and 0.75) applied to define the porosity gradients. (c) Schematic illustration of the LPFB process implemented for fabrication of the functionally graded porous Ti-6Al-4V Hip Replacement Implants.

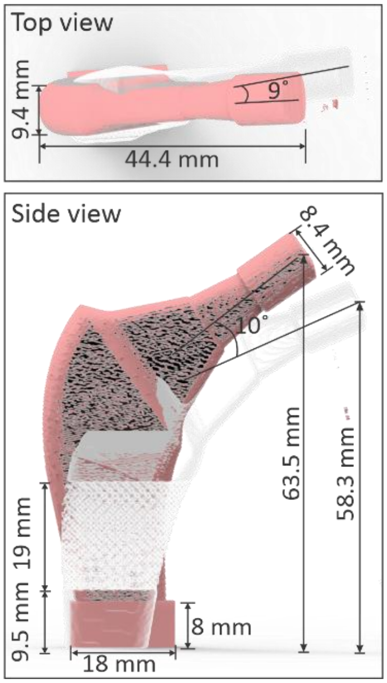

Figure 7.2. Dimensions of the designed and manufactured hip implant structures. Pink model represents the 3D printed implant, which is rotated from the primarily designed (transparent) implant state to simulate the applied loading by the human body during the compression tests (according to the BS ISO 7206-4 standard).

7.3.2. Printability: Maximizing surface area by minimizing unit cell size

Decreasing the unit cell size is one effective way to attain high specific surface areas; however, the limited resolution of additive manufacturing techniques hinders pushing the surface area beyond a specific level. Hence, we designed and additively manufactured scaffolds with unit cell sizes starting from 0.5 mm to 4 mm, to evaluate the printing fidelity across different unit cell characteristics as demonstrated in Figure 7.3(a). All the designs fabricated at 0.5 mm unit cell size failed. The solidified connections in high porosity samples were disintegrated after the support powder was removed. The powder in the low porosity samples was either overheated at the macro-pore regions or stuck inside the macro-pores. This result led to clogging of the macro-pores, and therefore the samples could not be de-powdered. Increasing the unit cell size to 1 mm enhanced the chance of success for some geometry patterns at high porosity, *i.e.*, 0.75; however, de-powdering failure remained an issue for other samples at 0.25 porosity. Further increases in the unit cell size to 2 mm and larger, however, led to robustly successful 3D printing of the porous architectures. Therefore, we set the unit cell size to 2 mm for the remainder of the studies, unless otherwise noted.

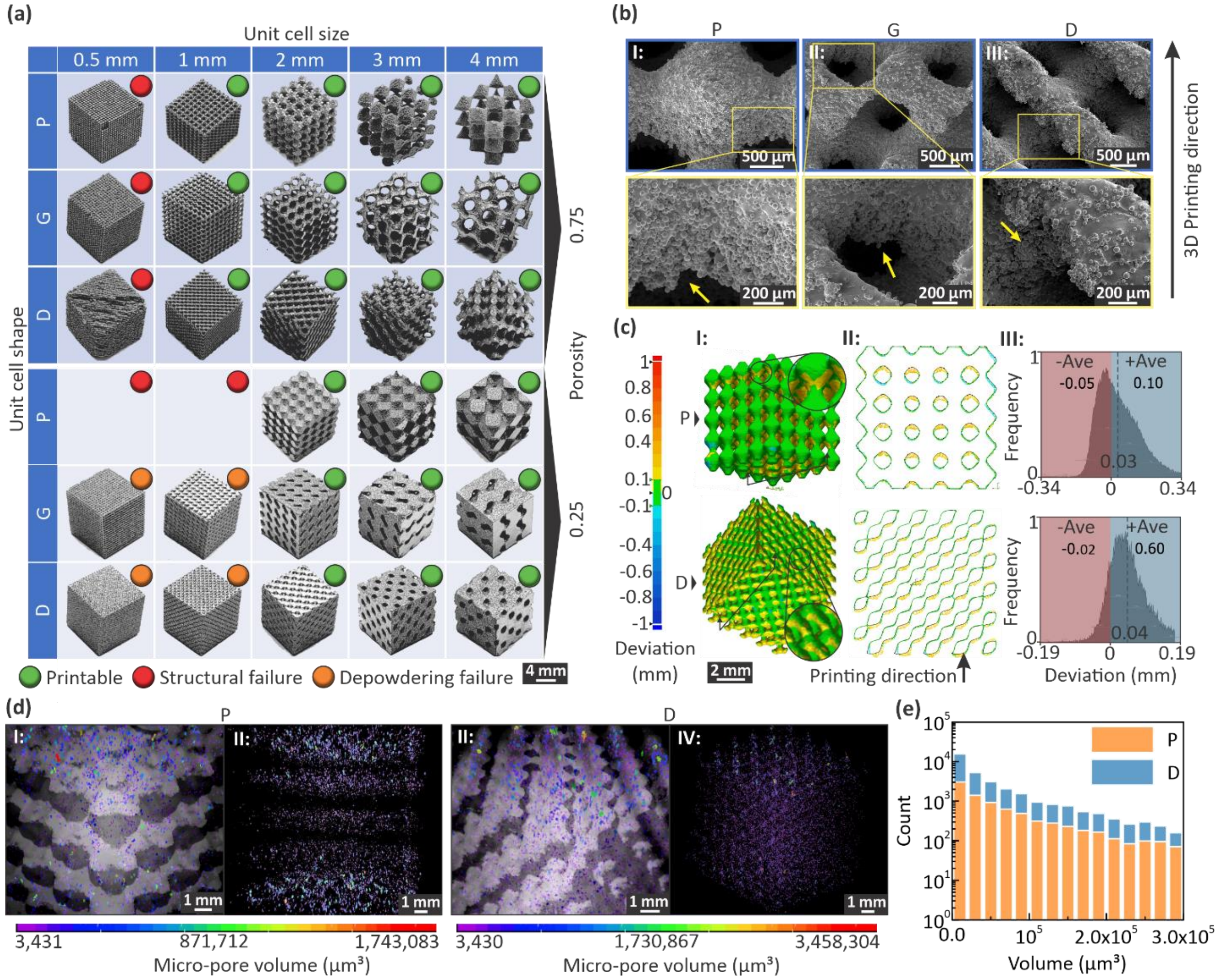

Figure 7.3. Printability and quality control analysis of the additively manufactured porous titanium constructs. (a) triply periodic minimal surface (TPMS)-based scaffold structures 3D printed at different unit cell shapes and unit cell sizes and their potential causes of 3D printing failure. (b) Scanning electron microscopy (SEM) images of the porous scaffold surfaces and representation of the aggregation of bonded powders concentrated at the hanging features. (c) I, II: Deviation maps in cross-sectional planes along the 3D printing direction between the computer-aided design (CAD) models and 3D printed scaffolds (green: regions with deviations below 0.1 mm). Comparing the X-ray imaged scaffolds with the corresponding CAD models demonstrates the embossments facing downward due to the heat concentration, and III: distribution of deviations over the scaffold surfaces. (d) The distribution of the closed micropores in the solid phase of the manufactured scaffolds imaged by X-ray tomography for I, II: P0.25-0.75 and III, IV: D0.25-0.75 structures. (e) Histogram of the micropores in terms of pore volume for P0.25-0.75 and D0.25-0.75 structures.

7.3.3.Printing fidelity and surface morphology

The LPBF-made structures were evaluated with X-ray tomography to compare their topological features to their corresponding CAD designs. Table 7.3 compares the porosities and surface areas of the 3D printed structures with those obtained from the STL models. Porosity was observed to deviate within ~20% of the CAD models. The 3D printed samples had larger values of their surface areas than predicted from the CAD designs, which we attribute to surface roughness effects as well as the powder aggregation in the hanging features. The SEM images of the pore surfaces for different geometries are shown in Figure 7.3(b). The scaffold surfaces are characterized by a layer-by-layer solidified metal pattern bonded with microscale printing powder augmenting the surface roughness (Figure 7.4). The surface roughness was further characterized by confocal laser microscopy, as shown in Figure 7.5. The surface roughness was calculated to be R_a = 36.97 µm on the solid surface of the implants which is in the range of the printing powder particle size.

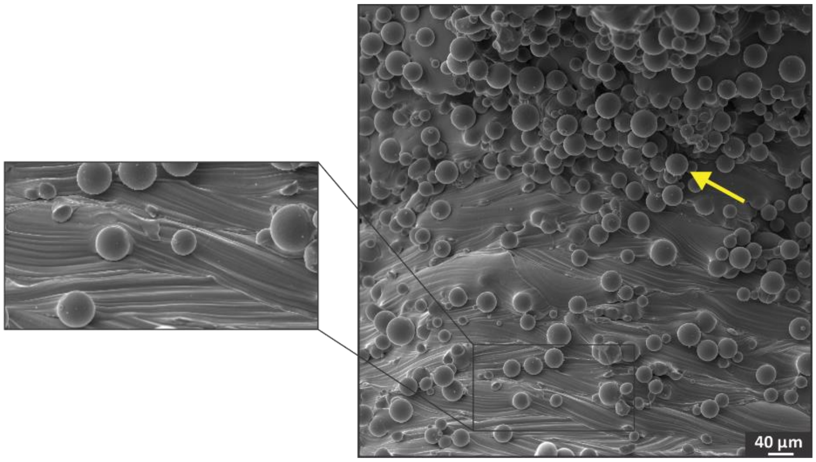

Figure 7.4. Scanning electron microscopy (SEM) images representing the surface morphology of additively manufactured porous constructs (P0.25-0.75). The image demonstrates the layer-by-layer fringes of solidified metal and the bonded printing powder (yellow arrow) on the surface leading to surface roughness in the order of powder size.

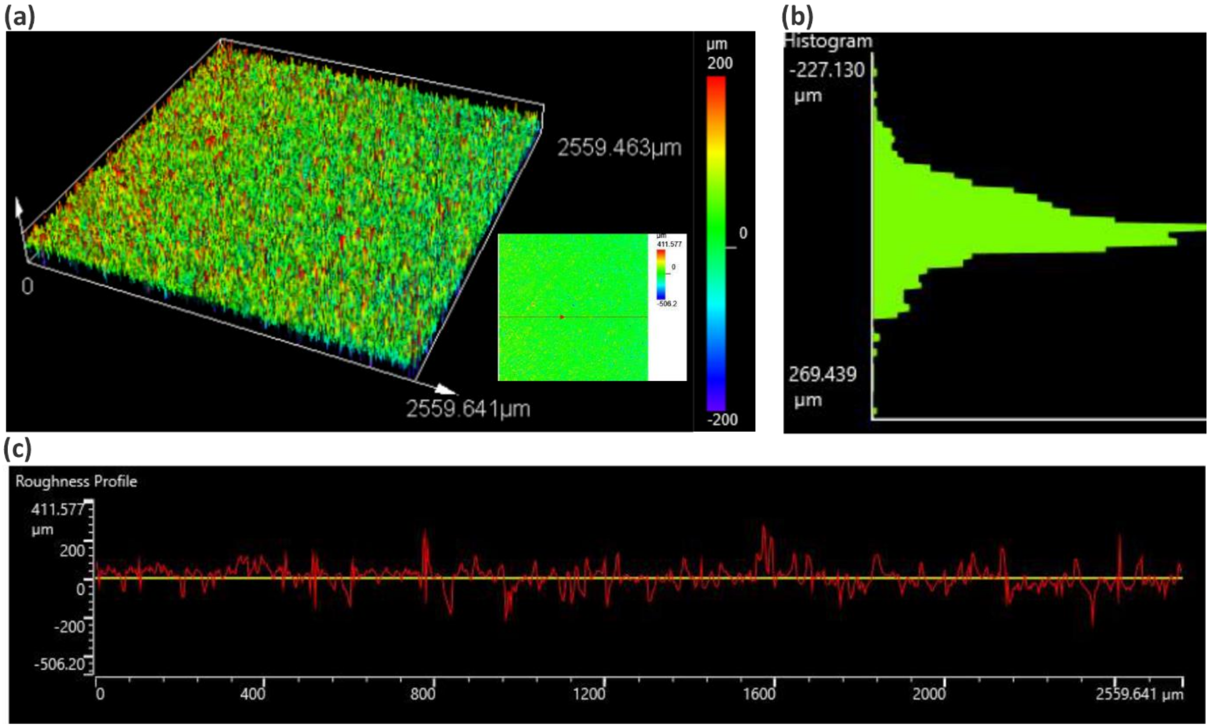

Figure 7.5. The results of confocal laser surface microscopy from the solid surface of the additively manufactured implants. (a) The 3D map and (b) distribution of the roughness over the surface. (c) The surface roughness profile along the direction shown in the inset of (a).

The overhanging features were accompanied by agglomerated powder particles due to the excessive heat-affected zone. In essence, the lower thermal conductivity of the powder (compared to that of solid metals) results in concentrated heat around the molten pools that finally lead to a gravity-driven downward overflow of molten pools due to the lack of sufficient cooling. This process accounts for the formation of sag (dross) defects, and consequently, significant localized deviations from CAD models, where overhanging geometries are present (see Figure 7.3(c) and Figure 7.6(a)). This phenomenon explains the larger surface areas and smaller unit cell pore sizes and porosities of the printed structures compared to CAD models. Similarly, we observed discrepancies in the unit cell pore sizes, as shown in Figure 7.6(a). The embossments deviated from the unit cell pore sizes for the fabricated models up to ~340 µm and ~190 µm for the P:0.25-0.75 and D:0.25-0.75, respectively. The range of the cell size for the fabricated scaffolds was originally designed to be ~600-1100 µm for P:0.25-0.75 sample, which was reduced by ~20-30% down to ~400-900 µm due to the bonded printing powder aggregates. The deviation maps at the cross-sectional plane perpendicular to the printing direction did not show significant deviations (Figure 7.6(b, c)).

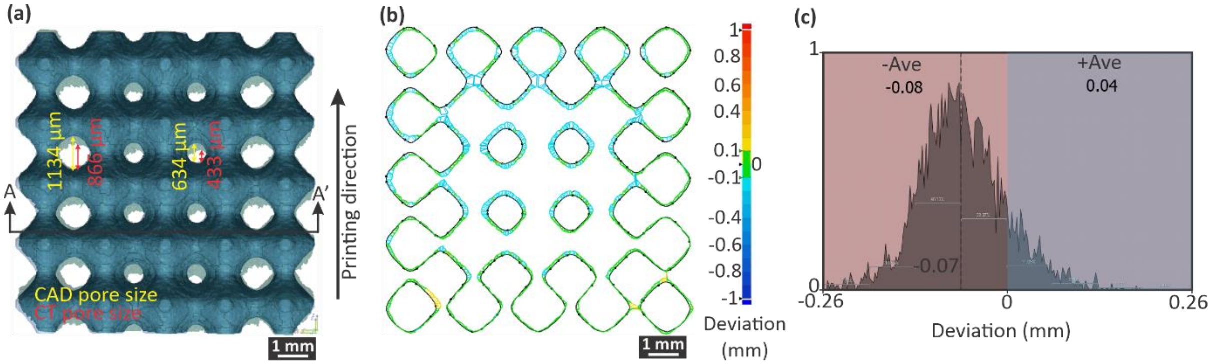

Figure 7.6. (a) Changes of the pore size in P:0.25-0.75 sample due to the embossments at regions with hanging features. (b) Deviation of the fabricated scaffolds (P0.25-0.75) from the computer-aided design (CAD) models in a cross-section (A-A') (shown in (a)) perpendicular to the 3D printing direction, and (c) the distribution of deviations over the scaffold surface.

The X-ray images taken were also indicative of the micro-porosity due to the formation of keyholes (Figure 7.7, Figure 7.3(d, e)), explained by the high energy intensity input and laser interaction time [288]. The micropore volumes ranged between 3.4×10^3 µm^3 and 3.5×10^6 µm^3 and were found to be more localized at the periphery of the scaffolds (Figure 7.7(a)). In addition, a larger number of such voids and defects were observed in the D structure compared to P. The results showed that the accumulative volume of the micro-porosity for the gradient scaffolds of the P and D geometries are 1.743×10^6 and 3.458×10^6 µm^3, which are almost two orders of magnitude smaller than the total volume of macro-pores, *i.e.*, 0.732 and 2.207 mm^3, respectively. The total micro-porosity volume ratio was in the range of ~0.4-0.5% of the solid volume (see Table 7.3). Note that the keyhole effect is more prominent for the porous structures due to their high specific surface areas. This is because we found the micro-porosity volume ratio in the solid cubic samples (*i.e.*, ~0.21%) was half of those of the porous constructs.

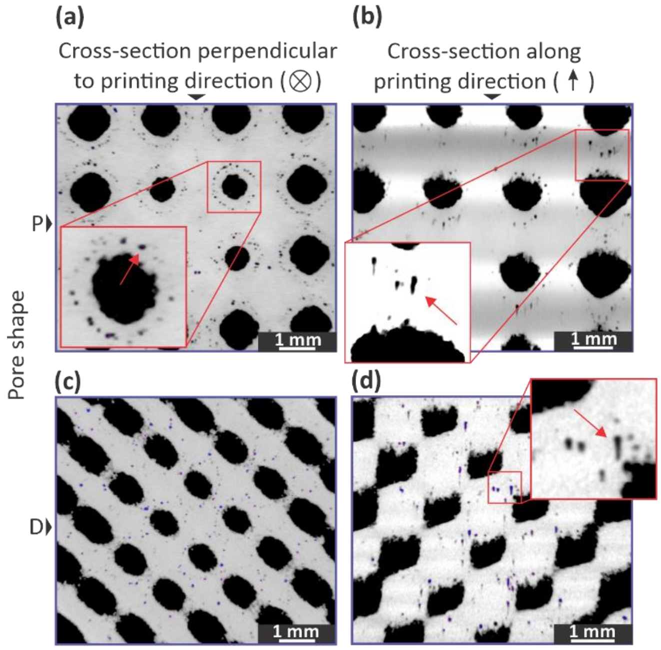

Figure 7.7. The microporosity and keyhole defects present in the solid phase of the scaffolds. X-ray images at cross-sectional planes perpendicular and along the printing directions for (a, b) P:0.25-0.75 and (c, d) D:0.25-0.75, respectively.

Table 7.3. Comparing the topological properties of the computer-aided design (CAD) models and their corresponding additively manufactured cubic porous scaffolds. The micro-porosity volume (V) involves the defects within the solid phase due to *e.g.*, keyhole effects.

Sample (cubic scaffold)	Relative density (ρ)			Volume (V)			Micro-porosity (%)	Surface area (S)		
	CAD	X-ray	Error (%)	CAD (mm^3)	X-ray (mm^3)	Error (%)		CAD (mm^2)	X-ray (mm^2)	Error (%)
P0.25-0.75	0.42	0.46	9.52%	422.79	460.31	8.87%	0.47%	1201.41	1416.47	17.90%
D0.25-0.75	0.42	0.51	21.43%	420.72	518.41	23.22%	0.42%	2046.54	2579.33	26.03%

7.3.4. Fluid permeability analysis

Fluid permeability is an important parameter combining the geometrical characteristics to quantify and to predict cells' and nutrition's ability to diffuse deep into the scaffold macro-pores. Previous reports have demonstrated the association of higher permeability with enhanced bone regeneration [289]. Fluid permeabilities were experimentally measured for the scaffolds (Figure 7.8(a)). Figure 7.8(b) represents the effect of the unit cell size on water permeability. Permeability varied over an order of 10^{-9} to 10^{-11} m^2. The increased permeability with unit cell size was due to the expanded unit cell pore sizes and decreased interfacial surface area with the fluid flow. The sensitivity of permeability to the unit cell size was less prominent for structures with higher porosity (*i.e.*, 0.75) at which no meaningful difference was observed between different geometries. The unit cell shape was found to play a more significant role at low porosity (*i.e.*, 0.25); G was found to be the most permeable structure. We explored the permeability-porosity relationships in Figure 7.8(c) for samples with a fixed 2 mm unit cell size. Increasing porosity results in an overall increase in permeability. Unit cell shape did not appear to have any significant effect on the measured permeability values. However, the samples with graded porosity distribution showed 60% improved longitudinal permeability compared to the uniform porosity counterparts with similar average porosity. We examined the gradient scaffolds for their transverse permeability (Figure 7.8(d)). The results indicated lower transverse permeability in the same order as their corresponding uniform porosity scaffolds. We attribute this result to the distance-to-center-based (radial) distribution of porosity (when the center is denser) topologically imposing a larger area of low porosity flow-resistance in the transverse direction along the path of fluid flow compared to when fluid flows along the longitudinal direction. Scaling analyses of the permeability showed that the empirical equations could well-describe the permeability-volume fraction relationships (R^2>0.94), as presented in Table 7.4. The power law was scaled with an exponent of ~2.3-4.0 that falls within the range reported in our previous work [240] for polydimethylsiloxane scaffolds with similar geometries.

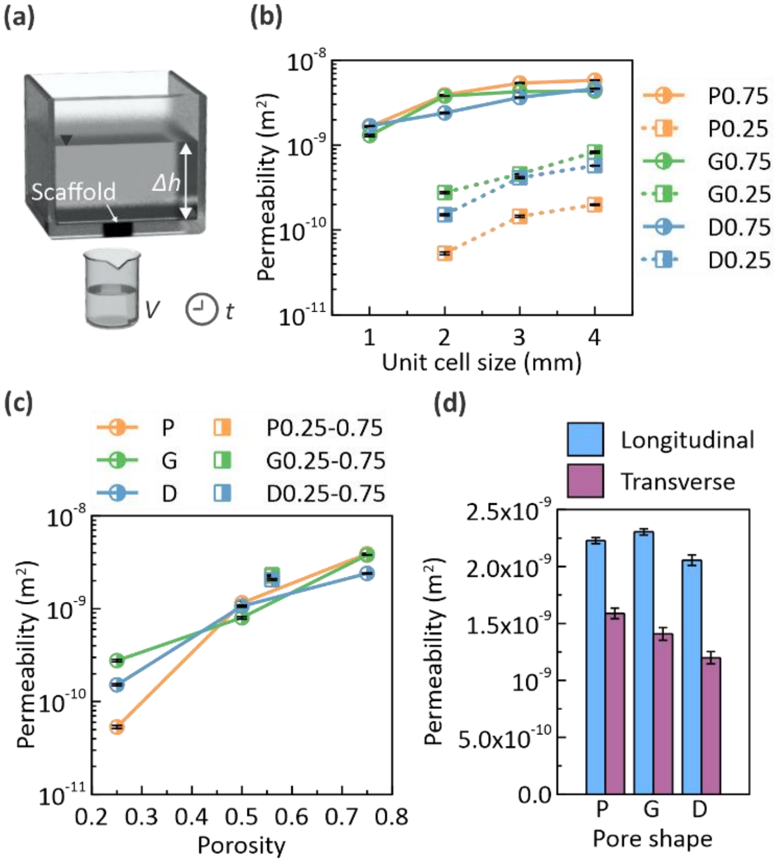

Figure 7.8. Permeability analysis of the cubic scaffolds. (a) Schematic illustration of the constant head permeability test setup. (b) The results of permeability for the scaffolds with different unit cell shapes, porosity, and unit cell sizes. (c) Permeability-porosity relationships for the P, G, and D structures, comparing uniform and gradient porosity distributions. (d) Comparing permeability values measured along the longitudinal (the direction along which porosity remains constant), and transverse (the direction along which porosity changes) directions for cubic scaffolds.

Table 7.4. The scaling analysis of the elastic properties and permeability as a function of porosity.

Fitting Equation	$E(MPa) = A(1-\varphi)^n$			$\sigma(MPa) = B(1-\varphi)^m$			$K(m^2) = C(\varphi)^p$		
Unit cell shape	A (MPa)	n	R^2	B (MPa)	m	R^2	$C\ (m^2)$	m	R^2
P	3770	1.05	0.9607	593	1.69	0.9643	1.42E-08	3.97	0.9910
G	3896	0.90	0.9921	449	1.43	0.9843	5.44E-09	2.55	0.9931
D	3112	0.62	0.9991	485	1.41	0.9973	5.74E-09	2.29	0.9348

7.3.5. Mechanical properties of porous scaffolds

The compressive behavior of the scaffolds with different unit cell sizes along with their failure mechanisms, are illustrated in Figure 7.9. The stress-strain curves in all cases start with a linear elastic region up until the first fracture failure at the scaffold strength point (see Figure 7.9(a)). After that, the typical stress fluctuations for porous materials were observed under the progressive multistep failure with compression. For P, most samples catastrophically failed once they reached the yield point. Smooth fluctuations were recorded for G; while for D, a high magnitude of stress changes was observed. Due to the brittle nature of failure in the scaffolds, most samples were shattered during the deformation. Therefore, none of them entered the post-plateau strain hardening densification region over the applied compressive strain. The elastic properties for different geometries and unit cell sizes are demonstrated in Figure 7.9(b, c) and Figure 7.10. The results do not suggest a significant dependence of the unit cell size on the elastic properties. The structure-property relationships for mechanical properties in terms of the volume fractions are presented in Table 7.4. Despite the obvious improvement of the elastic properties with the volume fraction, the results indicate larger mechanical properties (along the longitudinal direction) for those of graded scaffolds compared to the uniform porosity samples with similar average porosity (Figure 7.9(d, e)). This anisotropy means that the strengthening effect of the denser center not only compensates the weaker regions with high porosity at the periphery of the scaffold, but it also improves the overall mechanical stability compared to the uniform porosity distributions. This observation is in line with the fact that the mechanical properties in porous structures are scaled with relative density with a power of greater than 1 [145].

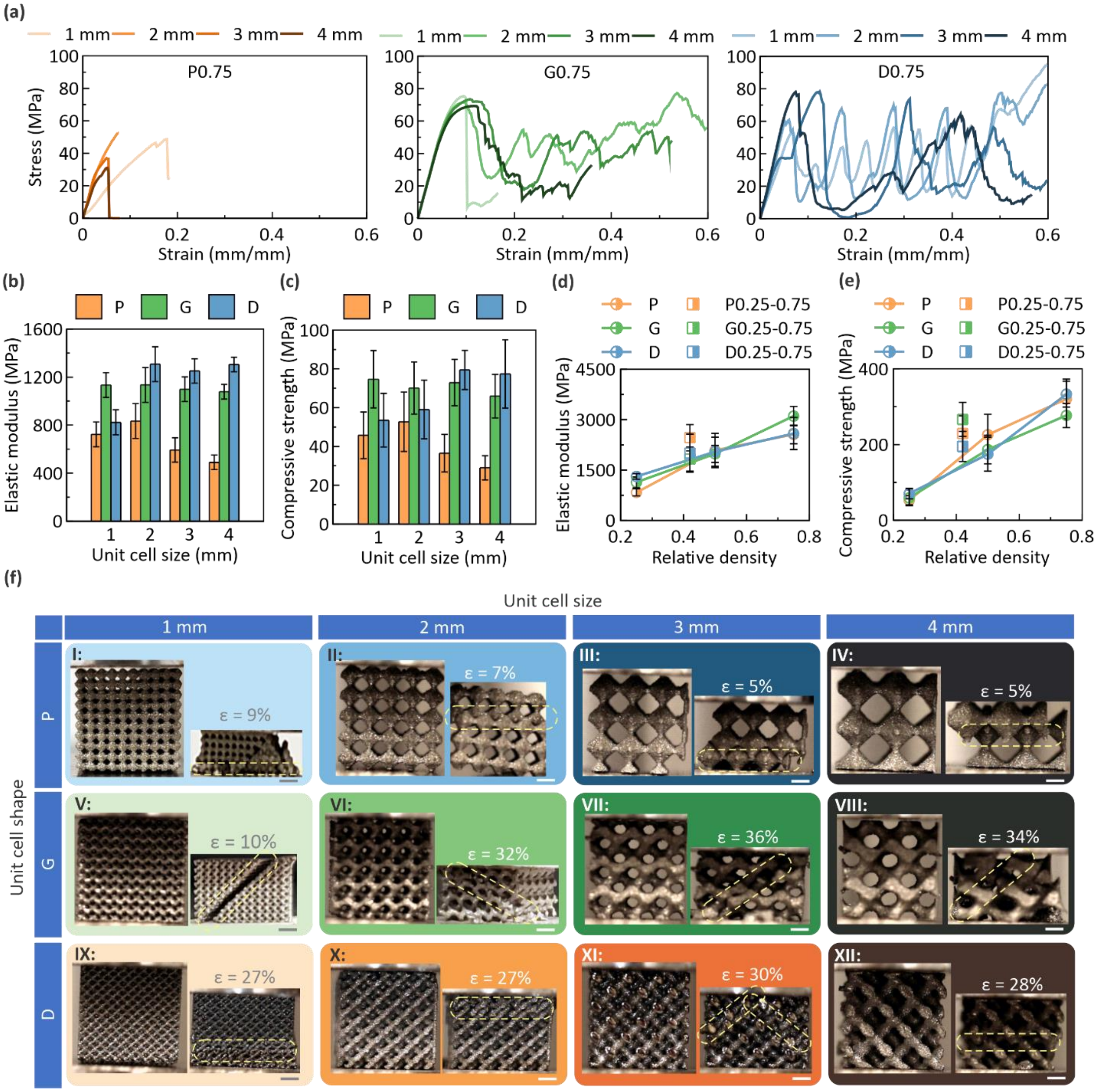

Figure 7.9. Characterization of the cubic porous scaffolds under compressive loading. (a) The results of compressive stress-strain curves for the scaffolds with the P, G, and D unit cell shapes at 0.75 porosity and different unit cell sizes. (b) Elastic modulus and (c) compressive strength resulted from the stress-strain curves for samples with 0.75 porosity. (d, e) Elastic modulus and compressive strength as a function of porosity for the uniform and gradient porosity distributions in the 2 mm unit cell size. (f) Failure mechanism of the cubic scaffolds (0.75 porosity) under compressive deformation before and after fracture for scaffolds representing bending dominated and stretching dominated failure patterns.

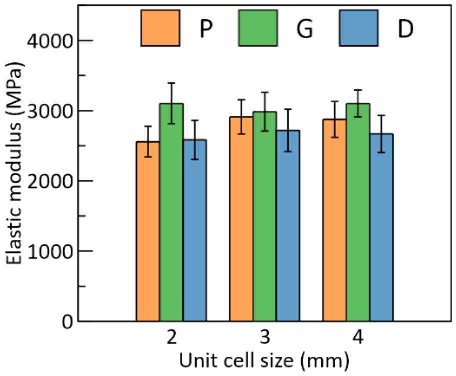

Figure 7.10. The results of the elastic modulus for different unit cell sizes of the P, G, and D structured cubic scaffolds at 0.25 porosity.

7.3.5.1. Compressive deformation mechanism of porous scaffolds

The analysis of deformation mechanisms can give valuable input for the topology optimization techniques that focus on strengthening the vulnerable regions of the porous construct. Besides, deformation localization can influence the mechanobiological responses of the cells and their growth patterns. The high porosity scaffolds' failures were monitored during the compressive deformation (see Figure 7.9(f)). From a topological standpoint, the P structure at high porosity involves narrow linkages (struts) connecting at the thick joints. Upon applying compression, the structure shows stretching-dominated deformation mode. For all unit cell sizes, the unbalanced distribution of material around the linkages imposes the highest stress concentration over the thinner sections of the linkages. Subsequently, buckling of struts led to the simultaneous catastrophic failure of layers and thereby the collapse of the first layer in each sample (Figure 7.9(f)I-IV). Due to the geometrical heterogeneity of P at high porosity and the associated failure mechanism, the structures experienced early catastrophic failures and therefore they did not have post-yield plateaus (Figure 7.9(a)). The bending-dominated geometries (D and G), however, exhibited a different deformation pattern. Failure for G was accompanied by a global 45˚ shear band formation (Figure 7.9(f)V-VIII) consistently across the unit cell sizes. The failure in the G and D structures were characterized by bending-dominated deformation of the internal struts and linkages. The failure patterns for D varied with the unit cell size. Horizontal bands of failure appeared in conjunction with the progression of a layer by layer failure with compression (see

Figure 7.9(f)IX, X, XII), each of which corresponds to a peak in the stress-strain curves. The failure pattern was altered at the 3 mm unit cell size, where 45° shear bands were developed, as indicated in Figure 7.9(f)XII.

7.3.5.2. Compressive response of porous hip implants

With insight into the compressive behavior of the cubic porous scaffolds and the positive effects discovered of functionally graded porosity designs on their mechanics and permeability, we assess the compressive response of the hip implants (under bodyweight simulating loads) with incorporated porous designs to evaluate the unit cell shape (P and D representative of the stretching-dominated and bending-dominated architectures, respectively) and porosity distribution (uniform versus gradient) effects (see Figure 7.11). First, note that the overall surface area of the implant was improved by 65% and 122% for the P and D structures, respectively, compared to the conventional solid implant design (Figure 7.11(a)). These figures can be further improved by involving a larger portion of the implant in the porous design. The results of the force-displacement data, along with the extracted elastic properties, are shown in Figure 7.11(b, c). The force-displacement patterns (Figure 7.11(c)) involved an elastic region that was followed by an abrupt stress drop, and thereafter, a further gradual decrease with the progression of failure. In terms of compressive strength, the results for the uniform and gradient porosity distribution did not show a meaningful difference for the P and D architectures; however, based on the results of Figure 7.8(c), the gradient design is featured with a highly improved permeability (about 140% for D and 277% for P structures) at the tissue interface that can promote the potential for implant integration and therefore long-term stability of the implant. Although introducing porosity to the implants has diminished the overall mechanical strength compared to the solid model, strengths of the solid implants were nonetheless sufficient to resist the body weight and loadings applied during daily activities. Note that the results represent the downscaled porous implant models and the strength further increases for implants in larger, practical scales. The results suggest the critical effect of unit cell shape, which increases our appreciation of opportunities in using additive manufacturing techniques here. Interestingly, despite stretching-dominated structures (such as P) being known for larger compressive strengths [290],[291] in this loading configuration, the D structure with a bending-dominated deformation mechanism has shown more promise in both mechanical strength and deformability, in addition to providing larger specific surface areas.

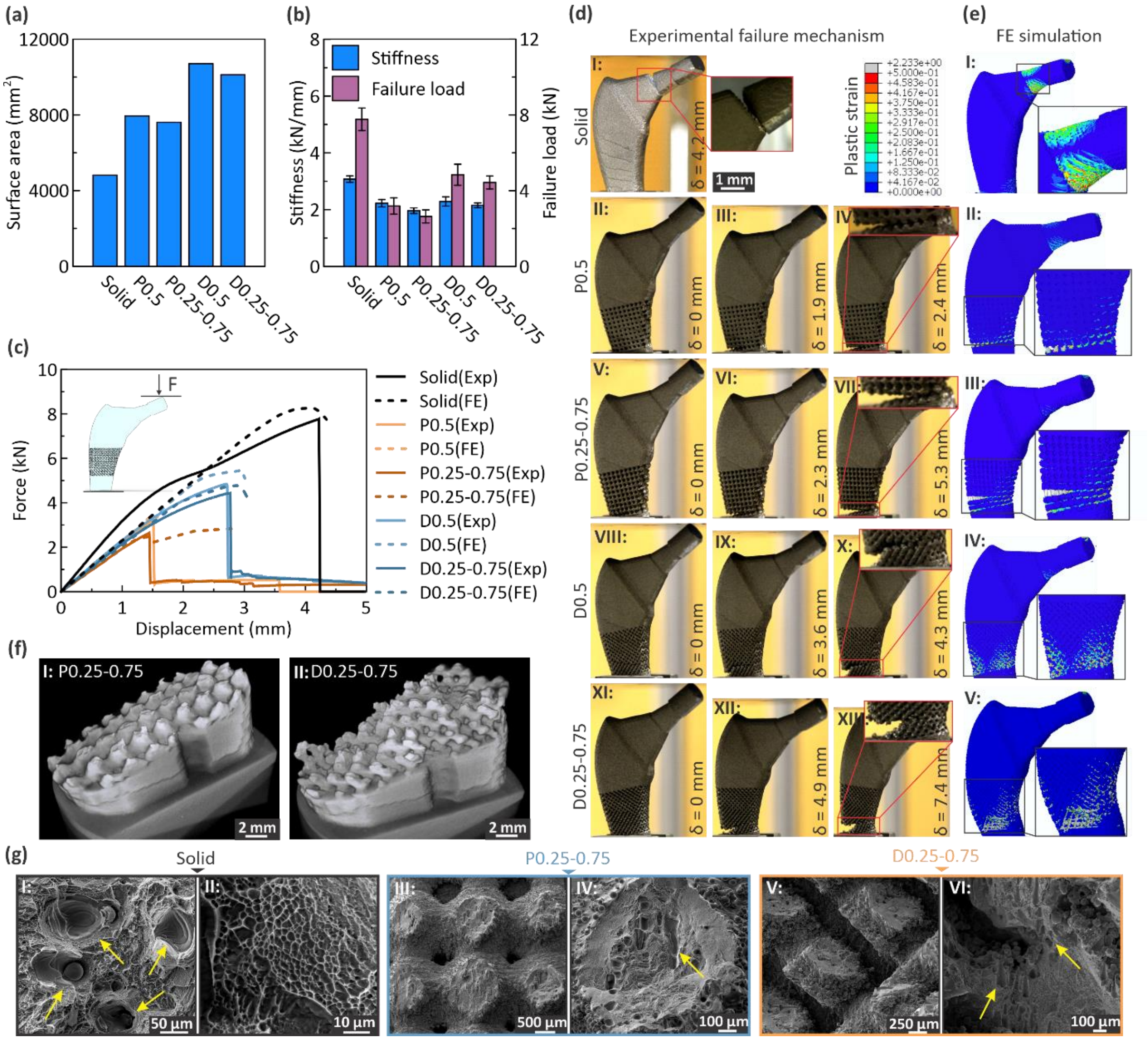

Figure 7.11. The compressive responses and physical properties of the additively manufactured hip implants. (a) Comparing the implant (a) surface area and (b) elastic properties for the solid models versus the porous designs with the stretching- and bending-dominated structures (*i.e.*, P and D, respectively) with the uniform and gradient porosity distribution. (c) Experimental and numerical force-displacement results predicted by the finite element model. (d) Experimental and (e) finite element (FE) representation of the deformation and failure mechanisms of the implants under compression. (f) Computed tomography (CT) imaging of the fracture surfaces of the implants with I: P0.25-0.75 and II: D0.25-0.75 architecture. (g) Scanning electron microscopy (SEM) images of the fracture surfaces for the solid and porous (P0.25-75 and D0.25-75) implants suggesting the presence of voids and structural defects (keyholes) at the surfaces of fractured struts.

7.3.5.3. Failure of hip implants

As opposed to the porous scaffolds where the entire construct was uniformly subjected to uniaxial compression, compressive loads on the implant bend the porous region on the stem and thereby introduce compressive *and* tensile regimes. The experimental and numerical failure mechanism for the implants is represented in Figure 7.11(d, e), respectively. While the solid sample failed at the implant stem neck (Figure 7.11(d)I), the failure in porous implants occurred in the porous region. The crack propagation initiated from the region close to the implant base (close to the clamping site) at the tensile region. The mechanism of failure was found to be similar for different porosity distributions, but more sensitive to the unit cell shape. In the P structure (Figure 7.11(d)II-VII), the narrow linkages fractured at the tensile region one after another, in correspondence with the failure mechanism observed for the P structured scaffold constructs. In the D structure, despite the crack starting from the same location as P, the propagation of failure shifted towards the upper layers, due to the original orientation of the internal struts relative to the loading direction (Figure 7.11(d)VIII-XIII). The above-mentioned failure patterns are observed in X-ray imaging from the fractured parts, as shown in Figure 7.11(f). The fracture surface's topology was characterized by SEM images, as shown in Figure 7.11(g) and Figure 7.12. The images indicate the presence of keyhole voids that likely contributes to crack progression (Figure 7.11(g)I, IV, VI, and Figure 7.12(a)II and Figure 7.12(b)IV). Additionally, binding of the Ti-6Al-4V powders could cause sharp edges and stress concentrations and therefore lead to crack initiation. There was also evidence of dimple formation on the fracture surface, which is indicative of ductile deformation as a part of the failure mechanism (Figure 7.11(g)II and Figure 7.12(a)IV, and Figure 7.12(b)III).

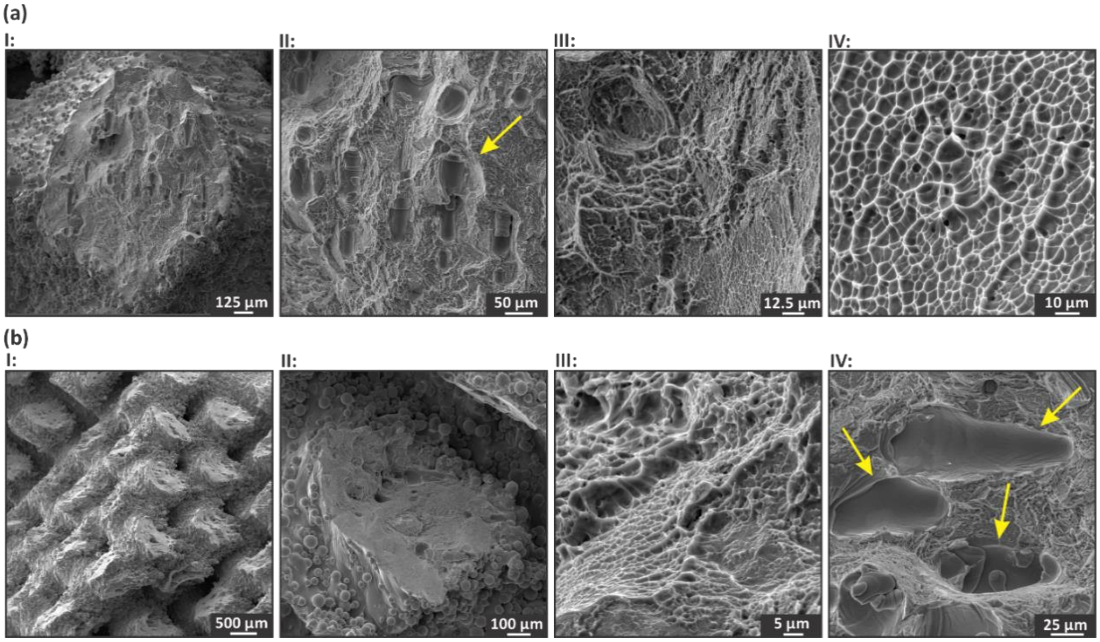

Figure 7.12. Scanning electron microscopy (SEM) images of the fracture surfaces for (a) P0.25-0.75 and (b) D0.25-0.75 samples. The fracture surfaces are characterized by keyhole void defects ((b)IV)) and ductile deformations ((a)IV)).

7.3.6. Finite element simulation

Finite element analyses were performed to evaluate the numerical models and the Johnson-Cook damage model in predicting the mechanical properties of the scaffolds. Figure 7.11(c) compares the computational force-displacement results (obtained with the Johnson-Cook damage model) with the experimental data. The calculated mechanical properties are also given in Table 7.5. As seen, the predicted results are in good agreement with the experimental data where the predicted and measured elastic properties are within ~13%. The computational deformation and damage localization for a perfect plastic material model (Figure 7.11(e)) and Johnson-Cook damage model (Figure 7.13) were obtained for the designed implants. The high damage density for the solid implant in both deformation models is in agreement with the experimental observations (Figure 7.11(e)I). In the P structure designs (Figure 7.11(e)II, III, and Figure 7.13(a)), successive failures of connections in the tensile region corresponded to the experimental failure mechanism shown in Figure 7.11(d)II, III. Damage localization for the scaffolds architected with D was followed by the formation of 45° shear bands in both gradient and uniform porosity samples (Figure 7.11(e)IV, V, and Figure 7.13(b)) that matched with the corresponding experimental observations. The computational results confirm the great potential of the FE models in predicting the mechanical behavior of the porous hip implants, and therefore, it can serve as a useful tool for design optimization of the internal porous architectures for high mechanical performance.

Table 7.5. Comparison between the elastic properties of the hip implants obtained from the finite element (FE) simulation with Johnson-Cook damage model and the experimental data.

Sample	Stiffness			Failure load		
	Experiment (kN/mm)	FE (kN/mm)	Deviation (%)	Experiment (kN)	FE (kN)	Deviation %
Solid	2.62	2.30	12.21%	7.77	8.27	6.46%
P0.5	2.23	2.30	3.32%	3.19	3.48	9.06%
P0.25-P0.75	1.96	1.92	2.21%	2.64	2.84	7.53%
D0.5	2.29	2.25	1.67%	4.84	5.45	12.60%
D0.25-D0.75	2.15	2.07	3.84%	4.43	4.77	7.57%

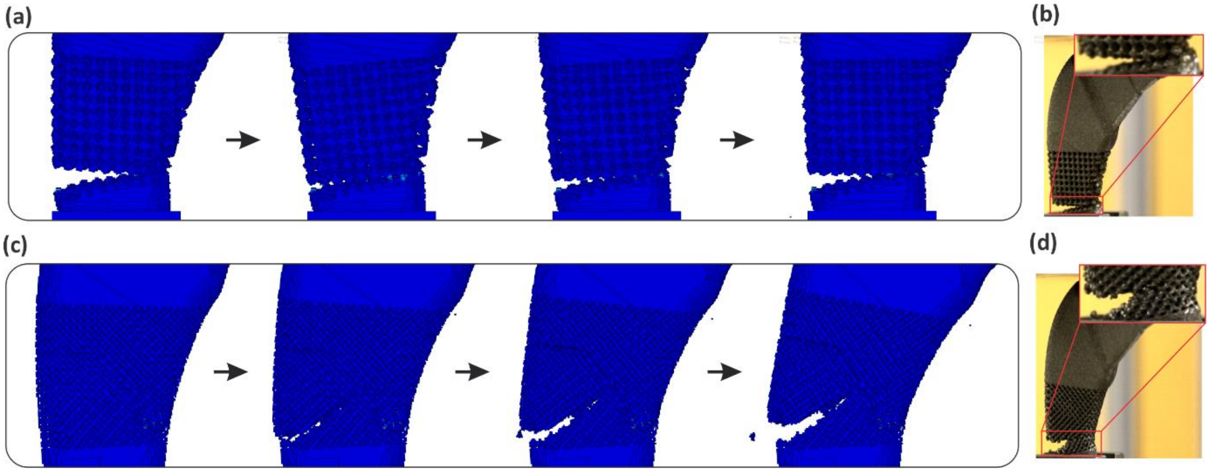

Figure 7.13. Comparison of experimental failure with the numerical finite element (FE) results of deformation mechanism obtained by the Johnson-Cook failure model. Deformation for P0.25-0.75 obtained by (a) FE and (b) experimental compression and D0.25-0.75 obtained by (c) FE and (d) experimental compression.

7.3.7. *In vitro* biocompatibility study

As a proof a concept, we evaluated the *in vitro* biocompatibility of the implants by infilling the interconnected macro-pores of the porous constructs with a cell-laden hydrogel and exposing the Ti-6Al-4V surface to the fibroblast 3T3 cell line suspension. Figure 7.14(a) shows the results of the live/dead assay for the scaffold (P0.25-0.75 as an example) exposed to the cell-medium suspension. The results suggest adherence of the cells to the scaffold surfaces due to the additively manufactured metal constructs' intrinsic surface roughness. The surface roughness resulted from binding of the Ti-6Al-4V printing powder particles provided favorable conditions for the cells to be trapped into the free gaps between the printing powders. The biocompatibility studies for the cell-laden GelMA inside the macro-pores are represented in Figure 7.14(b), which indicate viabilities over 90% (see Figure 7.14(c)), confirming biosafety and cell-friendly characteristics of the materials and procedures. The procedure for delivering the cells deep into the scaffold is assisted by the permeable unit cell shapes at the surface of the scaffold. This method allows the incorporation of high cell densities (1×10^7 cells/ml) to be integrated within the scaffold structure by simple casting. Also, since no shear stress is applied to the cells (which is common in other techniques such as direct bioprinting due to the injection process), high viability was maintained [292]. We note that the hydrophilic nature of titanium facilitated diffusion of the cell-laden prepolymer without the formation of defects and bubbles.

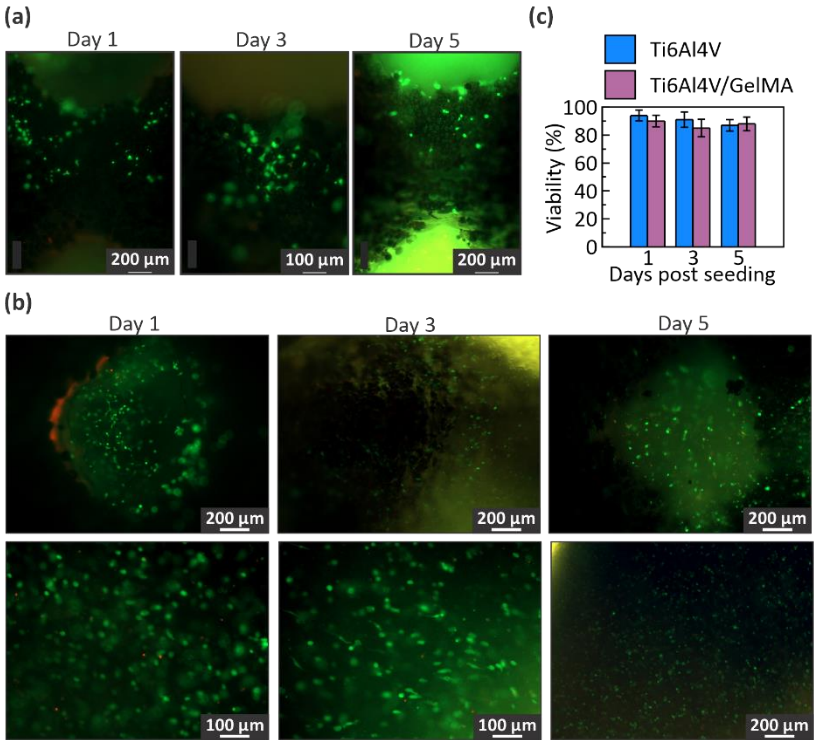

Figure 7.14. ***In vitro*** **live/dead biocompatibility study of the additively manufactured porous constructs (P0.25-0.75) incorporated with 3T3 fibroblast cells and cell-laden hydrogel matrices (green: live and red: dead**

cells). (a) Live/dead images of the cells coated on the surface of porous constructs representing the cells trapped in the gaps between the printing powder. (b) Fluorescent images of cell-laden gelatin methacryloyl (GelMA) hydrogel matrix filling the interconnected macro-pores of the porous constructs, and (c) the results of viability for cells coated on the surface of porous constructs (labeled as Ti-6Al-4V in the legend) and cell-laden GelMA (labeled as Ti-6Al-4V/GelMA) over the course of 5 days.

7.4. Conclusions

This study explores efficient approaches to design and to manufacture next-generation gradient porous implants that target better long-term integration with the surrounding tissue. Understanding the basic properties from these cubic scaffolds can be translated to tune locally functional implants with engineered internal unit cell shapes. From the perspective of printability, the current technology allows printing customized unit cell shapes with high specific surface areas (with a unit cell size threshold of 2 mm) that is desired for cell ingrowth. On the other hand, the surface roughness resulting from the agglomeration of printing powder not only enhances the specific surface area but also encourages the cells to cover the implant surface as they are trapped within the gaps between the particles. The gradient porosity design introduced in this work significantly promotes fluid permeability at the tissue interface (leading to more desirable conditions for bone ingrowth) while maintaining (for implants) or improving (for scaffolds) the overall mechanical elastic properties. The interconnectivity and high permeability of the scaffolds with gradient porosity enabled facile diffusion of cell-laden hydrogels and thereby the potential for delivery of cells and biomolecules into the porous constructs. In addition to porosity and its distribution patterns, unit cell shape was found to have significant effects on the mechanical response of the implants. As opposed to reports indicating greater mechanical strength for stretching-dominated architectures (such as P) under uniaxial compression, bending-dominated architectures (such as D) were associated with greater strength and deformability, when it comes to complex loading scenarios such as those in total hip implants. We also demonstrated the potential of FE simulations for reliable prediction of the elastic properties of implants, which can be of great use for integration with optimization algorithms based on big data analysis tools as well as machine-learning-based design procedures.

Chapter 8. Conclusions and Future Work

8.1.Conclusions

In this research, material jetting of high viscose conductive composite inks for the development of flexible electronics was discussed. However, the flexibility of 3d printed silicone-based sensors was diminished due to mixing with conductive additives. Besides, 3D printing of complex and overhanging architected elastomeric structures is challenging due to the viscose nature of silicone. Hence, novel template-assisted technologies were introduced for fabricating architected structures for healthcare applications. Thus, the following conclusions and achievements can be drawn from this thesis:

- Drop-on-demand material jetting was employed for high-speed 3D printing of sandwiched carbon fiber-silicone (S-MCF/SR) sensors. The composite ink was optimized and carbon fiber concentration of 30 wt.% showed printability, conductivity, and UV crosslinking. S-MCF/SR sensors showed a relative resistance change up to ∼40 under cyclic stretching with a strain amplitude of 10%. The proposed sensors were used to detect index finger and arm motions as showcases.
- A novel template-assisted 3D printing of porous silicone constructs through the low cost and accessible extrusion 3D printing of plastic molds was proposed. The on-demand shrinking behavior of the silicone-based elastomers was exploited to enable 3D printing of the fine porous scaffold structures at a larger scale compatible with the resolution of extrusion plastic 3D printers. The high shrinking ability of the silicone constructs (up to ~70% volumetric shrinkage) allowed forming the silicone constructs with pore sizes in the range of 500–600 μm. The fabricated silicone constructs showed full strain recovery under extreme compressive loadings, and the biocompatibility confirmed its safety for potential use as tissue constructs.
- A novel accessible and low-cost fabrication method was introduced for the development of 3D architected high-flex structures for sensing applications. Since a thin layer of graphene was embedded within the porous silicone surface, the sensors showed high

flexibility and strain recovery as well as electrical sensitivity. By manipulating the structures' design, various gauge factors ranging from 1 to 10 were obtained. The sensors could resist harsh conditions and showed long-term durability over 12 months.

- The development of complex 3D architected hydrogels is not feasible with direct bioprinting technologies. A novel template-assisted process was proposed for the biofabrication of 3D cellularized hydrogel scaffolds with complex internal interconnected macro-channels for perfusing body fluids. Unlike direct bioprinting, the bio-templating approach was compatible with even low viscose hydrogels and high cell concentrations, when cell viability of over 90% was observed. The proposed method enabled the biofabrication of thick vascularized tissues that is an ongoing challenge in the field of tissue engineering.
- The design criteria for architected porous implants and tissue engineering scaffolds was explored in terms of mechanical and physical properties. Gradient macroporosity design (*i.e.*, higher macroporosity at the periphery and lower macroporosity at the center) improved biopermeability at the tissue interface while maintained the mechanical strength of the structure. The structures with various designs of macropores and relative densities showed different mechanical and permeability properties.

8.2. Future work

The research described in this dissertation was focused on developing novel fabrication techniques for forming architected structures, which are challenging to develop using current 3D printing systems to be used for healthcare applications. This research can be extended as the following:

- The proposed sensors can be integrated with triboelectric nanogenerators, which convert the user's movement to electricity and develop a self-powered platform to have no need for an external power source.

- Material jetting of silicone-based inks with a mixture of multidimensional additives (such as carbon nanotube (1D) and graphene (2D)) can lower the percolation threshold, enhance the conductivity, and consequently improve flexibility.
- The porous structures architected with internally interconnected macroporosity developed in this research have a high surface area. The surface of the shrunk elastomeric structures can be functionalized with charged molecules to be used as a drug capturing device that can fit into the vessels for removing excess chemotherapy drugs such as doxorubicin.
- The developed vascularized tissue can be encapsulated with various cell types for forming multicellular/multifunctional tissues. The cell types existing on the interior surface of human blood vessels (*i.e.*, endothelial cells (ECs)) can also be cultured on the surface of the developed tissue with interconnected complex pathways to better mimic the vascularization.
- The architected Ti implants, developed in Chapter 7, can be infilled with an antimicrobial biodegradable hydrogel acting as a bioactive component in the biphasic implant to prevent potential infections. The proposed hydrogel can be designed to have the degradation rate in the range of bone regeneration. The hydrogel can even be modified to enable co-delivery of angiogenic and osteoinductive molecules for enhanced bone regeneration.

Letter of Copyright Permission

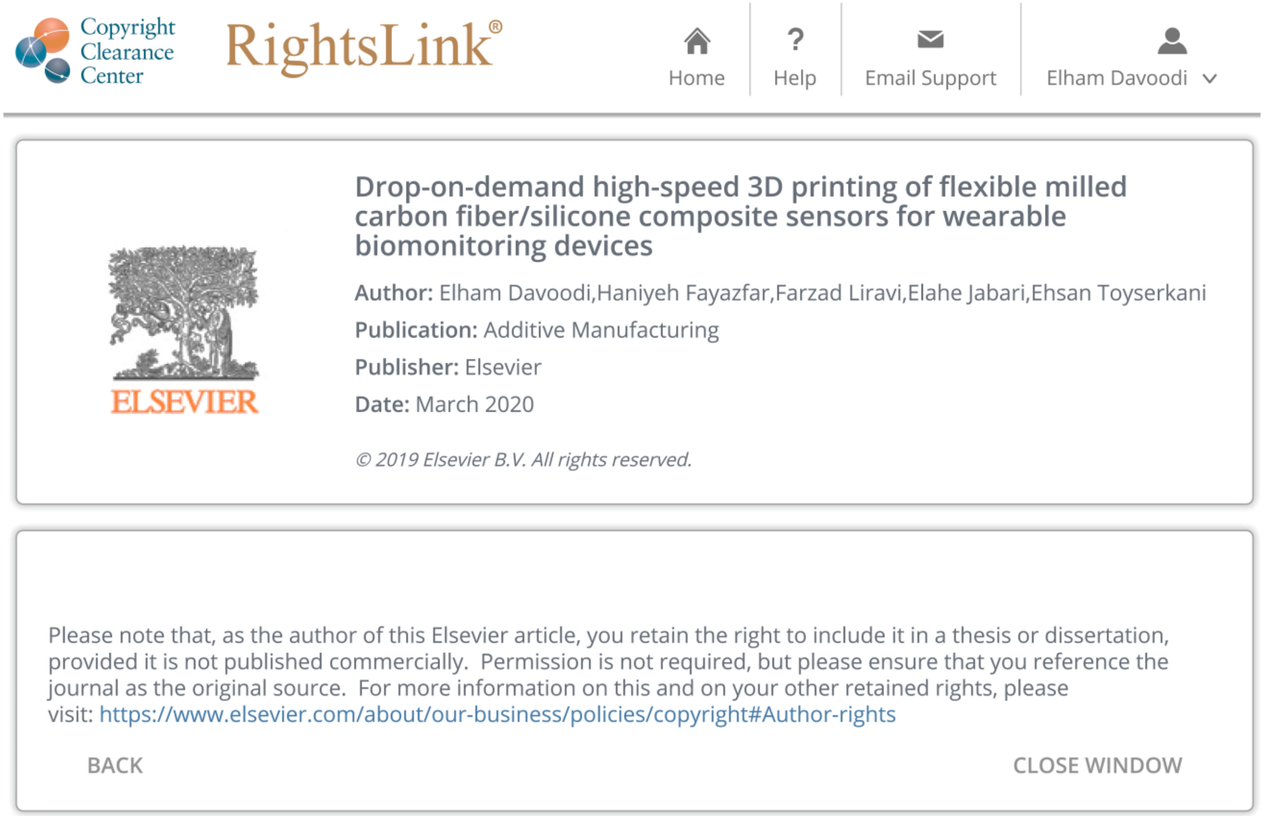

Drop-on-demand high-speed 3D printing of flexible milled carbon fiber/silicone composite sensors for wearable biomonitoring devices

Author: Elham Davoodi,Haniyeh Fayazfar,Farzad Liravi,Elahe Jabari,Ehsan Toyserkani

Publication: Additive Manufacturing

Publisher: Elsevier

Date: March 2020

© 2019 Elsevier B.V. All rights reserved.

Please note that, as the author of this Elsevier article, you retain the right to include it in a thesis or dissertation, provided it is not published commercially. Permission is not required, but please ensure that you reference the journal as the original source. For more information on this and on your other retained rights, please visit: https://www.elsevier.com/about/our-business/policies/copyright#Author-rights

Sacrificial 3D printing of shrinkable silicone elastomers for enhanced feature resolution in flexible tissue scaffolds

Author: Elham Davoodi,Hossein Montazerian,Ali Khademhosseini,Ehsan Toyserkani

Publication: Acta Biomaterialia

Publisher: Elsevier

Date: November 2020

© 2020 Acta Materialia Inc. Published by Elsevier Ltd. All rights reserved.

Please note that, as the author of this Elsevier article, you retain the right to include it in a thesis or dissertation, provided it is not published commercially. Permission is not required, but please ensure that you reference the journal as the original source. For more information on this and on your other retained rights, please visit: https://www.elsevier.com/about/our-business/policies/copyright#Author-rights

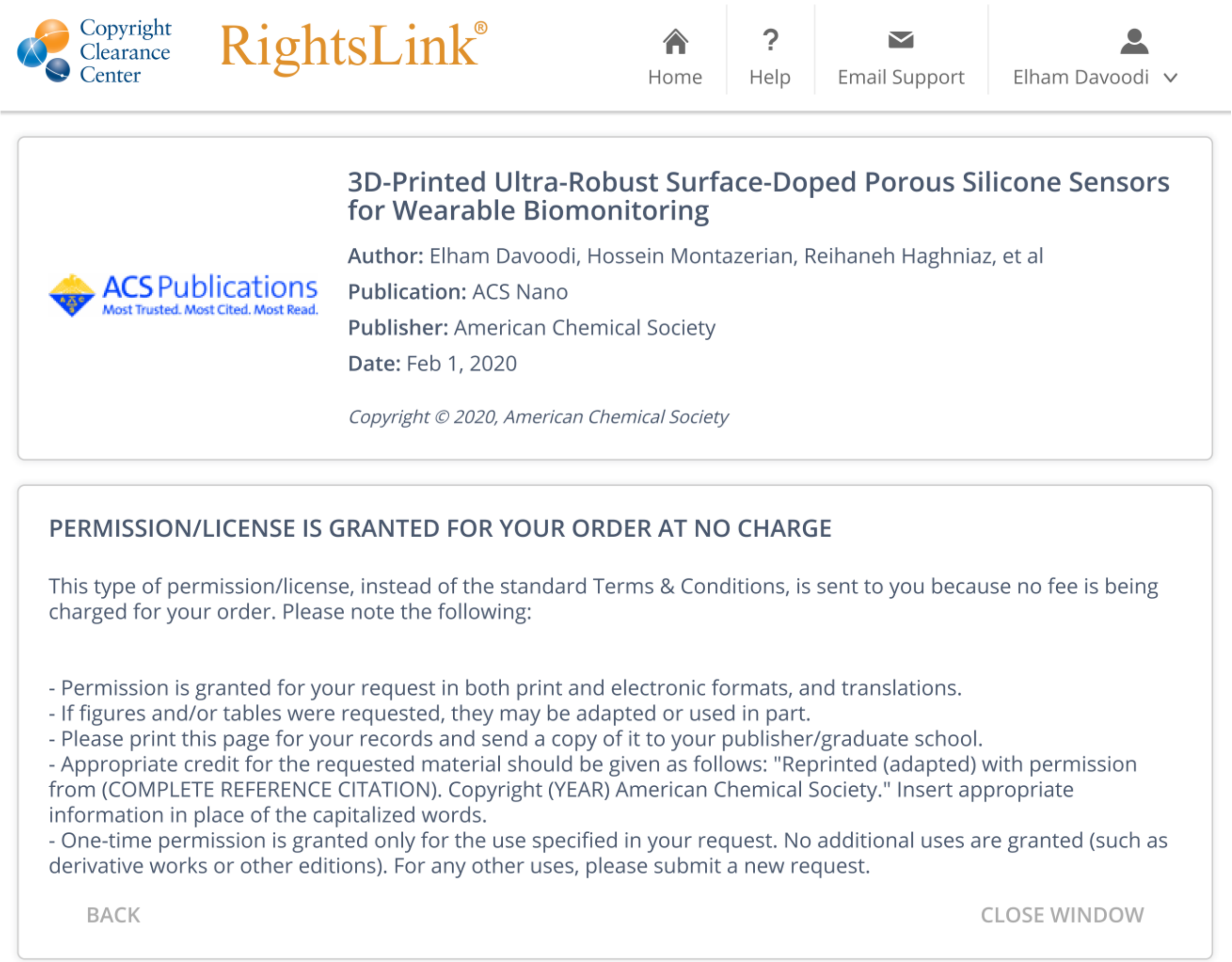

3D-Printed Ultra-Robust Surface-Doped Porous Silicone Sensors for Wearable Biomonitoring

Author: Elham Davoodi, Hossein Montazerian, Reihaneh Haghniaz, et al

Publication: ACS Nano

Publisher: American Chemical Society

Date: Feb 1, 2020

Copyright © 2020, American Chemical Society

PERMISSION/LICENSE IS GRANTED FOR YOUR ORDER AT NO CHARGE

This type of permission/license, instead of the standard Terms & Conditions, is sent to you because no fee is being charged for your order. Please note the following:

- Permission is granted for your request in both print and electronic formats, and translations.
- If figures and/or tables were requested, they may be adapted or used in part.
- Please print this page for your records and send a copy of it to your publisher/graduate school.
- Appropriate credit for the requested material should be given as follows: "Reprinted (adapted) with permission from (COMPLETE REFERENCE CITATION). Copyright (YEAR) American Chemical Society." Insert appropriate information in place of the capitalized words.
- One-time permission is granted only for the use specified in your request. No additional uses are granted (such as derivative works or other editions). For any other uses, please submit a new request.

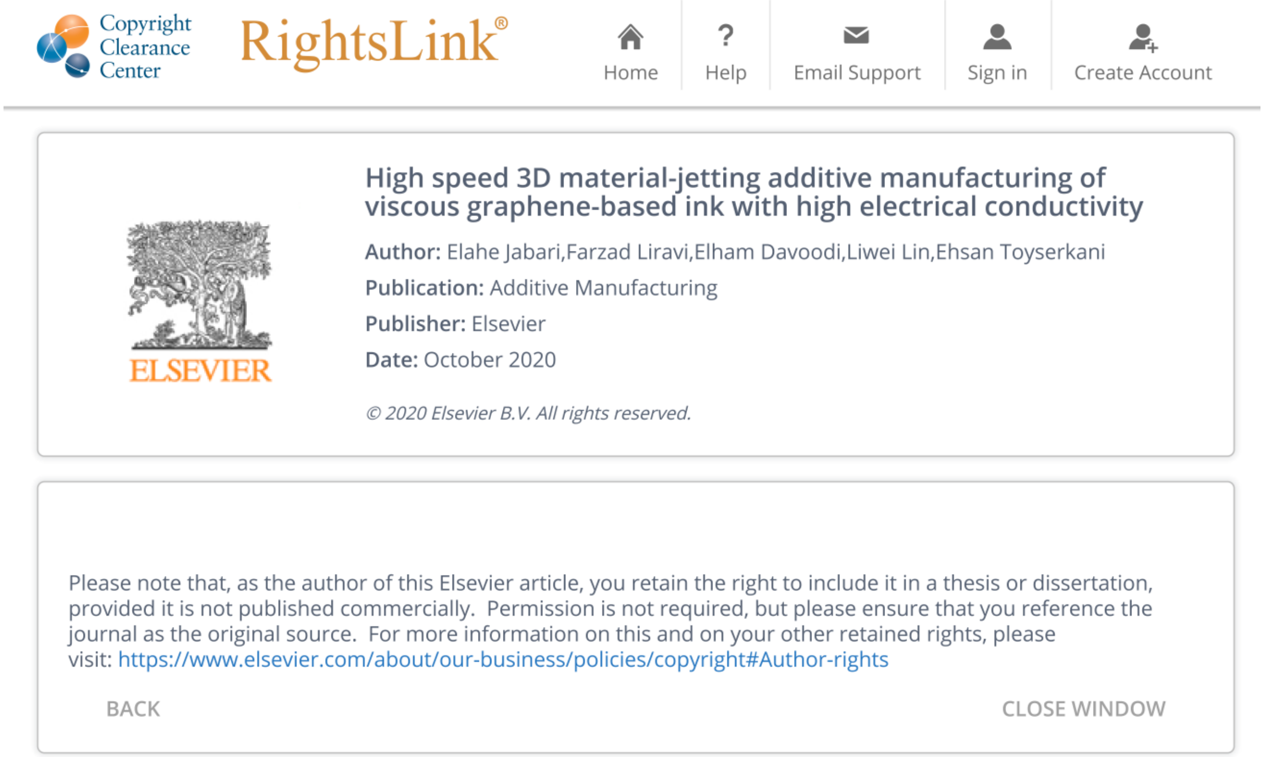

High speed 3D material-jetting additive manufacturing of viscous graphene-based ink with high electrical conductivity

Author: Elahe Jabari,Farzad Liravi,Elham Davoodi,Liwei Lin,Ehsan Toyserkani

Publication: Additive Manufacturing

Publisher: Elsevier

Date: October 2020

© 2020 Elsevier B.V. All rights reserved.

Please note that, as the author of this Elsevier article, you retain the right to include it in a thesis or dissertation, provided it is not published commercially. Permission is not required, but please ensure that you reference the journal as the original source. For more information on this and on your other retained rights, please visit: https://www.elsevier.com/about/our-business/policies/copyright#Author-rights

References

1. Eisler, P., *My life with the printed circuit*. 1989: Lehigh University Press.
2. Ford, S. and M. Despeisse, *Additive manufacturing and sustainability: an exploratory study of the advantages and challenges*. Journal of cleaner Production, 2016. **137**: p. 1573-1587.
3. Kruth, J.-P., M.-C. Leu, and T. Nakagawa, *Progress in additive manufacturing and rapid prototyping*. CIRP Annals-Manufacturing Technology, 1998. **47**(2): p. 525-540.
4. Joshi, P.C., et al. *Direct digital additive manufacturing technologies: Path towards hybrid integration*. in *2012 Future of Instrumentation International Workshop (FIIW) Proceedings*. 2012. IEEE.
5. Ahn, J.-H. and J.H. Je, *Stretchable electronics: materials, architectures and integrations.* Journal of Physics D: Applied Physics, 2012. **45**(10): p. 103001.
6. Ko, S.H., et al., *All-inkjet-printed flexible electronics fabrication on a polymer substrate by low-temperature high-resolution selective laser sintering of metal nanoparticles.* Nanotechnology, 2007. **18**(34): p. 345202.
7. Van Osch, T.H., et al., *Inkjet printing of narrow conductive tracks on untreated polymeric substrates.* Advanced Materials, 2008. **20**(2): p. 343-345.
8. Kaskela, A., et al., *Aerosol-synthesized SWCNT networks with tunable conductivity and transparency by a dry transfer technique.* Nano letters, 2010. **10**(11): p. 4349-4355.
9. Pardo, D.A., G.E. Jabbour, and N. Peyghambarian, *Application of screen printing in the fabrication of organic light-emitting devices.* Advanced Materials, 2000. **12**(17): p. 1249-1252.
10. Davoodi, E., et al., *Drop-on-demand high-speed 3D printing of flexible milled carbon fiber/silicone composite sensors for wearable biomonitoring devices.* Additive Manufacturing, 2020. **32**: p. 101016.

11. Davoodi, E., et al., *Sacrificial 3D printing of shrinkable silicone elastomers for enhanced feature resolution in flexible tissue scaffolds.* Acta Biomaterialia, 2020. **117**: p. 261-272.
12. Davoodi, E., et al., *3D-Printed Ultra-Robust Surface-Doped Porous Silicone Sensors for Wearable Biomonitoring.* ACS Nano, 2020. **14**(2): p. 1520-1532.
13. Ning, F., et al., *Additive manufacturing of carbon fiber reinforced thermoplastic composites using fused deposition modeling.* Composites Part B: Engineering, 2015. **80**: p. 369-378.
14. Zhong, W., et al., *Short fiber reinforced composites for fused deposition modeling.* Materials Science and Engineering: A, 2001. **301**(2): p. 125-130.
15. Nikzad, M., S.H. Masood, and I. Sbarski, *Thermo-mechanical properties of a highly filled polymeric composites for Fused Deposition Modeling.* Materials & Design, 2011. **32**(6): p. 3448-3456.
16. Manapat, J.Z., et al., *High-Strength Stereolithographic 3D Printed Nanocomposites: Graphene Oxide Metastability.* ACS Applied Materials & Interfaces, 2017. **9**(11): p. 10085-10093.
17. Park, B.K., et al., *Direct writing of copper conductive patterns by ink-jet printing.* Thin Solid Films, 2007. **515**(19): p. 7706-7711.
18. Huang, L., et al., *Graphene-based conducting inks for direct inkjet printing of flexible conductive patterns and their applications in electric circuits and chemical sensors.* Nano Research, 2011. **4**(7): p. 675-684.
19. Paulsen, J.A., et al. *Printing conformal electronics on 3D structures with Aerosol Jet technology*. IEEE.
20. Seifert, T., et al., *Additive Manufacturing Technologies Compared: Morphology of Deposits of Silver Ink Using Inkjet and Aerosol Jet Printing*. Industrial & Engineering Chemistry Research, 2015. **54**(2): p. 769-779.
21. Huang, S.H., et al., *Additive manufacturing and its societal impact: a literature review.* The International Journal of Advanced Manufacturing Technology, 2013. **67**(5-8): p. 1191-1203.

22. Baumers, M., et al., *The cost of additive manufacturing: machine productivity, economies of scale and technology-push.* Technological Forecasting and Social Change, 2016. **102**: p. 193-201.
23. Wong, K.V. and A. Hernandez, *A review of additive manufacturing.* International scholarly research notices, 2012. **2012**.
24. Amjadi, M., et al., *Highly Stretchable and Sensitive Strain Sensor Based on Silver Nanowire–Elastomer Nanocomposite.* ACS Nano, 2014. **8**(5): p. 5154-5163.
25. Cochrane, C., et al., *Design and Development of a Flexible Strain Sensor for Textile Structures Based on a Conductive Polymer Composite.* Sensors, 2007. **7**(4): p. 473-492.
26. Boland, C.S., et al., *Sensitive, High-Strain, High-Rate Bodily Motion Sensors Based on Graphene–Rubber Composites.* ACS Nano, 2014. **8**(9): p. 8819-8830.
27. Larimi, S.R., et al., *Low-cost ultra-stretchable strain sensors for monitoring human motion and bio-signals.* Sensors and Actuators A: Physical, 2018. **271**: p. 182-191.
28. Liu, C.-X. and J.-W. Choi, *Patterning conductive PDMS nanocomposite in an elastomer using microcontact printing.* Journal of Micromechanics and Microengineering, 2009. **19**(8): p. 085019-085019.
29. Guo, F.M., et al., *Stretchable and compressible strain sensors based on carbon nanotube meshes.* Nanoscale, 2016. **8**(46): p. 19352-19358.
30. Le, T., et al. *Inkjet-printed graphene-based wireless gas sensor modules*. IEEE.
31. Secor, E.B., et al., *Inkjet Printing of High Conductivity, Flexible Graphene Patterns.* The Journal of Physical Chemistry Letters, 2013. **4**(8): p. 1347-1351.
32. Christ, J.F., et al. *3D printing of highly elastic strain sensors using polyurethane/multiwall carbon nanotube composites*. International Society for Optics and Photonics.

33. Huang, H., et al., *A three-dimensional elastic macroscopic graphene network for thermal management application.* J. Mater. Chem. A, 2014. **2**(43): p. 18215-18218.
34. Samad, Y.A., et al., *Graphene Foam Developed with a Novel Two-Step Technique for Low and High Strains and Pressure-Sensing Applications.* Small, 2015. **11**(20): p. 2380-2385.
35. Li, J., et al., *Fabrication of highly reinforced and compressible graphene/carbon nanotube hybrid foams via a facile self-assembly process for application as strain sensors and beyond.* Journal of Materials Chemistry C, 2017. **5**(10): p. 2723-2730.
36. Sha, J., et al., *Three-Dimensional Printed Graphene Foams.* ACS Nano, 2017. **11**(7): p. 6860-6867.
37. Zhu, C., et al., *Highly compressible 3D periodic graphene aerogel microlattices.* Nature Communications, 2015. **6**(1): p. 6962-6962.
38. Sayyar, S., et al., *UV Cross-Linkable Graphene/Poly(trimethylene Carbonate) Composites for 3D Printing of Electrically Conductive Scaffolds.* ACS Applied Materials & Interfaces, 2016. **8**(46): p. 31916-31925.
39. Duan, S., et al., *Fabrication of Highly Stretchable Conductors Based on 3D Printed Porous Poly(dimethylsiloxane) and Conductive Carbon Nanotubes/Graphene Network.* ACS Applied Materials & Interfaces, 2016. **8**(3): p. 2187-2192.
40. Jang, H., et al., *Graphene-Based Flexible and Stretchable Electronics.* Advanced Materials, 2016. **28**(22): p. 4184-4202.
41. Norotte, C., et al., *Scaffold-free vascular tissue engineering using bioprinting.* Biomaterials, 2009. **30**(30): p. 5910-5917.
42. Zhang, Y., et al., *Characterization of printable cellular micro-fluidic channels for tissue engineering.* Biofabrication, 2013. **5**(2): p. 025004.
43. Zhang, Y., Y. Yu, and I.T. Ozbolat, *Direct Bioprinting of Vessel-Like Tubular Microfluidic Channels.* Journal of Nanotechnology in Engineering and Medicine, 2013. **4**(2): p. 0210011-0210017.
44. Lee, V.K., et al., *Generation of Multi-scale Vascular Network System Within 3D Hydrogel Using 3D Bio-printing Technology.* Cellular and Molecular Bioengineering, 2014. **7**(3): p. 460-472.

45. Gao, Q., et al., *Coaxial nozzle-assisted 3D bioprinting with built-in microchannels for nutrients delivery.* Biomaterials, 2015. **61**: p. 203-215.
46. Golden, A.P. and J. Tien, *Fabrication of microfluidic hydrogels using molded gelatin as a sacrificial element.* Lab on a Chip, 2007. **7**(6): p. 720-725.
47. Skylar-Scott, M.A., et al., *Biomanufacturing of organ-specific tissues with high cellular density and embedded vascular channels.* Science Advances, 2019. **5**(9): p. eaaw2459.
48. Contessi Negrini, N., et al., *Tissue-mimicking gelatin scaffolds by alginate sacrificial templates for adipose tissue engineering.* Acta Biomaterialia, 2019. **87**: p. 61-75.
49. Wang, M., X. Yang, and L. Liang, *Fabrication of a Microfluidic System Using Micromolded Alginate Gel as a Sacrificial Material for Tissues Engineering.* Journal of Chemistry, 2020. **2020**: p. 3148652.
50. Homan, K.A., et al., *Bioprinting of 3D Convoluted Renal Proximal Tubules on Perfusable Chips.* Scientific Reports, 2016. **6**(1): p. 34845.
51. Kolesky, D.B., et al., *3D Bioprinting of Vascularized, Heterogeneous Cell-Laden Tissue Constructs.* Advanced Materials, 2014. **26**(19): p. 3124-3130.
52. Kolesky, D.B., et al., *Three-dimensional bioprinting of thick vascularized tissues.* Proceedings of the National Academy of Sciences, 2016. **113**(12): p. 3179-3184.
53. Wu, W., A. DeConinck, and J.A. Lewis, *Omnidirectional Printing of 3D Microvascular Networks.* Advanced Materials, 2011. **23**(24): p. H178-H183.
54. Song, K.H., et al., *Complex 3D-Printed Microchannels within Cell-Degradable Hydrogels.* Advanced Functional Materials, 2018. **28**(31): p. 1801331.
55. Qian, Y., et al., *Stretchable Organic Semiconductor Devices.* Advanced Materials, 2016. **28**(42): p. 9243-9265.

56. Leigh, S.J., et al., *A Simple, Low-Cost Conductive Composite Material for 3D Printing of Electronic Sensors.* PLOS ONE, 2012. **7**(11): p. e49365.
57. Mohd Radzuan, N.A., A.B. Sulong, and J. Sahari, *A review of electrical conductivity models for conductive polymer composite.* International Journal of Hydrogen Energy, 2017. **42**(14): p. 9262-9273.
58. Sayyar, S., et al., *Processable conducting graphene/chitosan hydrogels for tissue engineering.* Journal of Materials Chemistry B, 2015. **3**(3): p. 481-490.
59. Golafshan, N., M. Kharaziha, and M. Fathi, *Tough and conductive hybrid graphene-PVA: Alginate fibrous scaffolds for engineering neural construct.* Carbon, 2017. **111**: p. 752-763.
60. Kaur, G., et al., *Electrically conductive polymers and composites for biomedical applications.* RSC Advances, 2015. **5**(47): p. 37553-37567.
61. Yamada, T., et al., *A stretchable carbon nanotube strain sensor for human-motion detection.* Nature Nanotechnology, 2011. **6**(5): p. 296-301.
62. Liu, Y., M. Pharr, and G.A. Salvatore, *Lab-on-Skin: A Review of Flexible and Stretchable Electronics for Wearable Health Monitoring.* ACS Nano, 2017. **11**(10): p. 9614-9635.
63. Cho, K.-J., et al., *Review of manufacturing processes for soft biomimetic robots.* International Journal of Precision Engineering and Manufacturing, 2009. **10**(3): p. 171-181.
64. Yan, C., et al., *Highly Stretchable Piezoresistive Graphene–Nanocellulose Nanopaper for Strain Sensors.* Advanced Materials, 2014. **26**(13): p. 2022-2027.
65. Muth, J.T., et al., *Embedded 3D Printing of Strain Sensors within Highly Stretchable Elastomers.* Advanced Materials, 2014. **26**(36): p. 6307-6312.
66. Kanoun, O., et al., *Flexible Carbon Nanotube Films for High Performance Strain Sensors.* Sensors, 2014. **14**(6): p. 10042-10071.
67. Montazerian, H., et al., *A frameless picture frame test with embedded sensor: Mitigation of imperfections in shear*

characterization of woven fabrics. Composite Structures, 2019. **211**: p. 112-124.

68. Montazerianoliaee, H., *Development of stretchable sensors for enhanced shear characterization of woven fabric composites*. 2018.
69. Jeong, C.K., et al., *A Hyper-Stretchable Elastic-Composite Energy Harvester*. Advanced Materials, 2015. **27**(18): p. 2866-2875.
70. Luan, P., et al., *Epidermal Supercapacitor with High Performance*. Advanced Functional Materials, 2016. **26**(45): p. 8178-8184.
71. Zheng, Y., et al., *Smart, stretchable and wearable supercapacitors: prospects and challenges*. CrystEngComm, 2016. **18**(23): p. 4218-4235.
72. Bessonov, A., et al., *Highly reproducible printable graphite strain gauges for flexible devices*. Sensors and Actuators A: Physical, 2014. **206**: p. 75-80.
73. Zakaria, M.Y., et al., *Effect of the addition of milled carbon fiber as a secondary filler on the electrical conductivity of graphite/epoxy composites for electrical conductive material*. Composites Part B: Engineering, 2015. **83**: p. 75-80.
74. Wu, Z.-S., et al., *Alternating Stacked Graphene-Conducting Polymer Compact Films with Ultrahigh Areal and Volumetric Capacitances for High-Energy Micro-Supercapacitors*. Advanced Materials, 2015. **27**(27): p. 4054-4061.
75. Tavakoli, M., et al., *Carbon doped PDMS: conductance stability over time and implications for additive manufacturing of stretchable electronics*. Journal of Micromechanics and Microengineering, 2017. **27**(3): p. 035010.
76. Sau, K.P., D. Khastgir, and T.K. Chaki, *Electrical conductivity of carbon black and carbon fibre filled silicone rubber composites*. Die Angewandte Makromolekulare Chemie, 1998. **258**(1): p. 11-17.
77. Sekiguchi, A., et al. *Stretchable and robust transistor of single wall carbon nanotube, gel and elastomeric materials*. in *2017 International Conference on Electronics Packaging (ICEP)*. 2017.

78. Xu, F., et al., *Highly Stretchable Carbon Nanotube Transistors with Ion Gel Gate Dielectrics.* Nano Letters, 2014. **14**(2): p. 682-686.
79. Zhu, J.-H., et al., *Electrical and Mechanical Performance of Carbon Fiber-Reinforced Polymer Used as the Impressed Current Anode Material.* Materials, 2014. **7**(8): p. 5438-5453.
80. Qu, M. and D.W. Schubert, *Conductivity of melt spun PMMA composites with aligned carbon fibers.* Composites Science and Technology, 2016. **136**: p. 111-118.
81. Mohd Radzuan, N.A., et al., *The effect of milled carbon fibre filler on electrical conductivity in highly conductive polymer composites.* Composites Part B: Engineering, 2017. **110**: p. 153-160.
82. Montazerian, H., et al., *Piezoresistive sensing in chopped carbon fiber embedded PDMS yarns.* Composites Part B: Engineering, 2019. **164**: p. 648-658.
83. Thongruang, W., R.J. Spontak, and C.M. Balik, *Correlated electrical conductivity and mechanical property analysis of high-density polyethylene filled with graphite and carbon fiber.* Polymer, 2002. **43**(8): p. 2279-2286.
84. Ram, R., et al., *Determination of percolation threshold and electrical conductivity of polyvinylidene fluoride (PVDF)/short carbon fiber (SCF) composites: effect of SCF aspect ratio.* Polymer International, 2017. **66**(4): p. 573-582.
85. Yang, L., et al., *Experimental and numerical studies on the sensitivity of carbon fibre/silicone rubber composite sensors.* Smart Materials and Structures, 2012. **21**(3): p. 035011-035011.
86. Jabari, E. and E. Toyserkani, *Micro-scale aerosol-jet printing of graphene interconnects.* Carbon, 2015. **91**: p. 321-329.
87. Le, T., et al. *Inkjet-printed graphene-based wireless gas sensor modules*. in *2012 IEEE 62nd Electronic Components and Technology Conference*. 2012.
88. Trachtenberg, J.E., et al., *Extrusion-based 3D printing of poly(propylene fumarate) scaffolds with hydroxyapatite gradients.* Journal of Biomaterials Science, Polymer Edition, 2017. **28**(6): p. 532-554.

89. Huang, P., Z. Xia, and S. Cui, *3D printing of carbon fiber-filled conductive silicon rubber.* Materials & Design, 2018. **142**: p. 11-21.
90. Jakus, A.E., et al., *Three-Dimensional Printing of High-Content Graphene Scaffolds for Electronic and Biomedical Applications.* ACS Nano, 2015. **9**(4): p. 4636-4648.
91. Liravi, F. and E. Toyserkani, *A hybrid additive manufacturing method for the fabrication of silicone bio-structures: 3D printing optimization and surface characterization.* Materials & Design, 2018. **138**: p. 46-61.
92. Liravi, F., R. Darleux, and E. Toyserkani, *Nozzle dispensing additive manufacturing of polysiloxane: dimensional control.* International Journal of Rapid Manufacturing, 2015. **5**(1): p. 20-43.
93. Liravi, F., R. Darleux, and E. Toyserkani, *Additive manufacturing of 3D structures with non-Newtonian highly viscous fluids: Finite element modeling and experimental validation.* Additive Manufacturing, 2017. **13**: p. 113-123.
94. Naito, K., Y. Tanaka, and J.-M. Yang, *Transverse compressive properties of polyacrylonitrile (PAN)-based and pitch-based single carbon fibers.* Carbon, 2017. **118**: p. 168-183.
95. Chen, B., K. Wu, and W. Yao, *Conductivity of carbon fiber reinforced cement-based composites.* Cement and Concrete Composites, 2004. **26**(4): p. 291-297.
96. Qu, M., F. Nilsson, and D.W. Schubert, *Effect of Filler Orientation on the Electrical Conductivity of Carbon Fiber/PMMA Composites.* Fibers, 2018. **6**(1): p. 3.
97. Kim, T.A., et al., *Single-walled carbon nanotube/silicone rubber composites for compliant electrodes.* Carbon, 2012. **50**(2): p. 444-449.
98. Srivastava, S., et al., *Nanocarbon Reinforced Rubber Nanocomposites: Detailed Insights about Mechanical, Dynamical Mechanical Properties, Payne, and Mullin Effects.* Nanomaterials, 2018. **8**(11): p. 945-945.
99. Wang, M., et al., *Enhanced electrical conductivity and piezoresistive sensing in multi-wall carbon*

nanotubes/polydimethylsiloxane nanocomposites: Via the construction of a self-segregated structure. Nanoscale, 2017. **9**(31): p. 11017-11026.

100. Kong, J.H., et al., *Simple and rapid micropatterning of conductive carbon composites and its application to elastic strain sensors.* Carbon, 2014. **77**: p. 199-207.
101. Zhou, L.-y., et al., *Multimaterial 3D Printing of Highly Stretchable Silicone Elastomers.* ACS Applied Materials & Interfaces, 2019. **11**(26): p. 23573-23583.
102. Roh, S., et al., *3D Printing by Multiphase Silicone/Water Capillary Inks.* Advanced Materials, 2017. **29**(30): p. 1701554.
103. Gomes, R.N., et al., *Antimicrobial graphene nanoplatelets coatings for silicone catheters.* Carbon, 2018. **139**: p. 635-647.
104. Davoodi, E., et al., *Nano-porous anodic alumina: fundamentals and applications in tissue engineering.* Journal of Materials Science: Materials in Medicine, 2020. **31**(7): p. 60.
105. Rahbari, A., et al., *Predicting permeability of regular tissue engineering scaffolds: scaling analysis of pore architecture, scaffold length, and fluid flow rate effects.* Computer Methods in Biomechanics and Biomedical Engineering, 2017. **20**(3): p. 231-241.
106. Song, P., et al., *A Self-Powered Implantable Drug-Delivery System Using Biokinetic Energy.* Advanced Materials, 2017. **29**(11): p. 1605668.
107. Bae, W.-G., et al., *Snake fang–inspired stamping patch for transdermal delivery of liquid formulations.* Science Translational Medicine, 2019. **11**(503): p. eaaw3329.
108. Ahadian, S., et al., *Micro and nanoscale technologies in oral drug delivery.* Advanced Drug Delivery Reviews, 2020.
109. Chen, Y.Y., B.R. Kingston, and W.C.W. Chan, *Transcribing In Vivo Blood Vessel Networks into In Vitro Perfusable Microfluidic Devices.* Advanced Materials Technologies. **n/a**(n/a): p. 2000103.
110. Nguyen, N., et al., *Inertial Microfluidics with Integrated Vortex Generators Using Liquid Metal Droplets as Fugitive Ink.* Advanced Functional Materials, 2019. **29**(27): p. 1901998.

111. Lim, H.-R., et al., *Advanced Soft Materials, Sensor Integrations, and Applications of Wearable Flexible Hybrid Electronics in Healthcare, Energy, and Environment.* Advanced Materials, 2020. **32**(15): p. 1901924.
112. Jabari, E., et al., *High Speed Three-Dimensional Material-Jetting Additive Manufacturing of Viscous Graphene-based Ink with High Electrical Conductivity.* Additive Manufacturing, 2020: p. 101330.
113. Montazerian, H., et al., *Integrated Sensors in Advanced Composites: A Critical Review.* Critical Reviews in Solid State and Materials Sciences, 2020. **45**(3): p. 187-238.
114. Montazerian, H., et al., *Graphene-Coated Spandex Sensors Embedded into Silicone Sheath for Composites Health Monitoring and Wearable Applications.* Small, 2019. **15**(17): p. 1804991.
115. Wolf, M.P., G.B. Salieb-Beugelaar, and P. Hunziker, *PDMS with designer functionalities—Properties, modifications strategies, and applications.* Progress in Polymer Science, 2018. **83**: p. 97-134.
116. O'Bryan, C.S., et al., *Self-assembled micro-organogels for 3D printing silicone structures.* Science Advances, 2017. **3**(5): p. e1602800.
117. Bernardi, L., et al., *On the large strain deformation behavior of silicone-based elastomers for biomedical applications.* Polymer Testing, 2017. **58**: p. 189-198.
118. Zheng, S., et al., *Multiple modulus silicone elastomers using 3D extrusion printing of low viscosity inks.* Additive Manufacturing, 2018. **24**: p. 86-92.
119. Plott, J. and A. Shih, *The extrusion-based additive manufacturing of moisture-cured silicone elastomer with minimal void for pneumatic actuators.* Additive Manufacturing, 2017. **17**: p. 1-14.
120. Ozbolat, V., et al., *3D Printing of PDMS Improves Its Mechanical and Cell Adhesion Properties.* ACS Biomaterials Science & Engineering, 2018. **4**(2): p. 682-693.
121. Liravi, F., et al., *High-speed material jetting additive manufacturing of silicone structures: mechanical characterization.* Progress in Additive Manufacturing, 2019. **4**(4): p. 479-495.

122. Hinton, T.J., et al., *3D Printing PDMS Elastomer in a Hydrophilic Support Bath via Freeform Reversible Embedding.* ACS Biomaterials Science & Engineering, 2016. **2**(10): p. 1781-1786.
123. Liravi, F. and E. Toyserkani, *Additive manufacturing of silicone structures: A review and prospective.* Additive Manufacturing, 2018. **24**: p. 232-242.
124. Rodrigue, H., et al., *3D soft lithography: A fabrication process for thermocurable polymers.* Journal of Materials Processing Technology, 2015. **217**: p. 302-309.
125. Skylar-Scott, M.A., et al., *Voxelated soft matter via multimaterial multinozzle 3D printing.* Nature, 2019. **575**(7782): p. 330-335.
126. Hamidi, A. and Y. Tadesse, *3D printing of very soft elastomer and sacrificial carbohydrate glass/elastomer structures for robotic applications.* Materials & Design, 2020. **187**: p. 108324.
127. Mygind, T., et al., *Mesenchymal stem cell ingrowth and differentiation on coralline hydroxyapatite scaffolds.* Biomaterials, 2007. **28**(6): p. 1036-1047.
128. HuangáGoh, W. and A. HoseináSakhaei, *Highly stretchable hydrogels for UV curing based high-resolution multimaterial 3D printing.* Journal of Materials Chemistry B, 2018. **6**(20): p. 3246-3253.
129. Zhang, X., et al., *Nozzle flow behavior of aluminum/polycarbonate composites in the material extrusion printing process.* Journal of Applied Polymer Science, 2019. **136**(12): p. 47252.
130. Walker, S., et al., *Zero-support 3D printing of thermoset silicone via simultaneous control of both reaction kinetics and transient rheology.* 3D Printing and Additive Manufacturing, 2019. **6**(3): p. 139-147.
131. Saggiomo, V. and A.H. Velders, *Simple 3D Printed Scaffold-Removal Method for the Fabrication of Intricate Microfluidic Devices.* Advanced Science, 2015. **2**(9): p. 1500125.
132. Mohanty, S., et al., *Fabrication of scalable and structured tissue engineering scaffolds using water dissolvable sacrificial 3D printed moulds.* Materials Science and Engineering: C, 2015. **55**: p. 569-578.

133. Dahlberg, T., et al., *3D printed water-soluble scaffolds for rapid production of PDMS micro-fluidic flow chambers.* Scientific Reports, 2018. **8**(1): p. 3372.
134. Montazerian, H., et al., *Permeability and mechanical properties of gradient porous PDMS scaffolds fabricated by 3D-printed sacrificial templates designed with minimal surfaces.* Acta Biomaterialia, 2019. **96**: p. 149-160.
135. Rankouhi, B., et al., *Failure Analysis and Mechanical Characterization of 3D Printed ABS With Respect to Layer Thickness and Orientation.* Journal of Failure Analysis and Prevention, 2016. **16**(3): p. 467-481.
136. Murphy, C.M. and F.J. O'Brien, *Understanding the effect of mean pore size on cell activity in collagen-glycosaminoglycan scaffolds.* Cell adhesion & migration, 2010. **4**(3): p. 377-381.
137. Boley, J.W., et al., *Shape-shifting structured lattices via multimaterial 4D printing.* Proceedings of the National Academy of Sciences, 2019. **116**(42): p. 20856-20862.
138. Battista, D., V. Luchnikov, and P. Nardinocchi, *Shape-shifting of polymer beams and shells due to oil extraction.* Extreme Mechanics Letters, 2020. **36**: p. 100655.
139. Egunov, A.I., J.G. Korvink, and V.A. Luchnikov, *Polydimethylsiloxane bilayer films with an embedded spontaneous curvature.* Soft Matter, 2016. **12**(1): p. 45-52.
140. Holmes, D.P., et al., *Bending and twisting of soft materials by non-homogenous swelling.* Soft Matter, 2011. **7**(11): p. 5188-5193.
141. Zhou, Y., et al., *Highly stretchable, elastic, and ionic conductive hydrogel for artificial soft electronics.* Advanced Functional Materials, 2019. **29**(1): p. 1806220.
142. Liu, Y., et al., *Soft and elastic hydrogel-based microelectronics for localized low-voltage neuromodulation.* Nature Biomedical Engineering, 2019. **3**(1): p. 58-68.
143. Montazerian, H., et al., *Porous scaffold internal architecture design based on minimal surfaces: a compromise between permeability and elastic properties.* Materials & Design, 2017. **126**: p. 98-114.

144. Montazerian, H., et al., *Longitudinal and radial permeability analysis of additively manufactured porous scaffolds: Effect of pore shape and porosity.* Materials & Design, 2017. **122**: p. 146-156.
145. Ashby, M.F., et al., *Metal foams: a design guide*. 2000: Elsevier.
146. Nichol, J.W., et al., *Cell-laden microengineered gelatin methacrylate hydrogels.* Biomaterials, 2010. **31**(21): p. 5536-5544.
147. Tavafoghi, M., et al., *Engineering Tough, Injectable, Naturally Derived, Bioadhesive Composite Hydrogels.* Advanced Healthcare Materials, 2020. **9**(10): p. 1901722.
148. Palchesko, R.N., et al., *Development of Polydimethylsiloxane Substrates with Tunable Elastic Modulus to Study Cell Mechanobiology in Muscle and Nerve.* PLOS ONE, 2012. **7**(12): p. e51499.
149. Schneider, F., et al., *Mechanical properties of silicones for MEMS.* Journal of Micromechanics and Microengineering, 2008. **18**(6): p. 065008.
150. Rumens, C.V., et al., *Swelling of PDMS networks in solvent vapours; applications for passive RFID wireless sensors.* Journal of Materials Chemistry C, 2015. **3**(39): p. 10091-10098.
151. Sartori, S., et al., *Biomimetic polyurethanes in nano and regenerative medicine.* Journal of Materials Chemistry B, 2014. **2**(32): p. 5128-5144.
152. Pang, Y., et al., *Flexible, highly sensitive, and wearable pressure and strain sensors with graphene porous network structure.* ACS applied materials & interfaces, 2016. **8**(40): p. 26458-26462.
153. Luo, S., P.T. Hoang, and T. Liu, *Direct laser writing for creating porous graphitic structures and their use for flexible and highly sensitive sensor and sensor arrays.* Carbon, 2016. **96**: p. 522-531.
154. Lu, Y., et al., *Flexible neural electrode array based-on porous graphene for cortical microstimulation and sensing.* Scientific reports, 2016. **6**: p. 33526.
155. Li, N., et al., *Three-dimensional graphene foam as a biocompatible and conductive scaffold for neural stem cells.* Scientific reports, 2013. **3**: p. 1604.

156. Jung, G.S. and M.J. Buehler, *Multiscale mechanics of triply periodic minimal surfaces of three-dimensional graphene foams.* Nano letters, 2018. **18**(8): p. 4845-4853.
157. Li, Y., Y.A. Samad, and K. Liao, *From cotton to wearable pressure sensor.* Journal of Materials Chemistry A, 2015. **3**(5): p. 2181-2187.
158. Rahimi, R., M. Ochoa, and B. Ziaie, *Direct laser writing of porous-carbon/silver nanocomposite for flexible electronics.* ACS applied materials & interfaces, 2016. **8**(26): p. 16907-16913.
159. Kang, S., et al., *Highly Sensitive Pressure Sensor Based on Bioinspired Porous Structure for Real-Time Tactile Sensing.* Advanced Electronic Materials, 2016. **2**(12): p. 1600356.
160. Zhang, N., et al., *A wearable all-solid photovoltaic textile.* Advanced Materials, 2016. **28**(2): p. 263-269.
161. Chen, J., et al., *Micro-cable structured textile for simultaneously harvesting solar and mechanical energy.* Nature Energy, 2016. **1**(10): p. 16138.
162. Zhang, N., et al., *Progress in triboelectric nanogenerators as self-powered smart sensors.* Journal of Materials Research, 2017. **32**(9): p. 1628-1646.
163. Qin, Y., et al., *Lightweight, superelastic, and mechanically flexible graphene/polyimide nanocomposite foam for strain sensor application.* ACS nano, 2015. **9**(9): p. 8933-8941.
164. Kwon, D., et al., *Highly sensitive, flexible, and wearable pressure sensor based on a giant piezocapacitive effect of three-dimensional microporous elastomeric dielectric layer.* ACS applied materials & interfaces, 2016. **8**(26): p. 16922-16931.
165. Zhang, F., et al., *Flexible and self-powered temperature–pressure dual-parameter sensors using microstructure-frame-supported organic thermoelectric materials.* Nature communications, 2015. **6**: p. 8356.
166. Li, T., et al., *Porous ionic membrane based flexible humidity sensor and its multifunctional applications.* Advanced Science, 2017. **4**(5): p. 1600404.

167. Jiang, K., et al., *Excellent humidity sensor based on LiCl loaded hierarchically porous polymeric microspheres.* ACS applied materials & interfaces, 2016. **8**(38): p. 25529-25534.
168. Singh, H., et al., *A porous, crystalline truxene-based covalent organic framework and its application in humidity sensing.* Journal of Materials Chemistry A, 2017. **5**(41): p. 21820-21827.
169. Liu, M.-Q., C. Wang, and N.-Y. Kim, *High-sensitivity and low-hysteresis porous mimtype capacitive humidity sensor using functional polymer mixed with TiO2 microparticles.* Sensors, 2017. **17**(2): p. 284.
170. Pang, Y., et al., *Wearable humidity sensor based on porous graphene network for respiration monitoring.* Biosensors and Bioelectronics, 2018. **116**: p. 123-129.
171. Zhong, S., C. Zhan, and D. Cao, *Zeolitic imidazolate framework-derived nitrogen-doped porous carbons as high performance supercapacitor electrode materials.* Carbon, 2015. **85**: p. 51-59.
172. Xiong, Z., et al., *Mechanically Tough Large-Area Hierarchical Porous Graphene Films for High-Performance Flexible Supercapacitor Applications.* Advanced Materials, 2015. **27**(30): p. 4469-4475.
173. Li, H., et al., *An All-Stretchable-Component Sodium-Ion Full Battery.* Advanced Materials, 2017. **29**(23): p. 1700898.
174. Niu, Z., et al., *Highly Compressible and All-Solid-State Supercapacitors Based on Nanostructured Composite Sponge.* Advanced materials, 2015. **27**(39): p. 6002-6008.
175. Zhou, X., et al., *Highly sensitive acetone gas sensor based on porous ZnFe2O4 nanospheres.* Sensors and Actuators B: Chemical, 2015. **206**: p. 577-583.
176. Yavari, F., et al., *High sensitivity gas detection using a macroscopic three-dimensional graphene foam network.* Scientific reports, 2011. **1**: p. 166.
177. Frutiger, A., et al., *Capacitive soft strain sensors via multicore–shell fiber printing.* Advanced Materials, 2015. **27**(15): p. 2440-2446.

178. Matsuhisa, N., et al., *Printable elastic conductors with a high conductivity for electronic textile applications.* Nature communications, 2015. **6**: p. 7461.
179. Chizari, K., et al., *3D printing of highly conductive nanocomposites for the functional optimization of liquid sensors.* Small, 2016. **12**(44): p. 6076-6082.
180. Guo, S.Z., et al., *3D printed stretchable tactile sensors.* Advanced Materials, 2017. **29**(27): p. 1701218.
181. Mohammed, M.G. and R. Kramer, *All-Printed Flexible and Stretchable Electronics.* Advanced Materials, 2017. **29**(19): p. 1604965.
182. Agarwala, S., et al., *Wearable bandage-based strain sensor for home healthcare: combining 3D aerosol jet printing and laser sintering.* ACS sensors, 2018. **4**(1): p. 218-226.
183. Hindermann-Bischoff, M. and F. Ehrburger-Dolle, *Electrical conductivity of carbon black–polyethylene composites: Experimental evidence of the change of cluster connectivity in the PTC effect.* Carbon, 2001. **39**(3): p. 375-382.
184. Li, Y., et al., *Poly (propylene)/graphene nanoplatelet nanocomposites: melt rheological behavior and thermal, electrical, and electronic properties.* Macromolecular Chemistry and Physics, 2011. **212**(18): p. 1951-1959.
185. Du, D., P. Li, and J. Ouyang, *Graphene coated nonwoven fabrics as wearable sensors.* Journal of Materials Chemistry C, 2016. **4**(15): p. 3224-3230.
186. Wang, L., et al., *Flexible, Graphene-Coated Biocomposite for Highly Sensitive, Real-Time Molecular Detection.* Advanced Functional Materials, 2016. **26**(47): p. 8623-8630.
187. Yuan, W., et al., *Small and light strain sensors based on graphene coated human hairs.* Nanoscale, 2015. **7**(39): p. 16361-16365.
188. Boland, C.S., et al., *Sensitive, high-strain, high-rate bodily motion sensors based on graphene–rubber composites.* ACS nano, 2014. **8**(9): p. 8819-8830.
189. Ho, D.H., et al., *Stretchable and multimodal all graphene electronic skin.* Advanced Materials, 2016. **28**(13): p. 2601-2608.

190. Kim, J., et al., *Highly Transparent and Stretchable Field-Effect Transistor Sensors Using Graphene–Nanowire Hybrid Nanostructures.* Advanced Materials, 2015. **27**(21): p. 3292-3297.
191. Rinaldi, A., et al., *A flexible and highly sensitive pressure sensor based on a PDMS foam coated with graphene nanoplatelets.* Sensors, 2016. **16**(12): p. 2148.
192. Cui, J. and S. Zhou, *Highly conductive and ultra-durable electronic textiles via covalent immobilization of carbon nanomaterials on cotton fabric.* Journal of Materials Chemistry C, 2018. **6**(45): p. 12273-12282.
193. Luis E, L.H., Juha S, Yeong WY, *A Review of Medical Silicone 3d-Printing Technologies and Clinical Applications.* J Orthop Ther, 2018. **2018**(06): p. 1-9.
194. Cebo, T., et al., *Chemical vapour deposition of freestanding sub-60 nm graphene gyroids.* Applied Physics Letters, 2017. **111**(25): p. 253103.
195. Nakanishi, K., et al., *Compressive behavior and failure mechanisms of freestanding and composite 3D graphitic foams.* Acta Materialia, 2018. **159**: p. 187-196.
196. Xiong, C., et al., *The recent progress on three-dimensional porous graphene-based hybrid structure for supercapacitor.* Composites Part B: Engineering, 2018.
197. Zhang, Q., et al., *Three-dimensional printing hollow polymer template-mediated graphene lattices with tailorable architectures and multifunctional properties.* ACS nano, 2018. **12**(2): p. 1096-1106.
198. Chen, Z., et al., *Lightweight and flexible graphene foam composites for high-performance electromagnetic interference shielding.* Advanced materials, 2013. **25**(9): p. 1296-1300.
199. Tabassian, R., et al., *Functionally Antagonistic Hybrid Electrode with Hollow Tubular Graphene Mesh and Nitrogen-Doped Crumpled Graphene for High-Performance Ionic Soft Actuators.* Advanced Functional Materials, 2018. **28**(5): p. 1705714.
200. Wu, C., et al., *Three-dimensional highly conductive graphene–silver nanowire hybrid foams for flexible and stretchable*

conductors. ACS applied materials & interfaces, 2014. **6**(23): p. 21026-21034.

201. Han, F., et al., *Fabrication of a flexible and stretchable three-dimensional conductor based on Au–Ni@ graphene coated polyurethane sponge by electroless plating.* Journal of Materials Chemistry C, 2018. **6**(30): p. 8135-8143.
202. Chen, M., et al., *Highly stretchable conductors integrated with a conductive carbon nanotube/graphene network and 3D porous poly (dimethylsiloxane).* Advanced functional materials, 2014. **24**(47): p. 7548-7556.
203. Luo, N., et al., *Hollow-Structured Graphene–Silicone-Composite-Based Piezoresistive Sensors: Decoupled Property Tuning and Bending Reliability.* Advanced Materials, 2017. **29**(40): p. 1702675.
204. Chen, Z., et al., *Three-dimensional flexible and conductive interconnected graphene networks grown by chemical vapour deposition.* Nature materials, 2011. **10**(6): p. 424.
205. Gui, X., et al., *Soft, highly conductive nanotube sponges and composites with controlled compressibility.* ACS nano, 2010. **4**(4): p. 2320-2326.
206. Samad, Y.A., et al., *Graphene foam developed with a novel two-step technique for low and high strains and pressure-sensing applications.* Small, 2015. **11**(20): p. 2380-2385.
207. Montazerian, H., et al., *Graphene-Coated Spandex Sensors Embedded into Silicone Sheath for Composites Health Monitoring and Wearable Applications.* Small, 2019: p. 1804991.
208. Yu, X., et al., *Graphene-based smart materials.* Nature Reviews Materials, 2017. **2**(9): p. 17046.
209. Rozicka, A., et al., *Apparent and intrinsic properties of commercial PDMS based membranes in pervaporative removal of acetone, butanol and ethanol from binary aqueous mixtures.* Journal of Membrane Science, 2014. **453**: p. 108-118.
210. Hernandez, Y., et al., *Measurement of multicomponent solubility parameters for graphene facilitates solvent discovery.* Langmuir, 2009. **26**(5): p. 3208-3213.

211. Hansen, C.M., *Hansen solubility parameters: a user's handbook*. 2002: CRC press.
212. Zhai, T., et al., *Piezoresistive and compression resistance relaxation behavior of water blown carbon nanotube/polyurethane composite foam.* Composites Part A: Applied Science and Manufacturing, 2015. **72**: p. 108-114.
213. Boland, C.S., et al., *Sensitive electromechanical sensors using viscoelastic graphene-polymer nanocomposites.* Science, 2016. **354**(6317): p. 1257-1260.
214. Lee, J.-Y., M. Jang, and S.-H. Shin, *Study on the depth, rate, shape, and strength of pulse with cardiovascular simulator.* Evidence-Based Complementary and Alternative Medicine, 2017. **2017**.
215. Himmels, P., et al., *Motor neurons control blood vessel patterning in the developing spinal cord.* Nature Communications, 2017. **8**(1): p. 14583.
216. Miller, J.S., et al., *Rapid casting of patterned vascular networks for perfusable engineered three-dimensional tissues.* Nature Materials, 2012. **11**(9): p. 768-774.
217. Tang, Y., et al., *In situ gas foaming based on magnesium particle degradation: A novel approach to fabricate injectable macroporous hydrogels.* Biomaterials, 2020. **232**: p. 119727.
218. De France, K.J., F. Xu, and T. Hoare, *Structured Macroporous Hydrogels: Progress, Challenges, and Opportunities.* Advanced Healthcare Materials, 2018. **7**(1): p. 1700927.
219. Grenier, J., et al., *Mechanisms of pore formation in hydrogel scaffolds textured by freeze-drying.* Acta Biomaterialia, 2019. **94**: p. 195-203.
220. Rusakov, D., A. Menner, and A. Bismarck, *High-Performance Polymer Foams by Thermally Induced Phase Separation.* Macromolecular Rapid Communications, 2020. **41**(11): p. 2000110.
221. Prasad, A., M.R. Sankar, and V. Katiyar, *State of Art on Solvent Casting Particulate Leaching Method for Orthopedic ScaffoldsFabrication.* Materials Today: Proceedings, 2017. **4**(2, Part A): p. 898-907.

222. Zhang, H., et al., *Direct 3D Printed Biomimetic Scaffolds Based on Hydrogel Microparticles for Cell Spheroid Growth.* Advanced Functional Materials, 2020. **30**(13): p. 1910573.
223. Johnston, T.G., et al., *Compartmentalized microbes and co-cultures in hydrogels for on-demand bioproduction and preservation.* Nature Communications, 2020. **11**(1): p. 563.
224. Xie, R., et al., *Engineering of Hydrogel Materials with Perfusable Microchannels for Building Vascularized Tissues.* Small, 2020. **16**(15): p. 1902838.
225. Cheng, C., et al., *Water-matrix interaction at the drop-drop interface during drop-on-demand printing of hydrogels.* International Journal of Heat and Mass Transfer, 2020. **150**: p. 119327.
226. Jabari, E., et al., *High speed 3D material-jetting additive manufacturing of viscous graphene-based ink with high electrical conductivity.* Additive Manufacturing, 2020. **35**: p. 101330.
227. Hong, H., et al., *Digital light processing 3D printed silk fibroin hydrogel for cartilage tissue engineering.* Biomaterials, 2020. **232**: p. 119679.
228. Teng, C.-L., et al., *Design of photocurable, biodegradable scaffolds for liver lobule regeneration via digital light process-additive manufacturing.* Biofabrication, 2020. **12**(3): p. 035024.
229. Magalhães, L.S.S.M., et al., *Printing 3D Hydrogel Structures Employing Low-Cost Stereolithography Technology.* Journal of Functional Biomaterials, 2020. **11**(1): p. 12.
230. Mishra, A.K., et al., *Autonomic perspiration in 3D-printed hydrogel actuators.* Science Robotics, 2020. **5**(38): p. eaaz3918.
231. Ali, M.A., M. Rajabi, and S. Sudhir Sali, *Additive manufacturing potential for medical devices and technology.* Current Opinion in Chemical Engineering, 2020. **28**: p. 127-133.
232. Unagolla, J.M. and A.C. Jayasuriya, *Hydrogel-based 3D bioprinting: A comprehensive review on cell-laden hydrogels, bioink formulations, and future perspectives.* Applied Materials Today, 2020. **18**: p. 100479.

233. Hu, Y., et al. *Tissue Organ Analogue Manufacturing by 3D Bio-Printing Technology for Tissue Engineering Applications*. in *Proceedings of the Seventh Asia International Symposium on Mechatronics*. 2020. Singapore: Springer Singapore.
234. Chimene, D., R. Kaunas, and A.K. Gaharwar, *Hydrogel Bioink Reinforcement for Additive Manufacturing: A Focused Review of Emerging Strategies.* Advanced Materials, 2020. **32**(1): p. 1902026.
235. Yamaguchi, S., et al., *Cell patterning through inkjet printing of one cell per droplet.* Biofabrication, 2012. **4**(4): p. 045005.
236. Chahal, D., A. Ahmadi, and K.C. Cheung, *Improving piezoelectric cell printing accuracy and reliability through neutral buoyancy of suspensions.* Biotechnology and Bioengineering, 2012. **109**(11): p. 2932-2940.
237. Kinstlinger, I.S., et al., *Generation of model tissues with dendritic vascular networks via sacrificial laser-sintered carbohydrate templates.* Nature Biomedical Engineering, 2020.
238. Tocchio, A., et al., *Versatile fabrication of vascularizable scaffolds for large tissue engineering in bioreactor.* Biomaterials, 2015. **45**: p. 124-131.
239. Gelber, M.K., et al., *Model-guided design and characterization of a high-precision 3D printing process for carbohydrate glass.* Additive Manufacturing, 2018. **22**: p. 38-50.
240. Montazerian, H., et al., *Permeability and mechanical properties of gradient porous PDMS scaffolds fabricated by 3D-printed sacrificial templates designed with minimal surfaces.* Acta biomaterialia, 2019. **96**: p. 149-160.
241. Nichol, J.W., et al., *Cell-laden microengineered gelatin methacrylate hydrogels.* Biomaterials, 2010. **31**(21): p. 5536-44.
242. Vinci, V.A. and S.R. Parekh, *Handbook of industrial cell culture: mammalian, microbial, and plant cells*. 2002: Springer Science & Business Media.
243. Pimienta, V., et al., *Complex shapes and dynamics of dissolving drops of dichloromethane.* Angewandte Chemie International Edition, 2011. **50**(45): p. 10728-10731.

244. Lee, A., et al., *3D bioprinting of collagen to rebuild components of the human heart.* Science, 2019. **365**(6452): p. 482-487.
245. Erdem, A., et al., *3D Bioprinting of Oxygenated Cell-Laden Gelatin Methacryloyl Constructs.* Advanced healthcare materials, 2020: p. 1901794.
246. Yue, K., et al., *Synthesis, properties, and biomedical applications of gelatin methacryloyl (GelMA) hydrogels.* Biomaterials, 2015. **73**: p. 254-271.
247. Wisotzki, E.I., et al., *Tailoring the material properties of gelatin hydrogels by high energy electron irradiation.* Journal of Materials Chemistry B, 2014. **2**(27): p. 4297-4309.
248. Noshadi, I., et al., *In vitro and in vivo analysis of visible light crosslinkable gelatin methacryloyl (GelMA) hydrogels.* Biomaterials Science, 2017. **5**(10): p. 2093-2105.
249. Budday, S., et al., *Fifty shades of brain: a review on the mechanical testing and modeling of brain tissue.* Archives of Computational Methods in Engineering, 2019: p. 1-44.
250. Salama, A. and A.J. Hamer, *Degenerative and rheumatoid arthritis (including joint replacement).* Surgery (Oxford), 2007. **25**(4): p. 160-165.
251. Sloan, M. and N. Sheth. *Projected volume of primary and revision total joint arthroplasty in the United States, 2030–2060*. in *American Academy of Orthopaedic Surgeons 2018 Annual Meeting (New Orleans, LA)*. 2018.
252. Bayliss, L.E., et al., *The effect of patient age at intervention on risk of implant revision after total replacement of the hip or knee: a population-based cohort study.* The Lancet, 2017. **389**(10077): p. 1424-1430.
253. Albrektsson, T., et al., *Bone loss around oral and orthopedic implants: An immunologically based condition.* Clinical implant dentistry and related research, 2019. **21**(4): p. 786-795.
254. Arabnejad, S., et al., *Fully porous 3D printed titanium femoral stem to reduce stress-shielding following total hip arthroplasty.* Journal of Orthopaedic Research, 2017. **35**(8): p. 1774-1783.

255. Kolken, H.M., et al., *Rationally designed meta-implants: a combination of auxetic and conventional meta-biomaterials.* Materials Horizons, 2018. **5**(1): p. 28-35.
256. Greer, A.I.M., et al., *Nanopatterned Titanium Implants Accelerate Bone Formation In Vivo.* ACS Applied Materials & Interfaces, 2020. **12**(30): p. 33541-33549.
257. Zadpoor, A.A., *Meta-biomaterials.* Biomaterials Science, 2020. **8**(1): p. 18-38.
258. Yuk, H., et al., *Tough bonding of hydrogels to diverse non-porous surfaces.* Nature materials, 2016. **15**(2): p. 190.
259. Bobbert, F., et al., *Additively manufactured metallic porous biomaterials based on minimal surfaces: A unique combination of topological, mechanical, and mass transport properties.* Acta biomaterialia, 2017. **53**: p. 572-584.
260. Sheydaeian, E., et al., *Material process development for the fabrication of heterogeneous titanium structures with selective pore morphology by a hybrid additive manufacturing process.* Materials & Design, 2017. **135**: p. 142-150.
261. Barui, S., et al., *3D inkjet printing of biomaterials with strength reliability and cytocompatibility: Quantitative process strategy for Ti-6Al-4V*. Biomaterials, 2019. **213**: p. 119212.
262. Callens, S.J., et al., *Substrate curvature as a cue to guide spatiotemporal cell and tissue organization.* Biomaterials, 2019: p. 119739.
263. Basalah, A., et al., *Characterizations of additive manufactured porous titanium implants.* Journal of Biomedical Materials Research Part B: Applied Biomaterials, 2012. **100B**(7): p. 1970-1979.
264. Khorasani, A.M., et al., *Modelling of laser powder bed fusion process and analysing the effective parameters on surface characteristics of Ti-6Al-4V.* International Journal of Mechanical Sciences, 2020. **168**: p. 105299.
265. Ataee, A., et al., *Ultrahigh-strength titanium gyroid scaffolds manufactured by selective laser melting (SLM) for bone implant applications.* Acta Materialia, 2018. **158**: p. 354-368.

266. Yang, L., et al., *Additive Manufacturing of Metals: The Technology, Materials, Design and Production*. 2018: Springer Publishing Company, Incorporated.
267. van Hengel, I.A., et al., *Selective laser melting porous metallic implants with immobilized silver nanoparticles kill and prevent biofilm formation by methicillin-resistant Staphylococcus aureus.* Biomaterials, 2017. **140**: p. 1-15.
268. Sheydaeian, E., et al., *On the effect of throughout layer thickness variation on properties of additively manufactured cellular titanium structures.* Additive Manufacturing, 2017. **18**: p. 40-47.
269. Basalah, A., S. Esmaeili, and E. Toyserkani, *On the influence of sintering protocols and layer thickness on the physical and mechanical properties of additive manufactured titanium porous bio-structures.* Journal of Materials Processing Technology, 2016. **238**: p. 341-351.
270. Li, Y., et al., *Additively manufactured functionally graded biodegradable porous iron.* Acta biomaterialia, 2019. **96**: p. 646-661.
271. Moridi, A., et al., *Deformation and failure mechanisms of Ti–6Al–4V as built by selective laser melting*. Materials Science and Engineering: A, 2019. **768**: p. 138456.
272. Li, Y., et al., *Additively manufactured functionally graded biodegradable porous zinc.* Biomaterials Science, 2020.
273. Wang, Y., et al., *Hip implant design with three-dimensional porous architecture of optimized graded density*. Journal of Mechanical Design, 2018. **140**(11).
274. Sheydaeian, E. and E. Toyserkani, *Additive manufacturing functionally graded titanium structures with selective closed cell layout and controlled morphology.* The International Journal of Advanced Manufacturing Technology, 2018. **96**(9): p. 3459-3469.
275. Zadpoor, A.A., *Additively manufactured porous metallic biomaterials.* Journal of Materials Chemistry B, 2019. **7**(26): p. 4088-4117.
276. Basalah, A., S. Esmaeili, and E. Toyserkani, *Mechanical properties of additive-manufactured porous titanium bio-structures with*

oriented macro-scale channels. The International Journal of Advanced Manufacturing Technology, 2016. **84**(9): p. 2239-2246.

277. du Plessis, A., et al., *Numerical comparison of lattice unit cell designs for medical implants by additive manufacturing.* Virtual and Physical Prototyping, 2018. **13**(4): p. 266-281.
278. Vilardell, A.M., et al., *Topology optimization and characterization of Ti6Al4V ELI cellular lattice structures by laser powder bed fusion for biomedical applications.* Materials Science and Engineering: A, 2019. **766**: p. 138330.
279. Qiu, C., et al., *Influence of processing conditions on strut structure and compressive properties of cellular lattice structures fabricated by selective laser melting.* Materials Science and Engineering: A, 2015. **628**: p. 188-197.
280. Hazlehurst, K.B., C.J. Wang, and M. Stanford, *An investigation into the flexural characteristics of functionally graded cobalt chrome femoral stems manufactured using selective laser melting.* Materials & Design, 2014. **60**: p. 177-183.
281. Bahraminasab, M., et al., *Multi-objective design optimization of functionally graded material for the femoral component of a total knee replacement.* Materials & Design, 2014. **53**: p. 159-173.
282. Kadkhodapour, J., et al., *The relationships between deformation mechanisms and mechanical properties of additively manufactured porous biomaterials.* Journal of the mechanical behavior of biomedical materials, 2017. **70**: p. 28-42.
283. Schindelin, J., et al., *Fiji: an open-source platform for biological-image analysis.* Nature methods, 2012. **9**(7): p. 676-682.
284. Nguyen, T.D., et al., *Scaffolds with a High Surface Area-to-Volume Ratio and Cultured Under Fast Flow Perfusion Result in Optimal O2 Delivery to the Cells in Artificial Bone Tissues.* Applied Sciences, 2019. **9**(11): p. 2381.
285. Osorio, M., et al., *Development of novel three-dimensional scaffolds based on bacterial nanocellulose for tissue engineering and regenerative medicine: Effect of processing methods, pore size, and surface area.* Journal of Biomedical Materials Research Part A, 2019. **107**(2): p. 348-359.

286. Taniguchi, N., et al., *Effect of pore size on bone ingrowth into porous titanium implants fabricated by additive manufacturing: an in vivo experiment.* Materials Science and Engineering: C, 2016. **59**: p. 690-701.
287. Ouyang, P., et al., *Hydromechanical mechanism behind the effect of pore size of porous titanium scaffolds on osteoblast response and bone ingrowth.* Materials & Design, 2019. **183**: p. 108151.
288. Matilainen, V.-P., et al., *Preliminary investigation of keyhole phenomena during single layer fabrication in laser additive manufacturing of stainless steel.* Physics Procedia, 2015. **78**: p. 377-387.
289. Mitsak, A.G., et al., *Effect of polycaprolactone scaffold permeability on bone regeneration in vivo.* Tissue Engineering Part A, 2011. **17**(13-14): p. 1831-1839.
290. Al-Ketan, O., et al., *Microarchitected stretching-dominated mechanical metamaterials with minimal surface topologies.* Advanced Engineering Materials, 2018. **20**(9): p. 1800029.
291. Kaur, M., et al., *3D printed stretching-dominated micro-trusses.* Materials & Design, 2017. **134**: p. 272-280.
292. Blaeser, A., et al., *Controlling shear stress in 3D bioprinting is a key factor to balance printing resolution and stem cell integrity.* Advanced healthcare materials, 2016. **5**(3): p. 326-333.

Appendix A. Statistical Analysis

Table A.1. Resolution VI fractional factorial design along with the volume response values. (The value of the volume was not obtained for those sets of parameters that were not successfully jetted).

Run order	Factors						Response
	MCF%	V	CyT	OT	CT	FCT	Volume
1	17	120	4	0.15	0.2	1.12	7.84E+08
5	17	120	2	0.15	0.2	0.02	3.04E+09
6	17	120	4	0.15	0.2	1.12	1.83E+09
8	17	120	4	0.2	0.2	0.02	1.85E+09
10	17	120	2	0.2	0.2	1.12	9.19E+08
16	17	100	4	0.15	0.2	0.02	1.86E+09
17	17	100	2	0.15	0.15	0.02	3.27E+09
19	17	100	4	0.2	0.15	0.02	1.58E+09
20	17	120	2	0.15	0.15	1.12	1.23E+09
21	17	100	4	0.2	0.2	1.12	1.8E+09
23	17	120	2	0.2	0.2	1.12	N/A
24	17	100	4	0.15	0.15	1.12	1.8E+09
25	17	100	2	0.15	0.2	1.12	1.68E+09
26	17	100	4	0.2	0.15	0.02	1.89E+09
27	17	100	2	0.2	0.2	0.02	3.35E+09
30	17	120	4	0.2	0.15	1.12	1.35E+09
31	17	100	4	0.15	0.2	0.02	1.38E+09
32	17	120	4	0.15	0.2	1.12	1.43E+09
41	17	100	2	0.15	0.2	1.12	1.44E+09
44	17	120	2	0.2	0.15	0.02	2.4E+09
46	17	100	4	0.15	0.2	0.02	1.86E+09
47	17	100	2	0.2	0.2	0.02	3.12E+09
48	17	100	4	0.2	0.15	0.02	1.64E+09
51	17	100	2	0.2	0.2	0.02	3.55E+09
52	17	120	4	0.2	0.15	1.12	1.28E+09
54	17	100	2	0.2	0.15	1.12	1.32E+09
58	17	100	4	0.2	0.2	1.12	1.35E+09
61	17	120	2	0.2	0.15	0.02	1.37E+09
63	17	120	2	0.15	0.15	1.12	N/A
64	17	120	2	0.15	0.2	0.02	2.41E+09
65	17	120	4	0.15	0.15	0.02	1.55E+09
66	17	120	4	0.15	0.15	0.02	1.48E+09
67	17	100	2	0.2	0.15	1.12	1.13E+09
70	17	120	4	0.2	0.15	1.12	1.35E+09
71	17	100	4	0.15	0.15	1.12	1.67E+09
72	17	100	2	0.15	0.2	1.12	1.37E+09
74	17	100	4	0.15	0.15	1.12	1.25E+09
78	17	100	2	0.2	0.15	1.12	1.02E+09
82	17	120	4	0.15	0.15	0.02	1.35E+09
88	17	100	4	0.2	0.2	1.12	1.32E+09

89	17	120	4	0.2	0.2	0.02	5.27E+08
90	17	120	2	0.2	0.2	1.12	N/A
91	17	120	2	0.2	0.15	0.02	1.43E+09
93	17	100	2	0.15	0.15	0.02	2.8E+09
95	17	120	2	0.15	0.15	1.12	N/A
99	17	120	4	0.2	0.2	0.02	3.82E+08
100	17	120	2	0.15	0.2	0.02	2.03E+09
102	17	100	2	0.15	0.15	0.02	3.07E+09
3	23.5	110	3	0.175	0.175	0.57	1.27E+09
18	23.5	110	3	0.175	0.175	0.57	9.57E+08
43	23.5	110	3	0.175	0.175	0.57	8.41E+08
73	23.5	110	3	0.175	0.175	0.57	8.87E+08
87	23.5	110	3	0.175	0.175	0.57	1.08E+09
98	23.5	110	3	0.175	0.175	0.57	1.33E+09
2	30	100	2	0.2	0.15	0.02	1.05E+09
4	30	100	2	0.15	0.2	0.02	1.15E+09
7	30	120	4	0.2	0.2	1.12	3.68E+08
9	30	120	4	0.15	0.15	1.12	2.7E+08
11	30	100	2	0.2	0.15	0.02	9.37E+08
12	30	100	2	0.15	0.2	0.02	1.11E+09
13	30	120	2	0.2	0.15	1.12	N/A
14	30	120	4	0.2	0.15	0.02	4.45E+08
15	30	100	4	0.2	0.2	0.02	3.55E+08
22	30	100	4	0.15	0.15	0.02	1.26E+09
28	30	120	2	0.2	0.15	1.12	N/A
29	30	120	2	0.2	0.2	0.02	N/A
33	30	100	4	0.2	0.2	0.02	7.72E+08
34	30	100	2	0.2	0.2	1.12	N/A
35	30	100	4	0.2	0.15	1.12	7.73E+08
36	30	100	2	0.15	0.15	1.12	N/A
37	30	120	4	0.2	0.15	0.02	6.89E+08
38	30	120	2	0.15	0.2	1.12	N/A
39	30	120	2	0.2	0.15	1.12	N/A
40	30	100	2	0.2	0.2	1.12	N/A
42	30	120	2	0.15	0.15	0.02	6.49E+08
45	30	100	4	0.15	0.2	1.12	3.79E+08
49	30	100	2	0.2	0.2	1.12	N/A
50	30	100	2	0.15	0.15	1.12	N/A
53	30	100	4	0.2	0.15	1.12	1.53E+08
55	30	120	4	0.15	0.15	1.12	N/A
56	30	120	2	0.15	0.2	1.12	N/A
57	30	120	2	0.2	0.2	0.02	N/A
59	30	100	2	0.15	0.2	0.02	8.01E+08
60	30	100	4	0.15	0.15	0.02	5.73E+08
62	30	120	4	0.15	0.2	0.02	5.33E+08
68	30	120	4	0.15	0.15	1.12	3.77E+08
69	30	100	4	0.15	0.15	0.02	4.89E+08
75	30	120	4	0.2	0.15	0.02	2.79E+08
76	30	120	4	0.15	0.2	0.02	2.74E+08

77	30	120	4	0.15	0.2	0.02	4.84E+08
79	30	100	4	0.15	0.2	1.12	5.23E+08
80	30	120	2	0.2	0.2	0.02	N/A
81	30	100	4	0.2	0.15	1.12	5.65E+08
83	30	100	4	0.15	0.2	1.12	4.59E+08
84	30	120	4	0.2	0.2	1.12	N/A
85	30	120	2	0.15	0.15	0.02	6.54E+08
86	30	100	2	0.15	0.15	1.12	N/A
92	30	120	4	0.2	0.2	1.12	N/A
94	30	120	2	0.15	0.15	0.02	5.81E+08
96	30	100	4	0.2	0.2	0.02	2.92E+08
97	30	100	2	0.2	0.15	0.02	8.51E+08
101	30	120	2	0.15	0.2	1.12	N/A

Table A.2. ANOVA for the standard deviation of volume in the fractional factorial design.

Source	DF	Adj SS	Adj MS	F-Value	P-Value
Model	27	4.49153E+19	1.66353E+18	17.21	0.000
Linear	6	2.57609E+19	4.29349E+18	44.41	0.000
MCF%	1	2.01645E+18	2.01645E+18	20.86	0.000
V	1	7.32116E+16	7.32116E+16	0.76	0.388
CyT	1	5.59420E+16	5.59420E+16	0.58	0.450
OT	1	3.10544E+15	3.10544E+15	0.03	0.858
CT	1	2.64633E+16	2.64633E+16	0.27	0.603
FCT	1	5.33074E+18	5.33074E+18	55.14	0.000
2-Way Interactions	15	8.64029E+18	5.76019E+17	5.96	0.000
MCF%*V	1	7.38128E+16	7.38128E+16	0.76	0.386
MCF%*CyT	1	1.00820E+17	1.00820E+17	1.04	0.312
MCF%*OT	1	8.57092E+16	8.57092E+16	0.89	0.351
MCF%*CT	1	9.71270E+15	9.71270E+15	0.10	0.753
MCF%*FCT	1	3.50546E+16	3.50546E+16	0.36	0.550
V*CyT	1	4.81843E+12	4.81843E+12	0.00	0.994
V*OT	1	2.99922E+15	2.99922E+15	0.03	0.861
V*CT	1	9.32593E+14	9.32593E+14	0.01	0.922
V*FCT	1	8.32604E+16	8.32604E+16	0.86	0.358
CyT*OT	1	2.62039E+16	2.62039E+16	0.27	0.605
CyT*CT	1	8.02701E+16	8.02701E+16	0.83	0.366

CyT*FCT	1	5.00093E+18	5.00093E+18	51.73	0.000
OT*CT	1	1.55730E+17	1.55730E+17	1.61	0.210
OT*FCT	1	8.48626E+15	8.48626E+15	0.09	0.768
CT*FCT	1	4.40995E+16	4.40995E+16	0.46	0.502
3-Way Interactions	6	8.45270E+17	1.40878E+17	1.46	0.211
MCF%*V*CyT	1	2.72839E+16	2.72839E+16	0.28	0.598
MCF%*V*OT	1	2.47706E+17	2.47706E+17	2.56	0.115
MCF%*V*CT	1	3.78151E+16	3.78151E+16	0.39	0.534
MCF%*V*FCT	1	3.25776E+17	3.25776E+17	3.37	0.072
MCF%*CyT*OT	1	5.08450E+16	5.08450E+16	0.53	0.472
MCF%*CyT*CT	1	3.87698E+15	3.87698E+15	0.04	0.842
Error	52	5.02707E+18	9.66745E+16		
Total	79	4.99423E+19			
R^2	89.93%				
Adjusted R^2	84.71%				

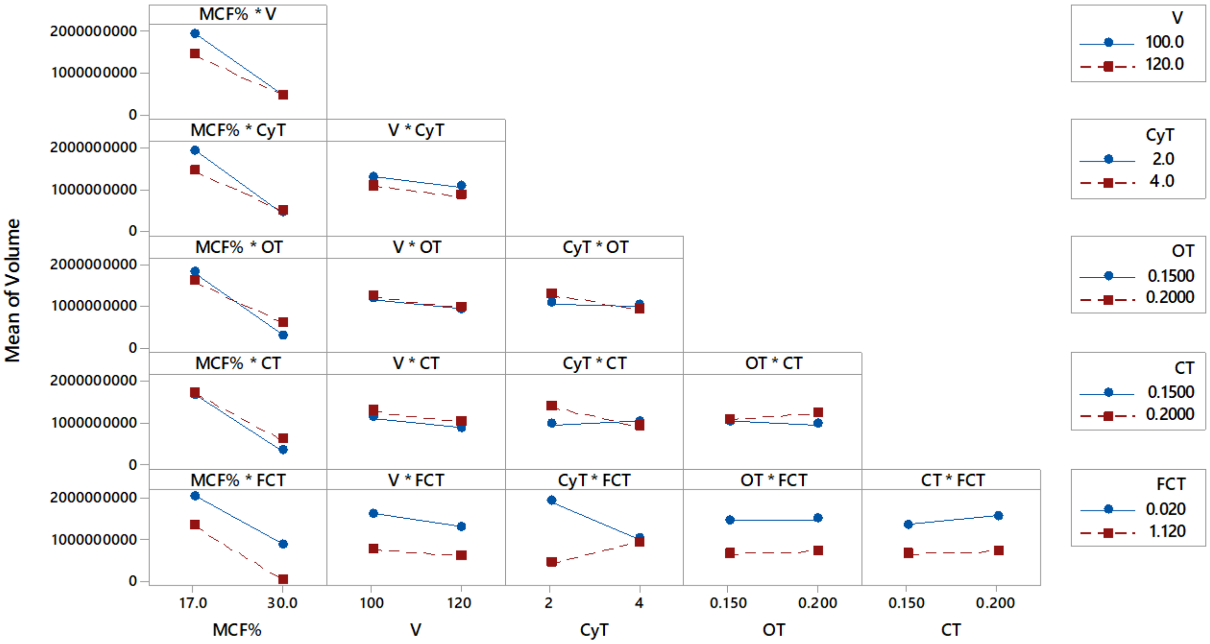

Figure A.1. The interaction plots of marginal means for volume

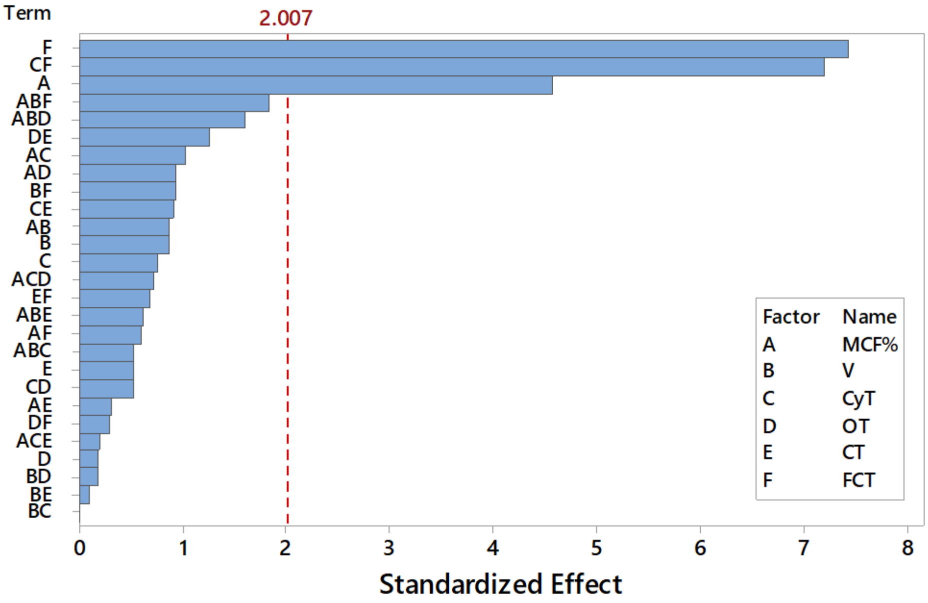

Figure A.2. Pareto chart of the standardized effects for volume

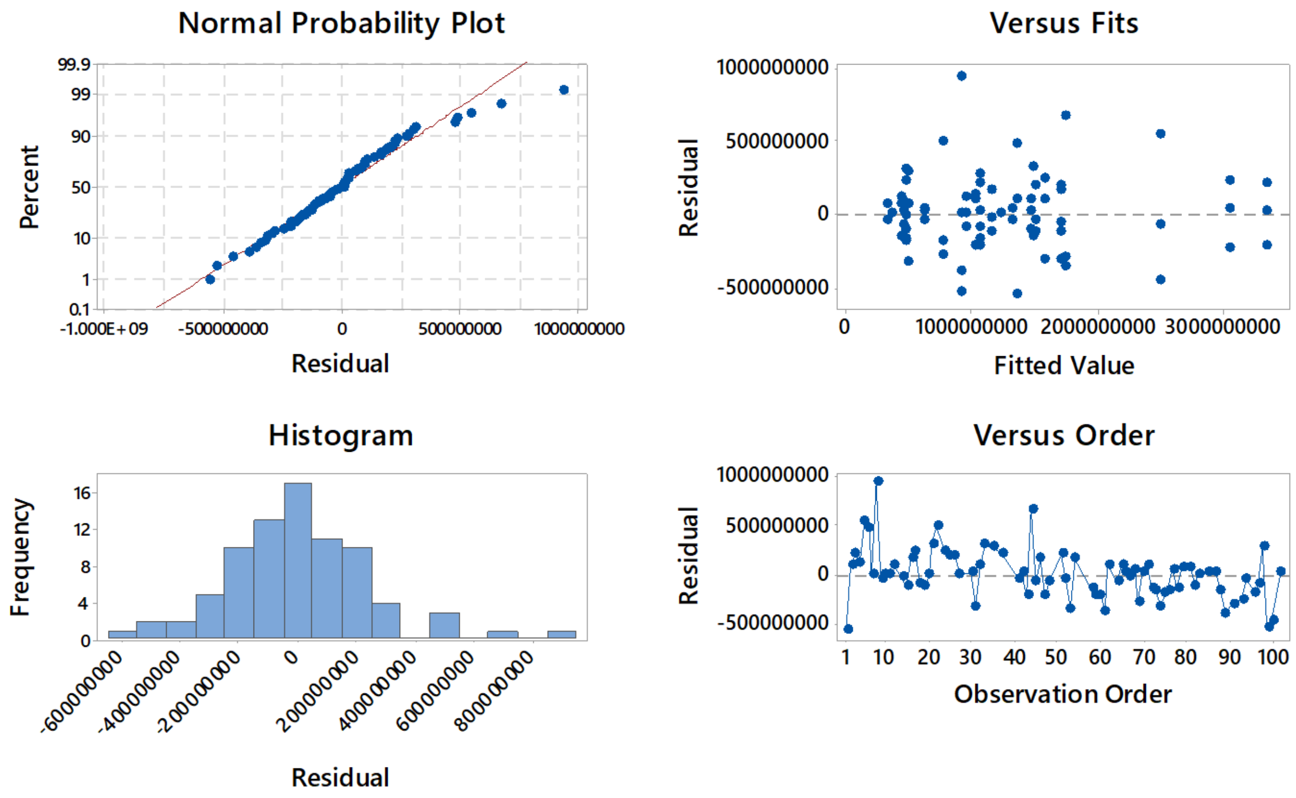

Figure A.3. Residual plots for volume response. These plots confirm that the residuals are randomly distributed and independent. Additionally, the residuals have constant variance. Due to unsuccessful jetting, the response value for some sets of parameters was not available. Therefore, small discrepancies and a few outliers are negligible.

Table A.3. ANOVA for the standard deviation of volume in the fractional factorial design after removing insignificant factors.

Source	DF	Adj SS	Adj MS	F-Value	P-Value
Model	4	3.57226E+19	8.93064E+18	47.10	0.000
Linear	3	3.29547E+19	1.09849E+19	57.94	0.000
MCF%	1	2.43896E+19	2.43896E+19	128.64	0.000
CyT	1	1.07979E+18	1.07979E+18	5.70	0.020
FCT	1	5.46652E+18	5.46652E+18	28.83	0.000
2-Way Interactions	1	4.31563E+18	4.31563E+18	22.76	0.000
CyT*FCT	1	4.31563E+18	4.31563E+18	22.76	0.000
Error	75	1.42198E+19	1.89597E+17		
Curvature	1	5.16694E+15	5.16694E+15	0.03	0.870

Lack-of-Fit	22	9.18754E+18	4.17616E+17	4.32	0.000
Pure Error	52	5.02707E+18	9.66745E+16		
Total	79	4.99423E+19			
R^2	71.53%				
Adjusted R^2	70.01%				